UNIVERSITY OF HELSINKI REPORT SERIES IN PHYSICS

HU-P-D263

ATOMISTIC STUDY OF SURFACE EFFECTS IN METALS

Simon Vigonski

Division of Materials Physics
Department of Physics
Faculty of Science
University of Helsinki
Helsinki, Finland

Institute of Physics
Faculty of Science and Technology
University of Tartu
Tartu, Estonia

ACADEMIC DISSERTATION

To be presented with the permission of the Faculty of Science of University of Helsinki, for public criticism in auditorium A110 of the Department of Chemistry (Chemicum), on January 4th, 2019, at 11 o'clock.

HELSINKI 2018

This study was carried out at the Institute of Technology, University of Tartu, Estonia.

The dissertation was admitted on the 30th of October 2018 in partial fulfilment of the requirements of the degree of Doctor of Philosophy in physics, and was allowed for defense by the Council of the Institute of Physics, University of Tartu.

Supervisors: Vahur Zadin, PhD
Institute of Technology
Faculty of Science and Technology
University of Tartu, Estonia

Flyura Djurabekova, PhD
Department of Physics and Helsinki Institute of Physics
Faculty of Science
University of Helsinki, Finland

Prof. Alvo Aabloo, PhD
Institute of Technology
Faculty of Science and Technology
University of Tartu, Estonia

Pre-evaluators: Sebastian Vielhauer, PhD
Institute of Physics
Faculty of Science and Technology
University of Helsinki, Estonia

Prof. Adam Foster, PhD
Department of Applied Physics
Aalto University, Finland

Opponent: Prof. Roberto Iglesias, PhD
Department of Physics
University of Oviedo, Spain

ISSN 0356-0961
ISBN 978-951-51-2793-8 (print)
ISBN 978-951-51-2794-5 (pdf)

European Union
European Regional
Development Fund

Investing
in your future

Table of Contents

Abstract

Atomistic simulations are a useful way to study nanoscale metal structures. At the nanoscale, the surface to volume ratio of the objects becomes large and surface effects start to play a critically important role. The internal stress near a surface can reach the GPa range and thus its effects should not be neglected when dealing with nanowires and other nanostructures. Similarly, surface diffusion of atoms is important in the manufacturing process and subsequent stability of nanostructures.

In the study of vacuum breakdown on Cu surfaces, dislocation activity and surface atom diffusion are thought to play a role in the formation of field enhancing emitters.

This work investigates a possible mechanism of nucleation of a nanofeature on metal surfaces under high electric fields in the presence of a near-surface defect, and the stability of Au nanowires with respect to surface diffusion. The simulation methods of molecular dynamics, kinetic Monte Carlo and finite elements are employed.

A subsurface Fe precipitate is used as an example of subsurface extended defects, and the nucleation of dislocations in regions of high stress concentration is simulated. A process of forming a protrusion on the surface near the precipitate due to dislocation propagation is shown, as well as the possibility of forming new voids on the precipitate interface.

Since atomistic simulations are heavily limited in size and time scales, larger scale simulations are conducted by using finite element modelling of nanoscale material behavior under external loading. However, such modeling requires the development of an accurate model of surface stress. In this work, a surface stress model is implemented into a continuum finite element model to enable faster calculations of more extensive nanoscale systems, as well as to combine the mechanical model with electrical effects in vacuum breakdown research. The internal stresses given by the model are validated in comparison with molecular dynamics simulations and against an analytical model of dislocation emission from a near-surface void.

Kinetic Monte Carlo simulation is a suitable tool to simulate diffusion processes. However, setting up KMC simulations requires a parametrization of atomic migration barriers. A consistent parametrization scheme, called the tethering method, is developed in the current work. The tethering method provides a robust automatic process to calculate migration barriers for on-lattice diffusion simulations. It allows the calculation of barriers for unstable processes, while having a minimal effect on stable barriers.

The tethering method is used to create a parametrization for Au, which is used to simulate nanowire junction fragmentation. Nanowire junctions break up in a process similar to Rayleigh instability. In conjunction with experiments, it is shown that junctions fragment at a low temperature when nanowires themselves remain whole.

Simulations demonstrate that the breakup can be explained by surface energy minimization due to atom diffusion and that the formation of a fragment at the nanowire crossing point is very reliable.

List of publications

I. S. Vigonski, F. Djurabekova, M. Veske, A. Aabloo, V. Zadin, Molecular dynamics simulations of near-surface Fe precipitates in Cu under high electric fields, Modelling Simul. Mater. Sci. Eng. 23 (2015) 025009. doi:10.1088/0965-0393/23/2/025009.

II. V. Zadin, M. Veske, S. Vigonski, V. Jansson, J. Muszinsky, S. Parviainen, A. Aabloo, F. Djurabekova, Simulations of surface stress effects in nanoscale single crystals, Modelling Simul. Mater. Sci. Eng. 26 (2018) 035006. doi:10.1088/1361-651X/aaa928.

III. S. Vigonski, M. Veske, A. Aabloo, F. Djurabekova, V. Zadin, Verification of a multiscale surface stress model near voids in copper under the load induced by external high electric field, Applied Mathematics and Computation. 267 (2015) 476–486. doi:10.1016/j.amc.2015.01.102.

IV. E. Baibuz, S. Vigonski, J. Lahtinen, J. Zhao, V. Jansson, V. Zadin, F. Djurabekova, Migration barriers for surface diffusion on a rigid lattice: challenges and solutions, Computational Materials Science. 146 (2017) 287–302. doi: 10.1016/j.commatsci.2017.12.054.

IV.a. E. Baibuz, S. Vigonski, J. Lahtinen, J. Zhao, V. Jansson, V. Zadin, F. Djurabekova, Data sets of migration barriers for atomistic Kinetic Monte Carlo simulations of Cu self-diffusion via first nearest neighbour atomic jumps, Data in Brief. 17 (2018) 739–743. doi:10.1016/j.dib.2018.01.066.

IV.b. E. Baibuz, S. Vigonski, J. Lahtinen, J. Zhao, V. Jansson, V. Zadin, F. Djurabekova, Data sets of migration barriers for atomistic Kinetic Monte Carlo simulations of Fe self-diffusion, Data in Brief. 19 (2018) 564–569. doi:10.1016/j.dib.2018.04.060.

V. S. Vigonski, V. Jansson, S. Vlassov, B. Polyakov, E. Baibuz, S. Oras, A. Aabloo, F. Djurabekova, V. Zadin, Au nanowire junction breakup through surface atom diffusion, Nanotechnology. 29 (2018) 015704. doi:10.1088/1361-6528/aa9a1b.

List of abbreviations

1NN	First nearest neighbor
2NN	Second nearest neighbor
BCC	Body centered cubic lattice
CEM	Corrected effective medium
CG	Conjugate gradient
CLIC	Compact Linear Collider
DC	Direct current
DFT	Density functional theory
EAM	Embedded atom method
FCC	Face centered cubic lattice
FEM	Finite element method
HCP	Hexagonal close-packed lattice
Kimocs	Kinetic Monte Carlo for surfaces
KMC	Kinetic Monte Carlo
MC	Monte Carlo
MD	Molecular dynamics
MEP	Minimum energy path
MS	Molecular statics
NEB	Nudged elastic band
NpT	Isothermal-isobaric ensemble
NVE	Microcanonical ensemble
NVT	Canonical ensemble
PE	Potential energy
P-K	Piola-Kirchhoff stress tensor

1 Introduction

Metal surfaces in the nanoscale are of considerable interest in nanotechnology research. Nanostructures, such as nanopillars, nanoparticles and nanowires have unique mechanical, electrical and optical properties that allow them to be useful in many technologies [1]. For example, historically, the most well-known use of metal nanoparticles was in colored glass [2]. Luster technology has existed since the 9th century in Mesopotamia, even if the practitioners did not realize the role or even the existence of nanoparticles [3].

In modern areas of research, a wide range of applications of nanostructures are being explored, like gold nanopillar electrodes for bioelectrical signals [4,5] and plasmonic trapping [6], gold nanowires in solar cells [7] and flexible displays [8], and nanoparticles in biochemical sensors [9].

Surface elastic and diffusion properties become extremely important for these structures due to their high surface to volume ratio. The elasticity and plasticity of nanowires play an important role in nanoelectromechanical systems [10,11] or nanophotonics [12], where periodic bending or large deformations are required. Loading results in dislocation nucleation and motion, both of which are thermally assisted processes [13,14]. This, together with the diffusion of atoms on the surface becomes important in thermal treatment of nanostructures. For example, thermal diffusion breakup was observed for Au [15,16], Ag [17], and Cu [18] nanowires.

Another area of interest is the field of vacuum breakdowns, where nanoscale surface modifications can lead to enhanced field emission followed by plasma formation in high-field conditions [19]. These effects are of critical importance in fusion reactors [20], vacuum circuit breakers [21], or particle accelerators [22]. In particular, the planned Compact Linear Accelerator (CLIC) [23–25] with its 100 MV/m accelerating gradient is faced with serious vacuum breakdown problems.

Direct current (DC) field emission experiments with the CLIC accelerating structures have shown field enhancement factors of the order of 100 in Cu [26], when the results were fitted to the Fowler-Nordheim emission model [27]. This points towards significant surface roughness or high aspect ratio nanopillars which would be responsible for the geometrical field enhancement. However, no such structures have ever been observed and the possible mechanisms of their formation are currently unknown. An indication that elasticity or dislocation properties of materials play a role in breakdown initiation comes from the fact that the breakdown resistance of metals is correlated with their crystal structure [26].

Atomistic simulations have proven to be an effective tool when the description of the microscopic behavior under extreme conditions is required. For example, the surface

stress effects in gold nanowires [28] and nanopillars [29] have been studied using molecular dynamics (MD) simulations. The diffusion of surface atoms during cold welding of silver and gold nanowires was identified using MD [30]. Kinetic Monte Carlo (KMC) simulations were used to study gold nanoparticle structural transitions [31] and Ge nanowire breakup [32].

In the study of breakdown initiation processes, MD simulations have also proven useful. Atomistic studies of dislocation nucleation around a sub-surface void [33] and temperature changes in a long thin protrusion [34,35] in high field conditions have provided insights into the possibilities of field emitter formation. Combined MD and finite element method (FEM) simulations [36] have indicated that a positive feedback mechanism exists between the heating and growth of an emitter [37].

The stability of nanotips is influenced strongly by their nanocrystalline structure [38] and surface diffusion properties [39,40]. Surface diffusion likely also plays a role in nanotip formation as atoms diffuse in the direction of field gradient, i.e. toward a higher surface curvature [41].

The available spatial and temporal extent of MD simulations is limited due to their computational complexity. It is desirable to use more scalable simulation techniques, like FEM, to model more extensive (but still nanoscale) features. FEM simulations have been used to study the field enhancement due to surface irregularities [42] and to model the plastic deformation under high field conditions [43]. However, standard continuum models do not include nanoscale surface effects. Therefore, to more precisely model nanoscale surfaces using the fast FEM technique, the macroscopic stress model needs to be extended by including the effects of surface stress. Previous efforts to achieve this include a combined level set and extended FEM approach [44] or an interatomic potential based approach [45].

1.1 Purpose and structure of this work

This work aims to understand the formation and disappearance of surface structures hypothesized to be the cause of vacuum breakdowns. To that end, atomistic computer simulations are used to study the nanoscale surface stress and diffusion of Cu and Au nanostructures. The objectives are as follows:

1. To investigate the dislocation behavior due to a near-surface precipitate with the aim of identifying a possibility of significant surface modification that would be relevant for the CLIC breakdown studies.
2. To develop, implement and validate a fast surface stress model for FEM that would take into account the crystallographic orientation of free surfaces, thus allowing us to extend the time and length scales of simulations compared to MD; to use the model to investigate the size effect of subsurface voids pertaining to dislocation nucleation.

3. To investigate the stability of surface nanostructures using KMC diffusion simulations and to develop a consistent automated method for the parametrization of materials for on-lattice KMC.

As a result, a multiscale suite of simulation techniques is developed and used to characterize the formation and stability of surface nanostructures. The surface stress model for FEM is validated qualitatively and quantitatively against MD simulations. The KMC model is confirmed by experiments.

The physical processes investigated in this work are introduced in chapter 0. Chapter 0 describes the three simulation methods used: MD (publications I-III), FEM (publications II-III), and KMC (publications IV-V). In particular, some specific techniques for calculating stress in MD are described in section 3.1.1. The new surface stress model for FEM (publications II-III) is described in section 3.2.1 and the tethering method for KMC parametrization (publication IV) is presented in sections 3.3.2-3.3.4.

Chapter 4 is based on publication I and fulfills objective 1. The MD method is used to study the effects of near-surface precipitates when the material is subjected to an external tensile stress originating from the electric field. Dislocation nucleation around a near-surface Fe precipitate in Cu is simulated and results are presented.

In chapter 0, based on publications II-III, the accuracy of the coupled surface and bulk stress model for FEM is validated in comparison to MD simulations by calculating stresses surrounding a void. It is used to calculate dislocation nucleation conditions around a void, which are then compared to a previously published analytical model.

Chapter 6 is based on publications IV-V and studies the surface diffusion of metal atoms using KMC simulations. The newly developed parametrization technique is used to generate a model for Au, which is used to study the diffusion-driven breakup of Au nanowires.

Finally, chapter 7 concludes the work and gives an outlook for future developments in the field.

1.2 Author's contribution

Publication I. The author planned and performed all simulations in the paper, analyzed all results and prepared the manuscript.

Publication II. The author conducted the MD simulations used in the paper together with M. Veske. The author performed the comparisons between the FEM and MD results and wrote the corresponding analysis sections of the manuscript.

Publication III. The author conducted the MD simulations used in the paper together with M. Veske. The author analyzed the results of the paper and prepared the manuscript.

Publication IV. The author developed the automatic barrier parametrization scheme and the tethering force approach for KMC calculations described in the paper and wrote the parts of the manuscript relating to those methods. **Publications IV.a** and **IV.b** are data articles accompanying publication IV that use the author's code to calculate barriers for Cu and Fe, respectively.

Publication V. The author used the methods of publication IV to generate a KMC parametrization for Au and conducted all simulations in the paper. The author analyzed the results and prepared the manuscript.

2 Physical phenomena near surfaces

2.1 Mechanical stress in bulk and near surfaces

The Cauchy stress [46–48] describes the forces acting in a material and is defined with the help of the Cauchy stress principle. The principle states that internal forces can be handled in the same way as external surface forces by defining an infinitesimal volume element with virtual surfaces. The internal tractions $\boldsymbol{t}$ acting across these virtual surfaces from one part of the material on another define the stress tensor:

$$\boldsymbol{t} = \boldsymbol{\sigma n}\,, \tag{1}$$

where $\boldsymbol{\sigma}$ is the Cauchy stress tensor and $\boldsymbol{n}$ is the normal vector of the virtual surface. The diagonal components of the tensor represent tensile or compressive forces while the off-diagonal components represent the shear forces. When angular momentum is balanced, the stress tensor is symmetric.

The Cauchy stress principle is specifically meant to handle the bulk stress field, but taking the virtual surfaces coincident with physical material surfaces and the tractions equal to the forces acting on them, surface stress is obtained.

In principle, there is no difference between physical material surfaces and virtual surfaces in the treatment of stress. This work, however, is specifically focused on the processes and forces occurring on physical surfaces.

The surface of a metal experiences stress due to the missing bonds on the side exposed to the vacuum [49]. The surface energy, and therefore the magnitude of surface stress depends on the crystallographic orientation of the surface [50].

In macroscopic applications, the surface stress of solid materials is usually disregarded, but on the nanoscale the stress field due to surfaces becomes important in describing sub-surface processes. For example, the motion of dislocations is influenced by surface stress. In extending surface effects into macroscale continuum modeling, the Cauchy-Born principle can be applied [45], which equates the continuum strain field with the atomistic displacements due to surface relaxation.

2.2 Dislocations

Under external stress, material initially deforms elastically. As the stress is increased, the deformation transitions into the plastic regime. The onset of plasticity occurs when the external stress becomes greater than the yield strength for the given material, and continues until the ultimate tensile stress is reached. Plastic deformations in metals are driven by extended linear defects, known as dislocations. Dislocations [51–53] occur in crystalline materials when a part of the material slips with respect to the adjacent part

causing a mismatch of atomic planes. The dislocation line marks the border between the slipped and unslipped region.

The dislocation is characterized by the Burgers vector $\boldsymbol{b}$ which shows the direction and magnitude of the slip. The Burgers vector is typically defined by comparing a Burgers circuit drawn in pristine material to that drawn around a dislocation. The direction and magnitude of the resulting mismatch constitute the Burgers vector. The angle between the Burgers vector and the dislocation line determines the character of the dislocation: when they are perpendicular, the dislocation has edge character, when they are parallel, the dislocation has screw character, and in other cases the dislocation has mixed character. The Burgers circuits for the edge and screw dislocations are illustrated in Figure 1.

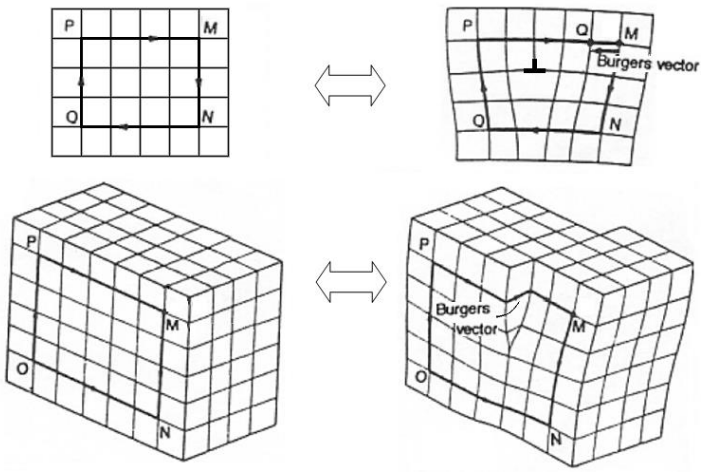

Figure 1. Burgers circuit constructions for the edge (top) and screw (bottom) dislocations. When a dislocation is present (right side), an extra step along the lattice is necessary to close the circuit compared to the undeformed material (left side). This extra step determines the Burgers vector of the dislocation. Image adapted from [54].

The dislocation line and the Burgers vector together determine the glide plane of the dislocation. Dislocation motion is driven by stress inside the material. Motion along the glide plane involves gradual slip of the material and is the main mechanism of plasticity in crystals. Motion perpendicular to the glide plane, called climb, requires the diffusion of vacancies toward or away from the dislocation line and is only significant at high temperatures.

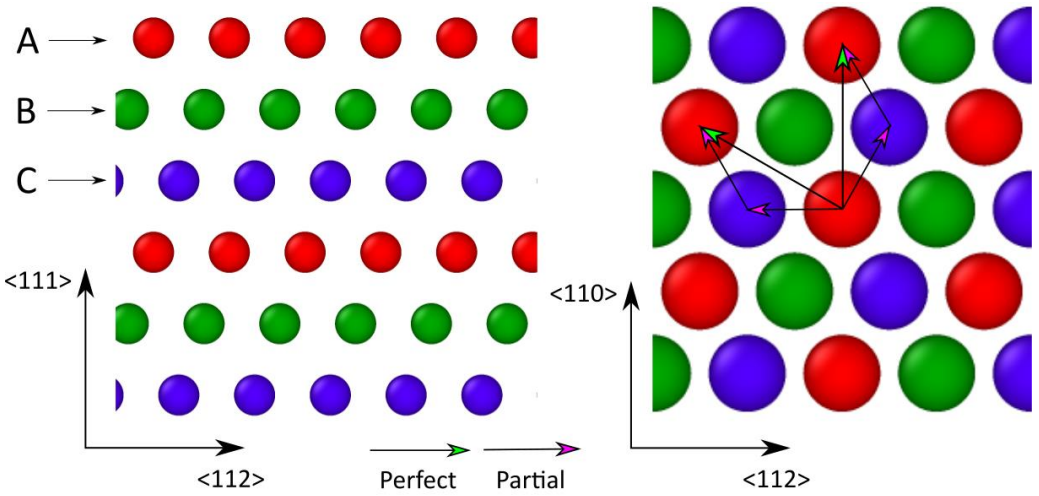

Figure 2. The FCC crystal structure. The layer structure in the <111> direction is shown on the left. Atoms are colored according to their layer (A, B, C). The slip system on the {111} surface is shown on the right. Two perfect dislocation Burgers vectors and four partial dislocation Burgers vectors are shown.

The energetically preferential slip planes and slip directions together constitute slip systems. In face centered cubic (FCC) crystals, slip occurs on the {111} planes in the <110> directions. Furthermore, perfect dislocations dissociate into partials surrounding a stacking fault. A partial dislocation involves a slip that does not restore the perfect lattice, but rather moves a layer of atoms into a non-lattice energy minimum. The partial dislocations in FCC crystals have a Burgers vector of $\frac{1}{6}$<112>, which move the atoms as illustrated in Figure 2.

In the <111> direction, the FCC crystal has an ABC layer structure, as seen on Figure 2, left. Atoms are colored according to their layer. In the right figure, the {111} surface is shown. All red atoms are in the A layer, all green atoms in the B layer below the A layer, and all blue atoms are in the C layer at the bottom. Two example perfect dislocations are shown, as well as their dissociation into partial dislocations. In case of perfect dislocations, atoms move from an A layer position to another A layer position, preserving the perfect lattice away from the dislocation core. In case of a partial dislocation in this example, atoms move from an A layer position to a C layer position, resulting in a local layer structure CBC, which corresponds to a hexagonal close-packed (HCP) structure. Examining the layer structure is thus a good way to detect dissociated dislocations in FCC crystals.

2.3 Surface atom diffusion

Once a surface nanofeature has appeared, surface diffusion begins to play a role in its stability. Surface diffusion is driven by thermal motion of atoms between energy basins.

At temperatures below the melting point, adatoms on metal surfaces spend most of their time near a potential energy minimum. There are finite energy barriers around such an adatom's position, which impede it from freely roaming around the surface. The barriers are easier to overcome at elevated temperatures giving rise to surface modifications due to diffusional processes. The transition of an adatom or a surface atom to a different potential energy minimum is a thermally activated stochastic process with a rate that depends on the system temperature:

$$\Gamma \sim \exp\left(-\frac{E_m}{k_B T}\right), \tag{2}$$

where T is the temperature, k_B is the Boltzmann constant, and E_m is the migration energy. The migration energy measures the height of the energy barrier that the atom needs to overcome in order to transition to a new potential well. The probability of quantum mechanical tunneling through the potential barrier is insignificant and is disregarded in this theory.

Figure 3 shows an example of an energy landscape along a transition path. The transition begins and ends at energy minima which correspond to equilibrium atomic positions. The energy barriers to transition from one minimum to another are shown on the figure and are different for the forward and reverse transitions along the same path. According to eq. (2), the rate for the forward process is smaller than that for the reverse process in this example. Therefore, this energy landscape results in directed diffusion towards the left hand side of the graph.

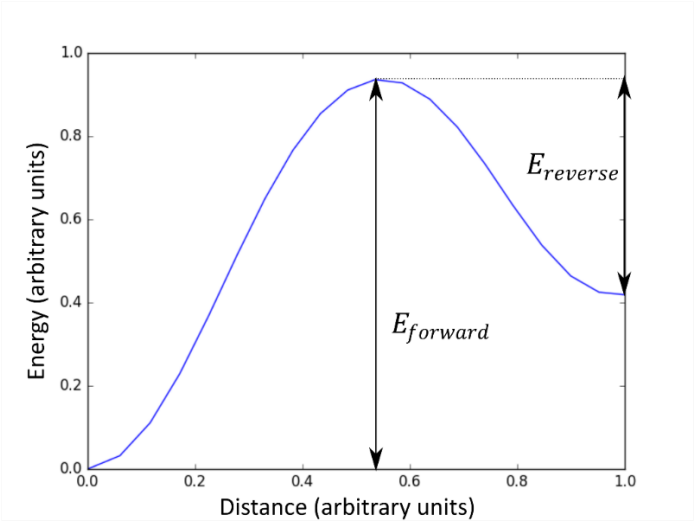

Figure 3. Example migration energy barrier for surface atom diffusion. In the beginning and end of the transition path are energy minima, and the atom must overcome an energy maximum in-between. The size of the migration barrier depends on the direction of the transition.

The energy landscape of a surface is affected by the topology (surface steps, adatom islands, roughness, etc.) and external factors, such as electric field. The dependence of the potential energy on the surface geometry lies at the core of KMC simulations, which will allow for analysis of stability of nanofeatures under normal condition, but at elevated temperatures.

3 Simulation methods

3.1 Molecular dynamics

The method of classical molecular dynamics [55–57] models atoms as point particles that move according to Newton's laws of motion based on interatomic interactions. Quantum effects are accounted for indirectly through interatomic interaction potentials. For metals, the embedded atom method (EAM) potential [58,59] is often used to describe the interactions. The EAM potential describes the energy of an atom as follows:

$$E = F_\alpha\left(\sum_{n=1}^{N}\rho_\beta(r_n)\right)+\frac{1}{2}\sum_{n=1}^{N}\phi_{\alpha\beta}(r_n)\,. \tag{3}$$

Both sums are over all atoms within the cutoff distance of the current atom. F is an embedding function which calculates the current atom's energy based on the local electron density. The local electron density is the sum of electron densities ρ contributed by each of the neighboring atoms. An atom's contribution to the electron density is symmetric and depends only on the distance r_n. The second contribution to the energy is the pairwise interaction ϕ between the current atom and neighboring atoms, which likewise depends only on the interatomic separation. The subscripts α and β refer to the atom species of the current atom and atom n, respectively. Thus, the electron density functions are associated with the neighboring atoms (because the current atom is being embedded into their electron density background), while the embedding function is associated with the current atom. The pairwise interaction function is associated with a specific pair of atom species.

The functional forms of F, ρ and ϕ are complicated and involve many parameters which are fitted empirically from experimental results or more precise quantum mechanical calculations, typically density functional theory (DFT). For ease of use in MD simulations these functions are given in a tabulated format. For Cu, the Sabochick-Lam [60] and the corrected effective medium (CEM) potential by Stave *et al.* [61] were used. For Au, the potential by Grochola *et al.* [62] was used. The Fe potential was by Mendelev *et al.* [63], while the Fe-Cu many-element functions were developed by Pasianot and Malerba [64] and compiled into a Fe-Cu-Ni ternary potential by Bonny *et al.* [65]. These potentials have been developed in order to accurately model the mechanical properties of the respective materials.

The force on the atom is calculated as the negative gradient of the energy and used in Newton's equation of motion:

$$\boldsymbol{f} = -\boldsymbol{\nabla}E = m\boldsymbol{a}\,, \tag{4}$$

where $\boldsymbol{a}$ is the atom's acceleration and m is its mass. This is then numerically integrated using discrete timesteps to obtain the atomic positions and velocities as functions of time, generating the phase space trajectories. This work uses the MD code LAMMPS [66], which applies the velocity form [67] of the Verlet algorithm [68]:

$$\begin{aligned} \boldsymbol{r}^{(n+1)} &= \boldsymbol{r}^{(n)} + \Delta t \boldsymbol{v}^{(n)} + \frac{\Delta t^2 \boldsymbol{f}^{(n)}}{2} , \\ \boldsymbol{v}^{(n+1)} &= \boldsymbol{v}^{(n)} + \frac{\Delta t \left[\boldsymbol{f}^{(n+1)} + \boldsymbol{f}^{(n)}\right]}{2} , \end{aligned} \tag{5}$$

where Δt is the timestep, parenthesized superscripts refer to the iteration number, and unit mass is assumed.

An appropriate value for the timestep is an order of magnitude shorter than the period of atomic oscillations around their equilibrium positions, which is the fastest process considered in the current work.

The initial conditions for the positions and velocities, $\boldsymbol{r}^{(0)}$ and $\boldsymbol{v}^{(0)}$, are given as inputs to the system. Starting velocities can be generated according to a Maxwell-Boltzmann distribution to conform to a desired temperature. The initial distribution of velocities is also used as a source of randomness when independent repeat simulations are required.

Simulations at constant temperature are accomplished with the help of a thermostat. The Berendsen thermostat [69] adjusts the temperature by rescaling velocities at each timestep by the factor λ:

$$\lambda = \sqrt{1 + \frac{\Delta t}{\tau}\left(\frac{T_0}{T} - 1\right)}, \tag{6}$$

where T_0 is the desired temperature, T is the instantaneous system temperature and τ is a parameter that determines the speed of achieving the set temperature. This expression results in a rate of change of temperature proportional to the difference from the desired temperature:

$$\Delta T = \frac{\Delta t}{\tau}(T_0 - T) . \tag{7}$$

In order to preserve the fluctuations expected from a canonical ensemble, the more complicated Nosé-Hoover thermostat [70,71] can be used. A fictitious particle that acts as an external heat bath is coupled to the system which effectively exerts a friction force on all atoms. The equations of motion are modified as follows [72]:

$$m\boldsymbol{a} = \boldsymbol{f} - \gamma m\boldsymbol{v}\,, \tag{8}$$

where $\boldsymbol{f}$ is the force due to interatomic interactions, as defined by eq. (4). The parameter γ changes as the simulation proceeds, with a rate that is proportional to the difference between the kinetic energy of the system and that of the fictitious particle representing the heat bath:

$$\dot{\gamma} = \frac{1}{M}\left(\sum_{n=1}^{N}\frac{\boldsymbol{p}_n^2}{m_n} - 3Nk_BT_0\right). \tag{9}$$

Here $\boldsymbol{p}$ is the particle momentum, T_0 is the desired temperature around which the system temperature will fluctuate and M is a mass parameter that determines the inertia of the fluctuations. Nosé and Hoover showed that equations of motion of this form result in correct canonical ensemble statistics.

3.1.1 Stress in molecular dynamics

To obtain a measure for spatial stress distribution, the virial [73] for each atom is computed and divided by a normalization volume. In case of pair potentials, the expression of the atomistic stress is:

$$\sigma_{ij} = -\frac{1}{\Omega}\left(mv_iv_j + \frac{1}{2}\sum_{n=1}^{N} r_i^n f_j\right), \tag{10}$$

where Ω is the normalization volume, m is the atom's mass, v_i the velocity components, f_i the force components, r_i^n the components of the displacement of atom n relative to the current atom, and the sum is over all other atoms within the cutoff distance. For many-body potentials like EAM that were used in the current work, LAMMPS uses a modification by Thompson *et al.* [74].

The normalization volume Ω is taken to be equal to the average Voronoi cell volume around the atom [28]. The Voronoi cells are constructed around all atoms using the code Voro++ [75]. For bulk atoms, the volume of the Voronoi cell contributes to the average volume directly, but for surface atoms additional processing is required because their Voronoi cells would extend into infinity. Surface atoms are identified using coordination analysis with suitably selected parameters (depending on the material; see publication I for details). For surface atoms, the volume is set to the average Voronoi cell volume in the system.

This approach also allows measuring the volume of voids appearing in the material during the simulation. The total volume of the simulation box is compared with the total Voronoi volume of all atoms, with the difference taken as the volume of the voids.

The Voronoi cells constructed around bulk atoms include any vacancies that might be present, therefore vacancies are not counted as voids and do not contribute to the void volume.

When stress is calculated in a simulation at finite temperature, temporal averaging is required to reduce the noise that arises due to thermal fluctuations of atoms [76].

The virial stress for the full simulation box is also used when controlling the external stress or pressure conditions of the system. The Parrinello-Rahman method [77] adjusts the shape and volume of the simulation cell to bring it into equilibrium with the desired external stress. A straightforward implementation [51] uses the system matrix $\boldsymbol{h}$ which defines the size and shape of the simulation cell at the current time step, and scaled coordinates $\boldsymbol{s} = \boldsymbol{h}^{-1}\boldsymbol{r}$ for the atoms. The equations of motion become

$$\begin{aligned} \ddot{\boldsymbol{s}} &= -\boldsymbol{h}^{-1}\frac{1}{m}\boldsymbol{f} - \boldsymbol{G}^{-1}\dot{\boldsymbol{G}}\dot{\boldsymbol{s}}\,, \\ W\ddot{\boldsymbol{h}} &= (-\boldsymbol{\sigma} - p\boldsymbol{I})(\boldsymbol{h}^{-1})^T\Omega - \boldsymbol{h}\boldsymbol{\Sigma}\,, \\ \boldsymbol{G} &= \boldsymbol{h}^T\boldsymbol{h}\,, \\ \boldsymbol{\Sigma} &= \boldsymbol{h}_0^{-1}(-\boldsymbol{\sigma}_{ext} - p\boldsymbol{I})(\boldsymbol{h}_0^{-1})^T\Omega_0\,. \end{aligned} \tag{11}$$

$\boldsymbol{\sigma}$ is the system virial stress and $\boldsymbol{\sigma}_{ext}$ is the desired external stress with a hydrostatic component $p = -\frac{1}{3}\mathrm{Tr}(\boldsymbol{\sigma}_{ext})$. The initial system shape is described by the system matrix $\boldsymbol{h}_0$ with the volume $\Omega_0 = \det \boldsymbol{h}_0$. Similarly, the current volume is $\Omega = \det \boldsymbol{h}$. The parameter W controls the speed at which the stress approaches the desired stress, similarly to the mass parameter in eq. (9). Finally, $\boldsymbol{I}$ is the identity matrix.

The implementation in LAMMPS uses equations of motion by Shinoda *et al.* [78] that combine constant temperature and constant stress equation into an NpT ensemble.

3.2 Finite element method

The finite element method [79,80] is used to solve boundary and initial value problems in continuous media. At its core, FEM is a method for solving partial differential equations on a mesh. The mesh constitutes the division of a simulation domain into a set of discrete non-overlapping elements. The differential equation over the whole domain is transformed into a set of algebraic equations by approximating the solution using basis functions defined by the space discretization. Because the solutions are only available at the element node points, the mesh is created denser in regions where the gradient of the solution is larger. In regions where the function of interest changes slowly in space, the mesh can be sparser to speed up calculations.

The set of equations obtained as a result of the FEM discretization is then solved either directly or iteratively. Direct solvers require significant amount of memory, but are

robust and typically arrive at a solution. Some examples of direct solvers are PARDISO [81] and MUMPS [82,83], which are used in the current work. Iterative solvers approach a solution starting from an initial guess and monitor the error at each iteration. They are not as memory demanding as direct solvers, but do not always converge on a solution.

In this work, a nonlinear system is solved, and a combined approach is required. A modified Newton method [84] is used to iterate the solution, and in every iteration the system is solved with the direct solver PARDISO.

Comsol Multiphysics [85] was used for FEM simulations in the current work.

3.2.1 Surface stress model in FEM

The surface is modeled as a thin elastic layer with a surface stress given by [86]:

$$\tau_{ij} = \tau_{ij}^0 + s_{ijkl}\varepsilon_{kl}\,, \tag{12}$$

where τ_{ij}^0 are the components of the initial surface stress, s_{ijkl} are the components of the surface elasticity tensor, ε_{ij} are the components of the surface elastic strain. The initial stress τ_{ij}^0 represents the inherent surface stress in case of zero strain. The values of τ_{ij}^0 and s_{ijkl} are inputs into the model and are taken from published MD results [87].

The surface elastic strain uses the large deformation model and is expressed as:

$$\boldsymbol{\varepsilon} = \frac{1}{2}(\boldsymbol{F_s}^T\boldsymbol{F_s} - \boldsymbol{I})\,, \tag{13}$$

where $\boldsymbol{F_s}$ is the surface deformation gradient tensor and $\boldsymbol{I}$ is the identity tensor. In terms of the surface displacement components u_{s_i}, the surface strain is:

$$\varepsilon_{ij} = \frac{1}{2}\left(\frac{\partial u_{s_i}}{\partial x_j} + \frac{\partial u_{s_j}}{\partial x_i} + \frac{\partial u_{s_k}}{\partial x_j}\frac{\partial u_{s_k}}{\partial x_i}\right). \tag{14}$$

The ratio of surface areas between the deformed and undeformed configuration is:

$$J_s = \sqrt{\det(\boldsymbol{F_s}^T\boldsymbol{F_s})} = \sqrt{\det(\boldsymbol{I} + 2\boldsymbol{\varepsilon})}\,. \tag{15}$$

The surface stress model is coupled to the bulk stress model through the boundary conditions. Bulk-to surface coupling is achieved by controlling the surface deformation:

$$\boldsymbol{u_s} := \boldsymbol{u_b}\,. \tag{16}$$

Deformation of the bulk material $\boldsymbol{u_b}$ is propagated to the surface, which modifies the surface stress according to eq. (12). The surface stress in turn is implemented as a boundary load on the bulk material:

$$\boldsymbol{f} := p\boldsymbol{n}J_s = \frac{1}{3}(\tau_{xx} + \tau_{yy} + \tau_{zz})\boldsymbol{n}J_s\,, \tag{17}$$

where $\boldsymbol{n}$ is the surface normal.

The relationships between the quantities and couplings of the whole model are schematically represented in Figure 4.

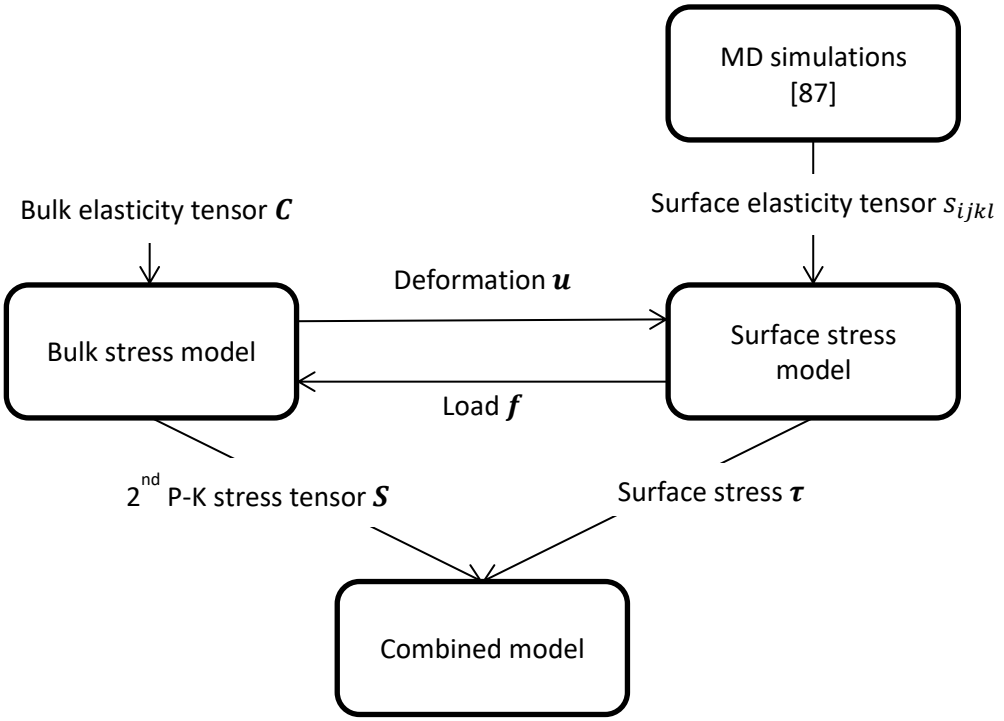

Figure 4. Coupling of the bulk and surface stress models in FEM. Surface parameters are taken from MD simulations [87].

The surface stress and elasticity parameters differ between crystal orientations. To approximate the properties of the geometrical surfaces present in FEM simulations, a weighted average is calculated as follows:

$$s_{ijkl} = \frac{1}{\sum_n \Phi^{\mathrm{n}}} \sum_q s_{ijkl}^q \Phi^q\,, \tag{18}$$

where Φ^q is the weight of the crystal surface q for the given geometrical surface and s^q_{ijkl} are the surface elasticity tensor components for that crystal surface. This procedure is illustrated in Figure 5. The weight is based on the angle between the surface normal of the model geometry surface, $\boldsymbol{n}_{gs}$, and the normal of the crystal surface, $\boldsymbol{n}_{cs}$. It equals 1 when the surface normals are parallel, and 0 when they are perpendicular.

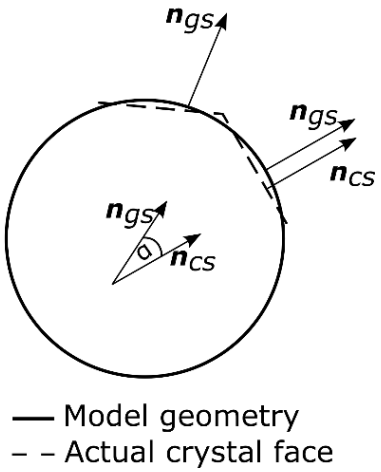

Figure 5. Weighing of surface parameters based on the local crystallographic orientation. At every point, weights for all implemented crystallographic surfaces are computed by finding the angles between them and the model surface.

Other surface properties are calculated similarly. Surface properties for the {100}, {110}, {111} and {112} surfaces are included. All other surfaces use the properties for the {112} surface. Furthermore, an isotropic approximation is used, where the direction-dependent elastic properties for the {110} and {112} surfaces are averaged. See publications II and III for the full details.

3.3 Atomistic Kinetic Monte Carlo

The KMC algorithm simulates the thermal motion of surface atoms by having them transition from one equilibrium position to another with a rate given by eq. (2), adding the attempt frequency ν:

$$\Gamma = \nu \cdot \exp\left(-\frac{E_m}{k_B T}\right) . \tag{19}$$

The rates Γ are used by the algorithm as weights to determine the atomic transitions that are likely to happen. For that, at each time step, all possible transitions are

compiled and the rate Γ_i for each is calculated from eq. (19). In order to select a process to perform, cumulative functions are calculated:

$$R_{\mathrm{i}} = \sum_{j=1}^{i} \Gamma_j \,. \tag{20}$$

Thus, $R_1 = \Gamma_1, R_2 = \Gamma_1 + \Gamma_2, \ldots, R_n = \sum_j^n \Gamma_j$, where n is the total number of processes possible at the current timestep. A random number $u \in (0,1]$ is generated and used to select the process i where $R_{i-1} < u \sum_j^n \Gamma_j < R_i$.

The selection process can be likened to a roulette wheel where the rates can be thought to designate sectors of the wheel with the size of each sector determined by the value of Γ_i. The cumulative function R_i is then the total amount that the wheel has to spin to land on sector i. The random number determines a random amount of spin, up to one full revolution. As a result of the algorithm, processes with higher rates have a proportionally higher chance to be chosen.

One of the advantages of KMC methods compared to other Monte Carlo methods is the possibility to take into account the advance of time and the analysis of time span for different processes to take place. This is possible by using the residence-time algorithm [88] that determines the time increment at each simulation step as follows:

$$\Delta t = -\frac{\log u}{\sum_i \Gamma_i}, \tag{21}$$

where u is a uniform random number and the sum is over all possible transition rates at the given timestep. It follows from eq. (21) that the time for a single KMC step to occur is random, but the total time over many steps is based on the transition rates in the system. When only slow processes take place (sum of rates is low), the timesteps are longer, and when fast processes occur (sum of rates is high), the timesteps become shorter.

3.3.1 Kimocs

Kimocs (Kinetic Monte Carlo for surfaces) [39] is an on-lattice atomistic KMC code that has been developed to simulate surface atom diffusion. Atoms in Kimocs can occupy certain well-defined lattice positions corresponding to an FCC or BCC lattice. For the FCC lattice, four orientations are possible, defined by the crystal direction along the z-axis: <100>, <111>, and two varieties of <110>, which differ by their rotation around the z-axis. Atomic transitions are carried out by moving an atom selected by the KMC algorithm from its lattice position to a nearby vacant lattice site.

Kimocs characterizes the local geometry around atom jumps by counting the number of first (1NN) and second nearest neighbors (2NN) in the jumping atom's initial and final positions. Thus, each possible transition is described by 4 numbers, a, b, c, d, where a is 1NN in the initial position, b is 2NN in the initial position, and c and d are 1NN and 2NN in the final position, respectively.

This model does not take into account the specific positioning of the neighboring atoms, only their total number. However, in the discussion below, the specific placement of neighbors will be referenced. To facilitate discussion, a set of 4 numbers characterizing a jump will be referred to as a *combination*, while all the possible atom placements that could result in that combination are called *permutations*.

The attempt frequency in eq. (19) is taken to be the same for all processes and acts as a coefficient to normalize the time estimate. However, to characterize a material for Kimocs simulations, the migration barriers have to be calculated for every possible combination of a, b, c, d. This is done using the Nudged Elastic Band (NEB) method [89] and interatomic potentials in MD. First, a permutation is chosen and the initial and final configurations are independently relaxed using the conjugate gradient (CG) algorithm. The NEB method then finds the saddle point on the minimum energy path (MEP) connecting the initial and final configurations. In the original publication for Kimocs [39], the choice of a permutation was arbitrary. In the current work, a more consistent way of choosing the permutation is described.

3.3.2 Permutation selection

The same combination of a, b, c, d can arise as a result of many different permutations, some of which can be highly unstable. The difference in the migration barrier between permutations can also be quite large, as seen in Figure 6. In a real system, all permutations are not equally likely to occur. Thus, an arbitrary choice of a permutation can lead to unreliable results if a highly non-representative permutation was chosen.

In the method of calculating migration barriers developed in this work, a permutation is chosen by calculating the potential energy of the system in the (unrelaxed) initial and final states. All possible permutations for each combination of a, b, c, d are scanned, and the one with the lowest sum of initial and final PE is chosen to represent that combination.

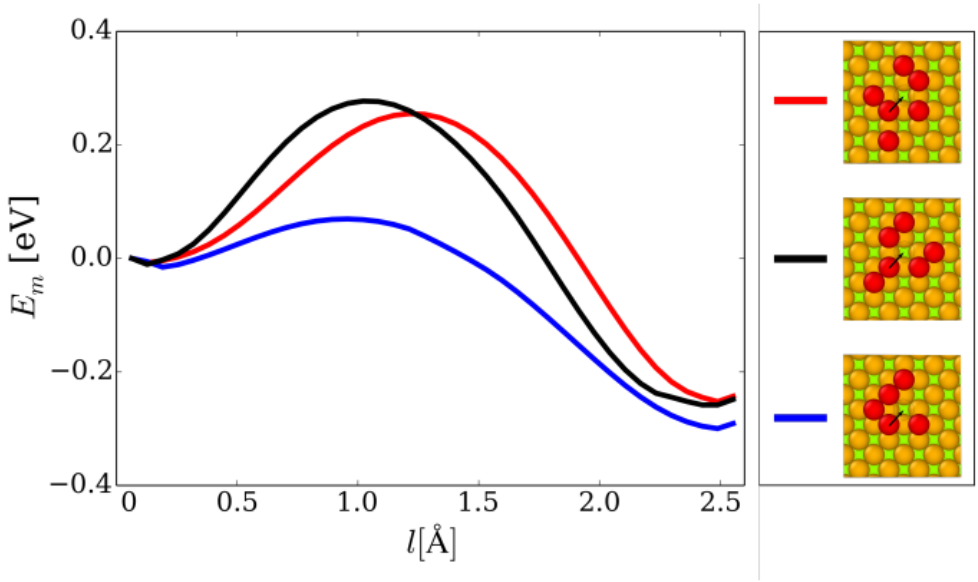

Figure 6. Minimum energy paths for three different permutations of the (5, 3, 7, 3) jump. Although the number of neighbors in the initial and final positions for all cases are the same, the different configurations of surrounding atoms have a significant effect on the MEP.

3.3.3 Tethering force approach

Because of the on-lattice nature of Kimocs, some of the possible transitions can result in unstable atomic configurations. This presents a problem when calculating migration barriers using NEB, as the surroundings of the jumping atom can change during the initial relaxation period, as well as during the subsequent NEB calculation. Previously, many barriers could not be calculated because of this instability. For processes with few neighbors ($a \leq 3$) where the jumping atom spontaneously moves into the final position, a workaround had been developed [39]. These processes were previously assigned a migration energy value of

$$E_m(a, b, c, d) = \epsilon a + \delta b + \epsilon c^{-1} + \delta d^{-1}\,, \tag{22}$$

where $\epsilon = 10^{-3}$eV and $\delta = 10^{-4}$eV. This allowed the inclusion of these processes in the simulation using a small non-zero barrier (avoiding a division by zero), but it did nothing to solve the problem with all other types of unstable processes.

To obtain a consistent set of migration barriers, an automatic method, using the tethering force approach, was developed in the current work. This approach applies an additional spring force to atoms, directed towards their initial lattice site in the NEB calculation, stabilizing the system and allowing almost all possible barriers to be calculated.

The tethering force binds atoms to their assigned lattice positions, preventing them from changing their placement during relaxation or the NEB process, while still allowing enough freedom to move around the jumping atom. The spring constant is an input parameter and affects the resulting MEP and the energy barrier. The higher the spring constant, the higher the calculated barrier because of the extra stiffness of the surrounding atoms. The spring constant was chosen to be 2 eV/Å^2, which is enough to stabilize almost all processes, while still having a minimal effect on the resulting MEPs.

Figure 7 shows a histogram where the energy barriers of all stable processes for Cu (those that could be calculated without tethering) are compared with the same processes calculated using tethering. The vast majority of differences are smaller than 0.5 eV, with most processes having an energy barrier difference close to 0.

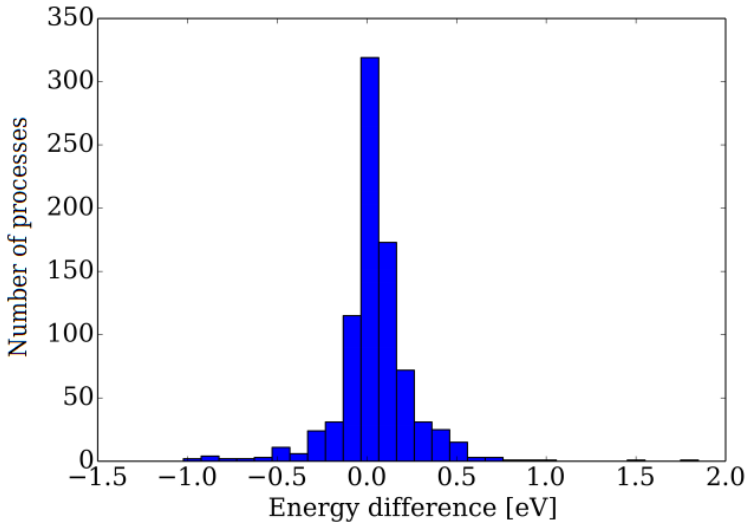

Figure 7. Histogram of energy differences of stable processes between tethered and non-tethered calculations for Cu.

The additional barriers that can be calculated for Cu using the tethering method are shown in Figure 8. Around 1600 new processes are available with energy barriers ranging from 0 to 2.5 eV. Many of these processes would either have been assigned an extremely low energy barrier using eq. (22), or forbidden entirely (effectively an infinite energy barrier). As seen from Figure 8, most of these barriers have an intermediate energy. Thus, the tethering force approach allows to calculate a significant number of barriers which would otherwise be unstable, while having a minimal effect on the stable barriers. The resulting dynamics of the whole system are validated in comparison with molecular dynamics (see section 3.3.4) and experiments (see section 6).

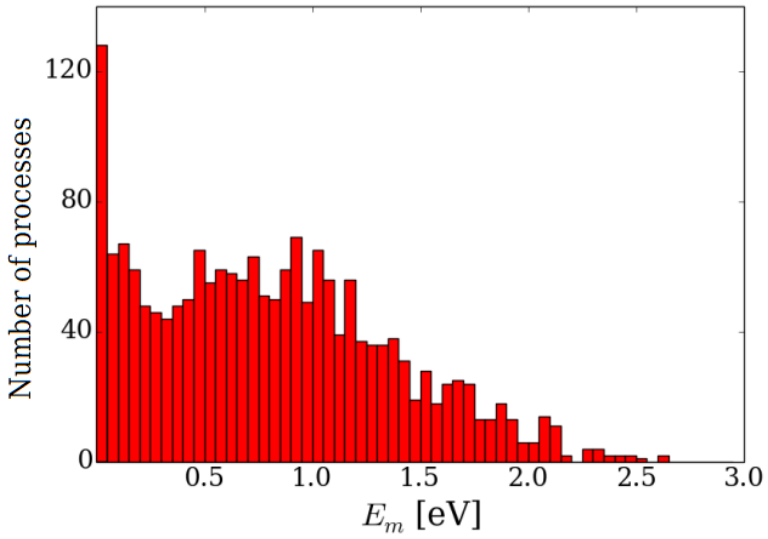

Figure 8. Histogram of unstable processes calculated using tethering for Cu. These processes could not be calculated previously.

3.3.4 Attempt frequency

If Γ is defined as in eq. (19), with a constant attempt frequency approximation, ν can be brought out of the summation and treated as a coefficient that scales the time estimate.

As a first approximation, the attempt frequency can be taken to be equal to the Debye frequency for the material. However, to obtain greater accuracy, the attempt frequency should be fitted using experimental or lower-level simulation data. In this work, the method of fitting the attempt frequency used in [39] is adopted.

The relaxation times of a small nanopillar are compared between MD and KMC simulations and the attempt frequency value is extracted. Figure 9 shows the relaxation times at different temperatures for Au. The times follow an Arrhenius-type dependence on the temperature. The attempt frequency acts as a scaling coefficient, moving the linearized graph up and down along the $\ln(t)$ axis. The attempt frequency was fitted by minimizing the sum of the differences between the MD and KMC data points. The final obtained Au attempt frequency value is $\nu = 1.22 \times 10^{17} \mathrm{s}^{-1}$.

The value is significantly higher than the typical atomic oscillation frequency in MD. This can be explained by the limited number of jumps included in the KMC model. Not all transitions that are possible in MD are taken into account, thus requiring the included jumps to happen more often to “keep up” with MD. In particular, 2NN or longer jumps in tungsten can have attempt frequencies several orders of magnitude higher than 1NN

jumps [90]. The difference in the slopes of the lines in Figure 9 also indicates a difference in the effective average migration energy barrier.

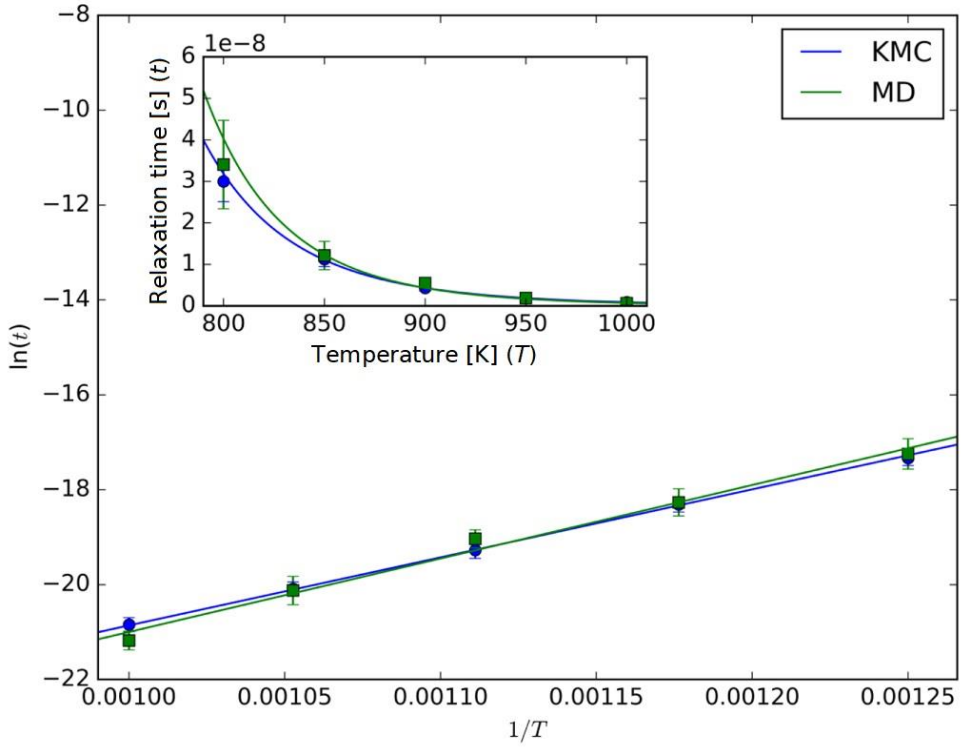

Figure 9. Fitting of the attempt frequency for Au to MD data by measuring nanopillar relaxation times at 800, 850, 900, 950 and 1000 K. The inset shows a non-linearized graph of the same data.

4 Dislocation behavior and stress around a precipitate

Previous works [33,34,91–93] conducted MD simulations of subsurface voids to investigate the origin of the hypothesized field enhancing nanotips that are thought to be responsible for vacuum breakdowns in CLIC [26]. Parviainen *et al.* studied the growth of a tip above a near-surface void and atom evaporation from tips due to an external electric field. Pohjonen *et al.* identified a surface tip formation mechanism due to a near-surface void through the emission of a prismatic dislocation loop. A prismatic loop in this context is a dislocation loop that moves on the slip planes perpendicular to the material surface, thus transporting atoms directly to the surface. The nucleation of a tip-forming prismatic dislocation loop becomes possible when the slip direction <110> is chosen perpendicular to the surface.

The objective of this study was to investigate the dislocation formation around the precipitate under high field conditions and compare it to the behavior around a void. Fe was chosen as the precipitate material because of its high mechanical strength, contrasting it to the void, and the fact that Fe is likely to become embedded in the Cu structures during machining.

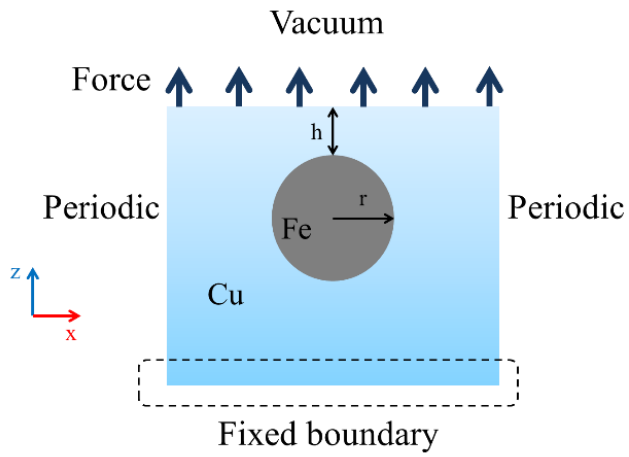

Figure 10. System setup for MD precipitate simulations. Force was applied to the top layers of atoms using the Maxwell stress equation. The distance of the precipitate from the surface of the material was varied. Crystal directions are x-<100>, y-<110>, z-<110>.

The effect of a high electric field was simulated by applying a z-directional force to the surface Cu atoms, as shown schematically in Figure 10. The approximation of constant electric field over the surface is valid as long as the surface deformation is negligible.

To avoid shockwave effects, force is not applied immediately, but rather ramped as the simulation proceeds. The magnitude of the force, and thus the electric field, is increased linearly as the simulation progresses. The simulation is stopped when the surface deformation increases and atoms start evaporating, as at that point the constant field approximation is no longer appropriate.

Similarly to previous simulations, the <110> direction was set perpendicular to the surface to enable favorable slip systems facing the open surface. Furthermore, using this system orientation, two different {111} planes lie at an angle to the surface close to 45°. The resolved shear stress along those planes due to the tensile stress on the surface is thus maximized, activating additional slip systems for dislocations to propagate to the surface.

In the following, the visualization of atomistic data was conducted with OVITO [94]. The spherical Fe precipitate acts as a stress concentrator, as seen in Figure 11. The precipitate provides favorable sites for dislocation nucleation under the effects of the tensile stress. Figures 11(a) and 11(c) show evidence of the presence of dislocations through the stacking faults, visualized using centrosymmetry analysis [95]. The centrosymmetry parameter quantifies the local symmetry of a crystal lattice. Atoms with a perfectly symmetrical neighbor arrangement obtain the value 0, while higher values indicate deviations from the perfect lattice. Thermal motion of atoms results in noise in the centrosymmetry figures, but at temperatures used in the current simulations, stacking faults are clearly distinguishable. Centrosymmetry for the Fe precipitate is not calculated and Fe atoms are shown in black.

Figures 11(b) and 11(d) present the atomistic stress distribution in the material immediately before dislocations nucleate (the stacking fault tetrahedra outlined in Figure 11(c) are already present in Figure 11(d)). The stress component shown is the resolved shear stress along the plane of the stacking fault in the direction of dislocation propagation, $\sigma_{x'z'}$, with the axes rotated as shown in the figure. Stress is concentrated above and below the precipitate at the angle close to 45° as predicted by Lubarda *et al.* [96], and dislocations form in those regions.

When the dislocations propagate to the material surface, steps or plateaus are created, as seen in Figure 12. Figures 12(a) and 12(c) show the top views of figures 12(b) and 12(d), respectively, with atoms colored according to their z-coordinate to show the formation of elevated regions. The passage of a dislocation can also be seen as slip of the material above the stacking fault, which explains the surface step forming at the point where the stacking fault intersects the surface. In case of figures 12(c) and 12(d), periodic boundary conditions allow one of the stacking faults to wrap around and reach the surface close to another stacking fault, resulting in a plateau. Such a situation could arise in case of an array of closely spaced subsurface defects that each act as dislocation nucleation sites.

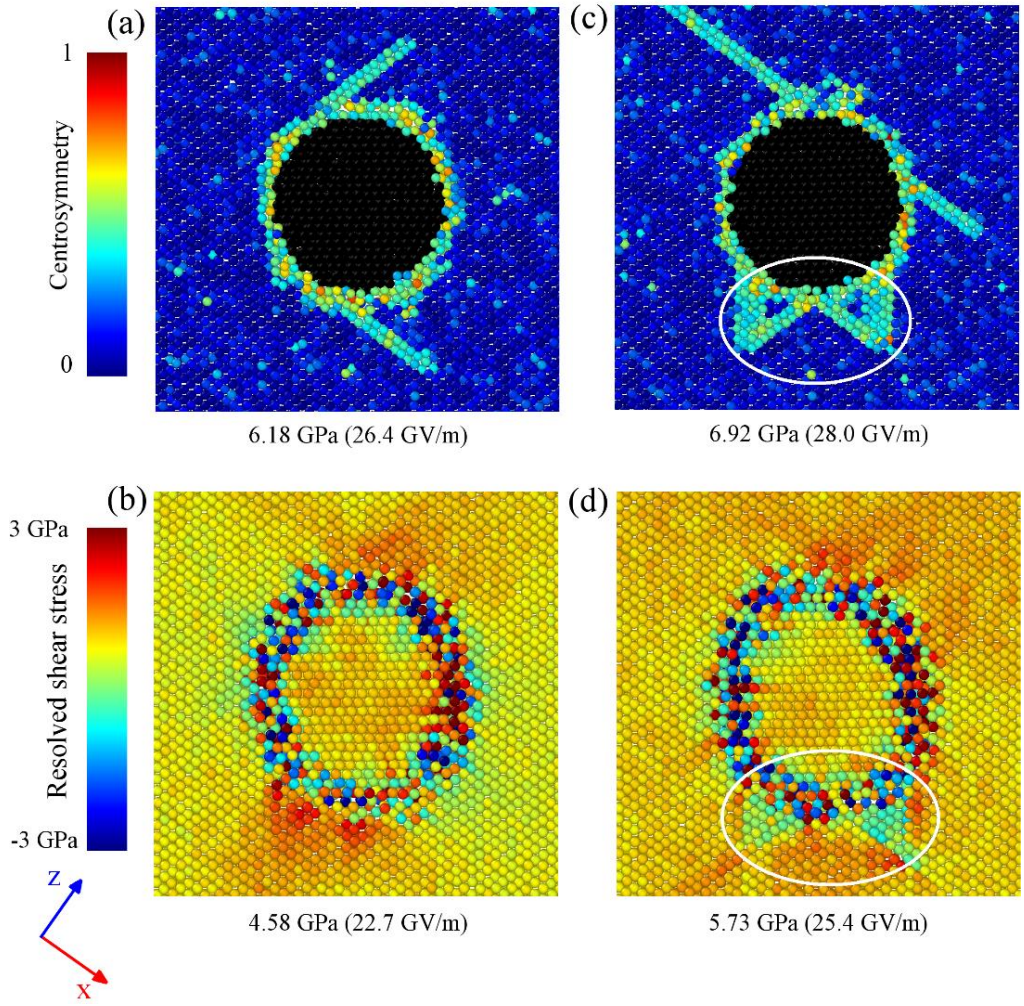

Figure 11. Stress concentration and dislocations around a Fe precipitate in Cu. Stacking fault configurations in two different simulations are shown in (a) and (c), with the corresponding stress distributions before their formation in (b) and (d). The stress component shown is the resolved shear stress $\sigma_{x'z'}$ along a glide plane of dislocations, with the axes as seen in the bottom left. The white outline shows stacking fault tetrahedra which influence the stress distribution.

Once a surface step has formed, continued application of stress results in further slip of the material above and below the stacking fault. Figure 13 shows the region below a surface step and its evolution as stress is increased. The stacking fault is revealed using adaptive common neighbor analysis [97], which classifies atoms according to their local crystalline environment. Stacking faults are identified as either single (extrinsic stacking fault) or double (intrinsic stacking fault) HCP layers in an otherwise

perfect FCC lattice [52]. The gradual slip of the layers surrounding the initial stacking fault results in splitting of the stacking fault and the growth of the surface step.

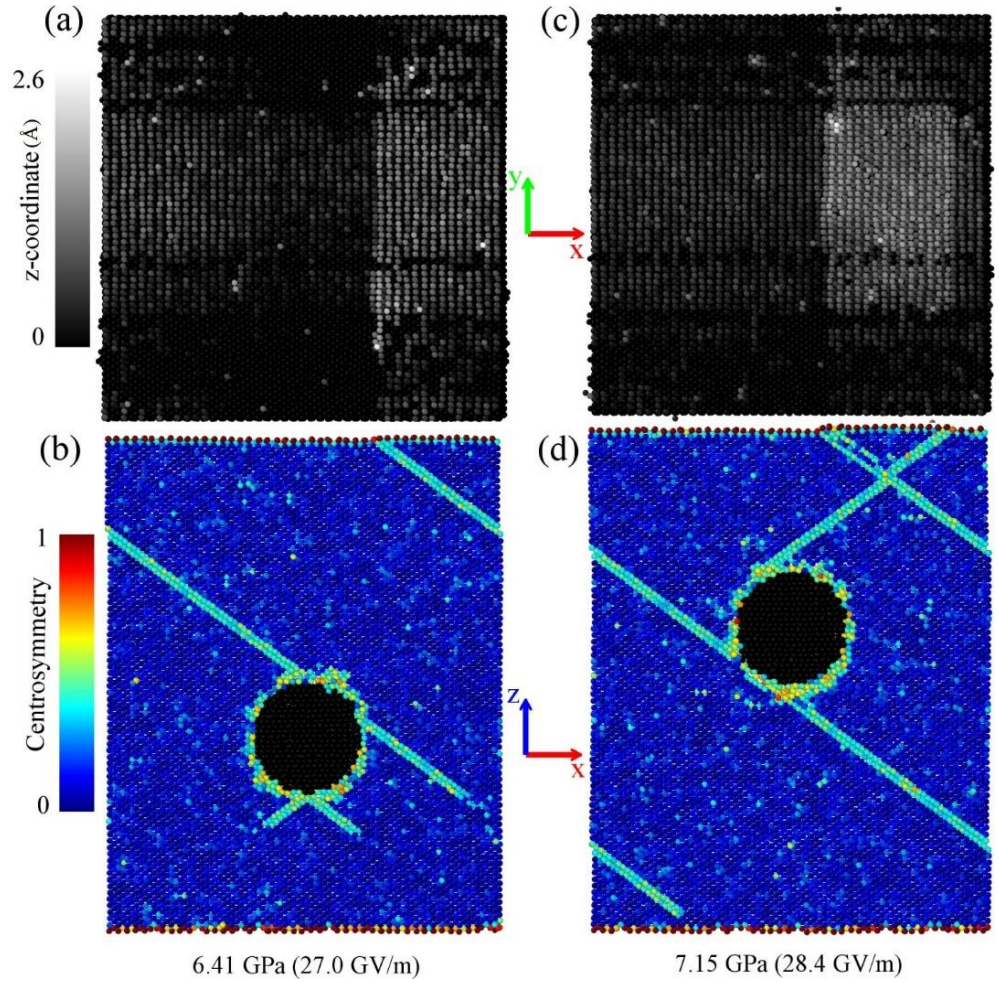

Figure 12. Formation of a step (a), (b) and plateau (c), (d) as a result of dislocations propagating to the surface. (a) and (c) are top views of (b) and (d), respectively.

As the applied stress is increased further, void formation is observed around the precipitate. Figure 14 shows the increase of the void volume as the stress is ramped. Void formation is a stochastic process: 14% of simulations (N=80) with the precipitate at a depth of 5.6 nm and 6.3% of simulations in case of the precipitate at the depth of 9.8 nm resulted in a void forming before significant surface evaporation. Void formation was observed both above and below the precipitate in areas of significant stress concentration. Voids act as additional stress concentrators and dislocation nucleation sites, as evidenced by the snapshots in Figure 14. The nucleated dislocations

also move on the vertical slip planes (Figure 14(d)). These dislocations can form prismatic loops, which are very effective at transporting atoms away from the void and onto the material surface [92,98].

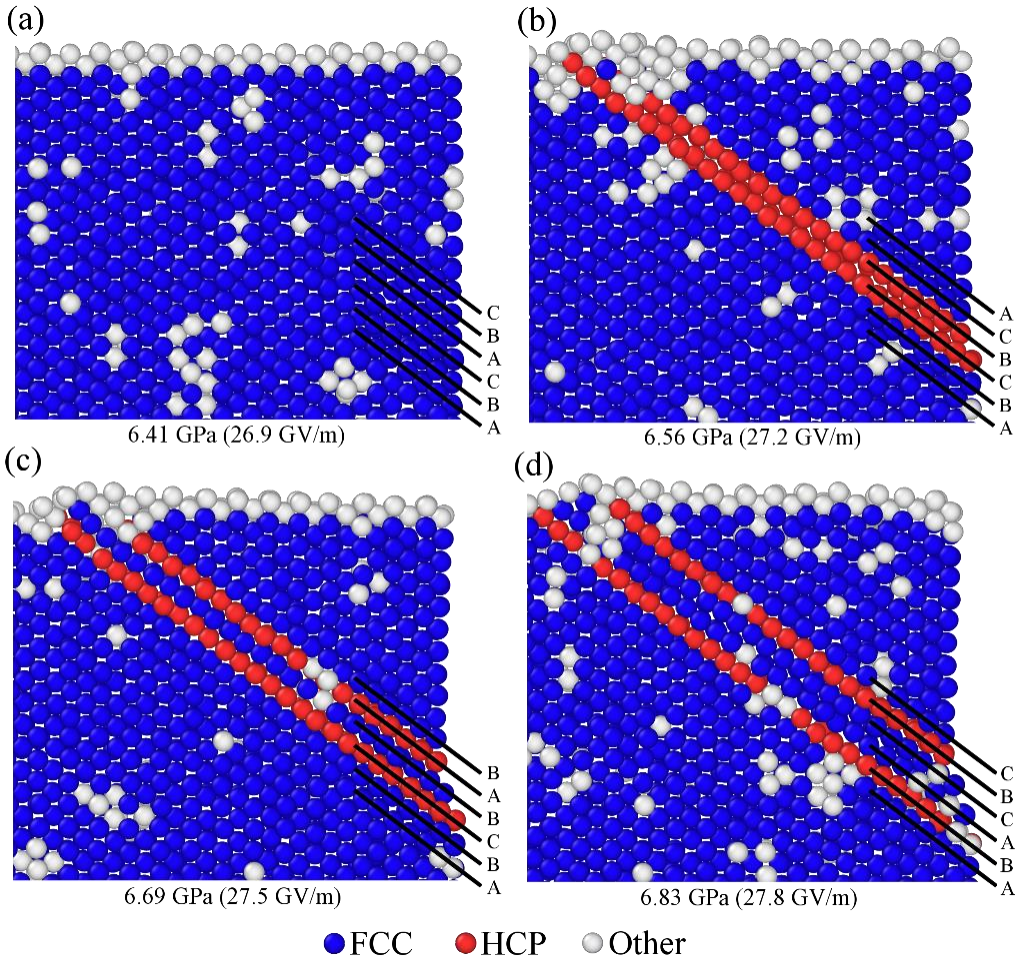

Figure 13. Splitting of the stacking fault and growth of the surface step. The initial situation is shown in (a) and the first surface step in (b). As stress is increased, the material slips above (c) and below (d) the stacking fault, resulting in plastic deformation of the material and growth of the surface step. The layer structure in each case is marked.

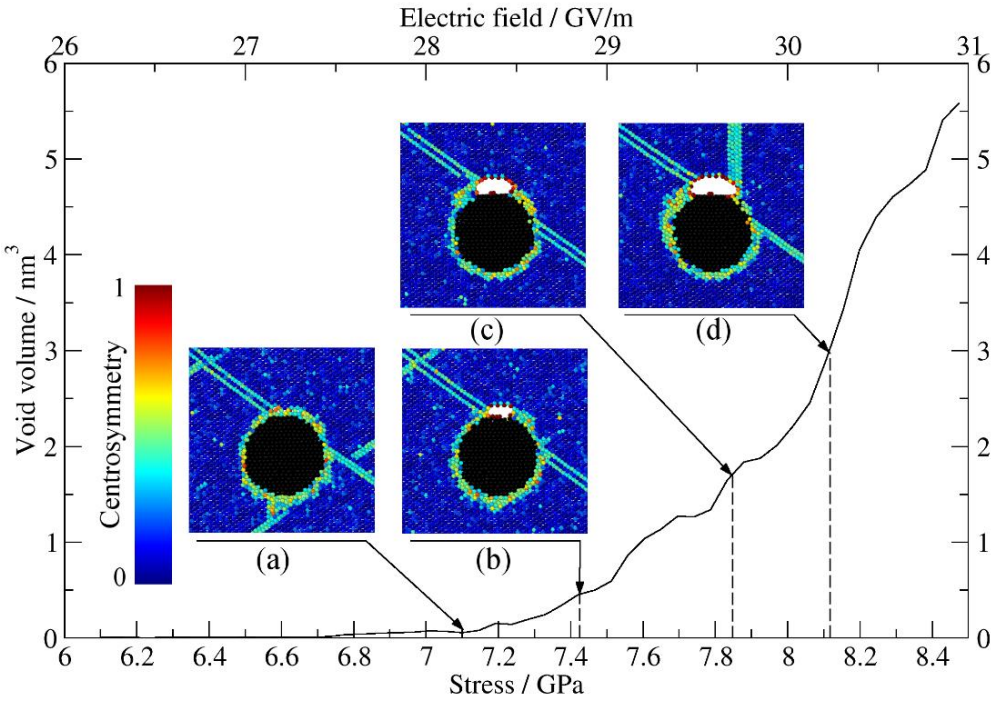

Figure 14. Evolution of a void close to the Fe precipitate due to increasing applied stress. Stress was ramped linearly in time and the corresponding electric field strength is shown on the alternative horizontal axis.

5 Stress near a sub-surface void

To obtain a better stress estimate around the void and extend the analysis to larger scales, a continuum approach was used. The coupled bulk and surface stress model for FEM was implemented and validated against MD simulations. Figure 15 shows a comparison between FEM and MD of shear stress distributions in three perpendicular slices around a void. The stress calculation in MD was performed at a temperature of 300 K as described in section 3.1.1, including time averaging to reduce the noise. The system is fully periodic in this case, showing that the FEM model accurately models the effect of the surface in the absence of any external effects. Removing the surface stress model from the calculation would result in no stress around the void.

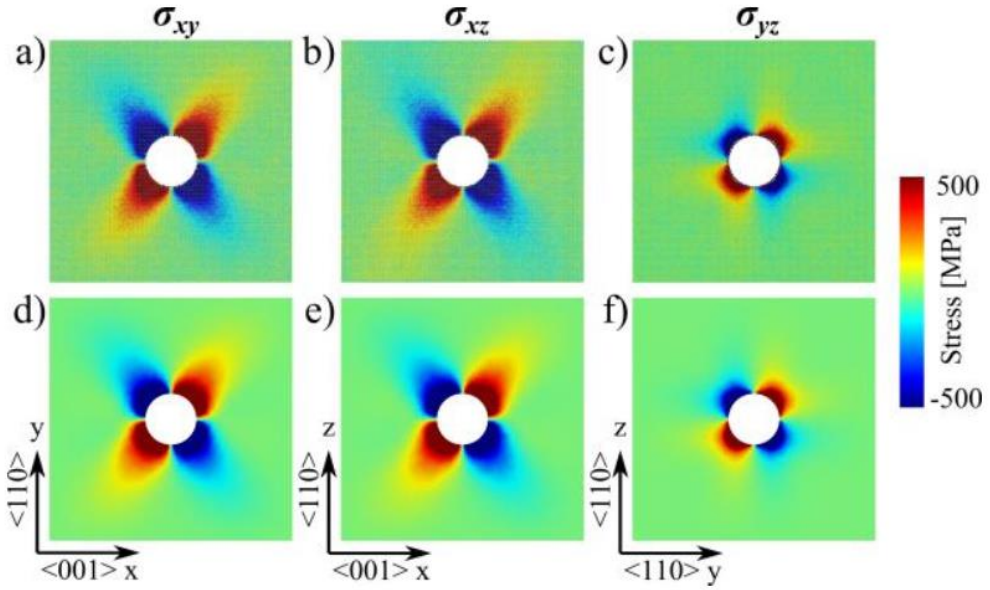

Figure 15. Shear stress distributions for an unstressed system calculated in MD (top row) and FEM (bottom row) using the coupled bulk and surface stress model.

The spherical void in this case provides a test of the surface approximation algorithm in FEM. The similarity between the FEM and MD results shows that using the limited number of surfaces is appropriate in this case. When an open surface is introduced and external stress applied, the situation changes somewhat, as seen in Figure 16. The distributions in the xz and yz planes are still very similar, but significant differences appear in the xy plane.

Possible reasons for the discrepancy include the isotropic approximation of the surface elastic properties, the lack of higher-index surfaces, and the differences in boundary conditions between the MD and FEM simulations. In particular, MD simulations were

run using the NVT ensemble, thus introducing additional stress in the x and y directions due to the Poisson effect. In FEM, symmetrical boundaries were applied, which force zero displacements normal to the boundary.

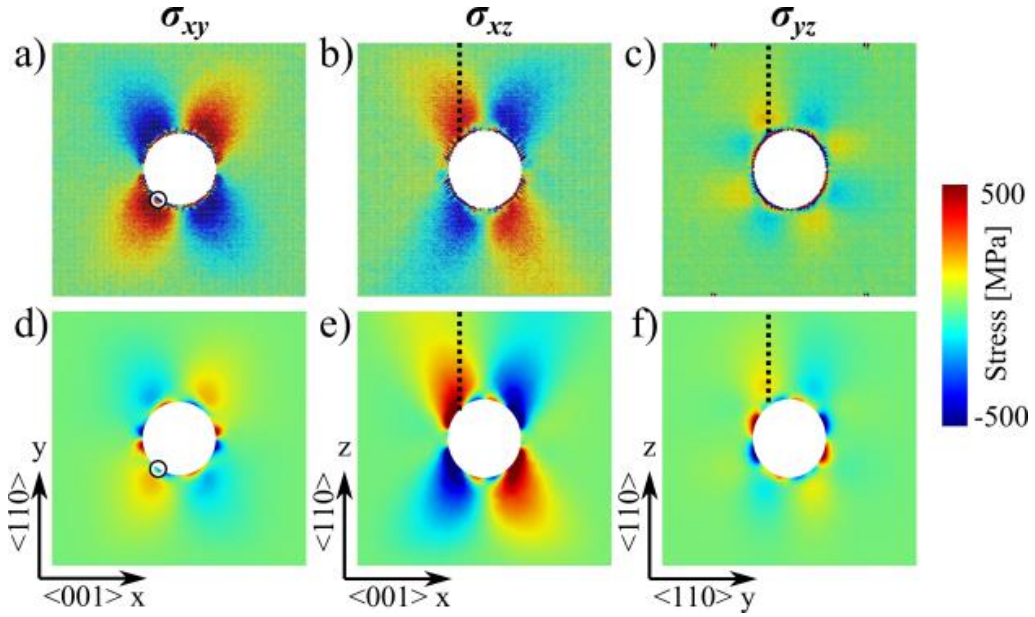

Figure 16. Comparison of shear stress distribution between MD (top row) and FEM (bottom row) simulations under 1.35 GPa external stress in the z-direction. Circles in (a) and (d) and dashed lines show the source of data for Figure 17.

Figure 17 shows a quantitative comparison of stresses as a function of the distance from the void surface. Stress values are taken along the dashed lines in Figure 16 and starting from the circles in Figure 16(a) and (d) (the line in those figures would be directed out of the page). The data for zero external stress is taken from simulations with a free surface. Despite the differences in the xy slice in Figure 16, the lines in Figure 17 show good agreement both for the stressed and unstressed cases, indicating that the inaccuracies in the model are likely not significant in practice.

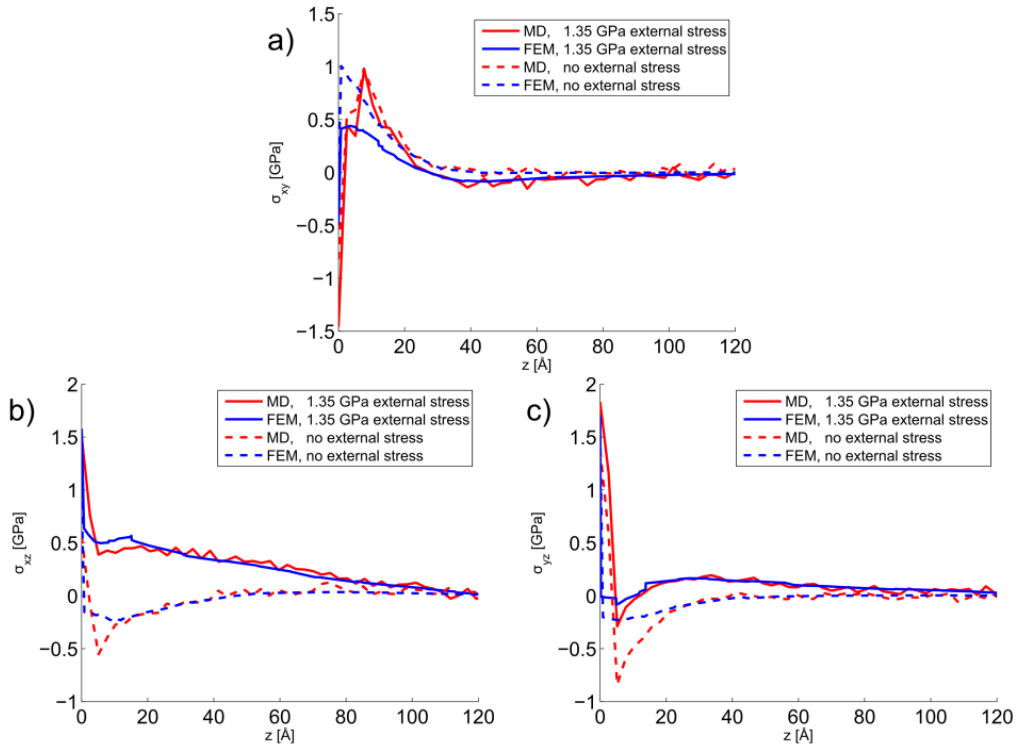

Figure 17. Quantitative comparison of stress as a function of distance from the void surface for stressed and unstressed systems. Data is taken starting from the circles and along the dashed lines in Figure 16.

As a further test of the surface approximation algorithm, simulations were conducted with different void shapes, including cubic, cut-cube and dodecahedral (publication III). In particular, the cut-cube void shape is similar to octahedral shapes that have been observed in Al [99]. Figure 18 presents the especially challenging case of a dodecahedral void where none of the surfaces correspond to those for which surface parameters were available. Nevertheless, both qualitative comparisons of the distributions and quantitative data (Figure 19) show excellent agreement.

Figure 19 also includes stress values for the case where the surface stress model in FEM was disabled. It can be seen that the surface stress model provides more accurate stress values and accounts for the oscillations very close to the surface (<2 nm).

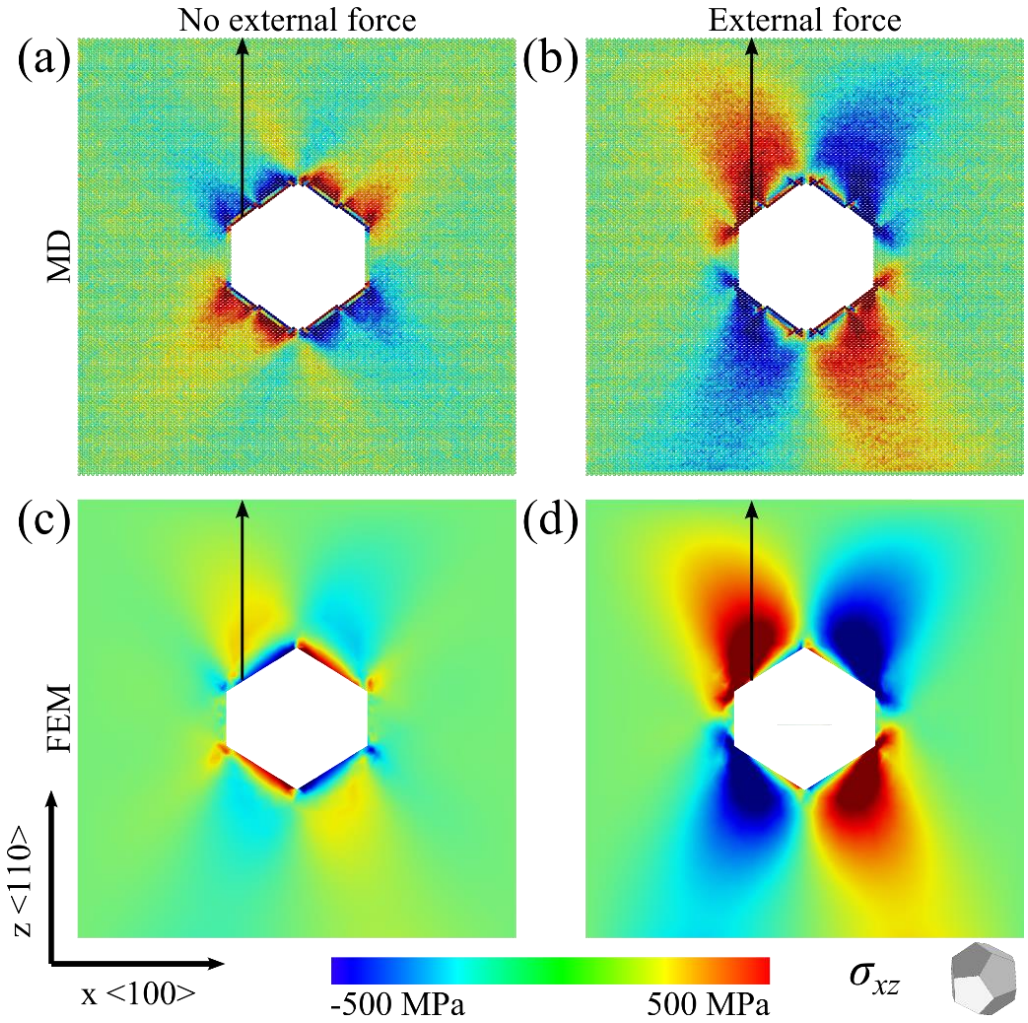

Figure 18. Comparison between the stress distribution in MD (top row) and FEM (bottom row) for a dodecahedral void. The lines show the data source for Figure 19.

The FEM surface stress model was used to test the analytical prediction given in [93]. The analytical model had been developed based on MD simulations and determines the maximum depth for a void to still be able to emit prismatic dislocation loops. This depends on the externally applied stress as well as the void dimensions. The results are given in terms of the void aspect ratio, defined as h_{cyl}/r , as shown in Figure 20(a)[1].

[1] d is the surface layer thickness used in the mathematical formulation of the FEM model; see publication II for details.

The analytical prediction, as well as the FEM simulation results are shown in Figure 20(b).

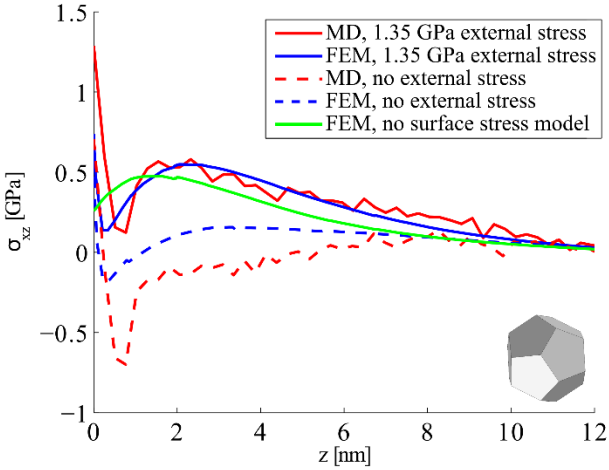

Figure 19. Quantitative comparison of stress as a function of the distance from the void surface. Data is taken along the lines in Figure 18. The green line presents the case of externally stressed system with the FEM surface model disabled.

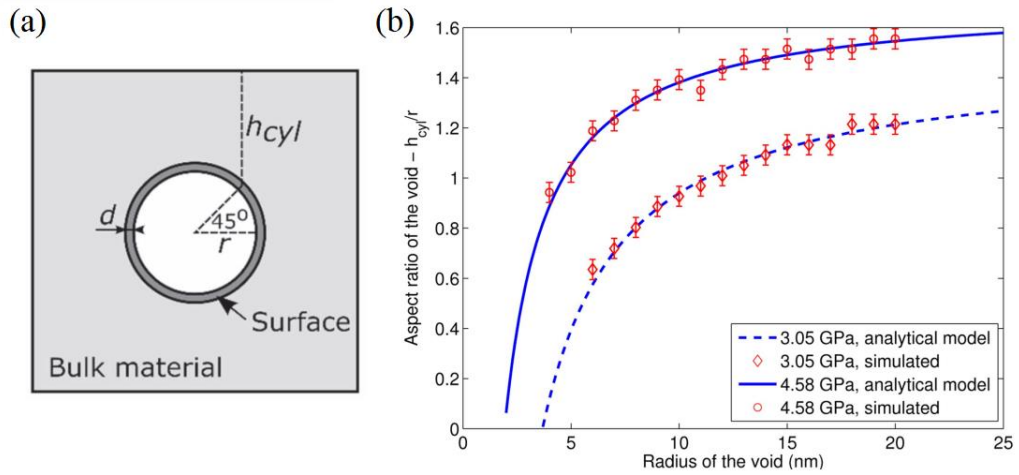

Figure 20. Aspect ratio of a void necessary for prismatic loop nucleation. The geometry of the system is defined in (a) and the dependence of the necessary aspect ratio on the void radius is shown in (b) for two external stress states. Nanoscale finite size effects decrease as the void radius increases and the aspect ratio approaches a constant value.

Dislocation nucleation occurs when sufficient local stress builds up at the void surface due to the interaction between the surface stress fields. Because of finite size effects,

small voids need to be proportionally closer to the surface (lower aspect ratio) to be able to nucleate prismatic loops. With increasing void size, finite size effects lose their importance and the aspect ratio becomes independent of the void radius. Thus, it can be seen that the current implementation is well suited for nanoscale surface simulations extending the available length and time scales compared to the MD method.

6 Thermal stability of nanowires

Surface features resulting from sub-surface dislocation activity are subject to thermal diffusion leading to their breakup and relaxation. The time that a nanostructure remains stable depends on factors like its size, shape, and temperature. The stability of FCC metal nanostructures was investigated in an experimental study, combined with KMC simulations.

Au nanowires were thermally treated for 10 minutes at 200 °C, 400 °C, 600 °C and 700 °C. Nanowires at elevated temperatures break up into fragments due to Rayleigh instability [15], as seen in Figure 21. As a thermally activated surface diffusion process, Rayleigh instability induced breakup is faster at higher temperatures.

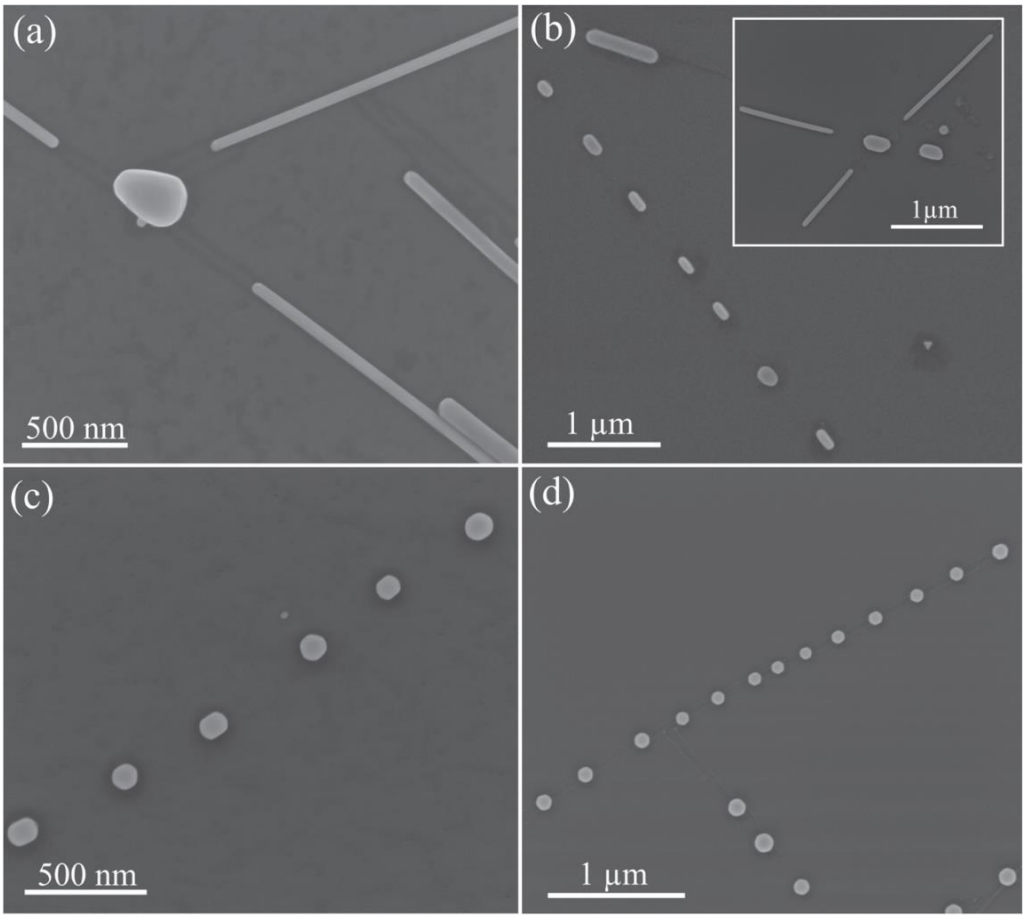

Figure 21. SEM images of nanowires and nanowire junctions after thermal treatment at 200 °C (a), 400 °C (b), 600 °C (c) and 700 °C (d).

At 200 °C, most nanowires remained whole. Figure 21(b) shows examples of both fragmented and unfragmented nanowires at 400 °C. At higher temperatures, most nanowires were fragmented. However, as seen from Figure 21(a) and Figure 21(b), nanowire junctions tend to fragment even when the nanowires themselves remain whole.

The developed automatic tethered barrier calculation and the resulting parametrization or Au for KMC simulations was applied to the study of nanowire junctions. Simulations show that breakup happens through a surface energy minimization process, where fragments bounded by the low-energy {111} and {100} surfaces form. Figure 22 shows the time evolution of a junction breakup in the case of two 1 nm <100> nanowires at 1000 K. The elevated temperature compared to experiments was chosen to speed up the simulations and achieve results in a reasonable timeframe. In Figure 22(b) it can be seen that breakup starts at the junction. This is borne out in the 20 repeated simulations where the first detachment always occurred at the junction. Furthermore, the central fragment was almost always the first to form completely.

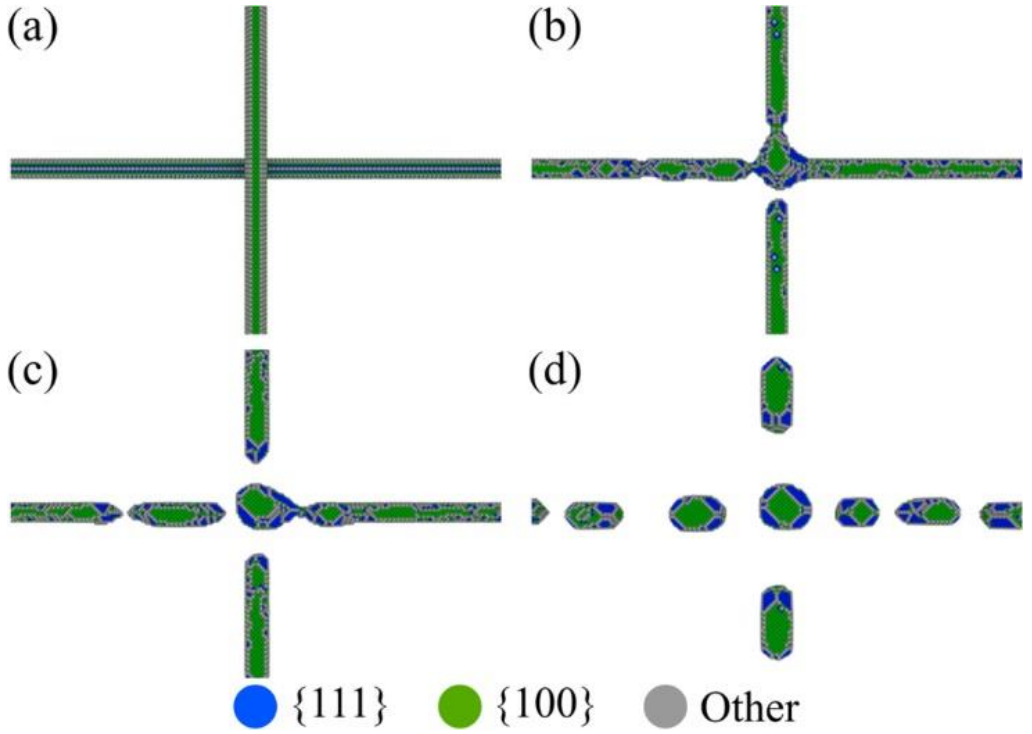

Figure 22. KMC simulation of the fragmentation of a junction of 1 nm radius Au nanowires at 1000 K. The nanowire orientations are <100>. Initial configuration with wires lying on top of each other (a), moment when the first detachment occurs (b), moment before the formation of a central fragment (c), and complete fragmentation of the nanowires (d).

The nanowires used in the experiment have a pentagonally twinned structure with the <110> crystallographic direction along the wire axis. The <100> orientation for the simulations, as well as the elevated temperature were chosen to facilitate the breakup process, as <110> nanowires are quite stable and require significantly more computational resources to simulate breakup. Nevertheless, reducing the wire length and radius resulted in a successful breakup simulation where all the features observed experimentally were observed also in the simulations within a reasonable computational time (Figure 23).

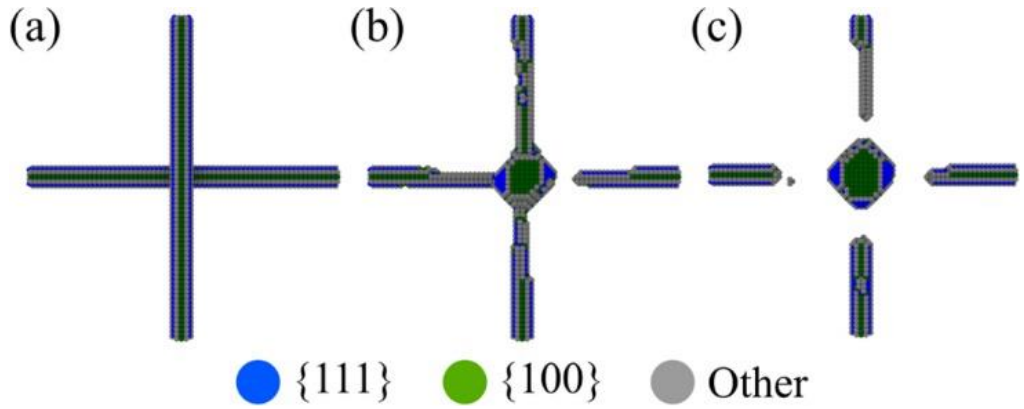

Figure 23. Nanowire junction breakup for 0.6 nm <110> Au nanowires. Initial configuration (a), first detachment (b), and complete formation of the central fragment (c).

KMC simulations show that the mechanism of nanowire junction breakup is independent of the wire size and orientation, which means that the results are transferable to experiments. In fact, the preference of {111} and {100} surfaces for the fragments is universal to FCC metals. Indeed, a similar situation has been observed for Ag nanowire junctions (Figure 24).

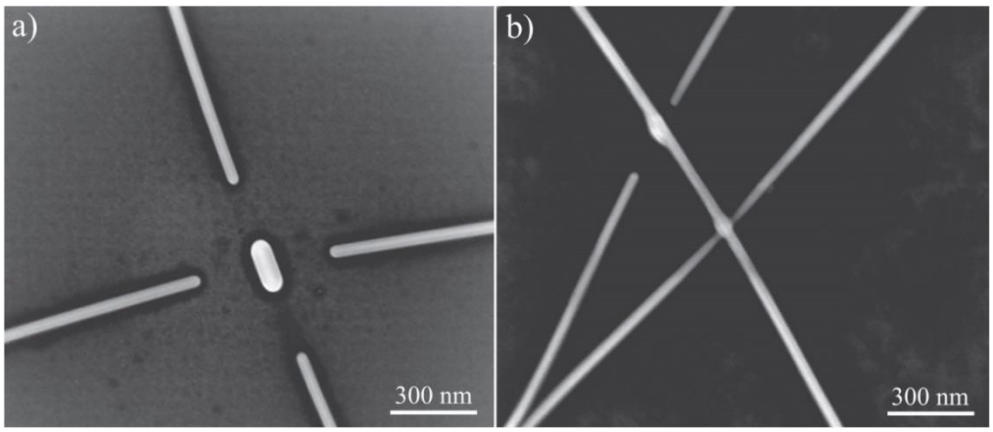

Figure 24. Ag nanowire junction breakup after thermal treatment at 125 °C for 10 minutes.

The remarkable reliability with which nanowire junctions start to fragment at the crossing point of the nanowires leads to the hypothesis that arranging nanowires in a regular overlapping pattern could be used as a means to manufacture ordered arrays of nanodots. Figure 25 shows a KMC simulation of such a pattern breaking at both junctions simultaneously. Because of the large number of atoms in this simulation, complete fragmentation could not be observed due to limited computational resources, but the formation of central nanodots is clearly seen.

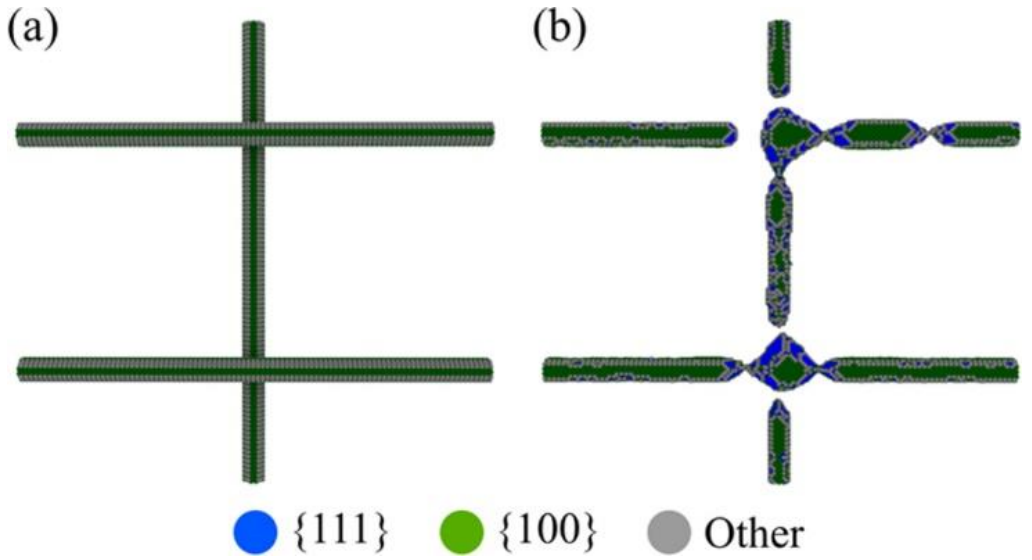

Figure 25. Fragmentation of an array of Au nanowire junctions. Initial configuration (a) and start of the formation of nanodots at the nanowire junctions (b).

From the performed experiments and KMC simulations, conclusions can be drawn about the stability of FCC metal nanostructures. Energetically, the {111} and {100} surfaces are clearly preferred, and surface atoms diffuse to form them. The diffusion speed is significantly higher at higher temperatures. The presence of additional surfaces can also accelerate atom diffusion, as seen from the junctions where surface atoms migrate to positions with more neighbors. The preferred shape of a nanostructure is thus a compact particle bounded by {111} and {100} surfaces. Any other structures, particularly elongated ones collapse or break up into smaller fragments. This remains true for structures on extended surfaces, such as those induced by externally applied stress or electric fields.

7 Conclusions

This work was concerned with atomistic simulations of metal surfaces to obtain a better understanding of surface modification under external stress and nanostructure stability. The methods used include molecular dynamics, kinetic Monte Carlo and a multiscale technique that extends the nanoscale effects into a continuum finite elements model. The unified picture of surface feature formation and stability is illustrated in Figure 26.

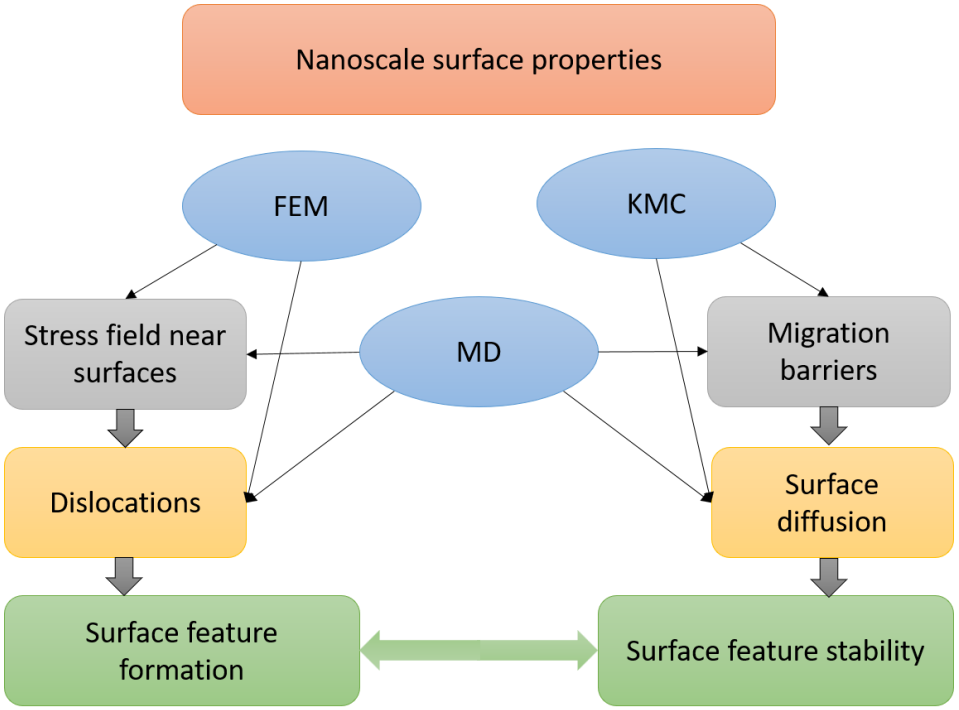

Figure 26. Schematic summary of the developed models. The FEM, MD and KMC methods are used to simulate nanoscale surface properties in the study of dislocations and surface diffusion. The result is a unified description of surface feature formation and stability.

The surface geometry modification was studied in the context of dislocation nucleation around extended defects in Cu. The procedure for obtaining estimates of the atomistic stress distributions in the material was described. The nucleation of dislocations around a Fe precipitate was shown in MD simulations under conditions of a high external electric field. The possibility of generating a surface protrusion due to the propagation of these dislocations and plastic deformation of the material was demonstrated. The simulations also showed plateau formation in case of closely spaced near-surface precipitates. This constitutes another dislocation-mediated surface roughness formation process in addition to the prismatic loop effect described in previous works. Under conditions of extreme stress, the formation of voids around the precipitate was

observed. Voids are known to be effective dislocation nucleation sites that facilitate surface modification.

MD simulations are very limited in terms of the material volume and physical time that can realistically be simulated. The much faster continuum FEM method was modified to include nanoscale surface stress effects with parameters for a number of Cu crystal surfaces taken from published MD estimates. As a result, a model was developed that produced stress distributions near surfaces that compared well with the more accurate MD simulations. This model was applied to simulate the finite size effects that govern dislocation nucleation around a sub-surface void. As expected, the finite size effects diminish as the size of the void is increased, but the extent was previously difficult to simulate in MD due to the large system size required.

Nanostructure stability was investigated using kinetic Monte Carlo to simulate surface atom diffusion. A reliable parametrization scheme for on-lattice KMC, the tethering method, was developed. This method enables the calculation of unstable migration barriers which are nevertheless necessary for a consistent treatment of on-lattice atomic jumps. The parametrization procedure was also automatized, creating a robust method of parametrizing an interatomic potential for KMC that does not require tedious manual tweaking.

The tethering method was applied to generate a parametrization for Au, which was used to simulate diffusion-driven fragmentation of nanowires. The simulations were done in conjunction with experiments and showed that nanowire junctions break up easily. Junction break-up occurs at even lower temperatures than the usual Rayleigh instability break-up known from literature. The KMC simulations show that this phenomenon is independent of the crystallographic orientation of the wires and can be explained by surface energy minimization due to surface atom diffusion. Crossing nanowires reliably form fragments at the junction points because of the presence of additional surfaces that attract atoms. This effect could be used to manufacture ordered arrays of nanodots. Therefore, any surface feature tends to relax to a shape that is bounded by energetically favorable surfaces {111} and {100}. Higher temperatures significantly accelerate the relaxation.

The good agreement with experimental observations confirms that the algorithm for parameterization of KMC models, that applies a tethering force on surface atoms to stabilize the system during barrier calculations, is appropriate for studying the surface diffusion on metal nanostructures.

The simulation techniques developed in this work are geared toward computational simplicity to enable fast scanning of large numbers of potentially interesting situations. Once they are identified, more precise simulations, like tracking dislocations in MD, can take over.

Further work with the field emitters should use the FEM surface stress model to enhance existing field emission calculations, using the dislocation nucleation and material failure conditions known from MD. The nanowire junctions present intriguing possibilities and further diffusion simulations should be conducted to identify more specific breakup conditions, including temperature dependence and timescale. This will provide insight both when breakup is desirable and when it should be prevented.

Follow-up studies should further explore the effect of the electric field on the material surface. In MD simulations, the geometrical field enhancement near surface features should be taken into account, and the force on surface atoms should vary based on local field conditions. In KMC simulations, the migration barriers can be modified based on the electric field. A multiscale approach is called for, using FEM to calculate field and charge distributions.

As nanotechnology and nanofabrication continue to advance, the mechanical properties of materials at the atomistic scale will no doubt continue to be an important area of research. Atomistic simulations, although more than half a century old, continue to see improvements. These are often tied to increasing computational resources and massive parallelism, but novel data processing algorithms are also significant. The tradeoff between accuracy, simplicity, and speed will likely remain an important decision when simulating nanoscale material properties.

Finally, multiscale approaches will become more and more important because macroscale material properties like elasticity or fatigue are determined by nanoscale defects like dislocations, frequently on time scales that are currently inaccessible to atomistic methods.

8 Acknowledgements

This work was supported by the Estonian Research Council grants PUT 57, PUT 1372 and the “Research internationalization” program of the European Regional Development Fund.

Computational resources were provided by the High Performance Computing Center of the University of Tartu, CSC – IT Center for Science Ltd (Finland), and the Finnish Grid and Cloud Infrastructure.

Visits abroad were supported through the national scholarship programs Kristjan Jaak and Dora Pluss, which are funded and managed by the Archimedes Foundation in collaboration with the Ministry of Education and Research of Estonia.

I especially want to thank my supervisors Vahur Zadin, Flyura Djurabekova and Alvo Aabloo for their incredible patience and invaluable advice. I want to thank my co-authors and co-workers for the fruitful discussions and arguments we have had: Kristian Kuppart, Robert Aare, Priit Priimägi and Kristjan Eimre from Tartu, and Ville Jansson, Ekaterina Baibuz, Mihkel Vekse, Jyri Kimari, Andreas Kyritsakis and Stefan Parviainen from Helsinki.

Finally, I want to thank my family on both sides of the Atlantic Ocean for their endless encouragement.

9 Summary in Finnish

Metallien pintailmiöiden atomistiset tutkimukset

Atomistiset simulaatiot ovat erinomainen tapa tutkia nanokokoisia metallirakenteita. Nanomittakaavassa pinta-alan suhde tilavuuteen on suuri, ja pinnalla tapahtuvat ilmiöt ovat hyvin merkittävässä roolissa. Sisäinen jännitys lähellä pintaa voi olla useita gigapascaleita, joten sen merkitys on huomioitava nanojohtimia ja muita nanorakenteita tutkittaessa. Myös atomien pintadiffuusio on tärkeä ilmiö nanorakenteiden valmistuksen ja vakauden kannalta.

Kuparipinnalla tapahtuvien tyhjiövalokaarien tutkimuksessa dislokaatioiden liikkeen ja pinta-atomien diffusion arvellaan vaikuttavan sähkökenttää vahvistavien emitterien muodostumiseen.

Tässä työssä tutkitaan nanomuodostelmien nukleaation mekanismia pintadefektien läheisyydessä voimakkaassa sähkökentässä, ja kultananojohtimien vakautta pintadiffuusion suhteen. Tutkimuksessa käytetään molekyylidynaamisia simulaatioita, kineettistä Monte Carloa ja elementtimenetelmää.

Pinnanalaista rautasaostumaa käytetään esimerkkitapauksena pinnan alle ulottuvista defekteistä, ja korkean jännityksen alueilla tapahtuvaa dislokaatioiden nukleaatiota simuloidaan. Dislokaatioiden etenemisen näytetään aiheuttavan ulkonemien muodostumista pinnalla lähellä saostumaa. Myös uusien tyhjiöiden muodostumisen saostuman rajapinnalle näytetään olevan mahdollista.

Koska atomististen simulaatioiden koko ja aikaskaala ovat hyvin rajallisia, suuremmat simulaatiot tehdään ulkoisen jännityksen alaisten nanomateriaalien elementtimallinnuksen avulla. Tällainen mallinnus kuitenkin vaatii tarkkaa mallia pintajännityksestä. Tässä työssä pintajännitysmalli toteutetaan jatkumoelementtimallissa, jotta suurempia nanosysteemejä voidaan simuloida nopeammin, ja jotta mekaaniset mallit saadaan yhdistettyä tyhjiövalokaaritutkimukseen. Mallin antamia sisäisen jännityksen arvoja verrataan molekyylidynaamisiin simulaatioihin ja pinnan lähellä sijaitsevan tyhiön emittoimien dislokaatioiden analyyttiseen malliin.

Kineettinen Monte Carlo on hyvä työkalu diffuusioprosessien simuloimiseen. KMCsimulaatio kuitenkin vaatii parametreina atomististen siirtymien energiavalleja. Tämän työn osana kehitetään johdonmukainen parametrisointijärjestelmä, nimeltään liekamenetelmä. Tämän menetelmän avulla voidaan laskea hilassa tapahtuvien siirtymien energiavallit luotettavasti ja automaattisesti. Myös epävakaiden siirtymien energiavallien laskeminen mahdollistuu, ilman suurta vaikutusta vakaiden siirtymien energiavalleihin.

Liekamenetelmällä luodaan parametrisaatio kultasysteemeille, jonka avulla simuloidaan risteävien nanojohtimien pirstoutumista. Nanojohtimien risteyskohdassa tapahtuva pirstoutuminen on Rayleigh'n epävakauden kaltainen prosessi. Yhdessä kokeellisten tutkimusten kanssa näytetään että risteyskohdat pirstoutuvat matalassa lämpötilassa, jossa yksittäiset nanojohtimet vielä pysyvät kokonaisina. Simulaatioiden perusteella pirstoutuminen voidaan selittää atomien diffuusion aiheuttamalla pintaenergian minimoitumisella. Risteyskohtaan muodostuu sirpale hyvin luotettavasti.

10 Summary in Estonian

Metallide pinnaefektide atomistlik uuring

Antud töös kasutati arvutisimulatsioone, et uurida metallide pinnaefekte nanoskaalas. Kuna nanoosakeste puhul on suur osa kõigist aatomitest pinna lähedal, muutuvad nanotehnoloogias pinnaefektid kriitiliselt oluliseks. Materjali sisemised mehaanilised pinged pinna läheduses on GPa suurusjärgus ning nanoosakestega opereerides ei saa seda arvestamata jätta. Nanostruktuuride tootmises ja kasutamises on samuti olulisel kohal pinna-aatomite difusioon.

Nimetatud omadused mängivad olulist rolli kõrge pinge süsteemides, kus elektrilised vaakumläbilöögid on suureks probleemiks. Levinud hüpoteesi järgi on vaakumläbilöögi tekkeks vajalik kõrge lokaalne elektriväli põhjustatud nanoskaalas pinnakareduste poolt, mis käituvad elektronide kiirgajatena. Selliste kiirgajate tekkemehhanismid ei ole lõpuni selged, kuid tõenäoline on seos kristallistruktuuri ja dislokatsioonide liikumisega.

Selles töös kasutati molekulaardünaamika, kineetilise Monte Carlo ja lõplike elementide meetodeid, et simuleerida metalli pinnal nanostruktuuride tekkemehhanisme ja stabiilsust. Täpsemalt vaadeldi dislokatsioonide aktiivsust vase pinna lähedal ja kulla nanotraatide lagunemist difusiooni toimel.

Eelnevates töödes kasutatud pinnaalune tühimik asendati raua lisandiga ja simuleeriti dislokatsioonide emissiooni selle ümbrusest kõrge välise mehaanilise pinge toimel. Näidati, et dislokatsioonide liikumise tulemusena on võimalik pinnakareduste teke, aga ka tühimike moodustumine lisandi ümber.

Et teostada ulatuslikumaid simulatsioone kui seda võimaldab molekulaardünaamika, kasutati lõplike elementide meetodit. Tavapärasele pideva keskkonna mudelile lisati mehaanilised pinnapinged, et korrektselt arvesse võtta nanoskaala efekte. Välja arendatud kombineeritud mudelit valideeriti molekulaardünaamika simulatsioonide ja analüütiliste arvutustega.

Kineetilise Monte Carlo difusiooni simulatsioonide jaoks arendati välja järjepidev ja automaatne parametriseerimise strateegia, mille abil saab arvutada Monte Carlo jaoks vajalikud energiabarjäärid ka ebastabiilsete protsesside jaoks. Antud meetodit kasutati, et koostada parameetrite komplekt kulla jaoks ning simuleerida nanotraatide lagunemist. Simulatsioonide ja eksperimentide abil näidati, et lagunemine toimub aatomite difusiooni toimel ning on seletatav pinnaenergia minimeerimise printsiibiga. Nanotraatide ühenduskohad lagunevad kiiremini ja madalamal temperatuuril kui ülejäänud traadi osad. Kuigi nanotraatide lagunemisest jäänud nanoosakesed paiknevad juhuslikult, siis traatide ühenduskohta tekkib nanoosake alati. Seega, on võimalik välja pakkuda uudne meetod regulaarsete ja kontrollitud nanostruktuuride tootmiseks.

References

[1] F.J. Heiligtag, M. Niederberger, The fascinating world of nanoparticle research, Materials Today. 16 (2013) 262–271. doi:10.1016/j.mattod.2013.07.004.

[2] P. Colomban, The Use of Metal Nanoparticles to Produce Yellow, Red and Iridescent Colour, from Bronze Age to Present Times in Lustre Pottery and Glass: Solid State Chemistry, Spectroscopy and Nanostructure, Journal of Nano Research. 8 (2009) 109–132. doi:10.4028/www.scientific.net/JNanoR.8.109.

[3] P. Sciau, C. Mirguet, C. Roucau, D. Chabanne, M. Schvoerer, Double Nanoparticle Layer in a 12th Century Lustreware Decoration: Accident or Technological Mastery?, Journal of Nano Research. 8 (2009) 133–139. doi:10.4028/www.scientific.net/JNanoR.8.133.

[4] D. Brüggemann, B. Wolfrum, V. Maybeck, Y. Mourzina, M. Jansen, A. Offenhäusser, Nanostructured gold microelectrodes for extracellular recording from electrogenic cells, Nanotechnology. 22 (2011) 265104. doi:10.1088/0957-4484/22/26/265104.

[5] S. Cherevko, C.-H. Chung, Gold nanowire array electrode for non-enzymatic voltammetric and amperometric glucose detection, Sensors and Actuators B: Chemical. 142 (2009) 216–223. doi:10.1016/j.snb.2009.07.023.

[6] K. Wang, K.B. Crozier, Plasmonic Trapping with a Gold Nanopillar, ChemPhysChem. 13 (2012) 2639–2648. doi:10.1002/cphc.201200121.

[7] G. Otnes, M.T. Borgström, Towards high efficiency nanowire solar cells, Nano Today. 12 (2017) 31–45. doi:10.1016/j.nantod.2016.10.007.

[8] T. Sannicolo, M. Lagrange, A. Cabos, C. Celle, J.-P. Simonato, D. Bellet, Metallic Nanowire-Based Transparent Electrodes for Next Generation Flexible Devices: a Review, Small. 12 (2016) 6052–6075. doi:10.1002/smll.201602581.

[9] Y. Lin, Y. Zou, Y. Mo, J. Guo, R.G. Lindquist, E-Beam Patterned Gold Nanodot Arrays on Optical Fiber Tips for Localized Surface Plasmon Resonance Biochemical Sensing, Sensors. 10 (2010) 9397–9406. doi:10.3390/s101009397.

[10] O.Y. Loh, H.D. Espinosa, Nanoelectromechanical contact switches, Nature Nanotechnology. 7 (2012) 283. doi:10.1038/nnano.2012.40.

[11] M. Li, R.B. Bhiladvala, T.J. Morrow, J.A. Sioss, K.-K. Lew, J.M. Redwing, C.D. Keating, T.S. Mayer, Bottom-up assembly of large-area nanowire resonator arrays, Nature Nanotechnology. 3 (2008) 88. doi:10.1038/nnano.2008.26.

[12] W. Wang, Q. Yang, F. Fan, H. Xu, Z.L. Wang, Light Propagation in Curved Silver Nanowire Plasmonic Waveguides, Nano Lett. 11 (2011) 1603–1608. doi:10.1021/nl104514m.

[13] C.A. Schuh, J.K. Mason, A.C. Lund, Quantitative insight into dislocation nucleation from high-temperature nanoindentation experiments, Nat Mater. 4 (2005) 617–621. doi:10.1038/nmat1429.

[14] S. Ryu, K. Kang, W. Cai, Predicting the dislocation nucleation rate as a function of temperature and stress, Journal of Materials Research. 26 (2011) 2335–2354. doi:10.1557/jmr.2011.275.

[15] S. Karim, M.E. Toimil-Molares, A.G. Balogh, W. Ensinger, T.W. Cornelius, E.U. Khan, R. Neumann, Morphological evolution of Au nanowires controlled by Rayleigh instability, Nanotechnology. 17 (2006) 5954. doi:10.1088/0957-4484/17/24/009.

[16] M.E.T. Molares, A.G. Balogh, T.W. Cornelius, R. Neumann, C. Trautmann, Fragmentation of nanowires driven by Rayleigh instability, Applied Physics Letters. 85 (2004) 5337–5339. doi:10.1063/1.1826237.

[17] D. P. Langley, M. Lagrange, G. Giusti, C. Jiménez, Y. Bréchet, N. D. Nguyen, D. Bellet, Metallic nanowire networks: effects of thermal annealing on electrical resistance, Nanoscale. 6 (2014) 13535–13543. doi:10.1039/C4NR04151H.

[18] H. Li, J.M. Biser, J.T. Perkins, S. Dutta, R.P. Vinci, H.M. Chan, Thermal stability of Cu nanowires on a sapphire substrate, Journal of Applied Physics. 103 (2008) 024315. doi:10.1063/1.2837053.

[19] S. Calatroni, A. Descoeudres, J.W. Kovermann, M. Taborelli, H. Timko, W. Wuensch, F. Djurabekova, K. Nordlund, A. Pohjonen, A. Kuronen, Breakdown studies for the CLIC accelerating structures, in: Proc. LINAC2010, Tsukuba, 2010: pp. 217–219. http://epaper.kek.jp/LINAC2010/papers/mop070.pdf (accessed August 23, 2018).

[20] N. Holtkamp, The status of the ITER design, Fusion Eng. Des. 84 (2009) 98–105. doi:10.1016/j.fusengdes.2008.12.119.

[21] U. Schumann, S. Giere, M. Kurrat, Breakdown voltage of electrode arrangements in vacuum circuit breakers, IEEE Transactions on Dielectrics and Electrical Insulation. 10 (2003) 557–562. doi:10.1109/TDEI.2003.1219637.

[22] J.W. Wang, G.A. Loew, Field emission and rf breakdown in high-gradient room-temperature linac structures, in: Proc. Joint School RF Engineering for Accelerators, Stanford, 1997. http://slac.stanford.edu/cgi-wrap/getdoc/slac-pub-7684.pdf (accessed August 23, 2018).

[23] R.W. Assmann *et al.*, A 3 TeV e^+e^- Linear Collider Based on CLIC Technology, CERN, Geneva, 2000. http://cds.cern.ch/record/461450 (accessed August 23, 2018).

[24] H. Braun *et al.*, CLIC 2008 parameters, in: F. Tecker (Ed.), CLIC-Note-764, Geneva, 2008. http://cern.ch/tecker/par2007.pdf (accessed August 23, 2018).

[25] The CLIC Collaboration, Updated baseline for a staged Compact Linear Collider, ArXiv:1608.07537 [Hep-Ex, Physics:Physics]. (2016). doi:10.5170/CERN-2016-004.

[26] A. Descoeudres, Y. Levinsen, S. Calatroni, M. Taborelli, W. Wuensch, Investigation of the dc vacuum breakdown mechanism, Phys. Rev. ST Accel. Beams. 12 (2009) 092001. doi:10.1103/PhysRevSTAB.12.092001.

[27] R.H. Fowler, L. Nordheim, Electron emission in intense electric fields, Proc. R. Soc. London, Ser. A. 119 (1928) 173–181.

[28] J. Diao, K. Gall, M.L. Dunn, J.A. Zimmerman, Atomistic simulations of the yielding of gold nanowires, Acta Materialia. 54 (2006) 643–653. doi:10.1016/j.actamat.2005.10.008.

[29] L.A. Zepeda-Ruiz, B. Sadigh, J. Biener, A.M. Hodge, A.V. Hamza, Mechanical response of freestanding Au nanopillars under compression, Appl. Phys. Lett. 91 (2007) 101907. doi:10.1063/1.2778761.

[30] Z.S. Pereira, E.Z. da Silva, Cold Welding of Gold and Silver Nanowires: A Molecular Dynamics Study, J. Phys. Chem. C. 115 (2011) 22870–22876. doi:10.1021/jp207842v.

[31] X. He, F. Cheng, Z.-X. Chen, The Lattice Kinetic Monte Carlo Simulation of Atomic Diffusion and Structural Transition for Gold, Scientific Reports. 6 (2016) 33128. doi:10.1038/srep33128.

[32] T. Müller, K.-H. Heinig, B. Schmidt, Template-directed self-assembly of buried nanowires and the pearling instability, Materials Science and Engineering: C. 19 (2002) 209–213. doi:10.1016/S0928-4931(01)00465-9.

[33] A.S. Pohjonen, S. Parviainen, T. Muranaka, F. Djurabekova, Dislocation nucleation on a near surface void leading to surface protrusion growth under an external electric field, J. Appl. Phys. 114 (2013) 033519. doi:10.1063/1.4815938.

[34] S. Parviainen, F. Djurabekova, A. Pohjonen, K. Nordlund, Molecular dynamics simulations of nanoscale metal tips under electric fields, Nucl. Instrum. Methods Phys. Res., Sect. B. 269 (2011) 1748–1751. doi:10.1016/j.nimb.2010.12.058.

[35] S. Parviainen, F. Djurabekova, H. Timko, K. Nordlund, Electronic processes in molecular dynamics simulations of nanoscale metal tips under electric fields, Computational Materials Science. 50 (2011) 2075–2079. doi:10.1016/j.commatsci.2011.02.010.

[36] M. Veske, A. Kyritsakis, K. Eimre, V. Zadin, A. Aabloo, F. Djurabekova, Dynamic coupling of a finite element solver to large-scale atomistic simulations, Journal of Computational Physics. 367 (2018) 279–294. doi:10.1016/j.jcp.2018.04.031.

[37] A. Kyritsakis, M. Veske, K. Eimre, V. Zadin, F. Djurabekova, Thermal runaway of metal nano-tips during intense electron emission, J. Phys. D: Appl. Phys. 51 (2018) 225203. doi:10.1088/1361-6463/aac03b.

[38] M. Veske, S. Parviainen, V. Zadin, A. Aabloo, F. Djurabekova, Electrodynamics—molecular dynamics simulations of the stability of Cu nanotips under high electric field, J. Phys. D: Appl. Phys. 49 (2016) 215301. doi:10.1088/0022-3727/49/21/215301.

[39] V. Jansson, E. Baibuz, F. Djurabekova, Long-term stability of Cu surface nanotips, Nanotechnology. 27 (2016) 265708. doi:10.1088/0957-4484/27/26/265708.

[40] J. Frantz, M. Rusanen, K. Nordlund, I.T. Koponen, Evolution of Cu nanoclusters on Cu(100), J. Phys.: Condens. Matter. 16 (2004) 2995. doi:10.1088/0953-8984/16/17/027.

[41] V.T. Binh, N. Garcia, S.T. Purcell, Electron Field Emission from Atom-Sources: Fabrication, Properties, and Applications of Nanotips, in: P.W. Hawkes (Ed.), Advances in Imaging and Electron Physics, Elsevier, 1996: pp. 63–153. doi:10.1016/S1076-5670(08)70156-3.

[42] J. Norem, Z. Insepov, Can surface cracks and unipolar arcs explain breakdown and gradient limits?, ArXiv:1208.0847 [Physics.Acc-Ph]. (2012). http://arxiv.org/abs/1208.0847 (accessed August 23, 2018).

[43] V. Zadin, A. Pohjonen, A. Aabloo, K. Nordlund, F. Djurabekova, Electrostatic-elastoplastic simulations of copper surface under high electrical fields, Phys. Rev. ST Accel. Beams. 17 (2014) 103501.

[44] J. Yvonnet, H.L. Quang, Q.-C. He, An XFEM/level set approach to modelling surface/interface effects and to computing the size-dependent effective properties of nanocomposites, Comput Mech. 42 (2008) 119–131. doi:10.1007/s00466-008-0241-y.

[45] H.S. Park, P.A. Klein, G.J. Wagner, A surface Cauchy–Born model for nanoscale materials, Int. J. Numer. Meth. Engng. 68 (2006) 1072–1095. doi:10.1002/nme.1754.

[46] A.F. Bower, Applied mechanics of solids, CRC Press, Boca Raton, 2010.

[47] D. Roylance, Mechanics of Materials, (2000).

[48] E.B. Tadmor, R.E. Miller, R.S. Elliott, Continuum mechanics and thermodynamics: from fundamental concepts to governing equations, Cambridge University Press, Cambridge, UK; New York, 2012.

[49] R. Shuttleworth, The Surface Tension of Solids, Proc. Phys. Soc. A. 63 (1950) 444. doi:10.1088/0370-1298/63/5/302.

[50] L. Vitos, A.V. Ruban, H.L. Skriver, J. Kollár, The surface energy of metals, Surface Science. 411 (1998) 186–202. doi:10.1016/S0039-6028(98)00363-X.

[51] V.V. Bulatov, W. Cai, Computer simulations of dislocations, Oxford University Press, Oxford; New York, 2006.

[52] D. Hull, D.J. Bacon, Introduction to dislocations, Butterworth-Heinemann, Oxford, 2011.

[53] J.P. Hirth, J. Lothe, Theory of dislocations, 1982.

[54] D.G.G. Andrade, J.B. Vílchez, Scheme of the Burgers` vector in edge and screw dislocations, (2008), Creative Commons Attribution-Share Alike 3.0 Unported license, https://en.wikipedia.org/wiki/File:Vector_de_Burgers.PNG (accessed August 23, 2018).

[55] D.C. Rapaport, The art of molecular dynamics simulation, Second Edition, Cambridge University Press, New York, 2004.

[56] J.M. Haile, Molecular dynamics simulation. Elementary methods, John Wiley & Sons, Inc., New York, Chichester, Brisbane, Toronto, Singapore, 1992.

[57] V. Brázdová, D.R. Bowler, Atomistic computer simulations: a practical guide, John Wiley & Sons, 2013.

[58] M.S. Daw, M.I. Baskes, Semiempirical, Quantum Mechanical Calculation of Hydrogen Embrittlement in Metals, Phys. Rev. Lett. 50 (1983) 1285–1288. doi:10.1103/PhysRevLett.50.1285.

[59] M.S. Daw, M.I. Baskes, Embedded-atom method: Derivation and application to impurities, surfaces, and other defects in metals, Phys. Rev. B. 29 (1984) 6443–6453. doi:10.1103/PhysRevB.29.6443.

[60] M.J. Sabochick, N.Q. Lam, Radiation-induced amorphization of ordered intermetallic compounds CuTi, CuTi2, and Cu4Ti3: A molecular-dynamics study, Phys. Rev. B. 43 (1991) 5243–5252. doi:10.1103/PhysRevB.43.5243.

[61] M.S. Stave, D.E. Sanders, T.J. Raeker, A.E. DePristo, Corrected effective medium method. V. Simplifications for molecular dynamics and Monte Carlo simulations, The Journal of Chemical Physics. 93 (1990) 4413–4426. doi:10.1063/1.458724.

[62] G. Grochola, S.P. Russo, I.K. Snook, On fitting a gold embedded atom method potential using the force matching method, The Journal of Chemical Physics. 123 (2005) 204719. doi:10.1063/1.2124667.

[63] M.I. Mendelev, S. Han, D.J. Srolovitz, G.J. Ackland, D.Y. Sun, M. Asta, Development of new interatomic potentials appropriate for crystalline and liquid iron, Philosophical Magazine. 83 (2003) 3977–3994. doi:10.1080/14786430310001613264.

[64] R.C. Pasianot, L. Malerba, Interatomic potentials consistent with thermodynamics: The Fe–Cu system, Journal of Nuclear Materials. 360 (2007) 118–127. doi:10.1016/j.jnucmat.2006.09.008.

[65] G. Bonny, R.C. Pasianot, N. Castin, L. Malerba, Ternary Fe–Cu–Ni many-body potential to model reactor pressure vessel steels: First validation by simulated thermal annealing, Philos. Mag. 89 (2009) 3531–3546. doi:10.1080/14786430903299824.

[66] S. Plimpton, Fast Parallel Algorithms for Short-Range Molecular Dynamics, J. Comput. Phys. 117 (1995) 1–19. doi:10.1006/jcph.1995.1039.

[67] W.C. Swope, H.C. Andersen, P.H. Berens, K.R. Wilson, A computer simulation method for the calculation of equilibrium constants for the formation of physical clusters of molecules: Application to small water clusters, The Journal of Chemical Physics. 76 (1982) 637–649. doi:10.1063/1.442716.

[68] L. Verlet, Computer "Experiments" on Classical Fluids. I. Thermodynamical Properties of Lennard-Jones Molecules, Phys. Rev. 159 (1967) 98–103. doi:10.1103/PhysRev.159.98.

[69] H.J.C. Berendsen, J.P.M. Postma, W.F. van Gunsteren, A. DiNola, J.R. Haak, Molecular dynamics with coupling to an external bath, The Journal of Chemical Physics. 81 (1984) 3684–3690. doi:10.1063/1.448118.

[70] S. Nosé, A molecular dynamics method for simulations in the canonical ensemble, Molecular Physics. 52 (1984) 255–268. doi:10.1080/00268978400101201.

[71] W.G. Hoover, Canonical dynamics: Equilibrium phase-space distributions, Phys. Rev. A. 31 (1985) 1695–1697. doi:10.1103/PhysRevA.31.1695.

[72] E.B. Tadmor, R.E. Miller, Modeling materials: continuum, atomistic, and multiscale techniques, Cambridge University Press, Cambridge; New York, 2011.

[73] N.C. Admal, E.B. Tadmor, A unified interpretation of stress in molecular systems, Journal of Elasticity. 100 (2010) 63–143.

[74] A.P. Thompson, S.J. Plimpton, W. Mattson, General formulation of pressure and stress tensor for arbitrary many-body interaction potentials under periodic

boundary conditions, The Journal of Chemical Physics. 131 (2009) 154107. doi:10.1063/1.3245303.

[75] C. Rycroft, Voro++: a three-dimensional Voronoi cell library in C++, Lawrence Berkeley National Laboratory. (2009). http://escholarship.org/uc/item/8sf4t5x8 (accessed August 23, 2018).

[76] J.A. Zimmerman, E.B. WebbIII, J.J. Hoyt, R.E. Jones, P.A. Klein, D.J. Bammann, Calculation of stress in atomistic simulation, Modelling and Simulation in Materials Science and Engineering. 12 (2004) S319–S332. doi:10.1088/0965-0393/12/4/S03.

[77] M. Parrinello, A. Rahman, Polymorphic transitions in single crystals: A new molecular dynamics method, Journal of Applied Physics. 52 (1981) 7182–7190. doi:10.1063/1.328693.

[78] W. Shinoda, M. Shiga, M. Mikami, Rapid estimation of elastic constants by molecular dynamics simulation under constant stress, Phys. Rev. B. 69 (2004) 134103. doi:10.1103/PhysRevB.69.134103.

[79] G.R. Liu, S.S. Quek, The finite element method: a practical course, Butterworth-Heinemann, Oxford ; Boston, 2003.

[80] D. Raabe, Computational Materials Science: the simulation of materials microstructures and properties, Wiley-VCH, 1998.

[81] O. Schenk, K. Gärtner, W. Fichtner, A. Stricker, PARDISO: a high-performance serial and parallel sparse linear solver in semiconductor device simulation, Future Generation Computer Systems. 18 (2001) 69–78. doi:https://doi.org/10.1016/S0167-739X(00)00076-5.

[82] P.R. Amestoy, I.S. Duff, J.-Y. L'Excellent, Multifrontal parallel distributed symmetric and unsymmetric solvers, Computer Methods in Applied Mechanics and Engineering. 184 (2000) 501–520. doi:10.1016/S0045-7825(99)00242-X.

[83] P. Amestoy, I. Duff, J. L'Excellent, J. Koster, A Fully Asynchronous Multifrontal Solver Using Distributed Dynamic Scheduling, SIAM J. Matrix Anal. & Appl. 23 (2001) 15–41. doi:10.1137/S0895479899358194.

[84] P. Deuflhard, A modified Newton method for the solution of ill-conditioned systems of nonlinear equations with application to multiple shooting, Numerische Mathematik. 22 (1974) 289–315. doi:10.1007/BF01406969.

[85] COMSOL Multiphysics® Modeling Software, (n.d.). https://www.comsol.com/ (accessed August 23, 2018).

[86] J.S. Vermaak, C.W. Mays, D. Kuhlmann-Wilsdorf, On surface stress and surface tension I. Theoretical considerations, Surface Science. 12 (1968) 128–133.

[87] V.B. Shenoy, Atomistic calculations of elastic properties of metallic fcc crystal surfaces, Phys. Rev. B. 71 (2005) 094104. doi:10.1103/PhysRevB.71.094104.

[88] A.B. Bortz, M.H. Kalos, J.L. Lebowitz, A new algorithm for Monte Carlo simulation of Ising spin systems, Journal of Computational Physics. 17 (1975) 10–18. doi:10.1016/0021-9991(75)90060-1.

[89] G. Henkelman, G. Jóhannesson, H. Jónsson, Methods for Finding Saddle Points and Minimum Energy Paths, in: S.D. Schwartz (Ed.), Theoretical Methods in Condensed Phase Chemistry, Springer Netherlands, 2002: pp. 269–302. doi:10.1007/0-306-46949-9_10.

[90] G. Antczak, G. Ehrlich, Long Jump Rates in Surface Diffusion: W on W(110), Phys. Rev. Lett. 92 (2004) 166105. doi:10.1103/PhysRevLett.92.166105.

[91] A.S. Pohjonen, Dislocation mechanisms leading to protrusion growth under electric field induced stress on metal surfaces, University of Helsinki, 2013.

[92] A.S. Pohjonen, F. Djurabekova, K. Nordlund, A. Kuronen, S.P. Fitzgerald, Dislocation nucleation from near surface void under static tensile stress in Cu, J. Appl. Phys. 110 (2011) 023509. doi:10.1063/1.3606582.

[93] A.S. Pohjonen, F. Djurabekova, A. Kuronen, S.P. Fitzgerald, K. Nordlund, Analytical model of dislocation nucleation on a near-surface void under tensile surface stress, Philosophical Magazine. 92 (2012) 3994–4010. doi:10.1080/14786435.2012.700415.

[94] A. Stukowski, Visualization and analysis of atomistic simulation data with OVITO–the Open Visualization Tool, Modelling Simul. Mater. Sci. Eng. 18 (2010) 015012. doi:10.1088/0965-0393/18/1/015012.

[95] C.L. Kelchner, S.J. Plimpton, J.C. Hamilton, Dislocation nucleation and defect structure during surface indentation, Phys. Rev. B. 58 (1998) 11085–11088. doi:10.1103/PhysRevB.58.11085.

[96] V.A. Lubarda, M.S. Schneider, D.H. Kalantar, B.A. Remington, M.A. Meyers, Void growth by dislocation emission, Acta Materialia. 52 (2004) 1397–1408. doi:10.1016/j.actamat.2003.11.022.

[97] A. Stukowski, Structure identification methods for atomistic simulations of crystalline materials, Modelling Simul. Mater. Sci. Eng. 20 (2012) 045021. doi:10.1088/0965-0393/20/4/045021.

[98] R.E. Rudd, E.T. Seppälä, L.M. Dupuy, J. Belak, Void coalescence processes quantified through atomistic and multiscale simulation, J Computer-Aided Mater Des. 14 (2007) 425–434. doi:10.1007/s10820-007-9054-0.

[99] K.H. Westmacott, R.E. Smallman, P.S. Dobson, The Annealing of Voids in Quenched Aluminium and a Determination of the Surface Energy, Metal Science Journal. 2 (1968) 177–181. doi:10.1179/030634568790443530.

Publications

I

IOP Publishing Modelling and Simulation in Materials Science and Engineering

Modelling Simul. Mater. Sci. Eng. **23** (2015) 025009 (17pp) doi:10.1088/0965-0393/23/2/025009

Molecular dynamics simulations of near-surface Fe precipitates in Cu under high electric fields

Simon Vigonski[1,2], **Flyura Djurabekova**[2], **Mihkel Veske**[1,2], **Alvo Aabloo**[1] **and Vahur Zadin**[1,2]

[1] Intelligent Materials and Systems Lab, Institute of Technology, University of Tartu, Nooruse 1, 50411 Tartu, Estonia
[2] Department of Physics and Helsinki Institute of Physics, University of Helsinki, PO Box 43 (Pietari Kalmin katu 2), 00014 Helsinki, Finland

E-mail: simon.vigonski@ut.ee

Received 10 June 2014, revised 1 December 2014
Accepted for publication 23 December 2014
Published 22 January 2015

Abstract

High electric fields in particle accelerators cause vacuum breakdowns in the accelerating structures. The breakdowns are thought to be initiated by the modification of material surface geometry under high electric fields. These modifications in the shape of surface protrusions enhance the electric field locally due to the increased surface curvature. Using molecular dynamics, we simulate the behaviour of Cu containing a near-surface Fe precipitate under a high electric field. We find that the presence of a precipitate under the surface can cause the nucleation of dislocations in the material, leading to the appearance of atomic steps on the surface. Steps resulting from several precipitates in close proximity can also form protruding plateaus. Under very high external fields, in some cases, we observed the formation of voids above or below the precipitate, providing additional dislocation nucleation sites.

Keywords: molecular dynamics, precipitates, near-surface voids

(Some figures may appear in colour only in the online journal)

1. Introduction

Vacuum breakdowns have been the focus of considerable interest due to the damage they can cause to structures exposed to high electric fields [1]. The conditions for vacuum breakdowns occur in several applications such as particle accelerators [2, 3] and fusion reactors [4].

The Compact Linear Collider (CLIC) is a new accelerator design, proposed at CERN to perform electron–positron beam collisions at energies from 0.5 to 5 TeV with optimal performance at 3 TeV [5]. To achieve these energies, very high accelerating gradients over 100 MV m^{-1} are needed [6]. Repeated breakdowns near the surface of the accelerating structures become a key problem under these conditions [7]. It was found that the optimal operational conditions, such as the optimal energy consumption and the frequency of replacements of expensive parts, can be achieved if the breakdown rate is kept at a low value, less than 3×10^{-7}1/pulse/m [8].

The applied electric field causes surface atoms to become charged and affects them with the Lorentz force, resulting in tensile stress in the material [9]. The generated stresses usually fall below the yield strength of the structural materials, unless the electric field is very high. Experiments show that electric fields of the order of hundreds of MV m^{-1} cause vacuum breakdowns near a copper surface held in an ultrahigh vacuum [10], although these fields are well below the critical fields for field-assisted atom evaporation [11]. The measurements of electron emission currents in the experiments at electric fields designed for accelerator operation can be fairly well fit to the Fowler–Nordheim equation [12] or its modifications [13–15], assuming a strong local field enhancement β. In copper, β is usually in the range of 30 to 140 [10], but never below 20 [16]. The enhanced fields lead to significant stress on the surface, which may result in plastic deformations underneath the surface, especially in the presence of extended defects. These, in turn, may yield surface protrusions, the candidates for breakdown sites.

Currently, the field enhancement factor is explained by the existence of a needle-like field emitting tips on the electrode surface, which may locally enhance the applied electric field. However, the existence of these tips is hypothetical, as they have never been observed experimentally and the exact mechanism producing these field emitting tips is not known [10].

The behaviour of long, thin field emitters was investigated by means of molecular dynamics (MD) simulations [17]. It was seen that Joule heating due to the electron current in the tip can change the shape, dramatically reducing its stability. A kinetic Monte Carlo study of Cu surface evolution [18] showed that nanoclusters (>10 nm in diameter) placed on a flat surface eventually flatten due to surface relaxation effects. These facts may explain the absence of direct experimental observations of sharp tips.

Previously, different attempts were made to develop a theoretical model which can explain the onset of the vacuum breakdown phenomenon [19]. Insepov *et al* investigated possible mechanisms leading to a breakdown event using MD [20, 21]. In [20], the evaporation of large atomic clusters from a pre-existing protrusion was shown. In [22], heating of a microprotrusion, caused by Joule heating and the Nottingham effect, was studied. In other works, the influence of microscale molten particles in a high gradient system was investigated [23]. The finite element method was applied in [24, 25] to investigate the field enhancement arising at the edges of the microcracks that can appear due to fatigue in the material under repeated loading. In all of these works, however, surface defects were already assumed to exist.

The average minimum electric field which causes vacuum breakdown was found to have a clear dependence on the material used as a cathode [10]. The correlation of this dependence with the crystal structure of the investigated materials is striking. Ranking the materials by their ability to withstand electric fields from lowest to highest values corresponds to the change of crystal structures from face-centred cubic (fcc) to hexagonal closed packed (hcp). This observation motivates the investigation of the elastoplastic response of materials on applied electric fields [26].

It was shown that in the presence of a sub-surface void, the tensile stress, which is exerted at the surface by the applied electric field, may cause mass transport of the material above the void, forming a protrusion on the surface [27]. It was also shown that the evolution of the

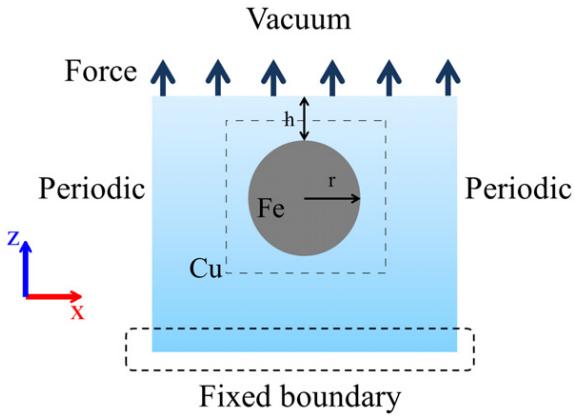

Figure 1. Cross section of the Cu cell with an Fe precipitate, which is described in the text by the depth (h) to radius (r) ratio. The three lowest layers are fixed and force is applied to the atoms initially in the top two layers. The top surface is exposed to vacuum and the surfaces in the x and y directions are periodic.

surface geometry under a strong external electric field leads to a positive feedback mechanism and catastrophic tip growth [28].

In this work, using MD simulations, we aim to investigate the effect of the presence of a different type of extended lattice defect—a precipitate—on surface roughening under an external electric field, since precipitates can also lead to dislocation nucleation, resulting in stable plastic deformation under external stress [29]. While voids can be interpreted as regions with different mechanical properties, precipitates are also regions with different properties, but contrary to the voids they have their own mechanical response which may interact with the mechanical properties of the matrix when an external stress is applied. We investigate the plastic deformations in a single crystal Cu under tensile stress in the presence of a near-surface defect by replacing a void with a precipitate that is mechanically stronger than Cu.

2. Methods

2.1. Simulation setup

Classical MD simulations were performed with the open source LAMMPS code [30]. For the interactions between the atoms, the Bonny *et al* many-body embedded atom method (EAM) potential [31] was used. Results were visualized with the OVITO software [32].

Figure 1 illustrates the geometry of the simulated system. The simulation cell dimensions were $16.7 \times 16.7 \times 19.9$ nm. The [1 1 0] crystal direction was chosen to coincide with the z direction, as that is the direction of slip in fcc crystals [33]. The x and y directions were set to the [0 0 1] and [1 $\bar{1}$ 0] crystal directions, respectively. The x and y boundaries were periodic. The spherical Fe precipitate was located in the centre of the simulation cell in the lateral directions. We selected Fe as an example of a strong precipitate. The relevant experimental elastic constants for Fe are $c_{11} = 226$ GPa and $c_{44} = 116$ GPa, in comparison to the elastic constants of Cu $c_{11} = 168.3$ GPa and $c_{44} = 75.7$ GPa [34]. The position along the z-axis varied for different simulations to analyse the effect of the depth-to-radius ratios of precipitates (h/r, where h and r, as in figure 1, are the depth of the precipitate measured from the surface of the material to the top of the precipitate and the radius, respectively). A precipitate with a radius

of 2.2 nm was simulated at two different depths: $h = 5.6$ nm ($h/r = 2.5$), in the following referred to as a 'shallow' precipitate, and $h = 9.8$ nm ($h/r = 4.5$), referred to as a 'deep' precipitate.

The Fe precipitate was inserted into the Cu matrix as a body-centred cubic (bcc) nanocrystal. The initial relaxation period of 20 ps relaxed the precipitate, creating a transition region between the bcc Fe core and the fcc Cu environment. The transition region of one to two atom layers extended into the precipitate, while the core remained bcc. Limited faceting of the precipitate was observed after relaxation. Longer relaxation times (up to 100 ps) did not cause significant changes in the structure of the precipitate compared to the configuration obtained after 20 ps. It was shown previously [35] that small Cu inclusions in Fe experience the phase transition into bcc, but no experimental evidence of phase transitions of Fe precipitates in Cu is available. Our test simulations showed that an Fe precipitate inserted as fcc was not stable and after relaxation turned into a multi-grained polycrystalline bcc inclusion. The spherical shape of the precipitate in the current work was chosen for simplicity.

The positions of the atoms in the three lowest layers were fixed throughout the whole simulation. The upper boundary was exposed to vacuum and force was applied to the atoms that were located in the upper two layers at the start of the simulation. The simulation was stopped when atoms started leaving the surface due to evaporation. The approximation of constant force on the surface atoms is valid as long as the surface deformation is insignificant.

The MD time step was 1 fs. The system was first relaxed for 20 ps to achieve thermodynamic equilibrium in the NpT isothermal–isobaric ensemble. Afterwards, a force was applied to the surface atoms, imitating an electrostatic force exerted at the conducting surface by an electric field. The expression for the force on the surface in the case of a uniaxial field normal to the surface is [27]

$$\boldsymbol{F} = \varepsilon_0 |\boldsymbol{E}|^2 A n, \tag{1}$$

where $\boldsymbol{E}$ is the electric field, A is the surface area, n is the surface normal and ε_0 is the vacuum permittivity. The total force acting on the surface was divided evenly among the atoms in the surface layers. The force was applied in the direction perpendicular to the surface to provide the desired uniaxial tensile stress. This approximation is appropriate since the surface remains relatively flat throughout the simulations. For the main simulations, the stress was linearly ramped with the constant ramping rate 45.8 MPa ps^{-1} over 200 ps until the structure yielded at the maximal value 9.16 GPa (corresponding to the electric field strength 32.2 GV m^{-1}). For the duration of the ramping, the ensemble was switched to the NVT canonical ensemble.

The temperature throughout all simulations was 600 K. The initial velocities of the atoms were generated pseudo-randomly to comply with the temperature, changing the seed number for every new simulation to mimic the stochastic nature of the process. For both cases of 'shallow' and 'deep' precipitates, 80 simulations were conducted.

The homogeneous dislocation nucleation stress for Cu when loaded in the [1 1 0] direction is 4.23 GPa [36]. At stresses lower than this, dislocation nucleation becomes a stochastic process. Unfortunately, the probability of such a process is rather difficult to estimate in MD simulations, which are severely limited by the timescales they can cover. Nucleation of dislocations is a complicated process that depends on many factors like temperature [37, 38], crystal orientation [36] and strain rate [39]. Schuh *et al* [37] investigated these dependences experimentally and provided quantitative data for probabilistic nucleation of dislocations. They showed that the probability of nucleation increases with temperature, and thus thermal fluctuations within the Cu sample play a significant role in the nucleation process. Their experimental investigation of the dependence on strain rate along with the simulations by Zhu *et al* [39] showed that the increase of strain rates increases the stress necessary for dislocation

nucleation. This means that the nucleation stress at strain rates typical in simulations is up to two times greater than at experimental strain rates depending on temperature [39].

We conducted additional simulations at lower stresses of 3.88 and 3.64 GPa to confirm the possibility of dislocation nucleation around the precipitate. The stress was ramped with the same rate as the main simulations to the target value, after which it was held constant for 1 ns. We simulated the system with each noted target stress 20 times and counted the observed nucleation dislocation instances. With 3.88 GPa maximum stress, dislocations appeared in 16 of 20 simulations. The dislocations nucleated at various times, from the ramping period to 0.9 ns after the maximum stress was reached. With 3.64 GPa maximum stress, 7 of the 20 simulations had dislocations.

From this data, we can conclude that dislocations nucleate at lower stresses, albeit with a probability that decreases as the stress is decreased. In this work, we investigated the processes that can happen in copper in the presence of precipitates and the mechanisms that may lead to modification of the material surface which contains the precipitates and is held under high electric field. Real materials have dislocations already present, and their interaction with precipitates could proceed similarly to our simulation. Moreover, the dislocations may appear at the interface of precipitates due to the interaction of precipitates with strain fields of other extended defects forming and existing in the extreme operational conditions of accelerating structures.

Many of the simulation parameters were chosen to coincide with the work of Pohjonen *et al* [27] to compare our results to the case with a near-surface void. Specifically, the dimensions of the system, the crystallographic orientation of the free surface, the relaxation time and the ramping rate of stress were the same as in [27].

2.2. Identification of newly formed voids

To identify newly formed voids during the simulation, we have developed a method which calculates the volume of the voids with the help of Voronoi cells. The algorithm proposed by Dupuy and Rudd [40] can be used to identify surfaces in MD simulations, however, it fails to detect new surfaces that appear during the simulation.

The algorithm used in the present work for calculating the void volume is as follows (the C++ code is available as supplementary material). The interface between the Fe precipitate and Cu constitutes the main region of interest. A cubic observation box with a side length of 12.8 nm was defined around this region, as depicted by the dashed line in figure 1. This length is approximately three times the radius of the precipitate. The resulting volume of the box is sufficiently large to contain all phenomena of interest and sufficiently small to exclude the material surface from the analysis.

To calculate the volume of the appearing voids, the total volume of the atoms in the observation box is compared to the volume of the box itself. The atomic volumes are defined with the help of Voronoi cells, generated using the Voro++ code [41]. During the Voronoi tessellation, we limit the maximum possible Voronoi volume of each cell to a value $V_{\mathrm{v,max}}$ to ensure that the void region would not be covered by any cells. To define the numerical value of $V_{\mathrm{v,max}}$, we consider two extreme cases. The first case is a 'bulk' atom with all neighbours present. Its average Voronoi volume is calculated by dividing the total volume of all Voronoi cells in a void free lattice by the number of atoms, yielding $V_{\mathrm{v,ave}} = 0.0118\,\mathrm{nm}^3$. The second case is a hypothetical 'free' atom (with no neighbours) with the Voronoi cell volume $V_{\mathrm{v,max}} = 0.075\,\mathrm{nm}^3$. The value of $V_{\mathrm{v,max}}$ is defined to be large enough to cover vacancies appearing in the material and the amorphous regions around the Cu–Fe interface. The Voronoi volume of actual surface atoms falls between these two limiting values.

Voronoi cells adjacent to the observation box boundaries are cut by the planes of the box so as not to extend outside the region. If the observation box contains voids, the total volume of the Voronoi cells surrounding the atoms will be smaller than the volume of the box. Some atoms will have left the box due to mass transport towards the free surface as the material undergoes elastic and plastic deformation. The average atomic volume for bulk atoms around the void can also decrease as the formation of a void relaxes the stress in the system.

As the lattice constant of Fe is smaller than that of Cu, and $V_{\mathrm{v,max}}$ for Voronoi cell construction is taken to be independent of the atom type in the strained system, the presence of Fe atoms in the observation box does not significantly affect the calculation. The Fe precipitate deformation during the simulations is minimal with its atoms remaining close together. Thus the Voronoi cells surrounding the Fe atoms will act similarly to bulk atoms. $V_{\mathrm{v,max}}$ is selected from the relaxed configuration of the species with the larger lattice constant, ensuring that increasing average interatomic distance due to elastic deformation does not contribute to the volume calculation. The atoms surrounding the Cu–Fe interface do not affect the calculation, as $V_{\mathrm{v,max}}$ is large enough to cover the amorphous area between them.

The volume of voids present in the observation box is calculated in the following way:

$$V_{\mathrm{voids}} = V_{\mathrm{box}} - \sum_{i} V_i, \tag{2}$$

where V_{box} is the total volume of the observation box ($12.8^3\,\mathrm{nm}^3$) and V_i is the volume of the ith Voronoi cell. Since the size of a Voronoi cell is limited to the maximum Voronoi volume $V_{\mathrm{v,max}}$, the sum of the Voronoi cell volumes will be smaller than the volume of the box if any voids are present. The volume of the voids was calculated every picosecond in all simulations.

The present algorithm tends to underestimate the volume of the voids as the atoms adjacent to the void surface have larger Voronoi volumes than those in the bulk of the material. We estimate this error for each surface atom as the difference between its Voronoi volume and the average Voronoi volume for bulk atoms in a relaxed system, $V_{\mathrm{v,ave}}$. This difference is taken into account by detecting the atoms that constitute the surface of the void with the help of coordination analysis. The coordination number for all atoms is calculated with a cutoff distance of 0.42 nm. All atoms with a coordination number of 15 or less are taken to be surface atoms. The atomic volume of those atoms is reduced to the average atomic volume of the system at that time. This results in the approximate doubling of the void volume compared to uncorrected results. To validate this correction, a different correction method was also investigated. The relative error in volume calculation was studied by creating a spherical void of known volume into a relaxed system and calculating the volume with the described uncorrected algorithm. The relative error depends on the surface to volume ratio of the void and decreases as the volume of the void is increased. The voids formed in the simulations were rather small, and hence the relative error was estimated to be $\sim$100% (the correction factor depends on the volume). The final corrected volume is similar using both correction methods. Results are presented using the first coordination analysis correction.

2.3. Stress calculation

To calculate the local stress distribution in the system at specific points during the simulations, we utilized the following method. A snapshot of the system was taken during external force ramping before the event of interest occurred. The ramping of the external force was stopped and it was held constant to calculate stress at the conditions leading up to the event. The system was held at constant external force for 20 ps, followed by time averaging the per atom

virial [42] for another 20 ps. The time averaging is necessary to remove the noise due to thermal fluctuations of the atoms. The resulting time averaged virial for each atom was then divided by the Voronoi volume of that atom to obtain the per atom stress. The Voronoi volume calculation in this case is simpler than that described earlier for void detection, as no voids were present in any of the stress calculations. An ordinary Voronoi tessellation was used without any special constraints.

In the chosen orientation of the simulated system, the two slip planes of interest contain the y-axis, with the plane normal at an angle to the x and z directions. In this special case, to get the final resolved shear stress acting on the slip planes, the components of the stress tensor were transformed by a rotation around the y-axis to make the transformed z'-axis correspond to the slip plane normal. The transformed coordinates are shown in figure 2. The transformation results in the $\sigma_{x'z'}$ component of the stress tensor to correspond to the stress acting on the slip plane in the slip direction.

3. Results and discussion

3.1. Dislocation-mediated formation of surface steps

The influence of a high external electric field on the simulated material is demonstrated in figure 2, where the formation of stacking faults around the precipitate is shown. Stacking faults form when a layer of atoms moves away from its perfect lattice position [33]. The figure displays the cross-sections of central parts of two different simulation cells with deep precipitates ($h/r = 4.5$). In the upper figures 2(a) and (c), the Fe precipitate is shown in black and the Cu atoms are coloured according to the centrosymmetry parameter [43]. The colouring in the lower figures 2(b) and (d) represents the resolved shear stress acting on one of the slip planes of the system. The transformed $\sigma_{x'z'}$ component of the stress tensor is plotted, with the axes rotated as shown in the axis diagram.

The centrosymmetry parameter characterizes the adherence of an atom's neighbourhood to a perfect lattice. When normalized by the square of the lattice constant, centrosymmetry is 0 for a perfect lattice, around 0.3 for point defects or stacking faults and over 1 for surface atoms [44]. Centrosymmetry analysis is not conducted for the Fe atoms as the stresses present in the simulation are not sufficiently large to cause any significant change in the Fe lattice.

The external tensile stresses exerted on the surface due to the electric field are 6.18 GPa ($E = 26.4\,\mathrm{GV\,m^{-1}}$) and 6.92 GPa ($E = 28.0\,\mathrm{GV\,m^{-1}}$) in figures 2($a$) and ($c$), respectively. The majority of Cu atoms form a perfect lattice with a near-zero centrosymmetry parameter, displaying only occasional thermal fluctuations. The atoms at the Cu–Fe interface display centrosymmetry values characteristic of stacking faults as the lattice mismatch between the fcc Cu and bcc Fe causes them to adapt to the surface stresses and form a transitional region between the two lattice types.

Under the effects of the external stress, dislocations form around the precipitate. The dislocations are leading Shockley partials with a Burger's vector $\frac{1}{6}\langle 1\,1\,2\rangle$, corresponding to a half-slip. Expansion of dislocations of this type can be seen in figures 2(a) and (c) by the stacking faults which they encircle. A stacking fault is seen in the figures as a line resulting from the intersection of the stacking fault with the plane of the figure. In figure 2(a) the leading partial dislocation forming at the top of the precipitate expands towards the material surface due to the resolved shear stress acting on it. The other leading partial dislocation that forms below the precipitate also expands under the effects of the resolved shear stress. As the stress direction is the same for both mentioned dislocations and their directions of motion are opposite, we can conclude that the dislocation that forms below the precipitate has an opposite line sense

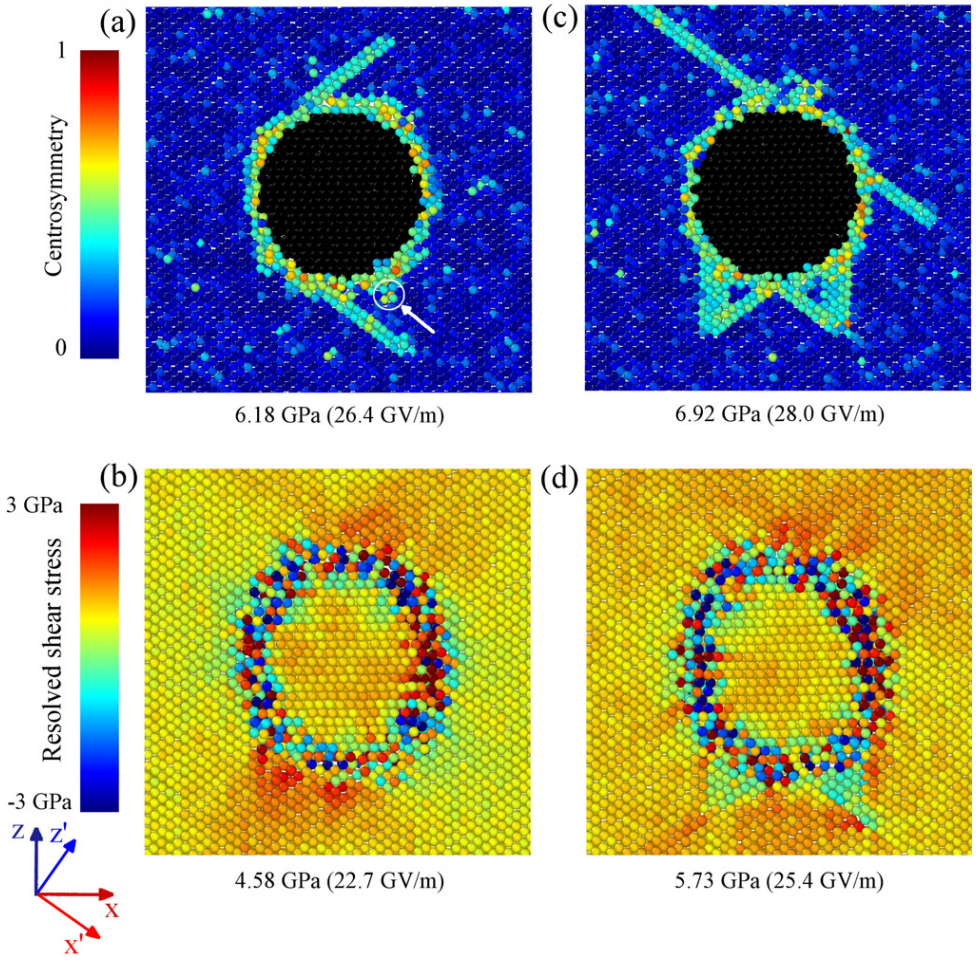

Figure 2. Snapshots of two simulations of a Cu cell with a deep Fe precipitate under strong tensile stress: (*a*) formation of a planar stacking fault at the top of the precipitate; (*b*) stress distribution before formation of the stacking faults; (*c*) two complete stacking fault tetrahedra under the precipitate and an extensive planar stacking fault at the top of the precipitate in a different simulation; (*d*) stress distribution before stacking fault formation in the second simulation. The stress plots show the $\sigma_{x'z'}$, with the directions as in the axes diagram. In (*a*) and (*c*), Fe atoms are drawn black.

compared to that of the upper dislocation. In the same figure we show the nucleation of a partial dislocation under the precipitate (marked by the arrow in figure 2(*a*)), which expands on a different (vertical) slip plane due to the elastic attraction between dislocations. When this dislocation intersects the dislocation earlier nucleated also under the precipitate, but on a different $\{1\,1\,1\}$ plane, they become locked and form a stacking fault tetrahedron.

Due to the randomness inherent in the system, a simulation with identical initial conditions but a different random seed results in a different configuration of dislocations around the precipitate, as shown in figure 2(*c*). Two stacking fault tetrahedra have formed below the precipitate by a mechanism similar to that in figure 2(*a*) when dislocations intersected and

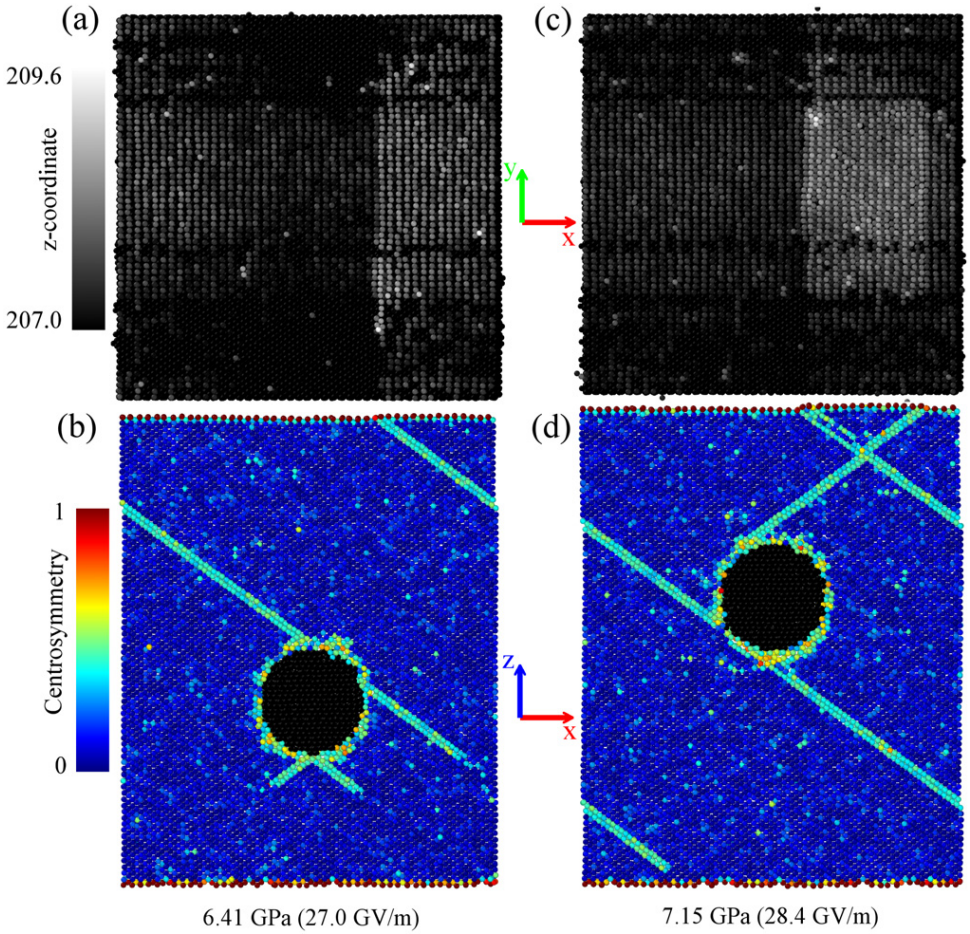

Figure 3. Formation of a step on the surface—(*a*) top view and (*b*) cross section of a deep precipitate; (*c*) top view and (*d*) cross section of a shallow precipitate. In (*a*) and (*c*), atoms are coloured according to their z coordinate while in (*b*) and (*d*) they are coloured by the centrosymmetry parameter. Fe atoms are coloured black in (*b*) and (*d*). Steps form on the surface where the stacking faults intersect it.

became locked. Above the precipitate, a dislocation nucleates in the region of high stress, depicted in figure 2(*d*). The expansion of the dislocation proceeds similarly to the ones described earlier. Eventually the dislocations become pinned at the bottom of the box, as the atoms are fixed in place due to the boundary conditions.

As can be seen in figures 2(*b*) and (*d*), the precipitate concentrates stress around it. The stress in figure 2(*b*) is calculated before either of the stacking faults in figure 2(*a*) appears in the simulation. In figure 2(*d*), the two stacking fault tetrahedra seen in figure 2(*c*) have already formed, but the stacking fault above the precipitate is still missing. The resolved shear stress shown in figures 2(*b*) and (*d*) acts on one of the slip planes of Cu, causing the motion of dislocations. The stacking fault below the precipitate in figure 2(*a*) and that above the precipitate in figure 2(*c*) move on this slip plane. The stress distribution is noisy at the precipitate perimeter, but extended regions of higher stress can clearly be seen in both figures where the corresponding stacking faults eventually form.

When the dislocation reaches the material surface, a partial step is created, as seen in figure 3. Figures 3(*a*) and (*b*) show the top view and the middle cross section, respectively, of a simulation cell with the deep precipitate under the tensile stress 6.41 GPa. Figures 3(*c*) and (*d*) are corresponding views of a simulation cell with the shallow precipitate under the tensile stress 7.15 GPa. The top views (figures 3(*a*) and (*c*)) map the *z* coordinate of the atoms to grayscale values. The Cu atoms in the cross-sections (figures 3(*b*) and (*d*)) are coloured according to the centrosymmetry parameter, while the Fe atoms are left black. As can be seen in figures 3(*a*) and (*b*), there is a visible step on the surface where the surface intersects with the stacking fault.

Figures 3(*c*) and (*d*) show a case where two dislocations have formed on different slip planes. In figure 3(*d*), the dislocation, which formed above the precipitate, has propagated to the surface, and created a step. Another dislocation formed below the precipitate on a different slip plane, and also propagated toward the surface. Due to the periodic boundary conditions in the lateral directions the dislocation wraps around the simulation box and intersects with the stacking fault formed by the first dislocation. A shift in the stacking fault can be seen where the dislocation has passed through it. As the second dislocation reaches the surface, it also forms a step, which in combination with the first step results in a plateau of atoms positioned higher than the original surface level. We observed the described intersection of dislocations because of the use of periodic boundaries. However, it can be interpreted in terms of two close precipitates (the one in the simulation cell and the image precipitate due to the periodic boundaries) and in reality, a similar situation can be realized when there are several precipitates or other imperfections in close proximity, providing sites for dislocation nucleation. Dislocations originating from two close precipitates in different slip planes could form a plateau similarly to the one we observed in our simulations.

The plateau represents a modification of surface geometry, which leads to enhancement of the electric field. Due to the low aspect ratio of the plateau, this enhancement is not significant in the context of our simulations. The further growth of this nucleus can be followed by using, for example, the technique suggested in [9], which has been successfully applied for the case of a near-surface void [45]. It can be seen that arrays of precipitates close to the material surface can facilitate protrusion formation similarly to the case of voids, as in [27]. Field enhancement due to the surface morphology changes has been shown to provide a positive feedback on the growth of surface protrusions [19]. An enhanced electric field results in the increase of the force experienced by surface atoms, leading to more dislocations being nucleated and a greater curvature of surface features. The greater curvature in turn increases the local field enhancement.

3.2. Stacking fault–surface interaction

When a leading partial dislocation reaches the surface, we observe the splitting of the stacking fault, as illustrated in figure 4. Here, common neighbour analysis helps to distinguish the atoms by colouring them according to their local lattice type. The fcc and hcp lattices differ by the positions of the atoms in adjacent layers, leading to different stacking sequences: ... ABCABC ... for fcc and ... ABABAB ... for hcp (equivalent to ... BCBCBC ... or ... ACACAC ...) [33]. Thus, the atoms for which the adjacent layers have different atom positions are marked as fcc, and ones where the adjacent layers have the same atom positions are marked as hcp. In figure 4, the A, B and C layers are shown for all cases (layers are labelled according to the positions that the atoms in those layers occupy). Figure 4(*a*) shows the initial configuration with the layers arranged in the fcc stacking sequence. In figure 4(*b*), the leading partial dislocation passes, displacing the atoms originally located in the A layer into the B layer

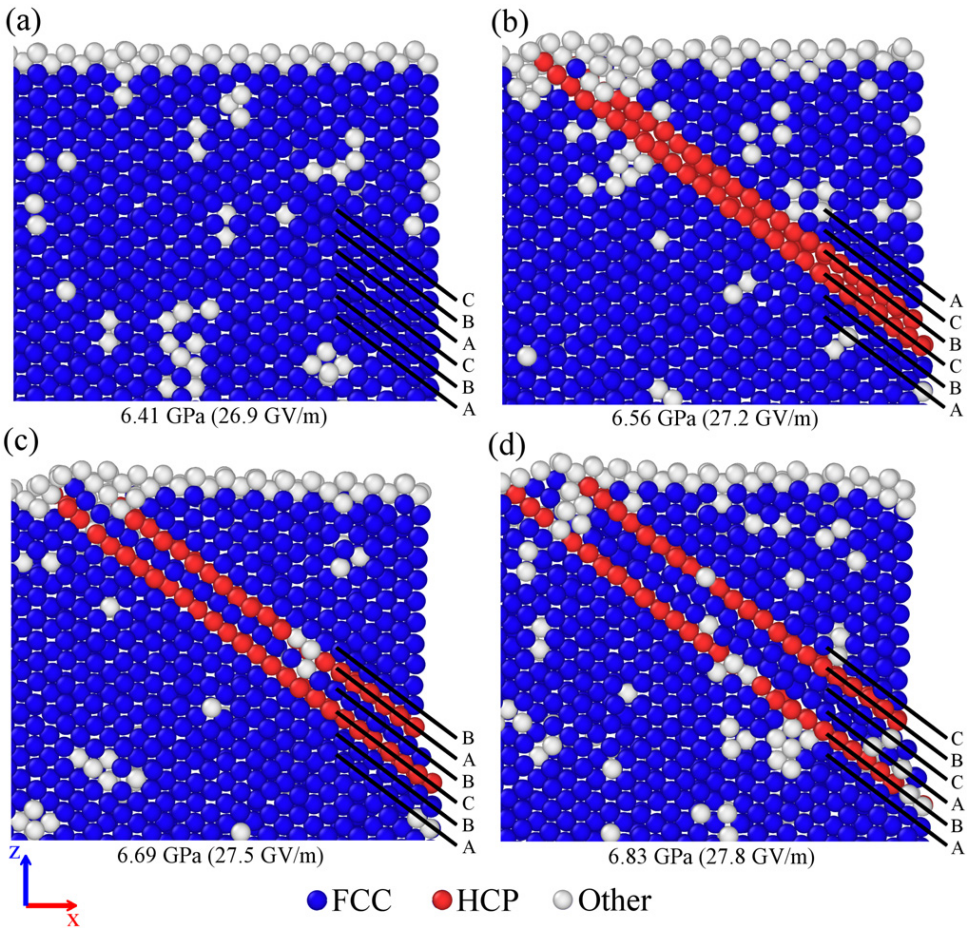

Figure 4. Splitting of a stacking fault at the surface. Atoms are coloured according to their local lattice type. Atom layers are marked with letters denoting the positions of their atoms. (*a*) Initial configuration; (*b*) slip has occurred resulting in a stacking fault; (*c*) the atoms in the layer immediately above the stacking fault have slipped once more; (*d*) as the whole system slips on the layer below the original stacking fault, the final pattern is created.

positions, creating a local stacking sequence of ABCBCA. The central layers CB constitute the stacking fault in the surrounding fcc lattice. Their local lattice type is hcp because for both the central C and central B layer the adjacent layers are of the same type. When the stacking fault has reached the surface, a new partial dislocation is generated in the layer immediately adjacent to one of the stacking fault layers. The new dislocation has the same Burger's vector as the original, but of the opposite line sense. Figure 4(*c*) shows the following step: as the new dislocation expands away from the surface, due to the resolved shear stress acting on it, the next layer of atoms slips, creating the local stacking sequence ABCBAB. In figure 4(*d*) the same process happens in the layer below the original stacking fault as all the layers above it slip further. All atoms starting from those in the bottom layer of the original stacking fault change their positions, with the final sequence of layers ABACBC.

From the original stacking sequence ABCABC, the central C layer undergoes a $\frac{1}{6}[1\,1\,\bar{2}]$ transition to become an A layer in the final configuration. The original central layer A has transitioned A $\rightarrow$ B $\rightarrow$ C by the vector $\frac{2}{6}[1\,1\,\bar{2}]$. The transitions for the final two layers BC are identical. In the case of C, it is C $\rightarrow$ A $\rightarrow$ B $\rightarrow$ C. In terms of Burger's vectors this can be written as $\frac{3}{6}[1\,1\,\bar{2}]$, which is equivalent to $\frac{1}{2}[0\,1\,\bar{1}] + \frac{1}{2}[1\,0\,\bar{1}]$. The latter expression represents two perfect dislocations, which leave behind a plastically deformed perfect crystal. The two layers of hcp atoms, which are separated by several layers of fcc atoms can be viewed as twinning faults, where the crystal orientation changes and the layer sequence is mirrored [33]. The material above the twinning faults experiences slip equivalent to the passage of two perfect dislocations. The stacking fault which has split into the two twinning faults represents the transition between the slipped and unslipped regions, with a twinned region in-between. The amount of slip in the twinned region varies linearly from 0 at the lower twinning fault to that equivalent to the passage of three partial dislocations at the upper twinning fault. Each layer in the twinned region is formed as a result of one partial dislocation. More dislocations can be nucleated in layers adjacent to the twin boundaries, leading to further slip of the upper part of material and the widening of the twinned region between the twinning faults.

A single dislocation originating from the precipitate can nucleate additional dislocations upon reaching the surface. These new dislocations also generate steps on the surface, as seen in figures 4(*b*) and (*c*). Through this process one surface step becomes a series of steps, increasing the change in local surface geometry. When combined with the action of several sub-surface precipitates and the formation of a plateau, the stacking fault splitting could lead to an increase in the protrusion height. This will tend to sharpen the protrusion, which will result in further enhancement of the electric field.

3.3. Void formation

Figure 5 shows the formation of voids as the stress on the system due to the electric field is increased. The plot in the figure is an example of a simulation where a void formation event was observed. The volume of voids is plotted against the stress applied to the system. The x-axis can also be taken to represent the progression of the simulation in time, as the stress is increased linearly with the time step. Void volume is calculated with the Voronoi cell method described above. At the external stresses shown in the figure, the stacking faults and the associated surface steps have already formed. Those processes are described in the previous section and shown in figures 2 and 3.

The void formation happens at stresses much larger than those required for dislocation nucleation. The voids start to form when the applied stress reaches 7.10 GPa ($E = 28.3\,\mathrm{GV\,m^{-1}}$), as seen in the graph in figure 5. Void formation begins at the interface region between Cu and Fe. The bond strength between two different types of atoms is weaker than the mono-elemental bond, either Fe–Fe or Cu–Cu, resulting in the separation of Cu atoms from the precipitate. As the stress increases, the void grows in volume. The formation of the void tends to reduce the local stress in the region. The stacking fault under the precipitate, which is only visible in the snapshot in figure 5(*a*), disappears in subsequent snapshots as a trailing partial dislocation completes the slip. The void formation is unaffected by the resulting plastic deformation because the regions are far apart. A similar plastic deformation happens in the upper left corner while moving from the image in figure 5(*b*) to the image in figure 5(*c*). In figure 5(*d*), a new leading partial dislocation is nucleated on the vertical slip plane, due to the presence of the void. The new leading partial dislocation expands towards the surface and creates a step. The leading partial is soon followed by a trailing partial, eliminating the stacking fault and completing the plastic deformation above the void. The volume of

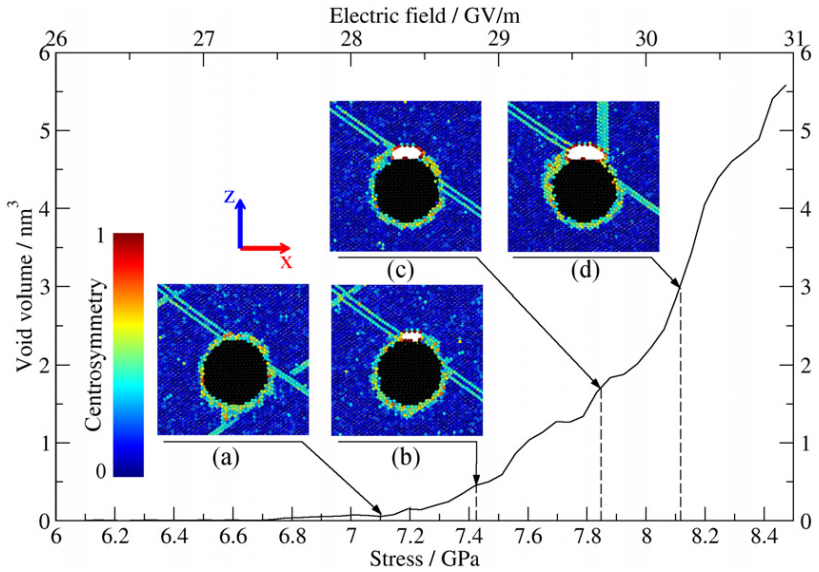

Figure 5. Example of the evolution of voids over time for a shallow precipitate. The snapshots show a cross section of the system as the electric field increases and the void forms. Fe atoms are black and Cu atoms are coloured according to centrosymmetry. The beginning of the simulation before the stress reaches 6 GPa is not shown.

the void gradually increased until the simulation was stopped when surface atoms started evaporating.

Figure 6 shows that voids can form both above and below the precipitate. The images given in figure 6 correspond to two different simulations of the shallow precipitates ($h/r = 2.5$). Figure 6(a) shows a void developing above the precipitate where a stacking fault interacts with it. Figure 6(c) shows a different simulation displaying void formation below the precipitate with the same geometry. The snapshots in figures 6(a) and (c) represent the final frames of the simulations, as extensive surface atom evaporation begins after this point and the approximation of constant force across the surface no longer applies. Random variations due to different initial random seeds result in a different configuration of stacking faults and a different stress distribution around the precipitate at the moment of void formation. The snapshots in figures 6(b) and (d) show the stress distribution in the system before the formation of voids in figures 6(a) and (c), respectively. The σ_{zz} component of the untransformed stress tensor is plotted in these figures. This component is concentrated in the regions where stacking faults intersect with the precipitate, and also above and below the precipitate. These regions exhibit void formation. The distributions of other components of the stress tensor (not pictured) do not correlate with the location of voids.

Eighty simulations with a shallow precipitate were performed. Eleven of them exhibited void formation before material failure, with behaviour similar to what can be seen in figure 5. Eight out of 80 simulations formed voids in case of the deep precipitate. As voids have been shown to cause protrusions on the surface of the material [28], the presence of precipitates can be an indirect cause of surface geometry change. Under high external stresses, mechanically strong precipitates enable the formation of voids around them which can in turn lead to a protrusion being generated. The voids also provide additional sites where dislocations can be nucleated. These dislocations expand towards the surface and create steps.

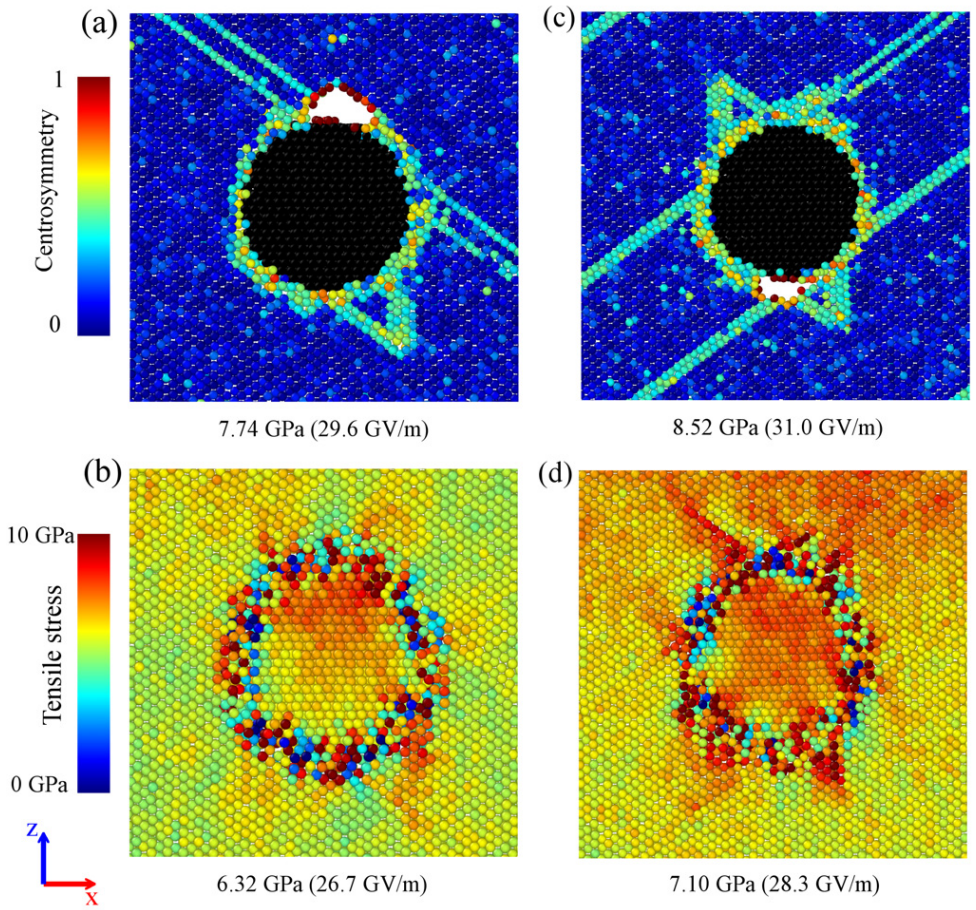

Figure 6. Voids forming around a shallow precipitate under tensile stress exerted by an external electric field in two simulations (*a*), (*b*) and (*c*), (*d*). The centrosymmetry parameter for Cu atoms is represented in (*a*) and (*c*), while Fe is black. Corresponding σ_{zz} before void formation is presented in (*b*) and (*d*).

This effect of voids is independent of the void location and can work also for voids below the precipitate.

4. Conclusions

In this work we performed MD simulations of single crystal Cu which contained a Fe precipitate under high external tensile stresses caused by an electric field. The simulations show that precipitates, which are stronger than Cu, could provide an indirect mechanism for surface geometry change and electric field enhancement. Under external stress caused by the electric field, dislocations nucleate at the Cu–Fe interface. When the dislocations reach the material surface, they create steps increasing the surface curvature and hence enhance locally the electric field. With multiple precipitates in close proximity, dislocations nucleated on different slip planes can reach the surface near each other. The resulting configuration of steps creates a plateau on the surface.

The region around the surface step provides an additional site for dislocation nucleation. Further slip can occur in the adjacent layers and create a series of steps. This mechanism increases the extent of surface geometry change. When combined with the formation of a plateau it could lead to the creation of a protrusion.

When the stress is increased, voids can form in the regions of high stress immediately above or below the precipitate as Cu separates from the stronger precipitate. Void formation is a random but not uncommon event. The voids offer additional sites for dislocation nucleation. Voids have also been previously shown to lead to a catastrophic protrusion growth on the surface [28]. They can appear in a material containing precipitates as a result of the application of a strong external electric field and introduce their own mechanism of surface protrusion formation.

Acknowledgments

This work was supported by Estonian Research Council Personal Research Grant #57 and the 'Research internationalisation' programme of the European Regional Development Fund. The authors thank CSC, the IT Center for Science Ltd (Finland) and the Finnish Grid and Cloud Infrastructure for grants of computation time. FD acknowledges gratefully the financial support from the Academy of Finland AMELIS project.

References

[1] Calatroni S, Descoeudres A, Kovermann J W, Taborelli M, Timko H, Wuensch W, Djurabekova F, Nordlund K, Pohjonen A and Kuronen A 2010 Breakdown studies for the CLIC accelerating structures *Proc. LINAC2010 (Tsukuba, Japan)* pp 217–9

[2] Wang J W and Loew G A 1997 Field emission and rf breakdown in high-gradient room-temperature linac structures *Proc. Joint School RF Engineering for Accelerators (Stanford, CA)*

[3] Descoeudres A, Ramsvik T, Calatroni S, Taborelli M and Wuensch W 2009 Dc breakdown conditioning and breakdown rate of metals and metallic alloys under ultrahigh vacuum *Phys. Rev. ST Accel. Beams* **12** 032001

[4] Holtkamp N 2009 The status of the ITER design *Fusion Eng. Des.* **84** 98–105

[5] Assmann R W *et al* 2000 *A 3 TeV e^+e^- Linear Collider Based on CLIC Technology* ed G Guignard (Geneva: CERN)

[6] Braun H *et al* 2008 *CLIC 2008 Parameters*, *CLIC-Note-764* ed F Tecker (Geneva: CERN)

[7] Braun H H, Döbert S, Wilson I and Wuensch W 2003 Frequency and temperature dependence of electrical breakdown at 21, 30, and 39 GHz *Phys. Rev. Lett.* **90** 224801

[8] Wang J W, Lewandowski J R, Van Pelt J W, Yoneda C, Riddone G, Gudkov D, Higo T and Takatomi T 2010 Fabrication technologies of the high gradient accelerator structures at 100 MV/m range *Proc. IPAC'10 (Kyoto, Japan)* pp 3819–21

[9] Djurabekova F, Parviainen S, Pohjonen A and Nordlund K 2011 Atomistic modeling of metal surfaces under electric fields: direct coupling of electric fields to a molecular dynamics algorithm *Phys. Rev.* E **83** 026704

[10] Descoeudres A, Levinsen Y, Calatroni S, Taborelli M and Wuensch W 2009 Investigation of the dc vacuum breakdown mechanism *Phys. Rev. ST Accel. Beams* **12** 092001

[11] Tsong T T 1991 Effects of an electric field in atomic manipulations *Phys. Rev.* B **44** 13703–10

[12] Fowler R H and Nordheim L 1928 Electron emission in intense electric fields *Proc. R. Soc. Lond.* A **119** 173–81

[13] Murphy E L and Good R H 1956 Thermionic emission, field emission, and the transition region *Phys. Rev.* **102** 1464–73

[14] Forbes R G 1999 Refining the application of Fowler–Nordheim theory *Ultramicroscopy* **79** 11–23

[15] Jensen K L, Lau Y Y, Feldman D W and O'Shea P G 2008 Electron emission contributions to dark current and its relation to microscopic field enhancement and heating in accelerator structures *Phys. Rev. ST Accel. Beams* **11** 081001
[16] Timko H 2011 *Modelling Vacuum Arcs: From Plasma Initiation to Surface Interactions* (Helsinki: University of Helsinki)
[17] Parviainen S, Djurabekova F, Timko H and Nordlund K 2011 Electronic processes in molecular dynamics simulations of nanoscale metal tips under electric fields *Comput. Mater. Sci.* **50** 2075–9
[18] Frantz J, Rusanen M, Nordlund K and Koponen I T 2004 Evolution of Cu nanoclusters on Cu(1 0 0) *J. Phys.: Condens. Matter* **16** 2995
[19] Chatterton P A 1966 A theoretical study of field emission initiated vacuum breakdown *Proc. Phys. Soc.* **88** 231
[20] Insepov Z, Norem J H and Hassanein A 2004 New mechanism of cluster field evaporation in rf breakdown *Phys. Rev. ST Accel. Beams* **7** 122001
[21] Insepov Z, Norem J and Veitzer S 2010 Atomistic self-sputtering mechanisms of rf breakdown in high-gradient linacs *Nucl. Instrum. Methods Phys. Res.* B **268** 642–50
[22] Keser A C, Antonsen T M, Nusinovich G S, Kashyn D G and Jensen K L 2013 Heating of microprotrusions in accelerating structures *Phys. Rev. ST Accel. Beams* **16** 092001
[23] Nusinovich G S, Kashyn D and Antonsen T M 2009 Possible role of rf melted microparticles on the operation of high-gradient accelerating structures *Phys. Rev. ST Accel. Beams* **12** 101001
[24] Insepov Z, Norem J, Proslier T, Huang D, Mahalingam S and Veitzer S 2010 Modeling rf breakdown arcs, arXiv:1003.1736
[25] Norem J and Insepov Z 2012 Can surface cracks and unipolar arcs explain breakdown and gradient limits? arXiv:1208.0847
[26] Nordlund K and Djurabekova F 2012 Defect model for the dependence of breakdown rate on external electric fields *Phys. Rev. ST Accel. Beams* **15** 071002
[27] Pohjonen A S, Djurabekova F, Nordlund K, Kuronen A and Fitzgerald S P 2011 Dislocation nucleation from near surface void under static tensile stress in Cu *J. Appl. Phys.* **110** 023509
[28] Pohjonen A S, Parviainen S, Muranaka T and Djurabekova F 2013 Dislocation nucleation on a near surface void leading to surface protrusion growth under an external electric field *J. Appl. Phys.* **114** 033519
[29] Gilman J J 1959 Dislocation sources in crystals *J. Appl. Phys.* **30** 1584–94
[30] Plimpton S 1995 Fast parallel algorithms for short-range molecular dynamics *J. Comput. Phys.* **117** 1–19
[31] Bonny G, Pasianot R C, Castin N and Malerba L 2009 Ternary Fe–Cu–Ni many-body potential to model reactor pressure vessel steels: first validation by simulated thermal annealing *Phil. Mag.* **89** 3531–46
[32] Stukowski A 2010 Visualization and analysis of atomistic simulation data with OVITO—the open visualization tool *Modelling Simul. Mater. Sci. Eng.* **18** 015012
[33] Hull D and Bacon D J 2011 *Introduction to Dislocations* (Oxford: Butterworth-Heinemann)
[34] Lide D R 2005 *CRC Handbook of Chemistry and Physics* Internet Version 2005 (Boca Raton, FL: CRC Press)
[35] Blackstock J J and Ackland G J 2001 Phase transitions of copper precipitates in Fe–Cu alloys *Phil. Mag.* A **81** 2127–48
[36] Tschopp M A, Spearot D E and McDowell D L 2007 Atomistic simulations of homogeneous dislocation nucleation in single crystal copper *Modelling Simul. Mater. Sci. Eng.* **15** 693
[37] Schuh C A, Mason J K and Lund A C 2005 Quantitative insight into dislocation nucleation from high-temperature nanoindentation experiments *Nature Mater.* **4** 617–21
[38] Ryu S, Kang K and Cai W 2011 Predicting the dislocation nucleation rate as a function of temperature and stress *J. Mater. Res.* **26** 2335–54
[39] Zhu T, Li J, Samanta A, Leach A and Gall K 2008 Temperature and strain-rate dependence of surface dislocation nucleation *Phys. Rev. Lett.* **100** 025502
[40] Dupuy L M and Rudd R E 2006 Surface identification, meshing and analysis during large molecular dynamics simulations *Modelling Simul. Mater. Sci. Eng.* **14** 229

[41] Rycroft C 2009 *Voro++: A Three-Dimensional Voronoi Cell Library in C++* Lawrence Berkeley National Laboratory
[42] Sun Z H, Wang X X, Soh A K and Wu H A 2006 On stress calculations in atomistic simulations *Modelling Simul. Mater. Sci. Eng.* **14** 423
[43] Kelchner C L, Plimpton S J and Hamilton J C 1998 Dislocation nucleation and defect structure during surface indentation *Phys. Rev.* B **58** 11085–8
[44] Stukowski A 2012 Structure identification methods for atomistic simulations of crystalline materials *Modelling Simul. Mater. Sci. Eng.* **20** 045021
[45] Parviainen S, Djurabekova F, Pohjonen A and Nordlund K 2011 Molecular dynamics simulations of nanoscale metal tips under electric fields *Nucl. Instrum. Methods Phys. Res.* B **269** 1748–51

II

IOP Publishing Modelling and Simulation in Materials Science and Engineering

Modelling Simul. Mater. Sci. Eng. **26** (2018) 035006 (18pp) https://doi.org/10.1088/1361-651X/aaa928

Simulations of surface stress effects in nanoscale single crystals

V Zadin[1,2], M Veske[1,2], S Vigonski[1,2], V Jansson[2], J Muszinsky[2], S Parviainen[3], A Aabloo[1] and F Djurabekova[2]

[1] Intelligent Materials and Systems Lab, Institute of Technology, University of Tartu, Nooruse 1, 50411 Tartu, Estonia
[2] Helsinki Institute of Physics and Department of Physics, PO Box 43 (Pietari Kalmin katu 2), FI-00014 University of Helsinki, Finland
[3] GPM UMR 6634 CNRS, Normandie University, F-76800 St. Etienne du Rouvray, France

E-mail: vahur.zadin@ut.ee

Received 28 August 2017, revised 10 January 2018
Accepted for publication 19 January 2018
Published 15 February 2018

Abstract

Onset of vacuum arcing near a metal surface is often associated with nanoscale asperities, which may dynamically appear due to different processes ongoing in the surface and subsurface layers in the presence of high electric fields. Thermally activated processes, as well as plastic deformation caused by tensile stress due to an applied electric field, are usually not accessible by atomistic simulations because of the long time needed for these processes to occur. On the other hand, finite element methods, able to describe the process of plastic deformations in materials at realistic stresses, do not include surface properties. The latter are particularly important for the problems where the surface plays crucial role in the studied process, as for instance, in the case of plastic deformations at a nanovoid. In the current study by means of molecular dynamics (MD) and finite element simulations we analyse the stress distribution in single crystal copper containing a nanovoid buried deep under the surface. We have developed a methodology to incorporate the surface effects into the solid mechanics framework by utilizing elastic properties of crystals, pre-calculated using MD simulations. The method leads to computationally efficient stress calculations and can be easily implemented in commercially available finite element software, making it an attractive analysis tool.

Keywords: molecular dynamics, finite element analysis, multiscale simulations, high electric fields, surface stress

(Some figures may appear in colour only in the online journal)

1. Introduction

Interaction of an electric field with materials becomes increasingly important in a number of modern technologies under development. Some examples are the Compact Linear Collider [1, 2], free electron lasers [3], fusion reactors [4, 5] and atom probe tomography [6]. One frequently observed problem in these high electric field systems are vacuum arcs—the electric discharges in vacuum between two electrodes. These are also known as electrical breakdowns since they are commonly detected as a sudden voltage drop and a high electron current accompanied by significant power consumption. The electrical breakdowns lead to significant surface damage in high electric field devices and pose major limitations for the strength of the fields [7, 8]. Measurements of electron field emission currents from macroscopically flat surfaces suggest that some surface irregularities with diameters in the range of 17–25 nm [9] and heights up to 100 nm [10, 11] must be present to serve as field emitting tips. While such nanoscale emitters have never been observed experimentally [10], they are typically assumed to be possible sources of strong field emitting currents, precursors to a breakdown event. For example, Norem *et al* used molecular dynamics (MD) to simulate possible breakdown mechanisms [12, 13] and demonstrated in [12] evaporation of large clusters of atoms under high electric field while the finite element method (FEM) was utilized in [14, 15] to investigate field enhancement effects due to micro cracks caused by fatigue in the material surface. These works provide important insight in possible breakdown initiation mechanisms but do not explain what triggers initial surface roughening. Several experimental and theoretical works link material structure and properties to the breakdown initiation mechanism. Descoeudres *et al* [8] showed a correlation between the lattice type and its tolerance to the breakdowns; Nordlund and Djurabekova [16] linked breakdown probability to the dislocation motion in the material. Further MD studies by Pohjonen *et al* demonstrated surface modification of Cu containing a subsurface nanovoid due to the effect of an electric field [17, 18]. The short simulation times in MD simulations required exaggeration of applied electric fields in order to observe any dislocation activity [17, 18]. It was possible to decrease these fields considerably [19] by using FEM to simulate dynamic plastic deformations of a Cu surface with an applied external electric field.

To overcome the vast differences in time and length scales between experiments and simulations, a multi-scale approach is needed. While experimental time expands to seconds or even minutes [10], the breakdown process itself is relatively fast: when initiated, the process culminates in a sub-microsecond time interval [20, 21]. Methods with sufficient spatial resolution alone, such as MD, are still not sufficient to study the process due to the limitation of very short timescales—from pico- to nanoseconds. The time limitation can be overcome by using continuum methods, tailored to include nanoscale phenomena. For instance, it was shown [22] that these methods can be used for nanostructures of the size 2–10 nm, if the effects of surface stress are resolved [18, 22–24]. Nanoscale size effects have already been taken into account previously in different studies, in [25], the surface model was implemented using interatomic potential. In [23], an extended finite element method-based approach was used to simulate nanoscale size effects. In [26], an embedded atom hyper-elastic constitutive model was developed by He and Li. A different approach was used in [27] where the elastic properties of surfaces were calculated by MD methods. The onset of vacuum breakdown is however a complex phenomenon, which involves multiphysics processes, such as emission currents, Joule heating of material, and interaction of material surface with applied electric

Table 1. The details of the MD simulations.

Box size	$34.7 \times 34.7 \times 32.7\,\text{nm}^3$	$47 \times 47 \times 47\,\text{nm}$
Number of atoms	3.3 million atoms	8.8 million atoms
Void radius	$r_{\text{void}} = 5\,\text{nm}$	$r_{\text{void}} = 5\,\text{nm}$
Boundary conditions	Periodic boundaries in x and y directions. Fixed bottom, free/applied force in z direction	All boundaries are periodic
Temperature	293.15 K	293.15 K

fields [28, 29]. Bearing in mind the complexity of the problem, the existing approaches, although accurate and reliable, make the simulations computationally heavy.

While in [30] we implemented the surface stress model similarly to [31, 32] and analysed the sensitivity of different voids with uniform crystal faces, we will in this work propose an enhanced FEM bulk material model with an incorporated model of the surface stress in a fully coupled manner for the modelling of the mechanical behaviour of nanoscale FCC crystals. The model is capable of automatically approximating any crystal surface present in this model, as well as taking into account the size effects arising from nanoscale defects. As a suitable compromise we rely on MD simulations in order to obtain the elastic parameters for the surface region. This approach allows for simple implementations and low computational costs while still providing detailed information of the influence of the surface stress. We use a deep subsurface spherical void as a test stress concentrator and we compare the FEM model with MD simulations to analyse the stress distributions in nanoscale Cu.

2. Materials and methods

2.1. MD simulations

To study the material behaviour and possible protrusion formation mechanisms in a single Cu crystal, MD simulations were performed using the LAMMPS [33, 34] classical MD code. The atomic interactions were modelled using the embedded atom method potential by Sabochick *et al* [35]. Simulation results were visualized with the open-source OVITO software [36].

We conducted MD simulations to investigate the effect of surface stress on the inner surface of a spherical void buried deep under the surface. The void was considered to be buried under the surface, if no interactions of the strain fields between the surfaces of the material and the void were observed. The crystallographic orientation of the Cu cell was chosen so that one of the {111} slip planes along the {110} direction would intersect the surface perpendicularly. The MD simulations were performed by using two simulation cells of dimensions $34.7 \times 34.7 \times 32.7\,\text{nm}^3$ (3.3 million atoms) and $47 \times 47 \times 47\,\text{nm}^3$ (8.8 million atoms) to investigate possible adverse effects arising from the use of periodic boundaries. For the smaller cell the periodic boundaries were used only in lateral directions, while the bottom of the cell was fixed and the top was treated as open surface, where the force imitating the Lorenz force of the applied electric field (see below) was exerted. For the bigger cell, periodic boundary was applied in all directions while the simulations were conducted without any additional external loading. A 5 nm void was placed in the middle of each cell. The conducted MD simulations and their respective box sizes, void radii and boundary conditions are summarized in table 1. The geometry of the simulation setup is presented in figure 1.

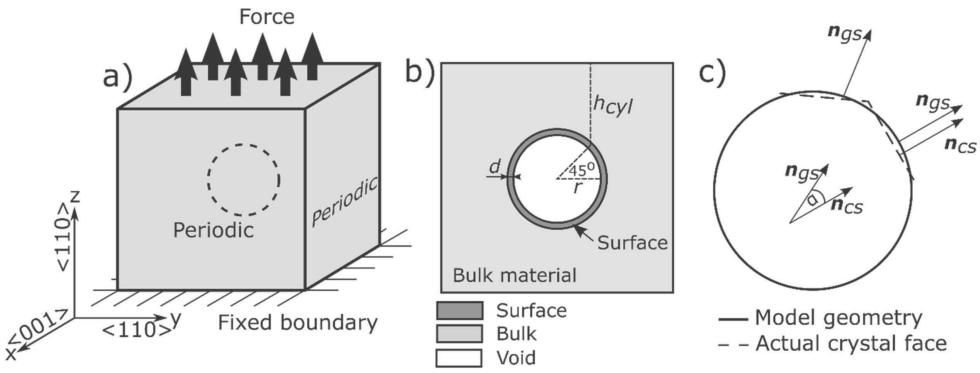

Figure 1. The simulation box setup in MD and FEM simulations (a), (b) and a schematic representation of the crystal face detection algorithm (c). The simulation cell is composed of a FCC Cu single crystal. External tensile stress is applied to the top two layers of atoms, the three bottom layers of atoms are fixed. The simulation cell is periodic in x and y directions.

The electric field and the electrons of the surface atoms interact due to the Lorentz force. The interaction strength is characterized by the Maxwell stress tensor, which, in case of DC electric fields, leads to the following expression for the force acting on the surface of the material [17, 37]

$$\mathbf{F} = \frac{1}{2}\varepsilon_0 |\mathbf{E_0}|^2 A\mathbf{n}, \tag{1}$$

where ε_0 is the vacuum permittivity, $\mathbf{E_0}$ is the electric field, A surface area and $\mathbf{n}$ the surface normal vector.

The simulations were conducted using 2 fs time step. In all cases the systems were equilibrated during 20 ps while the temperature was controlled by the Berendsen thermostat with a damping parameter of 0.1 ps. External stress was ramped during the 150 ps period by a gradual increase of the force acting on surface atoms until the final stress reached the value of 1.35 GPa. After that, the simulations were continued at the constant force for another 300 ps in order to obtain sufficient amount of data for the stress time average. Since the stress distribution was of particular interest, a lower temperature (293 K) and an external force was used to hinder the nucleation of dislocations that could cause the distortion of stress distribution.

2.2. Stress calculations in MD simulations

Different approaches to calculate the stress in the atomistic simulations exist. One of the most known methods is the virial theorem, reaching back to the work of Clausius and Maxwell, or more modern approaches, such as the ones developed by Hardy, Lutsko or Tsai [38–40]. While the latter ones can be considered more advanced and accurate than the virial theorem, excellent agreement between Hardy and virial stress approaches has been demonstrated if sufficient spatial or temporal averaging is applied [41, 42]. Thus, in the current work we rely on the virial stress, due to the readily available implementations in many MD codes. More specifically, in MD calculations conducted using LAMMPS, the basic form for the symmetric six-component virial for an atom is given by the following equation [43, 44]:

$$S_{ij} = -\left(mv_i v_j + \frac{1}{2}\sum_{n=1}^{N_p} {}^{n}r_i F_j \right), \tag{2}$$

where the first term represents the kinetic energy contribution and the second term the pairwise interaction contribution. m is the atom's mass, v_i the velocity components. The summation is over the atom's neighbours within the cutoff distance, where F_i are the force components of the pairwise interaction and ${}^{n}r_i$ are the components of the displacement of the neighbour n relative to the current atom. The details of the specific implementation are given in [43].

The estimate for continuum mechanical (Cauchy) stress was calculated from the virials for each atom, obtained from the MD simulations and correspondingly normalized with homogenization volume, that in this study is considered to be equal to the average atomic volume [41, 42]. The atomic volumes were obtained by finding non-overlapping Voronoi cells of atoms using the open-source Voro++ software [45]. The time averaging was conducted over 12 000 and 15 000 sequential time steps or 60 ps and 75 ps, respectively.

In addition to stress calculations, strain estimations are conducted according to [46, 47] using OVITO software.

2.3. Stress calculations using FEM

2.3.1. Bulk stress calculations. Successful simulation of surface stress requires combination of material bulk and surface models. In current approach, we assume a finite strain elasticity and consider the bulk and surface models to be separate but coupled by boundary conditions. In bulk models, large deformations are assumed. The material deformation is represented by the deformation gradient tensor (F_{ij}), connecting the deformed (x_i) and non-deformed configurations (X_i) [48, 49]

$$x_i = F_{ij} X_j. \tag{3}$$

The corresponding Green–Lagrange strain (ε) is calculated as

$$\varepsilon = \frac{1}{2}(F^T F - I). \tag{4}$$

Since large deformations are assumed, second Piola–Kirchoff stresses (S) are used [48, 49]

$$S = C : \varepsilon_{\mathrm{el}}. \tag{5}$$

The second Piola–Kirchoff stress, Cauchy stress (σ) and first Piola–Kirchoff stress (P) are related as $S = F^{-1}P$ and $\sigma = J^{-1}PF^T = J^{-1}FSF^T$, where $J = \det(F) = V/V_0$ is the ratio between the deformed and non-deformed volumes.

Since the simulated material is single crystal copper, we use anisotropic elasticity. The elastic parameters of material parameters are specified in table 2 [48].

2.3.2. Surface stress. In a simplified 1D example, the surface stress and the surface energy are related as [27, 50]

Table 2. The elastic properties of the bulk material [48] and the geometric parameters of the simulated surface layer in the calculations.

C_{11} (GPa)	C_{44} (GPa)	C_{12} (GPa)	$d\alpha$ (rad)	h (rad)	d_{ref} (Å)
168.4	75.4	121.4	0.24	0.3	3

$$\tau(e) = \gamma + \frac{\partial \gamma}{\partial e}, \tag{6}$$

where e is the elastic strain of the surface due to the surface tensile stress, γ the surface energy and τ the surface stress. To simulate the influence of the surface stress on the material behaviour, the bulk model must be extended to describe the surface properties as well. When FEM is considered, this can be done by geometrically resolving the surface layer and specifying explicitly the initial surface stress at zero strain, as well as the surface elastic properties. However, when the surface layer is modelled geometrically, a large number of elements are required to handle the mesh generation and stress calculation in this area. Another possible approach is to model the material surface mathematically using the thin layer approximation (the thickness of the layer is much smaller than the rest of the surface) with shell or membrane elements [51]. This approach unavoidably builds in additional mathematical complexity, which may even introduce some numerical errors in the bulk model, however, it significantly reduces the requirements for the mesh density.

In the current study, we handle the material surface by using mathematical modelling and the membrane elements. Thus, to simulate the surface layer behaviour, we add extra model available only at the geometrical surface of the material. The surface model setup is similar to the bulk model but has several important differences. Instead of simulating the area close to the surface in a full 3D approach, we use the thin film formulation where only the tangential components of the stress and strain over the surface will change [51]. This formulation is realized using 3D plane stress elements, able to deform both in-plane and out-plane direction while the bending stiffness is neglected. It can be ignored in the surface model, as the surface processes cannot be treated independently but are tightly coupled to the bulk material behaviour (discussed below) [27]. As a result, in the current model, the surface layer bending behaviour is controlled by the bulk material.

The surface layer thickness (d) in the normal direction is considered to be small, giving constant stress and strain distributions in that direction. As in the bulk case, if the surface undergoes deformation, the relation between deformed (x_i) and non-deformed (X_i) configurations can be expressed using the deformation gradient (F^s), so that $x_i = F^s_{ij} X_j$ and the corresponding Green–Lagrange strain tensor can be calculated as:

$$e = \frac{1}{2}(F^{s\,T} F^s - I). \tag{7}$$

Since the material surface undergoes deformation, the ratio of areas between deformed and non-deformed configurations is:

$$J = \sqrt{\det(F^{sT} F^s)} = \sqrt{\det(I + 2e)}. \tag{8}$$

Finally, the surface stress tensor is calculated as [27]

$$\tau_{ij} = \tau_{ij}^0 + S_{ijkl} e_{kl}, \tag{9}$$

where τ_{ij}^0 is the initial surface stress and S the fourth order surface elasticity tensor.

The incorporation of the finite size effects was later tested by comparing the simulation results with the analytical model, presented in [52]. The comparison was obtained by conducting series of simulations using different external stresses (3.05 and 4.58 GPa), while the depth of the void was increased (starting from the surface with 0.2 nm steps) and the radius of the void was scaled from 4 to 20 nm with 1 nm steps.

2.3.3. Coupling the surface and bulk stress models. To obtain the final stress–strain distribution in the nanoscale material due to the surface stress influence, both surface and bulk models must be coupled. The coupling is achieved by binding the two stress models using the boundary conditions and solving a nonlinear system of equations. As the deformation of the bulk material also causes the deformation of the surface, the bulk deformation is carried over to the surface model—every point in the surface model undergoes the deformation experienced by the boundary of the bulk model, leading to the predefined displacement in the surface stress model:

$$\mathbf{u}_{\text{surf}}(x, y, z) = \mathbf{u}_{\text{bulk}}(x, y, z). \tag{10}$$

The deformation of the surface leads to accumulation of the surface stress according to equation (9). The achieved surface stress is coupled to the bulk model by incorporating it into the pressure load boundary condition for the bulk material behaviour. The resulting distributed load at the surface elments of the bulk model is described as:

$$\mathbf{F} = p\mathbf{n}J, \tag{11}$$

where p is the pressure calculated in the surface stress model, $\mathbf{n}$ the unit normal vector in the deformed configuration and J defined in equation (8). The surface stress boundary condition is implemented as a follower load, meaning that the changes of the surface areas during the calculations are monitored and the loads are applied in the deformed frame (not in the initial, non-deformed one).

Finally, the stress distribution in the material is calculated using the principle of a virtual work—the work from all external loads is equal to the virtual work from internal strains:

$$\begin{aligned}\delta W = &\int_V (-\delta\varepsilon_{\text{el}}\colon \sigma + \delta\mathbf{u} \cdot \mathbf{F}_{\mathbf{v}})\mathrm{d}v \\ &+ \int_S (-\delta e\colon \tau + \delta\mathbf{u} \cdot \mathbf{F}_{\mathbf{s}})\mathrm{d}s + \int_{\mathrm{l}} (\delta\mathbf{u} \cdot \mathbf{F}_{\mathrm{l}})\mathrm{d}\mathrm{l},\end{aligned} \tag{12}$$

where $\delta\mathbf{u}$ represents the virtual displacements and $\mathbf{F}_i$ corresponds to the volumetric, surface or line forces. Since in our current work we use the thin film formulation for modelling the surface behaviour, we effectively use 3D plane stress elements, able to deform both in-plane and out-plane directions while neglecting bending stiffness (as discussed above). Intuitively, this leads to the analytical integration of the surface part in equation (12), resulting in the multiplication of the corresponding quantities with the thickness (d) of the modelled surface layer. An exhaustive mathematical description, however, remains out of the scope of the current paper and can be found in sufficient detail from several textbooks [48, 51].

The membrane thickness d is also used to introduce the size dependence, characteristic to the nanoscale systems, into the model (and avoid scale invariance during upscaling of the geometry). We consider $d = d_{\text{ref}} \cdot \frac{\kappa}{\kappa_{\text{ref}}}$, where κ is the curvature of the void and the subscript

Table 3. Elastic parameters of the crystal surfaces in the FEM simulations [27].

Crystal planes (k)	Nonzero components of initial surface stress tensor τ_{11}^0 (eV Å^{-2}), τ_{22}^0 (eV Å^{-2})	Bulk modulus S_{iijj} (eV Å^{-2})	Shear modulus S_{1212} (eV Å^{-2})
{001}	0.0649, 0.0649	0.017	−0.063
{111}	0.0343, 0.0343	−0.527	0.009
{110}	0.0621, 0.0373	−2.428	−0.352
Rest of the surface {112}	0.0474, 0.0382	−1.641	−0.252

ref characterizes the reference configuration—a void with 5 nm radius. The interface thickness d was initially obtained through the comparison with MD simulations.

2.3.4. Crystal face detection. Important part of the model implementation is the identification of crystal faces constituting the surface, since both the initial surface stress and the elastic properties of the surface are crystal orientation dependent. Two possible strategies can be used for that. The first one relies on the geometry setup—the initial geometry is well defined, where all the boundaries correspond directly to the crystal faces. In this case, all the surface properties are predefined by the user. The shortcoming of this method is the need to manually specify the crystal faces by constructing sufficiently accurate geometry.

In the second case, the geometry does not have boundaries corresponding directly to the crystal faces, but the boundaries follow the actual crystal faces only approximately. For example, if a perfectly spherical void is considered in the finite element model, this is an approximation of the actual material defect. In an actual crystal structure, a perfectly spherical hole cannot exist due to the atomistic nature of the matter. Instead, the surface of the defect (void) consists of patches of differently oriented crystal faces. In this case, a special algorithm must be used first to determine the crystal faces constituting the surface and secondly translate this information to construct the surface model which includes the corresponding effective surface elastic properties.

In current work we use the second approach—we reconstruct the crystal surface approximately using the identification algorithm presented below. By choosing this approach, we gain computational robustness and flexibility on expense of some accuracy.

The crystal face identification algorithm utilizes the Miller indices, characterizing every crystal plane. The indices provide the normal vectors to the crystal planes on surface of the studied void. In a FCC single crystal, we identify the crystal planes shown in table 3, which are presently included in the proposed algorithm.

In the following, we refer to the *geometrical surface* as the surface modelled by using conventional modelling tools available in the used FEM software. The *crystal surface,* however, is the surface which is constructed according to the proposed algorithm with the surface properties simulated by MD in the presence of a volumetric defect. In case of the geometrical surface, we do not model the crystal faces directly, while in case of the crystal surface, the faces appear naturally. This is illustrated in figure 1(c), where solid line represents the geometry surface and dashed line the actual crystal surface.

To identify approximately the crystal faces on the geometrical surface, we consider the surface normal vectors of the geometrical model $\mathbf{n}_{\mathrm{gs}}$ and the normal vector $\mathbf{n}_{\mathrm{cs}}^{k}$ of the crystal plane k; the latter arising from the orientation of material. In the case of parallel normal

vectors, the geometrical model represents the crystal surface accurately; otherwise approximately. To reconstruct a valid model of the crystal surface and identify the actual crystal faces k on the geometrical surface, we first find the angles between $\mathbf{n}_{\mathrm{gs}}$ and $\mathbf{n}_{\mathrm{cs}}^{k}$ (see figure 1(b))

$$\alpha^{k} = \cos^{-1}\left(\frac{\langle \mathbf{n}_{\mathrm{cs}}^{k}, \mathbf{n}_{\mathrm{gs}}\rangle}{|\mathbf{n}_{\mathrm{cs}}^{k}| \cdot |\mathbf{n}_{\mathrm{gs}}|}\right). \tag{13}$$

Both $\mathbf{n}_{\mathrm{gs}}$ and $\mathbf{n}_{\mathrm{cs}}^{k}$ must be specified in the material coordinate system (laboratory coordinate system), so that they follow the correct crystal orientation in the geometry. Finally we limit the maximum angle between $\mathbf{n}_{\mathrm{gs}}$ and $\mathbf{n}_{\mathrm{fs}}^{k}$ for that part of the geometrical surface to find the crystal face k. To do it, we use the smoothed Heaviside function (due to the practical considerations of avoiding sharp transitions, possibly leading to numerical problems). The smoothed Heaviside function, *flc2hs*, in Comsol Multiphysics is defined as:

$$H(\phi, h) = flc2hs(\phi, h) = \left(\frac{\phi}{h} > -1\right)\left(\frac{\phi}{h} < 1\right) \times \left(\frac{1}{2} + \frac{\phi}{h}\left(\frac{15}{16} - \frac{5}{8}\left(\frac{\phi}{h}\right)^{2} + \frac{3}{16}\left(\frac{\phi}{h}\right)^{4}\right)\right) + \left(\frac{\phi}{h} \geqslant 1\right), \tag{14}$$

where h is the width of the transition region from zero to one. Now, the crystal faces are identified according to:

$$\Phi^{k} = H(|\alpha^{k}| - d\alpha, h), \tag{15}$$

where $d\alpha$ is the maximum allowed angle between the normal vectors of the geometrical and the crystal surfaces. Finally, all crystal faces in a given crystal plane family are collected by summing the Φ_i. For example, for {100} plane family:

$$\Phi^{\{100\}} = \Phi^{(100)} + \Phi^{(010)} + \Phi^{(001)}. \tag{16}$$

Since the Heaviside function is used to detect the crystal faces, value of Φ^{k} stays always between 0 and 1, with 1 corresponding to the crystal plane k. Thus, the effective elastic properties of the surfaces, reflecting the collective behaviour of all present crystal faces, are now easily expressed as nonlinear functions of identified crystal faces:

$$\tau_{11}^{*} = \frac{1}{\sum_{k}\Phi^{k}}\sum_{q}\tau_{11}^{q}\Phi^{q},\ \tau_{22}^{*} = \frac{1}{\sum_{k}\Phi^{k}}\sum_{q}\tau_{22}^{q}\Phi^{q} \text{ and } S_{ijlm}^{*} = \frac{1}{\sum_{k}\Phi^{k}}\sum_{q}S_{ijlm}^{q}\Phi^{q}, \tag{17}$$

where q is the crystal plane family. The normalization with the sum of the Heaviside functions is conducted in order to ensure that possible overlaps of the smoothing zones in equation (15) would not lead to summations larger than unity and artificial amplification of the surface properties.

2.3.5. Finite element simulations. The finite element simulations were conducted using Comsol Multiphysics 4.4 and its Structural Mechanics and Membranes toolboxes [53]. Different meshes were tested during the calculations, and the final one consisted of ~132 000 mixed tetrahedral and hexahedral elements, with a minimum size of 0.5 nm and a maximum size of 1.93 nm. The hexahedral elements were generated concentrically around the void until the sides of the simulation box were reached using swept meshing. The tetrahedral elements were used only far away from the void, in low stress and strain regions. The equations for the

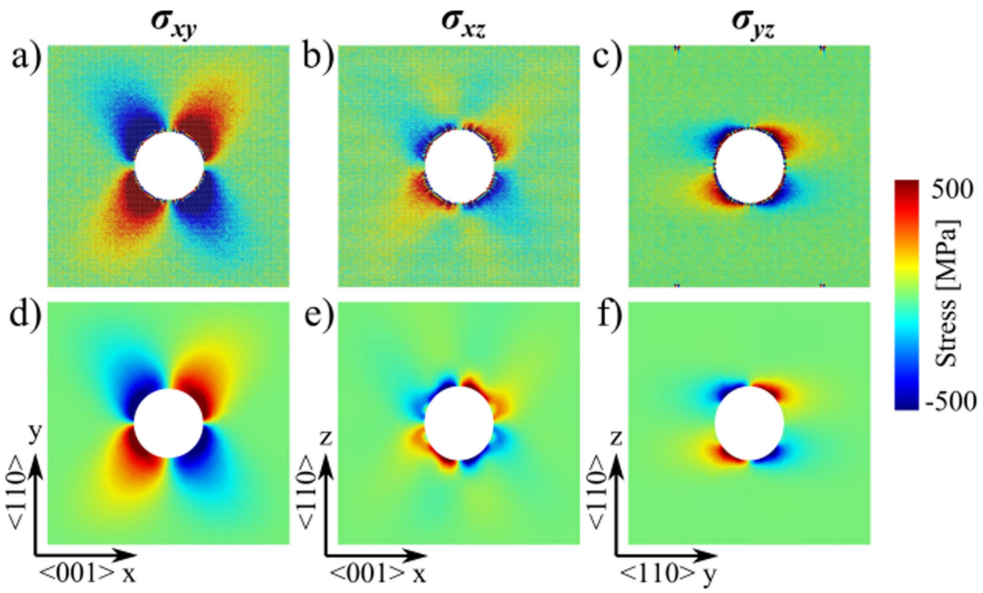

Figure 2. Shear stress distribution around the void without external tensile stress. (a)–(c) MD results; (b)–(d) FEM results. The relaxed material configurations demonstrate good agreement between the methods.

bulk material were solved using linear elements and for the surface behaviour, using quadratic elements. Since the obtained system of equations, describing the stress–strain relations in coupled bulk and surface models is highly nonlinear, the damped Newton type nonlinear solver [54] was used in conjunction with the Pardiso solver.

3. Results and discussion

3.1. Defect caused stress distribution and influence of the surface stress

To verify the calculations of FEM simulations, the shear stress obtained using FEM was compared to the results found from corresponding MD simulations. Both qualitative and quantitative comparisons of the results were conducted to evaluate the accuracy of the FEM model. The stress distributions are presented as cut planes from the simulated geometry; all slices are selected from the centre of the box and correspond to different crystallographic directions, specified in the figures. Both the MD and FEM simulations are coloured according to the shear stress component and are presented in figures 3–6.

The stress distributions without external force in case of a spherical void are presented in figure 2. The presented shear stress distributions overlap well for both MD and FEM simulations for all presented stress tensor components, demonstrating qualitatively similar behaviour due to the influence of surface stress. The most significant difference between the MD and FEM simulations can be observed for the σ_{xz} components near the leftmost and rightmost edges of void cross section—the crystal face interpolation algorithm causes slight distortion of material properties near the void surface leading to the deviation of stress distributions. However, the difference between the MD and FEM cases is small and the effect to the overall stress distribution caused by the void can be neglected.

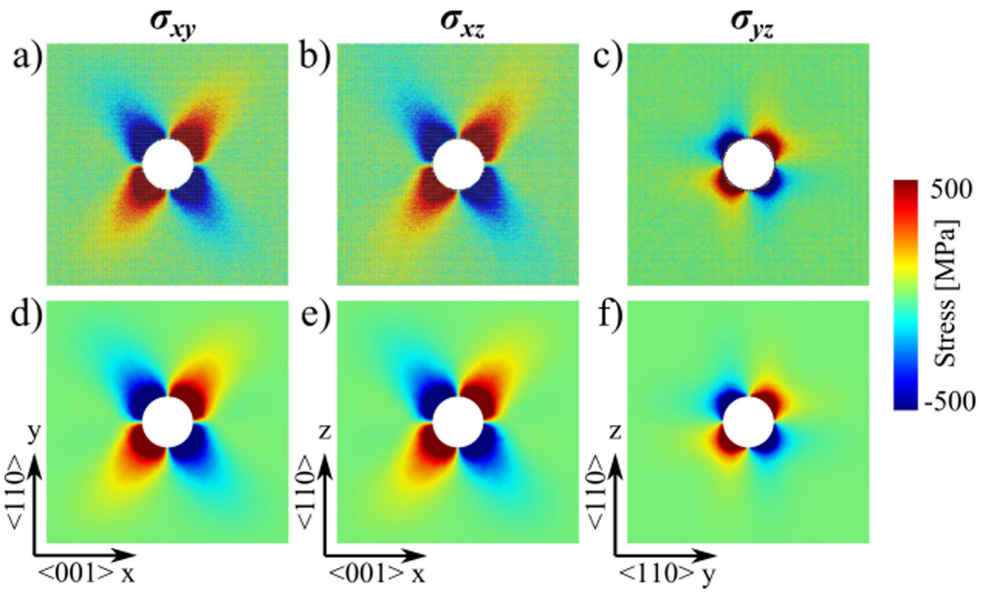

Figure 3. Shear stress distribution in Cartesian slices around the void without external tensile stress in case of fully periodic boundary conditions. This configuration corresponds to void in bulk material and extends the results for arbitrary crystal orientation. Left column—σ_{xy}, middle column—σ_{xz}, right column—σ_{yz}. Upper row—MD results, lower row—FEM results.

Although, in the previous studies we have considered a near surface void, the presence of the surface may influence the surface stress distribution near the void itself. Moreover, the crystal orientation with respect to the surface starts playing a critical role due to a high anisotropy of elastic properties of copper. To separate the internal surface stress distribution from the surface, as well as to avoid the necessity of rotation of the simulation cell in order to obtain the orientation independent result, we performed the current calculations of a void placed deep in the bulk. The results are presented in figure 3. Again, the comparison of MD and FEM simulations demonstrates good qualitative agreement—all presented stress components behave similarly. Compared to figure 2, only the σ_{xy} behaviour is the same, as in both cases the material is already periodic in that direction. Other presented stress tensor components, σ_{xz} and σ_{yz}, show considerable difference—indicating that limited material thickness around the void has significant influence on the stress distribution. However, changes in both MD and FEM agree, indicating that FEM can accurately capture the material behaviour in every crystal orientation.

To test the agreement between the methods for random direction, we conducted similar comparisons as in figure 3 for stress tensor components in the yz cut plane, rotated 45° around z axis. Although not shown here, the stress distributions obtained by both methods are very similar consistently with the previous figures.

The stress distribution due to the combined effect of surface stress and external force are presented in figure 4. Compared to the case without external force, the stress is distributed along the diagonal of the simulation cell and slightly stretched in the z direction. The main difference between the stress distributions can be explained by the approximations of the surface layers in FEM simulations. Compared to the case without an external stress (figure 2), several short-range distortions are visible in all presented stress components. These artefacts

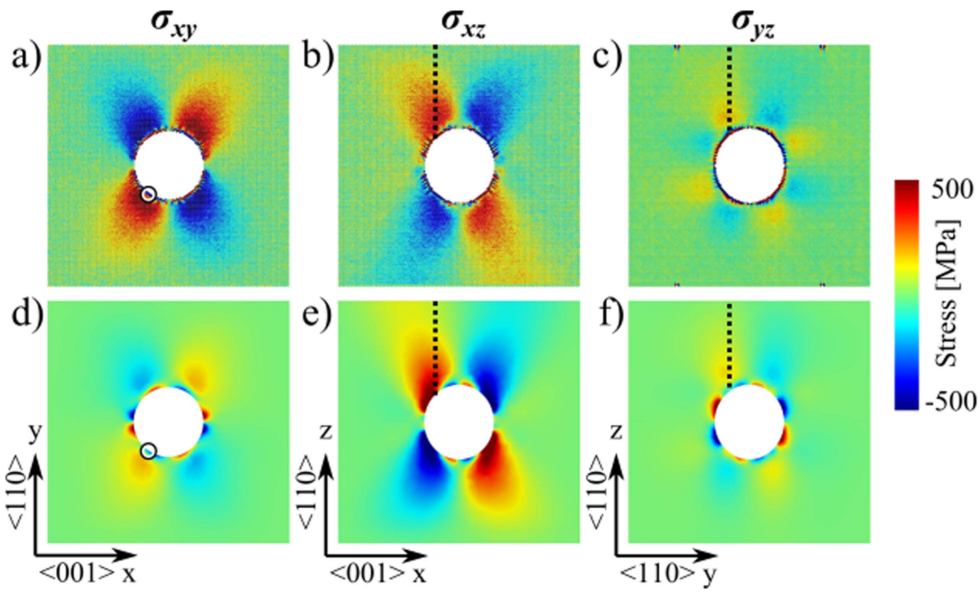

Figure 4. Shear stress distribution around the void with external 1.35 GPa tensile stress. Left column—σ_{xy}, middle column—σ_{xz}, right column—σ_{yz}. Upper row—MD results, lower row—FEM results. The circular marker and dashed lines in the figures represent the data plotted in figure 5.

are influenced by the mesh used in the FEM calculations in combination with the crystal face identification algorithm as both of them introduce smoothing and approximations of surface properties into the model. While the surface mesh over the void has relatively small elements (0.5 nm), element size starts to grow in the bulk material and amplifies the effect surface artefacts deeper in the bulk. On the other hand, the MD stresses near the surface are influenced by the numerical artefacts as well. The MD stresses depend on the volumes associated with atoms, that can be estimated using the Voronoi cells. The latter are poorly defined for the surface atoms as the cells expand deep into the void. However, the influence of these artefacts to the overall stress distribution is small, even if they introduce additional numerical noise in the system. They can be viewed as acceptable trade-offs for keeping the size of the elements in the bulk material relatively large while guaranteeing fast and computationally efficient calculations.

3.2. Quantitative comparison of MD and FEM stress estimations

Finally, quantitative comparisons of the stress tensor components in MD and FEM simulations are presented in figure 5. The data for the comparison was obtained by plotting the distribution of the shear stress component along the line in the z direction between the void surface (at the point where the shear stress has its maximum value) and the surface of the simulation cell. The MD results in figure 5 are presented by blue lines and the FEM results by red lines (dashed without external force, solid with external force). The horizontal axis represents the distance from the void surface in Ångström and the vertical axis gives the respective shear stress component σ_{xy}, σ_{xz} or σ_{yz} in GPa. For comparison, numerical values of the stress in the bulk around a stress-concentrating void can be found from the literature [18].

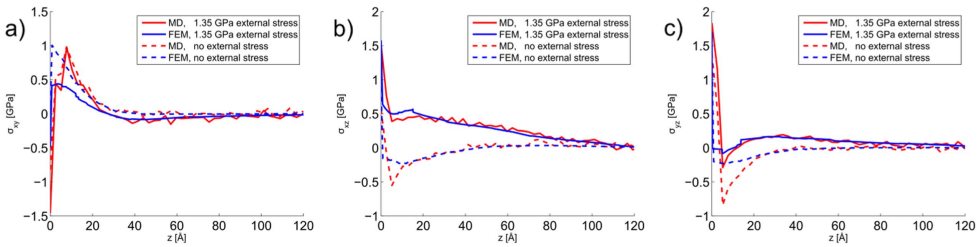

Figure 5. Shear stress along the line from FEM and MD simulations. On the x axis, the distance from void surface is in Å, on the y axis: (a) shear stress σ_{xy}, (b) shear stress σ_{xz}, (c) shear stress σ_{yz} in GPa. The data is plotted along the dashed line in the z direction presented in figure 4 for the corresponding stress components. σ_{xy} is presented, starting from the circular marker in figures 4(a) and (d), in the z direction (perpendicular to the schematics).

FEM and MD show again the same general trend in the stress distribution as in previous snapshots, demonstrating generally good agreement between the methods. All the presented lines can be divided into three main regions—the surface layer (<0.5 nm), close to the void region (distances under 2 nm) and the distant regions, further away. The maximum stress values stay always in the surface layer in both methods. However, since the both approaches need significant approximations in the surface layer area—MD due to the ill-defined atomic volumes for surface atoms and FEM due to uncertainties in choosing the surface layer thickness—the results differ by the factor of two.

When we consider the close to the void region, both models follow the same trends, while FEM generally underestimates the stresses. This can be caused by three mayor factors —the geometrical differences between the actual surfaces in MD and FEM, the accuracy of crystal surface reconstruction in FEM (we use only four crystal surface families) and the smoothing effects of the mesh. Since the mesh elements grow larger further away from the void, the smoothing occurs naturally as the stress calculated by FEM is the average over several atoms, while MD always provides the atomic stresses. Finally, the stress distribution is also affected by the elastic properties of the crystal surface.

Finally, the third distant region demonstrates excellent agreement between the MD and FEM simulations as all the stress values coincide.

The largest difference between the MD and FEM based methods appears in figures 4(a) and (d) where the xy component of the stress tensor is presented. However, more detailed data of σ_{xy} is plotted in figure 5(a) along the z direction from void towards surface. Numerical data in figure 5(a) also demonstrates very good agreement between the MD results and FEM calculations, cutting out only peak stress values near the surface. A similar behaviour is visible in figures 4(a) and (d) as well. The qualitative behaviour is captured, but maximum stress values remain lower than in the MD calculations.

There are several possible reasons for such discrepancy. The most significant one is the fact that the surface model, while capturing different crystal faces over the surface of the void, is isotropic in its nature. For example, if we consider (111) or (100) planes, their elastic properties are affected by the atom packing. Such effect, for example, is clearly visible in anisotropic behaviour or single crystals as well.

Another possible reason for the difference in σ_{xy} distribution may stand in fundamental differences between MD and FEM boundary condition implementations. While in MD, periodic boundary conditions with fixed box sides were used, it still allows atoms to move

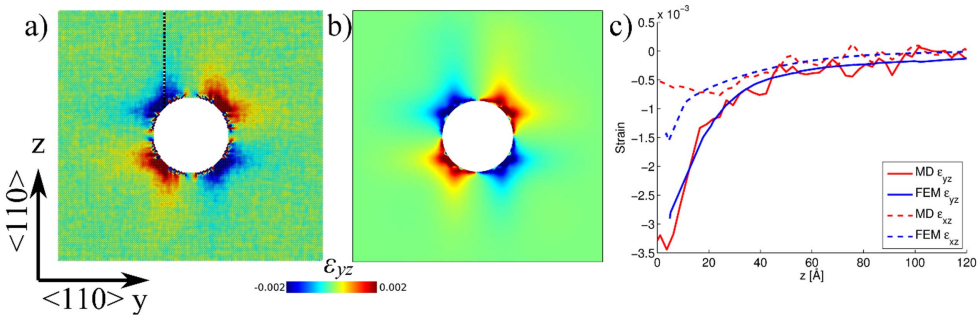

Figure 6. Distribution of ε_{yz} component of the strain tensor in MD (a) and FEM (b) simulations in case of fully periodic boundary conditions. The dashed line in (a) shows the location of plotted data in (c).

across the boundaries. In the case of FEM calculations, symmetry boundary conditions were used, forcing zero normal directional displacements. Thus, boundary conditions in continuum calculations are fundamentally more restrictive. Moreover, in the case of removing restrictions from box sides in the FEM simulation, significantly more pronounced σ_{xy} distribution—close to MD and unloaded FEM result—was observed. Thus, it is possible that applied symmetry boundary conditions are too restrictive and will artificially reduce σ_{xy} values. For example, in the case of external loading it completely suppresses the Poisson effect. As such, we consider this effect to be a limitation of the model, similar to the difference in the case of isotropic or anisotropic elastic materials.

Combination of data presented in figures 2–5 demonstrates that the proposed modelling approach can effectively capture the influence of the void and its surface on the stress distribution in the bulk material. The computational time required for the FEM simulations can be very short—minutes (on dual core desktop PC, in case of coarser meshes), compared to hours of extensive parallel MD calculations. The FEM model augmented by the proposed surface model can be used to assess the ability of nanodefects present in real materials to concentrate the stress. It will also allow to estimate the possible weak points in the structure where the crystal lattice may yield a dislocation at the stresses well below the tensile strength of the material. However, the more rigorous simulations such as MD with appropriate interatomic potentials will be needed to simulate the mechanism of nucleation of dislocations or their reactions in detail.

Using FEM as a tool for the stress calculations also provides significant advantage compare to MD methods by the way the methodology is implemented. For instance, the stress calculated in MD per atom does not result in a single interpretation of the obtained data due to the ambiguity of definition of the cross-sectional surface area of an atom. The finite element-based approach, however, relies on a continuum approximation, eliminating completely the need to consider volumes or cross-sectional areas of the atoms.

3.3. Estimation of strain in MD and FEM calculations

Finally, in addition to the stress estimates, strain obtained from both MD and FEM calculations are compared as well in figure 6. There, figure 6(a) represents the ε_{yz} component of the strain tensor in MD simulations while figure 6(b) shows the same quantity in FEM calculations. Figure 6(c) provides detailed quantitative comparison between FEM (blue line) and MD (red line) results for both ε_{yz} (solid lines) and ε_{xz} (dashed lines) at the dashed line

presented in figure 6(a). Strain, as defined by equations (3) and (4), relies only on the displacement and deformation gradient of the atoms, thus eliminating the need to use homogenization volumes as during the estimation of the stress. However, due to the thermal movement of atoms at nonzero temperatures, time averaging is still needed. Similarly, to the stress calculations, very good qualitative and quantitative agreement of the results is obtained with the results coinciding almost completely, in range of the nearest neighbour interpolation fluctuations of the MD strain components and providing a final validation to the model.

3.4. Finite size effect in FEM models

Many nanoscale effects are size dependent and arise in the case of small enough surface to volume ratios. Thus, a continuum model describing surface stress behaviour must include the characterization of the size effects well and demonstrate the diminishing of the surface stress during the upscaling of the void. To test the proposed model for ability to capture the finite size effect, we performed additional simulations of a near surface void with different radii in a single crystal Cu held under tensile stress. Stress was exerted on the Cu surface. The geometry and simulation condition were chosen to replicate those in MD simulations [52], where the analytical model to describe the dependence of void aspect ratio on the radius of the void was proposed. By the ratio of the void radius r to the void depth h_{cyl}, at which the maximal shear stress σ_{zx} was sufficient to nucleate a dislocation at the void surface (for details see [52] and figure 1). h_{cyl} stands for the height of the cylinder above the void up to the surface of the material with the base circumscribed by the region of the maximal shear stress on the surface of the void. By plotting this parameter (h_{cyl}/r) against the radius of the void, r, it was demonstrated that at some size of the void, the void ratio h_{cyl}/r became independent of the size of the void and the geometry became size invariant. Due to the size and time limitations, the MD results could not reproduce the entire curve $h_{\mathrm{cyl}}/r(r)$. By developing the present model, we have an opportunity to verify the finite size effect predicted by analytical model in [52]. If the curve can be reproduced by the present simulations, then the saturation of the dependence $h_{\mathrm{cyl}}/r(r)$ can be explained only by the surface stress on the surface of the void, since this effect becomes negligible with the growth of a nanovoid.

The results of size dependence of the surface stress model and the comparison with the analytical predictions is presented in figure 7 where the red markers represent the simulated data and blue lines represent the analytical model from [52], $h_{\mathrm{cyl}}/r = a/\sqrt{2} + c/r$, where coefficients a and c are obtained from the simulation data. The error bars correspond to the void depth increments (0.2 nm) in the present calculations. The analysis was performed for two different external stress cases—3.05 and 4.58 GPa—with corresponding threshold stresses for 2 and 3 GPa (corresponding to the increase of applied stress). In both cases, we see how the surface stress model follows the same behaviour as predicted by the analytical model very closely. While the FEM model succeeds in capturing accurately the behaviour of the size effects, the homogenization of the continuum approach leads to underestimation of stresses on the void surface and, consequently, to underestimation of the void aspect ratio as well. However, the close comparison between the analytical prediction [52] and the present FEM results support the analytical model and explain the size effects mostly due to the effects of surface stress on the surface of the void.

4. Conclusions

In this work, we have successfully developed a methodology to incorporate the surface stress effects into the solid mechanics framework. The developed methodology was tested by

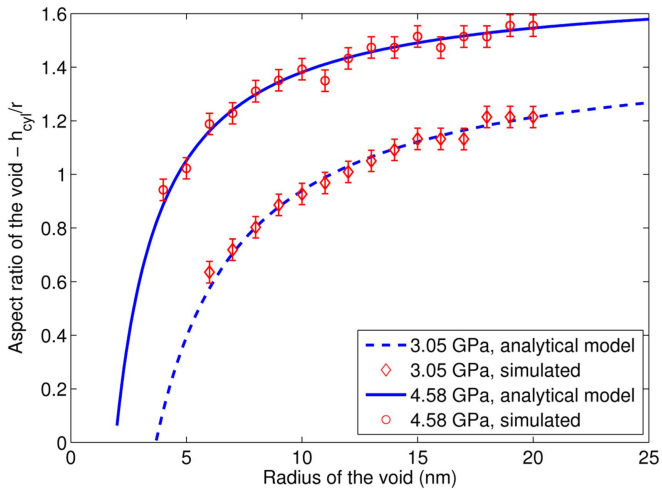

Figure 7. Aspect ratio of a void needed for dislocation nucleation in FEM simulations versus estimations by the analytical model published in [52]. Red circles and diamonds correspond to simulations; error bars represent the uncertainty due to the void depth increments ($\pm$0.2 nm).

applying a tensile stress on a single Cu crystal containing a test stress concentrator, in the shape of a spherical void. The proposed approach utilizes pre-calculated elastic properties of crystal surfaces from the MD simulations as input parameters and allows for calculating resulting stress distributions in a computationally efficient way. The comparison of stress estimates obtained using MD and FEM shows good qualitative and quantitative agreement between the two methods for all test cases, while additional validation is provided by the demonstration of similar agreement in the calculated shear strains as well. We have also demonstrated that the size effect, characteristic for nanoscale systems, is consistent with previous MD works. The methodology can be easily implemented using commercially available finite element solutions, making it an attractive analysis tool. Moreover, the needed input parameters for the elastic properties of the surfaces can be calculated using MD simulations or obtained from already published data. All these features make the proposed approach an attractive analysis tool for studying mechanical interactions in nanoscale materials. The simulation data, that forms the basis of the results (FEM and MD stresses and strains), are available on request.

Acknowledgments

This work is supported by Estonian Research Council grants PUT 57 and PUT 1372, and the national scholarship program Kristjan Jaak (funded and managed by Archimedes Foundation in collaboration with the Ministry of Education and Research of Estonia). Computing resources were provided by the Finnish IT Center for Science and the High Performance Computing Centre of the University of Tartu. V Jansson was supported by Academy of Finland (Grant No. 285382). F Djurabekova acknowledges funding support from the Academy of Finland (Grant No. 269696).

ORCID iDs

V Zadin https://orcid.org/0000-0003-0590-2583
M Veske https://orcid.org/0000-0003-2367-9215
S Vigonski https://orcid.org/0000-0002-2849-2882
V Jansson https://orcid.org/0000-0001-6560-9982
J Muszinsky https://orcid.org/0000-0002-3804-1073
S Parviainen https://orcid.org/0000-0003-4571-4640
A Aabloo https://orcid.org/0000-0002-0183-1282
F Djurabekova https://orcid.org/0000-0002-5828-200X

References

[1] Compact Linear Collider (CLIC) http://clic-study.web.cern.ch/
[2] Boland M J *et al* (CLIC) 2016 Updated baseline for a staged compact linear collider *CERN Yellow Reports* CERN-2016-004 (https://doi.org/10.5170/CERN-2016-004)
[3] O'Shea P G and Freund H P 2001 *Science* **292** 1853–8
[4] Holtkamp N 2009 *Fusion Eng. Des.* **84** 98–105
[5] Rohde V 2010 Arc surface damage in fusion reactors *Breakdown Physics Workshop (CERN)* 6–7.5
[6] Kelly T F and Larson D J 2012 *Annu. Rev. Mater. Res.* **42** 1–31
[7] Braun H H, Döbert S, Wilson I and Wuensch W 2003 *Phys. Rev. Lett.* **90** 224801
[8] Descoeudres A, Ramsvik T, Calatroni S, Taborelli M and Wuensch W 2009 *Phys. Rev. Spec. Top.—Accel. Beams* **12** 032001
[9] Grudiev A, Calatroni S and Wuensch W 2009 *Phys. Rev. Spec. Top.—Accel. Beams* **12** 102001
[10] Descoeudres A, Levinsen Y, Calatroni S, Taborelli M and Wuensch W 2009 *Phys. Rev. Spec. Top.—Accel. Beams* **12** 092001
[11] Forbes R G, Edgcombe C and Valdrè U 2003 *Ultramicroscopy* **95** 57–65
[12] Insepov Z, Norem J H and Hassanein A 2004 *Phys. Rev. Spec. Top.—Accel. Beams* **7** 122001
[13] Insepov Z, Norem J and Veitzer S 2010 *Nucl. Instrum. Methods Phys. Res.* B **268** 642–50
[14] Insepov Z, Norem J, Proslier T, Huang D, Mahalingam S and Veitzer S 2010 arXiv:1003.1736v4 [phys.]
[15] Insepov Z and Norem J 2012 *J. Vac. Sci. Technol.* A **31** 011302
[16] Nordlund K and Djurabekova F 2012 *Phys. Rev. Spec. Top.—Accel. Beams* **15** 071002
[17] Pohjonen A S, Djurabekova F, Nordlund K, Kuronen A and Fitzgerald S P 2011 *J. Appl. Phys.* **110** 023509
[18] Pohjonen A S, Parviainen S, Muranaka T and Djurabekova F 2013 *J. Appl. Phys.* **114** 033519
[19] Zadin V, Pohjonen A, Aabloo A, Nordlund K and Djurabekova F 2014 *Phys. Rev. ST Accel. Beams* **17** 103501
[20] Dyke W P and Trolan J K 1953 *Phys. Rev.* **89** 799–808
[21] Timko H *et al* 2010 *Phys. Rev.* B **81** 184109
[22] Guisbiers G and Buchaillot L 2008 *Nanotechnology* **19** 435701
[23] Yvonnet J, Quang H L and He Q-C 2008 *Comput. Mech.* **42** 119–31
[24] Jia M, Lai Y, Tian Z and Liu Y 2009 *Model. Simul. Mater. Sci. Eng.* **17** 015006
[25] Park H S, Klein P A and Wagner G J 2006 *Int. J. Numer. Methods Eng.* **68** 1072–95
[26] He M and Li S 2012 *Comput. Mech.* **49** 337–55
[27] Shenoy V B 2005 *Phys. Rev.* B **71** 094104
[28] Parviainen S, Djurabekova F, Timko H and Nordlund K 2011 *Comput. Mater. Sci.* **50** 2075–9
[29] Djurabekova F, Parviainen S, Pohjonen A and Nordlund K 2011 *Phys. Rev.* E **83** 026704
[30] Vigonski S, Veske M, Aabloo A, Djurabekova F and Zadin V 2015 *Appl. Math. Comput.* **267** 476–86
[31] Sharma P, Ganti S and Bhate N 2003 *Appl. Phys. Lett.* **82** 535–7
[32] Wei G, Shouwen Y and Ganyun H 2006 *Nanotechnology* **17** 1118
[33] LAMMPS Molecular Dynamics Simulator http://lammps.sandia.gov/
[34] Plimpton S 1995 *J. Comput. Phys.* **117** 1–19

[35] Sabochick M J and Lam N Q 1991 *Phys. Rev.* B **43** 5243–52
[36] OVITO—The Open Visualization Tool, http://ovito.org/
[37] Griffiths D J 1999 *Introduction to Electrodynamics* 3rd edn (Upper Saddle River, NJ: Addison-Wesley) (https://doi.org/10.1119/1.19136)
[38] Hardy R J 1982 *J. Chem. Phys.* **76** 622–8
[39] Lutsko J F 1988 *J. Appl. Phys.* **64** 1152–4
[40] Tsai D H 1979 *J. Chem. Phys.* **70** 1375–82
[41] Zimmerman J A, WebbIII E B, Hoyt J J, Jones R E, Klein P A and Bammann D J 2004 *Model. Simul. Mater. Sci. Eng.* **12** S319
[42] Cormier J, Rickman J M and Delph T J 2001 *J. Appl. Phys.* **89** 99–104
[43] Thompson A P, Plimpton S J and Mattson W 2009 *J. Chem. Phys.* **131** 154107
[44] 2017 LAMMPS Molecular Dynamics Simulator, manual http://lammps.sandia.gov/doc/Manual.html
[45] Voro++: A Three-Dimensional Voronoi Cell Library in C++, http://math.lbl.gov/voro++/
[46] Falk M L and Langer J S 1998 *Phys. Rev.* E **57** 7192–205
[47] Shimizu F, Ogata S and Li J 2007 *Mater. Trans.* **48** 2923–7
[48] Bower A F 2009 *Applied Mechanics of Solids* (Boca Raton, FL: CRC Press)
[49] Ottosen N S and Ristinmaa M 2005 *The Mechanics of Constitutive Modeling* (Amsterdam: Elsevier) (https://doi.org/10.1016/B978-0-08-044606-6.X5000-0)
[50] Vermaak J S, Mays C W and Kuhlmann-Wilsdorf D 1968 *Surf. Sci.* **12** 128–33
[51] Chapelle D and Bathe K-J 2011 *The Finite Element Analysis of Shells—Fundamentals* (Berlin: Springer) (https://doi.org/10.1007/978-3-642-16408-8)
[52] Pohjonen A S, Djurabekova F, Kuronen A, Fitzgerald S P and Nordlund K 2012 *Phil. Mag.* **92** 3994–4010
[53] Multiphysics Modeling and Simulation Software—COMSOL http://comsol.com
[54] Deuflhard P 1974 *Numer. Math.* **22** 289–315

III

Applied Mathematics and Computation 267 (2015) 476–486

Contents lists available at ScienceDirect

Applied Mathematics and Computation

journal homepage: www.elsevier.com/locate/amc

Verification of a multiscale surface stress model near voids in copper under the load induced by external high electric field

Simon Vigonski [a,b,*], Mihkel Veske [a,b], Alvo Aabloo [a], Flyura Djurabekova [b], Vahur Zadin [a,b]

[a] Intelligent Materials and Systems Lab, Institute of Technology, University of Tartu, Nooruse 1, 50411 Tartu, Estonia
[b] Helsinki Institute of Physics and Department of Physics, University of Helsinki, P.O. Box 43 (Pietari Kalmin katu 2), FI-00014 Helsinki, Finland

ARTICLE INFO

Keywords:
Finite element simulations
Molecular dynamics simulations
Multiscale simulations
Surface stress model
Void under copper surface

ABSTRACT

In the current study we use a model of surface stress for finite element method calculations to complement existing bulk stress models. The resulting combined model improves the accuracy of stress calculations near nanoscale imperfections in the material. We verify the results by simulating differently-shaped voids in single crystal copper both with FEM and with molecular dynamics, and compare the resulting stress distributions. The compared results agree well within small uncertainties, indicating that the implemented surface stress model is able to capture all the major features of the stress distributions in the material. Discrepancies occur near surfaces, where the crystal faces were not defined explicitly in the model. The fast and accurate FEM calculations can be used to estimate the stress concentration of specific extended defects, such as voids, while studying the dislocation-mediated mechanisms near these defects in the presence of external stresses by atomistic techniques.

1. Introduction

Materials in very high electric fields are subject to electric discharges between the electrodes – vacuum arcing or vacuum breakdowns – even in ultra-high vacuum conditions [1]. For example, vacuum breakdowns occur in free electron lasers [2], vacuum circuit breakers [3], fusion reactors [4] and particle accelerators [5,6]. An example of the latter is the proposed Compact Linear Collider (CLIC) at CERN [7], which is designed to accelerate electrons and positrons using high radiofrequency electric fields at room temperature. The proposed accelerating electric field is in the range 100 MV/m [8], while the desired maximum breakdown rate of the copper accelerating structures for optimal operation is estimated to be 3×10^{-7} 1/pulse/m [9].

Understanding the origins of electrical breakdowns is important for controlling them at the desired level. Experiments under DC conditions have shown that the emission currents prior to breakdown events fit the Fowler–Nordheim model [10], which includes a so-called local field enhancement factor β, which was determined to be in the range of 30 to 140 [11]. This is associated with nanoscale field emitters, whose existence is currently assumed, but not yet experimentally witnessed [11].

Nanoscale phenomena can be modeled by using atomistic methods. For example, the molecular dynamics (MD) method provides sufficient spatial and temporal resolution (from a few to hundreds of nanometers and up to a few nanoseconds,

* Corresponding author at: Intelligent Materials and Systems Lab, Institute of Technology, University of Tartu, Nooruse 1, 50411 Tartu, Estonia.
E-mail address: simon.vigonski@ut.ee (S. Vigonski).

http://dx.doi.org/10.1016/j.amc.2015.01.102
0096-3003/

respectively) [12,13]. Previous molecular dynamics (MD) simulations of surface roughening mechanisms have shown that dislocations nucleating at near-surface stress concentrators, like voids [14,15] or precipitates [16], play a role in the modification of surface topology when the material is subjected to strong external stress due to the applied electric field.

Nanoscale dislocation processes influence macroscopic phenomena. In case of a high electric field they may lead to gradual surface modification and, eventually, to vacuum breakdowns [6,17–19]. The time scale from the application of the electric field to breakdown can range from 100 ns to 1 ms, depending on the applied field strength, the electrode material and the surface geometry [11]. These time scales are unattainable to the atomistic simulations and a multiscale approach is needed to study such systems. The continuum bulk stress models typically used in FEM simulations of macroscale problems are not sufficiently accurate at nanoscales, where surface effects must be accounted for [14,20].

Previous work includes the XFEM-based approach by Yvonnet et al. [20], or Cauchy-Born constitutive modeling based on interatomic potentials by Park et al. [21], He and Li [22] or Javili and Steinmann, incorporating boundary potentials into FEM models [23–25]. While these methods are relevant and accurate, in the current work we aim to test a simpler way of incorporating the surface model together with the bulk model, in order to be able to analyze the effect of the surface stress in the vicinity of extended defects such as voids. We implement the surface stress model in similar way as presented in [26]. This approach, although not as accurate as suggested in [21–25], has the advantage of computational efficiency, which is very valuable for many applications, where it is necessary to assess the relevance of the process to the main mechanism. For instance, computationally cheap model can be used successfully as estimator for further molecular dynamics studies or in multiphysics simulations, where several physical phenomena are combined. This becomes especially important in modeling of material behavior under high electric fields, where multiphysics simulations utilizing thermal effects, emission currents, external electric fields and material stress must be taken into account simultaneously. Moreover, to obtain reliable results in nanoscale simulations, the effects discovered using continuum methods must be verified using more accurate approaches, like molecular dynamics as atomistic nature of the material that cannot be accessed using continuum approach, becomes important at these length scales. However, while the spherical shape of the void is motivated by the assumption of surface energy minimization, it was shown that under external stress initially spherical voids in copper can assume irregular shapes due to the anisotropy of the crystal structure [27]. Moreover, the anisotropic effects are enhanced by surface composition. The surface of nanovoids in real crystals consists of different crystal faces, each with its own surface stress value [28]. All the faces contribute to the total surface stress distribution, leading to its dependence on the amount of different crystal faces, their relative areas and structures. Hence, in the present work, we investigate different void shapes to analyze the surface stress model sensitivity and the effect of the shape on the stress concentration properties of voids.

We increase the complexity of the geometry by introducing lattice defects with different degree of complexity, gradually approaching the limiting spherical case. The void shapes serve the purpose of verifying the applied FEM model in case of controlled adverse surface configurations with planar edges and sharp vertices. This approach allows us to test the robustness and limits of the used model. We compare the behavior of the surface stress model implemented in FEM and the stresses calculated in MD simulations to test the sensitivity of the model. We aim to achieve sufficient accuracy for estimation of surface stress with FEM simulations, preserving the advantage of short simulation time even on an ordinary PC.

2. Methods

2.1. The coupled bulk and surface stress model

To simulate the surface stress effects on mechanical response of materials by using FEM, standard structural mechanics tools must be augmented with the surface behavior, leading to a combined model of bulk and surface material. First, to model the bulk we use the large deformation model. In this approach, material deformation is obtained using the deformation gradient tensor F, connecting the deformed (x_i) and undeformed (X_i) configurations [29]:

$$x_i = F_{ij}X_j \tag{1}$$

The deformation gradient is then used to calculate the corresponding Green–Lagrange strain (E):

$$E = \frac{1}{2}(F^T F - \mathrm{I}) \tag{2}$$

Finally, material stress (the second Piola–Kirchhoff stress tensor) (S) is obtained [30]:

$$S = C : E \tag{3}$$

where C is the elasticity tensor. Cauchy stress (σ) and the first Piola–Kirchhoff stress (P) are related to the second Piola–Kirchhoff (S) stress as $S = F^{-1}P$ and $\sigma = J^{-1}PF^T = J^{-1}FSF^T$, where the ratio between deformed and undeformed configurations is obtained as $J = \det(F) = V/V_0$. To simulate the material surface behavior, we assume already known information about initial surface stresses and the elastic properties of the surface. In the current study, we use elastic parameters calculated by Shenoy in [28]. We approximate the surface by a thin elastic layer, coupled to the bulk model. In this approach, we assume that the surface layer is thin compared to the dimensions of the rest of the geometry. The surface stress τ_{ij}, initial stress τ^0_{ij} and the surface deformations are connected as [28,31]:

$$\tau_{ij} = \tau_{ij}^0 + s_{ijkl}\varepsilon_{kl} \tag{4}$$

where ε_{kl} is the elastic strain of the surface and s the surface elasticity tensor. Unlike the bulk stress calculations, where the equations are specified in the volume occupied by the material, the surface stress model is active only in the surface layer and is defined in the local boundary coordinate system [32]. As in the case of bulk material, the surface model is derived using the assumption of large deformations – deformed (x_i) and undeformed (X_i) surface configurations are connected using the deformation gradient as $x_i = F_{ij}X_j$ and the surface elastic strain is

$$\varepsilon = \frac{1}{2}(F^T F - \mathrm{I}). \tag{5}$$

Since now we consider the surface, not the bulk behavior, the ratio of areas, instead of volumes, between deformed and undeformed configurations is calculated as

$$J_{surf} = \sqrt{\det(F^T F)} = \sqrt{\det(I + 2\varepsilon)}. \tag{6}$$

Incorporation of the surface stress influence of the material behavior is completed by two-way coupling of the bulk and surface models. This is done similarly to [26]. We set every surface point to follow the bulk material displacement according to the following boundary condition:

$$\mathbf{u}_{\mathrm{surf}}(x, y, z) = \mathbf{u}_{\mathrm{bulk}}(x, y, z) \tag{7}$$

Due to the deformation of the bulk material, surface deformation occurs, corrected now by the surface stress model. The stress in the surface is then introduced in the boundary condition of the bulk material:

$$F = p\mathbf{n}J_{surf} \tag{8}$$

where p is the pressure, calculated in the surface stress model as $p = \frac{1}{3}(\tau_{xx} + \tau_{yy} + \tau_{zz})$, $\mathbf{n}$ the unit normal vector in the deformed configuration and J_{surf} is defined in Eq. (6). This boundary condition is implemented as load follower – it takes into account the surface area changes during the simulation and guarantees the correct stress value at the boundary. The coupling between the bulk and surface models, as well as the key parameters are illustrated schematically in Fig. 1.

Finally, to obtain the stress distribution in the material, we utilize the principle of virtual work. In this case, the virtual work from the internal strains must equal the work from all external forces. As a result, we obtain the distributions of stresses, strains and displacements.

Since we simulate the material behavior on nanoscale, it becomes important to use an anisotropic description of the crystal. The components of the elasticity tensor are C_{11} = 168.4 GPa, C_{44} = 75.4 GPa, C_{12} = 121.4 GPa [29]. The elastic parameters of the crystal surfaces are presented in Table 1, where s_{iijj} and s_{1212} are the surface counterparts of the bulk and shear modulus, respectively. Since the crystal orientation of the material is known from the initial setup of the simulation, and the material defects consist of different voids with planar surfaces, each void surface is associated with crystal face with corresponding initial surface stresses and elastic properties. For simplicity we apply the isotropic model of surface stresses, and since the

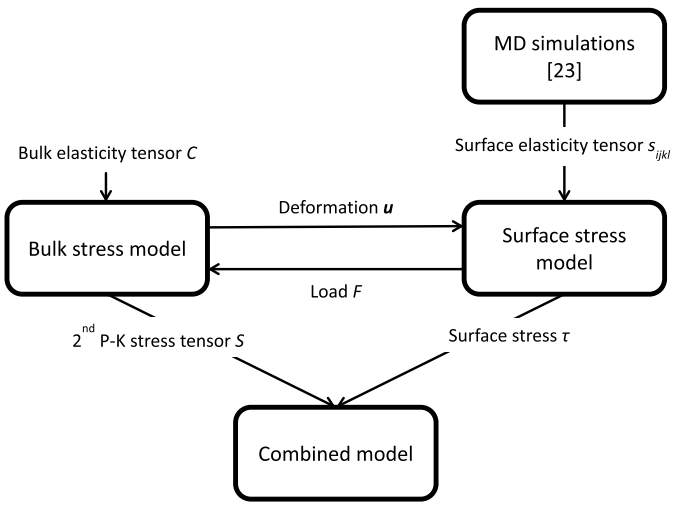

Fig. 1. Schematic of the combined bulk and surface stress model. Surface properties are taken from published MD simulations [23]. The model includes two-way coupling between the bulk and the surface, resulting in a combined stress value.

Table 1
Crystal surface parameters used in the simulations, where s_{iijj} and s_{1212} are the surface counterparts of the bulk and shear moduli, respectively [28].

Crystal planes	Nonzero components of initial surface stress tensor τ^0_{11} (eV/Å^2), τ^0_{22} (eV/Å^2)	Components of surface elasticity tensor	
		s_{iijj}(eV/Å^2)	s_{1212}(eV/Å^2)
{001}	0.0649, 0.0649	0.017	−0.063
{111}	0.0343,0.0343	−0.527	0.009
{110}	0.0621, 0.0373	−2.428	−0.352
Rest of the surface {112}	0.0474, 0.0382	−1.641	−0.252

elastic properties of the {110} and {112} crystal faces on the surfaces are direction-dependent, we use the average value of the anisotropic surface stresses τ_{11} and τ_{22} for the single value of surface stress (isotropic now as it is does not depend on orientation) for those crystal faces.

As shown in Table 1, some of the surface parameters show significant difference from their bulk counterparts. The elasticity tensor of the bulk must be positive definite to guarantee the stability of the bulk. However, this is not the case with the surface elasticity tensor as the surface of the material cannot exist independently of the bulk, rather it forms a coupled system with it [28].

Even though the material surfaces in the FEM simulations are modeled as infinitely thin layers, the calculations of surface stress incorporate mathematically finite thickness of the boundary layers. As the surface and bulk stress models are coupled, the stresses due to the surface effects extend into the bulk.

2.2. Simulated geometries

The simulated system is illustrated in Fig. 2(a). A single crystal Cu sample with a void in the middle corresponds to an extended Cu surface with a periodic network of voids due to the applied periodic boundary conditions in the lateral directions. This system is held under a strong external electric field. The electric field induces mechanical tensile stress in the material due to the interaction of the electrons of the surface atoms with the applied field, resulting in a Lorentz force [34]:

$$\sigma = \frac{\varepsilon_0 E^2}{2}, \tag{9}$$

where σ is the normal tensile stress on the surface, E is the magnitude of the applied electric field (normal to the surface) and ε_0 is the vacuum permittivity. The electric field and material interaction is modeled as a z-directional force acting on the free surface. The bottom boundary of the system is fixed to obtain non-zero stress inside the material. The stress distribution in the system was calculated both with and without external force acting on the material surface. The value of the force was chosen from previous studies where the influence of the void depth to surface modification was investigated [14]. To quantitatively compare the stress distributions in MD and FEM simulations, we present the variation of the local stress along a vertical line that starts at the surface of the void in the region of maximum stress and ends at the material surface, which is indicated as a black arrow in the following figures, where the actual stress distribution is presented.

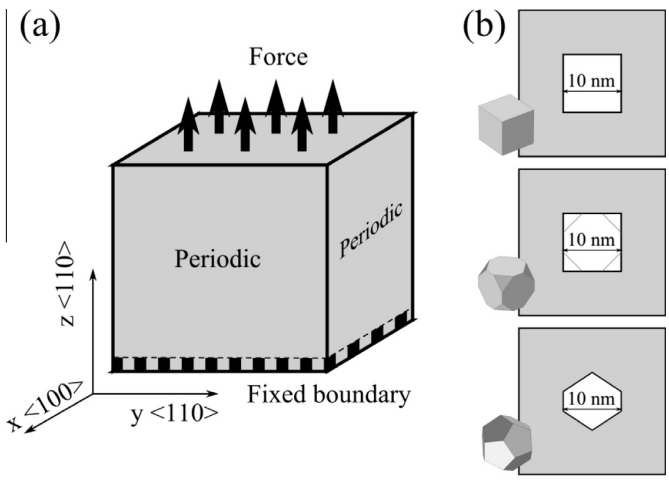

Fig. 2. Three void geometries were simulated – cube, cut-cube and dodecahedron. The simulation box is periodic in the lateral directions, external force is applied to the upper boundary; the lower boundary is fixed.

We studied a number of different void shapes with characteristic size of 10 nm, which can be seen in Fig. 2(b). In [33], we simulated a spherical void that has a well-defined surface. However, it represents only one special configuration of possible material defects. In the current work, we apply the surface stress model to a range of void geometries with increasing complexity, approaching step-by-step the limiting, spherical case. We start by simulating a simple cubic void (Fig. 2(b), top), continue with a cut-cube (Fig. 2(b), middle) and finally use a dodecahedron (Fig. 2(b), bottom). The cut-cube is a cube with the vertices cut off evenly. The middle cross-section of such a shape is still a square; the thin lines in Fig. 2(b) are a schematic representation of the cut vertices. The cross-section of the dodecahedron becomes an irregular hexagon. 3D models of the void shapes are added to the figure to help visualization.

The size of the simulation box was 34.7, 34.7 and 32.7 nm in the x, y and z-directions, respectively. The [1 1 0] crystal direction was set in the z-axis, the [0 0 1] crystal direction in the x-axis and the $[1\bar{1}0]$ crystal direction in the y-axis. In the chosen orientation, the faces of the cubic void are all either {1 0 0} or {1 1 0}. When the vertices of the cube are cut off, new crystal faces appear, which are not explicitly characterised by available elastic properties of the surfaces (see Table 1). The contribution of the new faces to the total surface stress increases further when the void assumes dodecahedral shape. This progression leads away from well-defined crystal faces towards the smooth spherical void simulated in [33]. In the current study we aim to investigate the sensitivity of the surface stress model by testing its accuracy with different geometrical configurations.

2.3. Simulation details

The FEM calculations were conducted using Comsol Multiphysics 4.4 [35] and its Structural Mechanics Toolbox. The geometries were discretized using tetrahedral quadratic elements while the solution of the equations was conducted using damped Newton solver [36] in conjunction with Pardiso. The Newton iterations were stopped when the relative residual became smaller than 10^{-6}.

The lateral sides of box were restricted to move only in the z-direction, making the box effectively periodic in the x- and y-directions. The bottom side of the box was fixed. The calculations were conducted using tetrahedral elements with quadratic or linear shape functions. The number of elements was from 1.0×10^5 to 1.4×10^5 .

MD simulations were run to benchmark the FEM results. The MD simulations were carried out with the open source MD code LAMMPS [37] using the Sabochick–Lam embedded atom method (EAM) potential for Cu [38]. The MD results were visualized with the open source OVITO software [39], Voronoi cells needed for proper stress calculations were found with the help of the open source code Voro++ [40].

The boundaries in the x- and y-directions in MD were periodic and three bottom layers of atoms were fixed. The box contained approximately 3.3×10^6 atoms. The timestep for all simulations was 2 fs. The temperature was set to 293.15 K throughout all simulations and held constant using the Berendsen thermostat [41]. The system was relaxed for 150 ps. After this, the external stress on the top surface was linearly ramped at the rate 9 MPa/ps during 150 ps. The system was simulated for another 300 ps at the maximal stress 1.35 GPa reached at the end of the ramping process.

Atomic stresses were calculated with and without an external stress for every atom in every time step. Atomic stresses were obtained by calculating the virial stress and dividing it with the atomic volume. The virial stress can be seen as a measure of the contribution of each atom into the total stress distribution in the system [42,43]. The atomic volumes for the bulk atoms were obtained from a Voronoi cell tessellation and for the surface atoms by calculating the average bulk atomic volume. This approach is needed since the Voronoi cells of the surface atoms extend into the void (or the volume above the surface), leading to a large error in atomic volume estimation. The surface atoms were determined by applying coordination analysis with a cutoff distance of 0.42 nm to the system. Thus, all nearest and second nearest neighbors of an atom were considered. All atoms with a coordination number less than or equal to 15 were considered as surface atoms. The resulting instantaneous atomic stress was averaged over 75 ps to reduce thermal fluctuations.

3. Results and discussion

3.1. Cubic void

The results of the MD and FEM simulations are presented in Fig. 3 where the distribution of the stress tensor component $_{xy}$ (parallel to the plane of the surface of the material) is plotted. Fig. 3(a) and (b) show the stress distribution in the MD system in the unstressed state and under 1.35 GPa external stress, respectively. Fig. 3(c) and (d) show the same results for FEM simulations.

In the relaxed system (Fig. 3(a) and (c)), regions of positive (red) and negative (blue) shear stress develop at the edges of the cubic void. At the corners of the void cross-section (the edges of the void), small regions of stress with the opposite sign are visible in Fig. 3(a) and (b), showing a fast change in the value of the local stress due to the surface effects near the region of the sharp transition from one crystal face to another. The FEM surface stress model also captures these effects (see Fig. 6), but they cannot be plotted in Fig. 3(c) and (d) since the actual surface stress (Eq. (4)) is calculated in the surface mesh that has infinitesimal thickness.

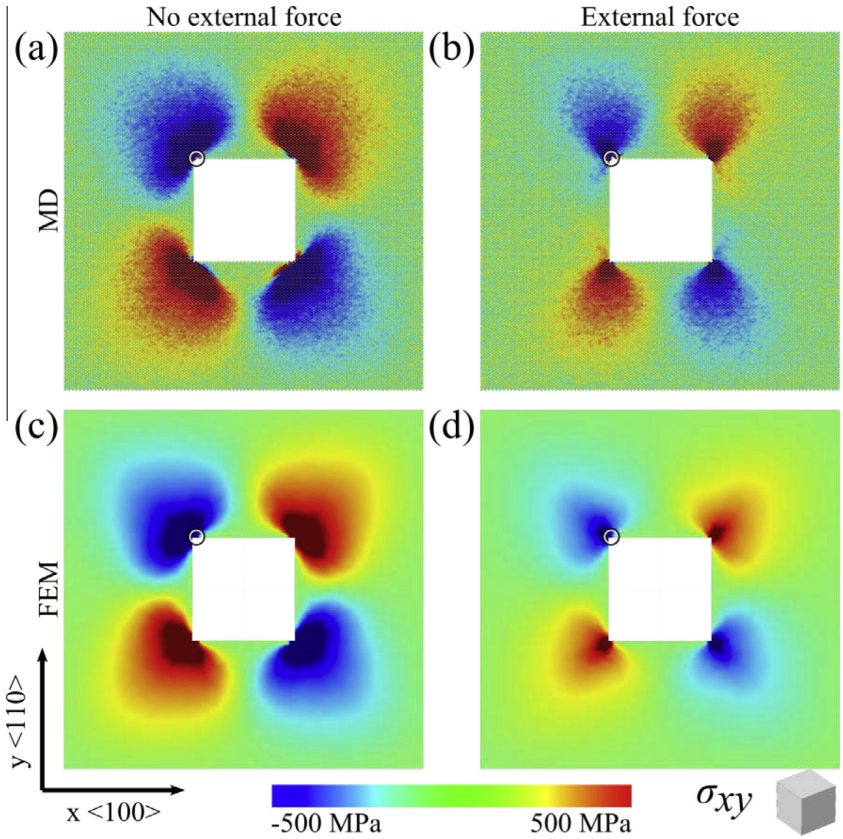

Fig. 3. Middle cross-sections of the shear stress distribution in MD simulations (top row) and finite element (bottom row) simulations, without (left column) and with external force applied (right column) in case of a cubic void. The *xy* component of the stress tensor is shown in the *xy* plane. The circles show the location of the line (in the *z*-direction) from the void surface to the material surface along which data was collected for Fig. 6.

The positions of the stressed regions are similar in both MD and FEM simulations. Differences in the absolute values and the extent of stress concentrations are affected by several factors. The geometry used in FEM represents a perfect shape, while the one in MD has atomistic resolution and can change during the simulation due to the stochastic movement of atoms. Also, the surface stress model in FEM contains a number of simplifications. One of the limitations of the surface stress model is the limited number of implemented crystal faces. In the FEM simulations, any surface which is not {1 1 1}, {1 1 0} or {1 0 0}, is considered to be {1 1 2}. While the FEM model describes the transitions between the different faces smoothly, the information on other possible faces is not yet included in the model. If this information were available, it would definitely improve on the accuracy of the calculations, especially for problems where the effect of surface stress is particularly important. Nevertheless, the currently proposed model is sufficient for many purposes as it includes the most commonly known crystal faces of copper and, hence, can provide an estimation of the effect of surface stress on plastic deformations near the surfaces of porous structural defects. The second significant simplification is the assumption of homogeneous surface properties, while the actual surface can show significantly inhomogeneous behavior (Table 1, [28]). This approximation may result in some differences between MD and FEM results. For example, Fig. 3(b) and (d) show similar general behavior, but different shapes of stress distributions. This difference is the result of the approximation of a homogeneous {1 1 0} surface – the surface stress, in this case, is clearly underestimated. While the current implementation captures with considerable accuracy the most important effects induced by surface stress, the problem of adverse behavior can be overcome by incorporating, for example, an anisotropic surface model.

The cubic void has sharp edges and vertices where the crystal faces have sharp transitions. In MD simulations, these transitions are obviously less sharp as the atoms at the edges and vertices re-arrange minimizing the surface energy and, hence, smearing the corners. This creates more pronounced differences at the edges due to the atomic level changes in the MD geometry and the smooth transition of surface properties at these edges implemented in the surface stress model in FEM. In addition, the stress calculated from the FEM surface stress model is assigned to an infinitesimal surface layer (with simulated

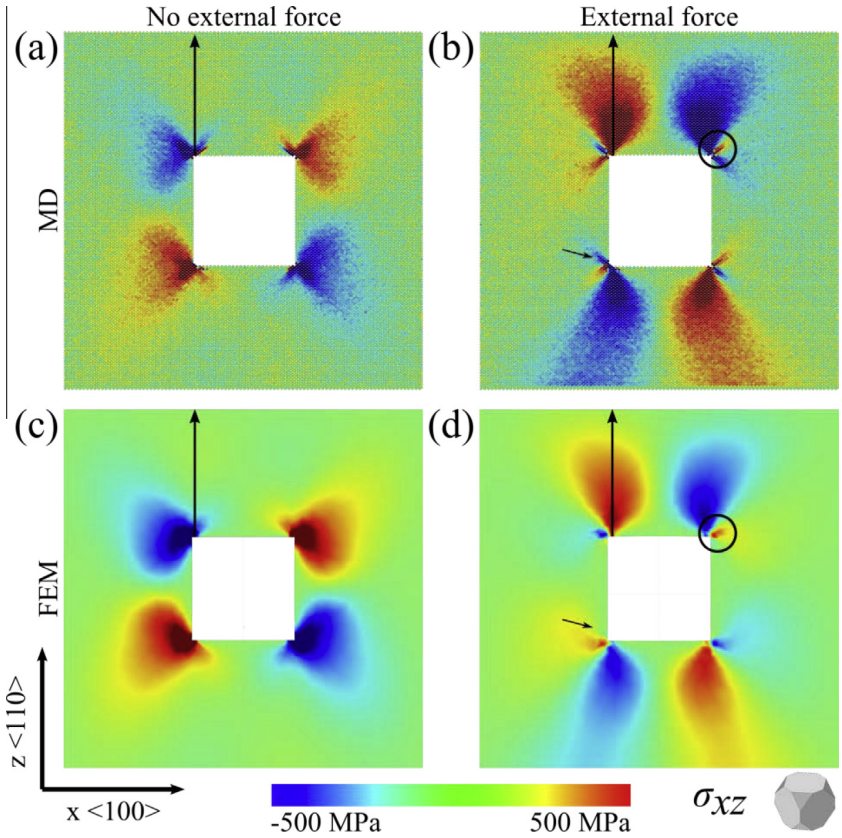

Fig. 4. Middle cross-sections of the σ_{xz} distribution in MD simulations (top row) and finite element (bottom row) simulations, without (left column) and with external force applied (right column) in case of a cut-cube void. The *xz* component of the stress tensor is shown in the *xz* plane. The main differences between MD and FEM results are marked by small circles and arrows. The black arrows show the lines from the point of the highest stress at the void surface to the surface of the material. Along these lines the data was collected for the plots in Fig. 6.

finite thickness *d*), while in MD simulations the stress is calculated from the atomic interactions, which allows for smooth extension into the material.

The large internal stresses near the edges and vertices of the cubic void simulated in MD yielded the nucleation of partial dislocations. This process was difficult to capture in the FEM model as only elastic deformations were accounted. However, since this shape is thermodynamically rather unstable and serves a purpose of analysis of contribution of different faces in the surface stress, we avoid the comparison of the $_{xz}$ and $_{yz}$ stress tensor components obtained in MD and FEM simulations. External stress reduces the surface stress on the void surface and the dislocations recede in the stressed system. This effect is reduced in the following geometries, since the sharp vertices causing excessive stress concentration are removed. As such, the other void geometries did not yield any dislocations, so the comparison of the stress distributions in those sections can be performed.

3.2. Cut-cube void

The second simulated geometry – the cut-cube void removes sharp stress concentrating corners of the previous, cubic void and moves towards the spherical shape presented in [33]. Since the geometries are similar, the discussion of the cubic void stress distribution in the *xy* plane applies in large extent also to the cut-cube void in the *xz* plane. When the system was simulated without external stress, we see a rapid change of sign of σ_{xz} near the edges of the void (in Fig. 4(a), the corners of the void cross section). This effect is also present in FEM results, but cannot be seen in the Fig. 4(c) for the same reason as in Fig. 3. When external stress is exerted on the surface of the material, the surface stress is reduced and this is clearly seen in both MD and FEM results (Fig. 4(b) and (d)). In fact, the extended areas of the stress distribution, seen in the unstressed systems in Fig. 4(a) and (c), shrink to the narrow areas almost the size of small lines (only one is marked by circles in both Fig. 4(b) and (d)). When the external stress is applied to the material surface the stress around the corners changes direction

compared to the unstressed system (the stress tensor component $_{xz}$ has an opposite sign, compare Fig. 4(a)–(d)). The FEM model captures well the sign changes as the external stress is applied. On the other hand, the stress distribution created in the presence of the external stress extends beyond the corners of the cross-section in MD simulations, as marked by the arrow in Fig. 4(b). This extension is not seen in FEM results, which is also a result of the simplifications used in the current model. However, this effect arising at sharp edges and vertices is not relevant in many calculations as these features would not appear naturally due to surface energy minimization.

3.3. Dodecahedral void

The case of the dodecahedral void in Fig. 5 confirms that the FEM surface stress model is able to capture the stresses due to the void surface as well as their interaction with the applied external stress. However, while the general behavior between FEM and MD remains the same, especially if external loading is considered, the approximations when constructing the surface stress model lead to some differences in the bulk stress distribution without external loading. This difference arises as the crystal faces which are not defined in the model and are approximated collectively as {1 1 2} faces come to dominate the void surface. Since the shape of the dodecahedron was chosen as a geometrical approximation of a spherical void to test the surface stress model, the discussed discrepancy found in the stress distribution is rather of little importance as the surfaces with undefined crystal faces are energetically unfavorable and rarely appear in real systems. The accurate quantitative prediction of surface stress around unusual surfaces requires incorporation of more crystal faces than currently present in Table 1. However, for many cases, especially, if large uniform surfaces with unknown crystal faces are not present, the used approximation is sufficient. The method is also useful for a qualitative description of the processes, such as estimating the effect of stress concentration of modeled void(s) before conducting MD simulations.

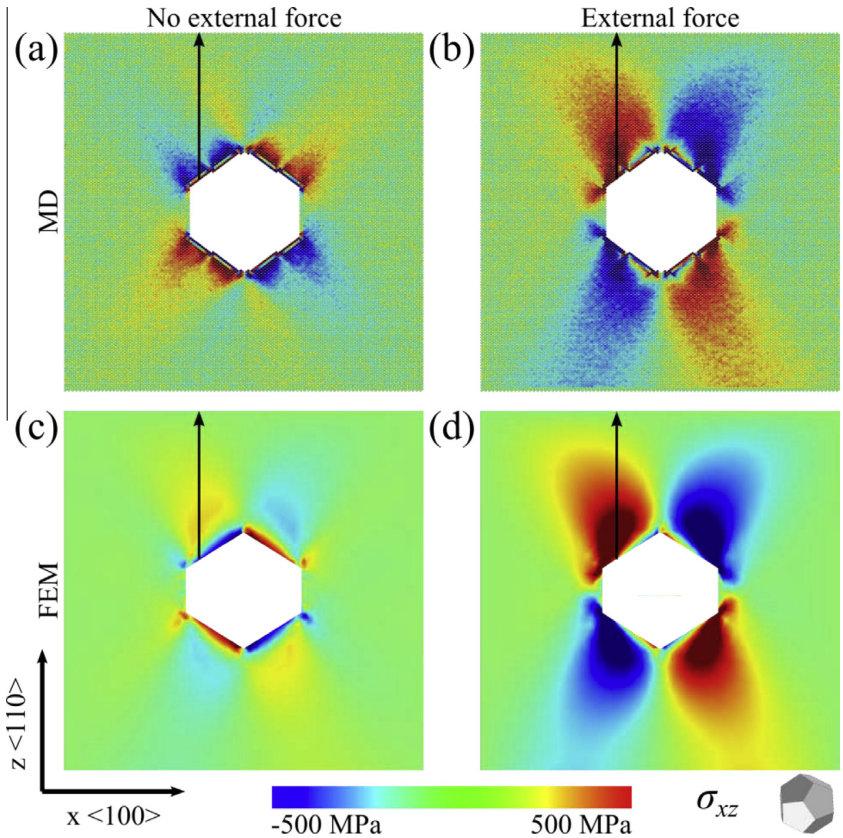

Fig. 5. Middle cross-sections of the shear stress distribution in MD simulations (top row) and finite element (bottom row) simulations, without (left column) and with external force applied (right column) in case of a dodecahedral void. The *xz* component of the stress tensor is shown in the *xz* plane. The black arrows show the lines from the point of the highest stress at the void surface to the surface of the material. Along these lines the data was collected for the plots in Fig. 6.

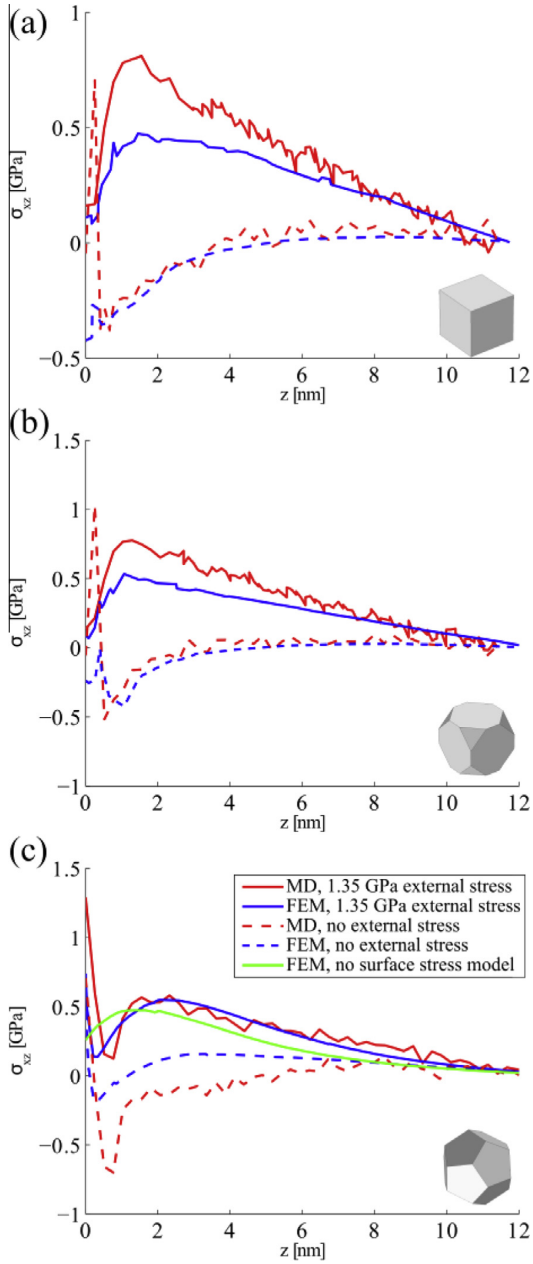

Fig. 6. Shear stress *xz* component distribution on a line between the void surface and the surface of Cu for the (a) cubic, (b) cut-cube and (c) dodecahedral void. The horizontal axis is the distance from the surface of void. Solid green line shows the stress distribution in FEM results with external stress, without taking into account the surface stress model. (For interpretation of the references to colour in this figure caption, the reader is referred to the web version of this article.)

3.4. Quantitative comparison

A quantitative comparison of the simulations is obtained by plotting the stresses along a line starting at the void surface and ending at the free surface, as shown in Fig. 3 by the circle marking its position and in Figs. 4 and 5 by the black arrows. The plots for the *xz*-component of the stress tensor are presented in Fig. 6. Three graphs are given for the cubic (a), the cut-cube (b) and the dodecahedral (c) voids. The horizontal axis measures distance from the void surface. The FEM results are

Table 2
Calculation times for MD and finite element simulations.

Void shape	Cube	Cut-cube	Dodecahedron	
MD (core-hours)	937	851	841	
FEM (core-minutes)	2.3	2.5	62[a]	23[b]

[a] With surface stress model.
[b] Without surface stress model.

drawn in blue and the MD results in red. The results for the system with no external stress are drawn with dashed lines and those for a stressed system with solid lines. In addition, the solid green line in Fig. 6(c) shows results for the externally stressed FEM system in which the surface stress model was disabled.

The surface stress model captures the general behavior of the reference MD stresses for all presented cases. The stress in the surface layer of the void has a large positive value, which quickly decreases, as seen from the red MD lines on the graph, just like in case of the cube, cut-cube and dodecahedron cross-sections (Figs. 3–5). In Fig. 6 it can also be seen that the FEM surface stress model includes this effect, even though it was not visible in the FEM cross-sections. Dashed lines in Fig. 6(a) and (b) show that the FEM model captures the stress distribution in the material in the case without external stress accurately by demonstrating excellent agreement with the MD calculations. The plotted stress in both FEM and MD cases gradually vanishes as the distance from the void surface increases. Differences arise between the FEM and MD results in the case with the external stress in Fig. 6(a) and (b) and the unstressed case in Fig. 6(c). As discussed previously in Sections 3.1–3.3, these are caused by the approximate representation of the elastic properties of the surfaces which are not explicitly described by the data in Table 1 but calculated with the smoothing algorithm presented in [33] and Eq. (8).

In the absence of the surface stress model, the stresses near the void deviate substantially from MD results both with and without external stress. If external stress is not applied, zero stress distribution is obtained in FEM calculations, which is not true for actual material behavior. On the other hand, if the external stress is present, the stress distribution is closer to the distribution obtained in the MD simulations (see the green line in Fig. 5). The use of the surface stress model is particularly important in the regions very close to the void surface (up to 2 nm). Beyond this distance even the original FEM model which does not account for the surface stress shows the same distribution of the stress in the material as in MD.

Besides the data presented in Figs. 3–6, we investigated the stress distribution in a diagonal cross section, passing through the vertices of the cubic void and the cuts of the cut-cube, by rotating the *xz*-plane by 45 degrees around the *z*-axis. The stress comparison between FEM and MD showed good agreement as in previously presented cases.

3.5. Calculation times

The calculation times for all simulations are given in Table 2. In the case of MD simulations, the times are for the complete simulations, including the periods of relaxation, ramping and averaging the internal stress. In the FEM case, the times are the sum of two runs with and without external stress. In both cases, these are the calculation times necessary to obtain the full set of results presented previously. The MD simulations were performed on a cluster using 128 Intel Xeon 2.6 GHz E5–2670 cores, while the FEM calculations were run on a PC with 4 Intel Core i7–3770 3.4 GHz cores.

The times for MD simulations practically do not depend on the system geometry. Most of the time is consumed by the calculation of interatomic forces and atomic stresses. In the absence of atomic stress calculation, the time required for MD simulations is 1.5 times shorter. The calculation time of the dodecahedral void in FEM is larger than that for other void shapes because in this case the mesh had to be refined to retain acceptable accuracy. From these simulations we can also see that neglecting the surface stress effect speeds up FEM calculations by about three times due to decreased nonlinear effects. When taking into account the need of parallelization of the MD calculations, FEM simulations use up to 3×10^4 times less computing resources.

4. Conclusions

We used a surface stress model in finite element simulations to obtain improved accuracy of standard continuum mechanics FEM results in nanoscale systems. The model uses material parameters for different crystal faces from MD simulations. We compared the resulting stress distribution in the material to analogous MD simulations and simulated single crystal copper containing regularly-shaped voids with and without external stress and investigated the behavior of the surface stress model near the voids.

The surface stress model developed previously in [33] was tested now for sensitivity to different geometrical conditions and showed overall a good agreement with MD results. The resulting stress distributions in both the unstressed and stressed states capture accurately the influence of the void surfaces. Addition of external stress reduces the surface effect and this is accurately represented in the FEM results. The model works particularly well near {1 0 0}, {1 1 0}, {1 1 1} and {1 1 2} surfaces where material parameters were available. Inaccuracies occur at the other faces, which were not included in the model. However, such faces are energetically unfavorable and do not occur in real systems to a significant extent. Taking into

account at least four main crystal faces of Cu gives a much better estimation of the stress distribution behavior near the surface of voids, improving the comparison of MD simulation results and continuum FEM calculations.

Compared to MD simulations, the FEM calculations are up to 3×10^4 times faster, depending on the desired accuracy. The used surface stress model proposes good opportunities for quickly testing different material geometries before launching calculations with more precise, but computationally demanding methods.

Acknowledgements

The MD calculations were performed on the Taito cluster of the Finnish IT Center for Science. This study was supported by the "Research internationalization" program of the European Regional Development Fund, Estonian Research Council Grant PUT 57 and the national scholarship program Kristjan Jaak, which is funded and managed by Archimedes Foundation in collaboration with the Ministry of Education and Research of Estonia.

References

[1] P. Osmokrovic, M. Vujisic, J. Cvetic, M. Pesic, IEEE Trans. Dielectr. Electr. Insul. 14 (2007) 803.
[2] F. Le Pimpec, R. Ganter, R. Betemps, Nucl. Instrum. Methods Phys. Res., Sect. A. 574 (2007) 7.
[3] U. Schumann, S. Giere, M. Kurrat, IEEE Trans. Dielectr. Electr. Insul. 10 (2003) 557.
[4] N. Holtkamp, Fusion Eng. Des. 84 (2009) 98.
[5] J.W. Wang, G.A. Loew, in: Proc. Joint School RF Engineering for Accelerators, Stanford, 1997.
[6] A. Descoeudres, T. Ramsvik, S. Calatroni, M. Taborelli, W. Wuensch, Phys. Rev. ST Accel. Beams 12 (2009) 032001.
[7] R.W. Assmann, F. Becker, R. Bossart, H. Burkhardt, H. Braun, G. Carron, W. Coosemans, R. Corsini, E.T. D'Amico, J.-P. Delahaye, S. Doebert, S. Fartoukh, A. Ferrari, G. Geschonke, J.-C. Godot, L. Groening, S. Hutchins, J.-B. Jeanneret, E. Jensen, J. Jowett, T. Kamitani, A. Millich, O. Napoly, P. Pearce, F. Perriollat, R. Pittin, J.-P. Potier, A. Riche, L. Rinolfi, T. Risselada, P. Royer, T. Raubenheimer, F. Ruggiero, R. Ruth, D. Schulte, G. Suberlucq, I. Syratchev, L. Thorndahl, H. Trautner, A. Verdier, I. Wilson, W. Wuensch, F. Zhou, F. Zimmermann, A 3 TeV E^+e^- linear collider based on CLIC technology, CERN, Geneva, 2000.
[8] H. Braun, R. Corsini, J.-P. Delahaye, A. De Roeck, S. Doebert, G. Geschonke, A. Grudiev, C. Hauviller, B. Jeanneret, E. Jensen, T. Lefevre, Y. Papaphilippou, G. Riddone, L. Rinolfi, W.-D. Schlatter, H. Schmickler, D. Schulte, I. Syratchev, M. Taborelli, R. Tomás, S. Weisz, W. Wuensch, A. Ferrari, in: F. Tecker (Ed.), CLIC-Note-764, Geneva, 2008.
[9] J.W. Wang, J.R. Lewandowski, J.W. Van Pelt, C. Yoneda, G. Riddone, D. Gudkov, T. Higo, T. Takatomi, in: Proc. IPAC'10, Kyoto, 2010, pp. 3819–3821.
[10] R.H. Fowler, L. Nordheim, Proc. R. Soc. London, Ser. A 119 (1928) 173.
[11] A. Descoeudres, Y. Levinsen, S. Calatroni, M. Taborelli, W. Wuensch, Phys. Rev. ST Accel. Beams 12 (2009) 092001.
[12] D.C. Rapaport, The art of molecular dynamics simulation, Second ed., Cambridge University Press, New York, 2004.
[13] E.B. Tadmor, Miller (Modeling Materials: Continuum, Atomistic, and Multiscale Techniques), Cambridge University Press, Cambridge, New York, 2011.
[14] A.S. Pohjonen, S. Parviainen, T. Muranaka, F. Djurabekova, J. Appl. Phys. 114 (2013) 033519.
[15] F. Djurabekova, S. Parviainen, A. Pohjonen, K. Nordlund, Phys. Rev. E 83 (2011) 026704.
[16] S. Vigonski, F. Djurabekova, M. Veske, A. Aabloo, V. Zadin, Modell. Simul. Mater. Sci. Eng. 23 (2015) 025009.
[17] A.S. Pohjonen, F. Djurabekova, K. Nordlund, A. Kuronen, S.P. Fitzgerald, J. Appl. Phys. 110 (2011) 023509.
[18] K. Nordlund, F. Djurabekova, Phys. Rev. ST Accel. Beams 15 (2012) 071002.
[19] V. Zadin, A. Pohjonen, A. Aabloo, K. Nordlund, F. Djurabekova, Phys. Rev. ST Accel. Beams 17 (2014) 103501.
[20] J. Yvonnet, H.L. Quang, Q.-C. He, Comput. Mech. 42 (2008) 119.
[21] H.S. Park, P.A. Klein, G.J. Wagner, Int. J. Numer. Method Eng. 68 (2006) 1072.
[22] M. He, S. Li, Comput. Mech. 49 (2012) 337.
[23] A. Javili, P. Steinmann, Comput. Methods Appl. Mech. Eng. 198 (2009) 2198.
[24] A. Javili, P. Steinmann, Comput. Methods Appl. Mech. Eng. 199 (2010) 755.
[25] D. Davydov, A. Javili, P. Steinmann, Comput. Mater. Sci. 69 (2013) 510.
[26] P. Sharma, S. Ganti, N. Bhate, Appl. Phys. Lett. 82 (2003) 535.
[27] L. Farrissey, M. Ludwig, P.E. McHugh, S. Schmauder, Comput. Mater. Sci. 18 (2000) 102.
[28] V.B. Shenoy, Phys. Rev. B 71 (2005) 094104.
[29] A.F. Bower, Appl. Mech. Solids, CRC Press, 2009.
[30] N.S. Ottosen, M. Ristinmaa, The Mechanics of Constitutive Modeling, Elsevier, 2005.
[31] J.S. Vermaak, C.W. Mays, D. Kuhlmann-Wilsdorf, Surf. Sci. 12 (1968) 128.
[32] D. Chapelle, K.-J. Bathe (The Finite Element Analysis of Shells – Fundamentals), Springer, 2011.
[33] V. Zadin, J. Muszynski, M. Veske, S. Vigonski, V. Jansson, S. Parviainen, A. Aabloo, K. Nordlund, F. Djurabekova, Submitted to Acta Materialia (2014).
[34] Z. Insepov, J. Norem, T. Proslier, D. Huang, S. Mahalingam, S. Veitzer, arXiv:1003.1736 [physics.acc-Ph] (2010).
[35] Http://www.comsol.com/ (n.d.).
[36] P. Deuflhard, Numer. Math. 22 (1974) 289.
[37] S. Plimpton, J. Comput. Phys. 117 (1995) 1.
[38] M.J. Sabochick, N.Q. Lam, Phys. Rev. B 43 (1991) 5243.
[39] A. Stukowski, Modell. Simul. Mater. Sci. Eng. 18 (2010) 015012.
[40] C. Rycroft, Lawrence berkeley national laboratory, (2009).
[41] H.J.C. Berendsen, J.P.M. Postma, W.F. van Gunsteren, A. DiNola, J.R. Haak, J. Chem. Phys. 81 (1984) 3684.
[42] D.H. Tsai, J. Chem. Phys. 70 (1979) 1375.
[43] A.K. Subramaniyan, C.T. Sun, Int. J. Solids Struct. 45 (2008) 4340.

IV

Computational Materials Science 146 (2018) 287–302

Contents lists available at ScienceDirect

Computational Materials Science

journal homepage: www.elsevier.com/locate/commatsci

Migration barriers for surface diffusion on a rigid lattice: Challenges and solutions

Ekaterina Baibuz [a,*], Simon Vigonski [b,a], Jyri Lahtinen [a], Junlei Zhao [a], Ville Jansson [a], Vahur Zadin [b,a], Flyura Djurabekova [a,c]

[a] Helsinki Institute of Physics and Department of Physics, P.O. Box 43 (Pietari Kalmin Katu 2), FI-00014 University of Helsinki, Finland
[b] Institute of Technology, University of Tartu, Nooruse 1, 50411 Tartu, Estonia
[c] National Research Nuclear University MEPhI, Kashirskoye sh. 31, 115409 Moscow, Russia

ARTICLE INFO

Article history:
Received 26 July 2017
Received in revised form 20 November 2017
Accepted 25 December 2017

Keywords:
Copper
Iron
Kinetic Monte Carlo
Surface diffusion
Rigid lattice
Migration barriers
Atomic jumps

ABSTRACT

Atomistic rigid lattice Kinetic Monte Carlo is an efficient method for simulating nano-objects and surfaces at timescales much longer than those accessible by molecular dynamics. A laborious part of constructing any Kinetic Monte Carlo model is, however, to calculate all migration barriers that are needed to give the probabilities for any atom jump event to occur in the simulations. One of the common methods of barrier calculations is Nudged Elastic Band. The number of barriers needed to fully describe simulated systems is typically between hundreds of thousands and millions. Calculations of such a large number of barriers of various processes is far from trivial. In this paper, we will discuss the challenges arising during barriers calculations on a surface and present a systematic and reliable tethering force approach to construct a rigid lattice barrier parameterization of face-centred and body-centred cubic metal lattices. We have produced several different barrier sets for Cu and for Fe that can be used for KMC simulations of processes on arbitrarily rough surfaces. The sets are published as Data in Brief articles and available for the use.

1. Introduction

Atomic diffusion on metal surfaces is a long term process that may induce undesirable topological modifications down to nanoscale, making these changes practically unnoticeable on large experimental surface areas which easily range from square micrometers to square centimetres. Understanding diffusion processes, including surface diffusion, becomes particularly important when dealing with applications that demand high technological precision ($\leqslant 1$ μm), such as the components of accelerating structures of the future Compact Linear Collider (CLIC) [1]. In CLIC, the accelerating structures are designed to operate for extensive times under high gradient electromagnetic fields, which present additional challenges for keeping the metal surfaces unmodified. For instance, surface diffusion enhanced by an electric field is believed to induce nanoscale surface roughening on copper parts of the accelerating structures. The roughening leads to uncontrollable appearance of local vacuum discharges, damaging the surface and increasing the power consumption, thus decreasing the efficiency of the accelerator [2,3].

It is important to note that surface diffusion may play a crucial role also on a nanoscale, in the process of shaping of growing nanoparticles. For example, in [4], we showed that in a magnetron sputtering inert gas condensation chamber, iron nanoclusters grow cubic or spherical depending on sputtering intensity through the competition between surface diffusion and atom deposition.

The evolution of surfaces is even on a nanoscale a long-term process, not easily accessible by many existing simulation models. The kinetic Monte Carlo (KMC) method was specifically developed to simulate slow diffusional processes, which take place while the system evolves towards the potential energy minimum. Unlike other Monte Carlo methods, KMC is not only able to capture the ground state of thermodynamic equilibrium, but also able to estimate sufficiently well the kinetic path and the required time of a system to move towards the ground state [5]. The latter is enabled through the residence time algorithm [6], which estimates the time needed to complete a single transition.

The physics behind the KMC model is described by the probabilities of diffusion transitions. These probabilities can be estimated via transition energy barriers. Thus, a successful KMC model relies on appropriate estimation of the energy barriers of all possible transitions in the system. The most accurate methods, thus far, involve calculations of the barriers on the fly using the dimer

* Corresponding author.
E-mail address: ekaterina.baibuz@gmail.com (E. Baibuz).

https://doi.org/10.1016/j.commatsci.2017.12.054
0927-0256/

method of finding potential transition paths on the potential energy surface [7] or applying self-learning procedures during the simulation [8–10]. Such methods usually operate off-lattice, allowing the inclusion of a large variety of possible transitions in the system, and require heavy computational resources. It is also common to use more simplified approaches for estimating the barriers, such as the approach of counting broken and newly forming bonds (the bonds before and after the transition) [11–13]. Such methods are less time consuming and easy to implement but they inevitably increase the uncertainty of the simulation results. Sophisticated mathematical techniques have been recently applied to calculate the energy barriers. Among them are cluster expansion [14,15], genetic programming [16], and artificial neural network [17–19] approaches. These methods are used to predict the energy barriers based on the local atomic environment. In [3], we presented the atomistic KMC (AKMC) model Kimocs for metal surfaces, in which we predefine the allowed transitions in the system and calculate the sets of energy barriers in advance.

Kimocs was designed to simulate evolution of nanofeatures on metal surfaces. It is clear that e.g. molecular dynamics (MD) methods are able to describe similar processes more accurately, since all the atomic configurations, which the system may have while evolving towards the energy minimum, occur naturally in MD. However, the limited time scale of MD methods does not allow to obtain any appreciable changes of a surface morphology with significant features and at temperatures well below the melting point. KMC, on the other hand, offers the possibility to reach rather long time scales with reasonable computational costs, provided that all the atomic jumps are described within the rigid lattice framework.

Since Kimocs was developed with the aim of simulating the temporal evolution of large nanofeatures, it was crucial to employ a parameterization scheme, which is both efficient and sufficiently accurate. We adopted the rigid lattice approximation, which describes an atomic system with all atoms occupying well defined positions in a given crystal structure. Within the rigid lattice approximation, a local atomic environment can be described by a finite number. Although, the rigid lattice approximation has inevitable intrinsic limitations (for example, if surface reconstruction is expected to occur during the process simulated by KMC on a rigid lattice, such process will not be taken into account), it is an efficient approximation to develop fast algorithms that are minimizing computational costs.

In Kimocs, we constrain the transitions in a system to atomic jumps into vacant lattice sites, which we will henceforth call vacancies. The jumps may happen on the surface as well as in the bulk.

The use of a rigid lattice and the limitation on the variety of transitions make it possible to precalculate the sets of barriers for each material (Cu and Fe in this work). Precalculation of the barriers allows us to reach the desired efficiency of the simulation algorithm that only needs to assign tabulated barrier values to atomic jumps in this case. To assure the accuracy of calculated barriers we use the Nudged Elastic Band method. Although such a parameterization scheme seems to be straightforward and easy to implemented, we faced a number of challenges, which are difficult to circumvent.

In this article, we will focus on the calculations of energy barriers for AKMC models with a rigid lattice. We will discuss the challenges of the rigid lattice parameterization and how these challenges can be overcome in order to precalculate the migration energy barrier sets. We will present the tethering force approach, which allows to create nearly complete sets of barriers for all possible transitions on a rigid lattice. We are using this approach together with the parameterization scheme of the Kimocs model, but it is applicable for any other parameterization scheme in a rigid lattice, where possible transitions are restricted to a certain type, e.g. first nearest neighbour jumps in face-centred cubic (FCC) lattices (as is the case in Kimocs).

The structure of this paper is as follows. In Section 2, we provide some details of our KMC model Kimocs and parameterizations that have been used with it earlier. In Section 2.3 we describe the challenges that arise when migration barriers are calculated on a rigid lattice of FCC and BCC structures. In Section 2.4 we present the possible solutions to circumvent the problems described in Section 2.3 and introduce the tethering force approach (Section 2.4.2), which allows for calculations of the barriers on semi-rigid lattice, restricting the freedom of surface atoms to relax far away from they positions on a rigid lattice. In Section 3, we present different sets of migration barriers and discuss the limitations of each set along with the limitations of the Kimocs parameterization approach in general. In Section 3.2 we concentrate specifically on the sets where tethering is used and how this approach affects the KMC simulation results. Finally, we summarize our conclusions in Section 4.

2. Methodology

2.1. Atomistic Kinetic Monte Carlo on a rigid lattice

Before describing the challenges, which we encountered during the parameterization of our AKMC code Kimocs [3] for simulations of surface diffusion processes, we will briefly outline the basic principles of a rigid lattice AKMC model in general and describe in detail special features of our Kimocs code. In an AKMC algorithm within the rigid lattice approximation, a diffusion process proceeds via atomic jumps to a neighbouring vacancy. The event, which includes the choice of an atom to jump and the jump itself, is selected randomly, but with respect to the magnitude of the corresponding transition rates, which are compared for all events. This way, more probable events occur more frequently. The transition rates for all events in the system are calculated according to the Arrhenius formula for thermally activated processes:

$$\Gamma = \nu \exp\left(\frac{-E_m}{k_B T}\right), \tag{1}$$

where ν is the attempt frequency for the transition to occur, k_B is the Boltzmann constant, T is the temperature of the system, E_m is the migration energy barrier, which the atom needs to overcome in order to move from one lattice site to another. For simplicity, ν is considered to be the same for all the transitions.

In Kimocs, the possible jumps in the system are restricted to primarily 1nn jumps in FCC and BCC materials, but 2nn jumps may also be allowed if necessary.

We precalculate the full set of the migration energy barriers, E_m, for all possible 1nn (and 2nn for BCC) jumps in the system to reduce the computation costs of simulations. The parameterization of the E_m barriers is done within the 1nn and 2nn shell. Taking into account only the atoms in the nearest neighbourhood would result in insufficient accuracy, since the interaction with the atoms in the 2nn position is also quite strong in both FCC and BCC lattices.

Using both 1nn and 2nn shells in the parameterization scheme allows us to reach higher accuracy but leads to the full 26 (20 in BCC) neighbouring atoms description, which we will further refer to as the 26D parameterization scheme. In this scheme, if all barriers are to be calculated, then even in a mono-elemental metal $\sim 2^{26}$ barriers are needed.

The original more approximative parameterization scheme of Kimocs uses only four parameters to describe events and we will therefore refer to it as the 4D parameterization scheme. Within this scheme, each jump event is represented by four numbers,

(a, b, c, d), listed in the order of the number of 1nn (a) and 2nn (b) atoms of the initial configuration of the jumping atom and the corresponding numbers (c and d) for the final vacant lattice site. The number of neighbours of the final vacancy is counted by assuming that the jump has not yet occurred, that is the jumping atom itself is included in c. It could also be illustrated as $a, b \rightarrow c, d$. A single permutation (a possible arrangement of neighbouring atoms and vacancies of the jumping atom, see example in Fig. 16) is chosen to represent all possible permutations for the given combination of the numbers (a, b, c, d). Thus, the corresponding migration barrier of such an event, $E_m(a, b, c, d)$, is a function of four parameters. An example of an event description in the 4D approximation is shown in Fig. 1. Such an approach significantly reduces the set of necessary barriers down to ~5000 for FCC and ~2000 for BCC lattice structures.

If for some reason no barrier could be calculated for a particular (a, b, c, d) combination, Kimocs assigns to this process a default near-infinite value (100 eV has been found to be enough), which will give a near-zero probability for the process to occur. This way we can forbid some improbable processes to occur.

The time evolution is an important aspect of a KMC model. The parameter that affects the time predicted by the calculated transition rates is the attempt frequency. In our parameterization scheme, we fit the attempt frequency to the MD simulations by comparing the flattening time of a surface nanotip as calculated by both KMC and MD (see details in [3]). In this manner, we obtain a sufficient accuracy for the time scale of our KMC simulations.

2.2. Nudged Elastic Band method

A key importance for any KMC model is the accuracy of migration energy barriers, which would allow to follow the correct kinetic path of the system towards the equilibrium. For systematic calculation of the actual values of the energy barriers for atomic jumps, we used the nudged elastic band (NEB) method [20–22] with semi-empirical potentials. The general algorithm we used for the calculation of a migration energy barrier with the NEB approach can be summarized as follows:

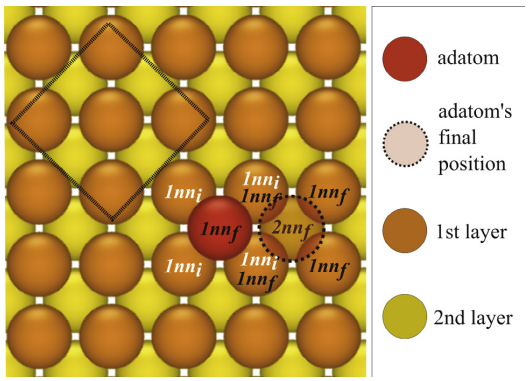

Fig. 1. Illustration of a (4,1,5,1) 1nn jump on a {1 0 0} FCC surface in Kimocs. Two surface layers are shown: top layer with orange circles and the layer below with yellow circles. The adatom (red circle) performs a jump from the site with four 1nn atoms and one 2nn atom (the atom right below the jumping atom) to a site (dashed semi-transparent circle) with five 1nn (including the jumping atom itself) and one 2nn atom below it (marked with $2nn_f$). The number of neighbours of the final vacancy is counted with the assumption that the jump has not yet occurred, that is, the jumping atom itself is included in c. To guide the eye, the FCC unit cell is shown with a square. (For interpretation of the references to colour in this figure legend, the reader is referred to the web version of this article.)

1. Relaxation stage: during this stage both the initial and final configurations of the event are relaxed towards the energy minimum.
2. Initial guess of the minimum energy path (MEP): usually, as an initial guess of MEP, the interpolation path from the relaxed initial position to the relaxed final one is chosen to be a straight line.
3. Relaxation of the interpolated path: initial energy path is relaxed towards MEP by using the NEB algorithm with MD and semi-empirical potentials.

For all the barrier sets for Cu surfaces mentioned in this article, we used the interatomic potential based on the Corrected Effective Medium Theory (CEM), developed by Stave et al. [23]. The potential describes well the properties of Cu surfaces [24]. The surface energies given by the CEM potential are in good agreement with both DFT calculations and experiments. The EAM potential developed by Mendelev et al. [25] was used for the barriers to describe the diffusion processes on Fe surfaces. Mendelev potential predicts well the general trend of surface energies of different surface orientations and vacancy formation energy [26], which was important for the studies in [4].

The energy barrier is found from the relaxed MEP as a difference in the potential energies of the initial configuration and the configuration at the saddle point. The different examples of MEP on potential energy surface profiles obtained with the NEB method are shown in Fig. 2. In the case of a symmetric jump (Fig. 2a), the potential energies of both the initial and final configurations are the same, thus the forward and reverse jumps have identical barriers and both events cause no change in the total potential energy. Such a case is rather specific and mostly, the barriers are asymmetric with respect to the potential energies in the initial and final configurations. If the final configuration has lower potential energy, the barrier towards it is also lower than the reverse one (see Fig. 2b). These barriers ensure that the more energetically favourable states are prioritised and the whole system evolves towards the potential energy minimum.

The barriers shown in Fig. 2a and b illustrate the processes that do not pose any problems in calculations with NEB. In this work we would like to focus on less clear situations, such as shown in Fig. 2c and d, which appear unavoidably during surface diffusion in a rigid lattice.

2.3. Challenges in barrier calculations on a rigid lattice

The situations in Fig. 2c and d are not trivial to interpret due to the absence of a clear saddle point on the MEP. Fig. 2c presents the case of spontaneous relaxation of an atom from initial ($l = 0.0$ in the figure) to final configurations ($l = \sim 2.5$ Å) in a rigid lattice during the NEB calculations. In a KMC algorithm, such a process should be assigned a small barrier to ensure that it happens with a high probability and within a short time. In [3], it was proposed to avoid the exactly zero barriers and instead use the following heuristic formula,

$$E_m(a, b, c, d) = \epsilon a + \delta b + \epsilon c^{-1} + \delta d^{-1} \quad (2)$$

where $\epsilon = 10^{-3}$ eV and $\delta = 10^{-4}$ eV. This formula is designed to prioritise the jumps of atoms with the fewest neighbouring atoms. It also assumes that it is more favourable for an atom to jump into a position with a higher number of neighbours. ϵ and δ are chosen so that the number of 1nn atoms contributes more into the value of migration barriers than the number of 2nn atoms.

The MEP in Fig. 2d has an even more complicated shape, making it impossible to find a barrier from it. The minimum that occurs between the initial and final configurations along the MEP show

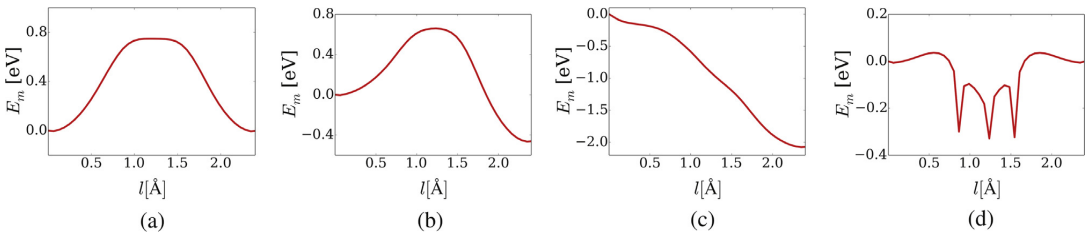

Fig. 2. Illustrative examples of minimum energy paths on potential energy surfaces for (a) a symmetric process; (b) an asymmetric process (c), a spontaneous process and (d) a process with several intermediate minima. l is the distance from the initial position of the jumping atom; E_m — potential energy (the energy reference is the potential energy at the initial position).

that there are energetically favourable positions, which are off the lattice sites, but the rigid lattice approximation prevents atoms from occupying them. For this kind of jumps, it is not straightforward whether such processes have to be completely excluded from the simulations, or allowed to happen with some probability.

It is clear that such situations may happen due to a conflict of using the rigid lattice and an attempt to take into account strong relaxation effects driven by surface tension. For instance, when the evolution of a surface is considered in KMC algorithms via atomic jumps to 1nn vacancies in well-defined lattice sites in a rigid lattice (as in our Cu studies), many configurations, which are possible due to surface relaxation effects, are not accessible. In some cases, the atoms might be inevitably forced into configurations, which are energetically unfavourable and thus, unstable. These may not occur in a real diffusion process during dynamic simulations, however, in the rigid lattice, these unstable positions may be necessary, as they provide the only path for a system to reach the potential energy minimum state. In other words, if atoms are forbidden to occupy unstable positions in a rigid lattice, it may lead a system to the unphysical "frozen" state with no stable positions available for atoms to jump to. If so, the equilibrium may never be reached. To ensure that the system continues evolving, jumps involving atoms in unstable initial or final positions, or even both of them, should also be available in a rigid lattice, although these should be assigned the barriers that are estimated using some other technique.

More specifically, we noticed that atoms in the initial or final configurations of many jump processes on rigid lattice FCC surfaces may move and change lattice sites during the relaxation stage of the barriers calculations, changing the neighbourhood configuration. In other words, the event (a, b, c, d) in the 4D parameterization scheme becomes the event (a', b', c', d') after the relaxation of the initial and final configurations and if the NEB calculations are then carried out, the barrier obtained in these calculations clearly cannot be used to describe the intended (a, b, c, d) event. We call such configurations that change during the relaxation stage as *unstable*.

An example of an unstable configuration is shown in Fig. 3a. The figure shows the configuration, which is initial for the event (2,1) → (8,1) and final for the reverse event (7,1) → (3,1) (Note, that we count the number of neighbours of the initial atom and final vacancy, i.e. a jumping atom is included in the number of 1nn of a final configurations, *c*, in both cases). In Fig. 3b, we show the configuration which is final for the event (2,1) → (8,1) and initial for the (7,1) → (3,1) event. Already during the initial relaxation stage, we noticed that the configuration in Fig. 3a turned into the configuration in Fig. 3b (the jumping atom shown with blue relaxed one monolayer down towards the higher number of neighbours). Thus, we recognize the event (2,1) → (8,1) as *spontaneous* and assign it a small near-zero barrier to ensure that this process happens at once when the initial configuration (2,1) of the process (2,1) → (8,1)

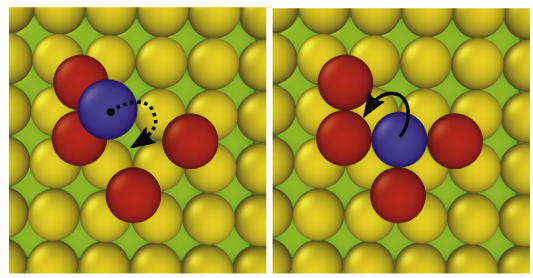

Fig. 3. Top view of (a) the unstable initial configuration of the process (2,1) → (8,1) (final configuration of (7,1) → (3,1)), (b) the initial configuration of the jump (7,1) → (3,1), which is also final of (2,1) → (8,1); yellow colour corresponds to surface atoms, red - adatoms, the jumping atom is shown with blue; in (a), the jumping atom is one monolayer above the adatoms, in (b) - on the same level; a full arrow shows a jump to one monolayer up; a dashed arrow - to one monolayer down. (For interpretation of the references to colour in this figure legend, the reader is referred to the web version of this article.)

occurs during KMC simulations. A spontaneous process can also be detected directly from the results of the NEB calculations: if the initial position has higher potential energy than the final position and the saddle point does not appear during the NEB relaxation towards the MEP (Fig. 2c).

On the other hand, the reverse event (7,1) → (3,1) in Fig. 3b should be assigned a high barrier so that this process will seldom take place in the simulations.

Such an assumption would allow to include (at least indirectly) the transitions to further than 1nn vacancy as a part of a multi-step transition. Thus the atoms, which were forced to the physically unstable positions during the first step, will relax during the next KMC step either back into the initial position or to another position, which is more stable. This issue will be discussed later with respect to the diffusion in BCC structures.

Moreover, the (a, b, c, d) event can also be modified during the NEB relaxation steps, although both initial and final configurations of the process are stable. Since the NEB algorithm forces the system towards the energy minimum at every step (see Section 2.2) — in some cases with many vacant lattice sites around the atoms (open surface, large vacancy clusters, etc.) — it may also force either a jumping atom away from its initial path or the surrounding atoms away from their initial positions, confusing the calculation of the barrier for the initially determined configuration. Fig. 4 shows an example of a transition on a void {1 1 1} surface, where the jumping atom (A) was dragged by the NEB relaxation procedure into the different final position (C) instead of the intended one (B), although both initial (A) and final (B) configurations of the intended process are stable.

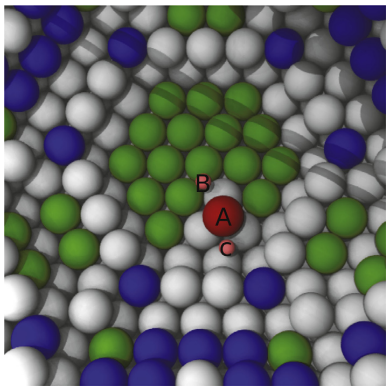

Fig. 4. Unstable process on the void {1 1 1} surface in FCC structure. Green atoms are part of the {1 1 1} surface, blue atoms are in the {1 0 0} surface, grey atoms are other surfaces. The jumping atom is red. It is set up to jump from the position A to position B, but instead it is dragged into C by NEB. (For interpretation of the references to colour in this figure legend, the reader is referred to the web version of this article.)

2.4. Possible solutions to circumvent uncertainties in barrier calculations on a rigid lattice

2.4.1. Simple model to avoid unstable configurations

In [3], we suggested a way to estimate the barriers of many unstable configurations. We assumed that all events with $a \leqslant 3$ (too few 1nn atoms) were spontaneous, since they are most likely to involve atoms in unstable initial configurations. These events were assigned barriers given by Eq. (2), regardless of the stability of the final positions. The maximum migration energy of processes with $a \leqslant 3$, which can be obtained with Eq. (2), is $E_m(3,6,1,1) = 0.0047$ eV, which is insignificant compared to even thermal energies (>0.025 eV). Most of the jumps from stable configurations to unstable ones, as (7,1) → (3,1) in Fig. 3 along with more exotic configurations as in Fig. 2d, are forbidden in this approach. However, some of this kind of processes were manually identified to cause a "frozen" state during the nanotip simulations. If that was the case, we used simplified approaches to calculate barriers of these processes: in the case if the jumps were from stable configurations to unstable ones, we performed the NEB calculations with partial relaxation of the final positions (the surrounding atoms were allowed to relax, while a jumping atom was fixed); in the case of more exotic configurations as in Fig. 2d, a barrier was either chosen as a difference between a maximum on the MEP and initial state energy or marked as spontaneous if initial state energy was the highest point on the MEP.

The use of Eq. (2) for all the atoms with less than three neighbours is not fully justified, although it was motivated by the possibility to avoid artificial scenarios. In AKMC simulations, it becomes problematic, when a small cluster of atoms with many possible processes with essentially zero barriers appears on a surface. Atoms might very well jump away in such an order that one or more atoms are left behind without any neighbours. An isolated atom, which has a zero probability to make a jump, has to be either considered removed from the system (which easily leads to the destruction of the surface) or left isolated. Either of these options is artificial as the current parameterization does not include evaporation events. Eq. (2) allows to circumvent evaporation of clusters of atoms. Nevertheless, there is still a chance that many events with ($a \leqslant 3$) might have higher barriers than given by Eq. (2). This may lead to over-relaxation of the surface: some events treated as spontaneous, need a longer time in reality before they can take place.

Although, a sufficiently large amount of barriers was eventually calculated in [3] to overcome the problem of a "frozen" state, the method of calculations was not efficient and time consuming since many of the processes were treated manually. Also the number of remaining forbidden events was still not negligible. In the next section, we present a recently developed automatized approach to calculate the migration energy barriers within the rigid lattice approximation that allows to tabulate the whole set of possible $E_m(a,b,c,d)$ barriers and minimise the use of Eq. (2).

2.4.2. Tethering force approach

Since surface relaxation effects in some cases may cause modifications of initial or final configurations during the NEB calculations of energy barriers, we deployed tethering forces on atoms to attract them towards the initial lattice positions. Thus, atoms are positioned on a semi-rigid lattice, where they are allowed to relax but only within the proximity of their initial lattice positions. This approach was specifically designed to calculate the barriers for unstable configurations and appears to be a plausible and efficient solution to the problem at hand.

The automatized scheme for barrier calculations utilizing the tethering force approach can be described as follows. To calculate the barrier, the method selects a configuration out of all permutations corresponding to the same numbers (a,b,c,d), which results in the lowest sum of the energies of the initial and final states. Since the choice of permutations is consistent, it is possible to obtain barriers for both $(a,b) \rightarrow (c,d)$ and the reverse $(c,d) \rightarrow (a,b)$ events from the same minimum energy path calculated by NEB. The energy of the system depends on the used interatomic potential, so the permutation selection process needs to be done for each potential separately.

After all configurations representing the families of different permutations are defined, the energy minimisation algorithm for initial and final positions is launched. As discussed above, some configurations, e.g. with too few neighbours, may be unstable. In our approach, we distinguish between the following different situations:

1. Both the initial and final positions minimise correctly. In this case, the NEB calculation proceeds.
2. The process is indicated as spontaneous either during minimisation or the NEB relaxation and assigned the migration energy according to Eq. (2). The reverse process is calculated as the energy difference between the initial and final states.
3. The jumping atom relaxes to some unrelated position from either the initial configuration or the final one. Alternatively, the neighbouring atoms move during the MEP calculations, resulting in a modified (a',b',c',d') event compared to the intended (a,b,c,d). In this case, we do not obtain the barrier for the (a,b,c,d) event. Moreover, the new event (a',b',c',d') cannot be identified either.

The processes described by the situation 3 are rather unlikely to happen on real surfaces, but inevitable in the rigid lattice approximation. These also present the biggest challenge in the calculation of the barriers. To address it, we use the tethering force approach. During minimisation, an additional spring tether is applied to all atoms in a simulation box. This spring attracts atoms to the lattice sites, where they belong. Depending on the strength of the spring tether, the atoms can deflect from their initial sites more loosely or more rigidly. In this manner, all the barriers, including the barriers for unstable configurations, may, in principle, be calculated.

Furthermore, we noticed that during the NEB relaxation, as the path of the jumping atom converges towards the MEP, the surrounding atoms sometimes also change their positions. These situations are particularly difficult to detect. Even though the initial and final states are relaxed (or tethered and relaxed), the potential energy landscape on the surface can favour different intermediate positions for the atoms. As a result, the energy values fluctuate along the path and extra energy minima occur (see Fig. 2d). It becomes unclear how to define a saddle point for such MEP. To reduce this effect, we apply tethering also during the NEB calculations. The spring in this case tethers the neighbouring atoms in each NEB image to their initial and final positions.

The tethering spring force complements the NEB spring force, which binds the atoms between images. The energy contribution from the tethering force is not included in the energy landscape and migration barrier calculation. However, the energy landscape is affected indirectly because tethering affects the positions of the surrounding atoms. In this way, the effect of the tethering force on migration barriers is minimized (see Section 3.2). Tethering is not used on a jumping atom, thus allowing it maximum freedom of movement to find the MEP. However, even with this approach there are processes with minimum energy paths similar to Fig. 2d. This issue will be addressed in Section 3.2.

Tethering force approach also allows to overcome the problem shown in Fig. 4, when a jumping atom is dragged by NEB into a position, which is different from the intended one.

We chose a constant value of the tethering force in such a way that it allows to increase significantly the number of barriers (including unstable configuration events) that can be calculated in a consistent manner. On the other hand, as the tethering force implicitly affects the migration barriers (see Fig. 11), it is advisable to use the lowest working force constant.

A number of stable and unstable configurations were chosen to test different tethering constants for copper with the CEM potential. Initial/final state minimisations and NEB calculations were performed with the tethering parameter values 0.0, 0.35, 0.5, 1.0 and 2.0 $eV/Å^2$. We found that all the values up to 1.0 $eV/Å^2$ are not sufficient to hold unstable atoms from relaxing to unrelated positions. With tethering parameter 2.0 $eV/Å^2$, all barriers were calculated successfully and the barriers for the event involving stable positions were also still reasonably close to the barriers calculated without tethering force (see Section 3.2 for details). Thus, the tethering parameter for Cu was chosen to be 2.0 $eV/Å^2$.

The tethering force approach helps to overcome the challenges introduced by a rigid lattice and calculate the barriers for many unstable configurations, for example in Fig. 5. The consistency of the tethering force approach allowed us to develop a framework for efficient barrier calculations in a rigid lattice. To produce a set of barriers for Kimocs simulations within the 4D parameterization scheme, the framework requires only an interatomic potential and the restricting parameter of how far away atoms can move from their initial positions (a 1nn distance for FCC materials). The method is not restricted to the use with Kimocs only, but can be generalized to any parameterization scheme in a rigid lattice.

In the next section, we will turn our attention to the different types of challenges that are especially important for the simulations of surface diffusion in BCC metals.

2.5. Specific challenges in parameterization of the {100} BCC surface and possible solutions

Parameterization of a KMC model for surface diffusion in BCC metals becomes challenging when a {100} surface is considered. The assumption that adatoms diffuse on the surface mostly via 1nn jumps is no longer valid. For instance, a jump of an adatom from a hollow site (on top of four surface atoms) to a neighbouring hollow site will be a 2nn jump (Fig. 6a). It has been previously seen that a diagonal exchange is one of the most probable processes on BCC {100} surfaces [27]. A diagonal exchange is a multi-step diffusion jump. In this process, an adatom dislodges a surface atom in a 1nn site and takes its place. After this, a surface atom is forced up to the surface (another 1nn jump), occupying a 3nn position with respect to the starting point of the first adatom, see Fig. 6e. Another possibility for the dislodged surface atom is to occupy a 2nn position with respect to the starting point of the initial adatom (Fig. 6b). However, this non-diagonal exchange process has much lower, but not completely negligible, probability than both a diagonal exchange and a 2nn jump [28]. In order to fully describe the diffusion on {100} BCC surfaces, all three types of processes should be included in the KMC algorithm: 2nn jumps to hollow sites, diagonal and non-diagonal exchange processes for all possible local atomic environments of the jumping atom.

In the rigid lattice description, atomic jump processes are characterized only by initial and final states of the system, the specific transition path from the initial to the final state does not play any role. Thus, we do not distinguish between the different transition paths resulting in the same initial and final states. In other words, the end result of single-atom jumps and concerted (exchange) jumps looks the same in Kimocs: like only one atom changed place. Diagonal and non-diagonal exchange processes will thus appear as effective 3nn and 2nn jumps, respectively, of the initial adatom in a rigid lattice (Fig. 6d and a, respectively). Thus, the rigid lattice parameterization scheme of BCC {100} surfaces should be extended to the 3nn coordination shell and include the distinction between the direct and the exchange jumps. This task turns out to be exceptionally demanding as the computational costs of a KMC algorithm increase with the increasing number of possible jumps in the system and as barriers must be calculated for all three types of jumps described above for various configurations.

Kimocs does not explicitly include the description of exchange processes, but an exchange process may effectively happen via two consecutive 1nn jumps: first, a surface atom below the jumping adatom breaks out of the surface layer and becomes an adatom itself. Then, the two adatoms with equal probability can fill in the formed vacancy in a spontaneous jump (see Figs. 6c and f). For this to occur, the surface atom must first overcome a barrier to occupy the 2nn or 3nn position with respect to the "jumping adatom". If these barriers are calculated directly by NEB for either process (to 2nn or 3nn positions), they are much higher than the barriers calculated for the processes of the dislodging of the surface atom by the jumping adatom. One of the solutions, which can be suggested to address this problem, is to lower the barrier artificially for those surface atoms which are close to the adatoms, but in that case artefacts may appear for some other permutations corresponding to the same numbers describing the event. At the same time, the direct 2nn jump can easily fit within the 4D parameterization scheme adopted in *Kimocs*. This only requires an additional step to distinguish between 1nn and 2nn jumps, while the event description numbers (a, b, c, d) can be used for both.

In the diagram shown in Fig. 7 we summarise the challenges, which arise from the use of a rigid lattice approximation to simulate surface diffusion processes and the solutions which can be used to circumvent the problems related to strong relaxation processes on the surface.

2.6. Sets of migration energy barriers

We used the approaches to circumvent the problems related to surface migration barrier calculations (see Section 2.4) in different Kimocs parameterization tables, referred hereafter as *Sets*. Here we

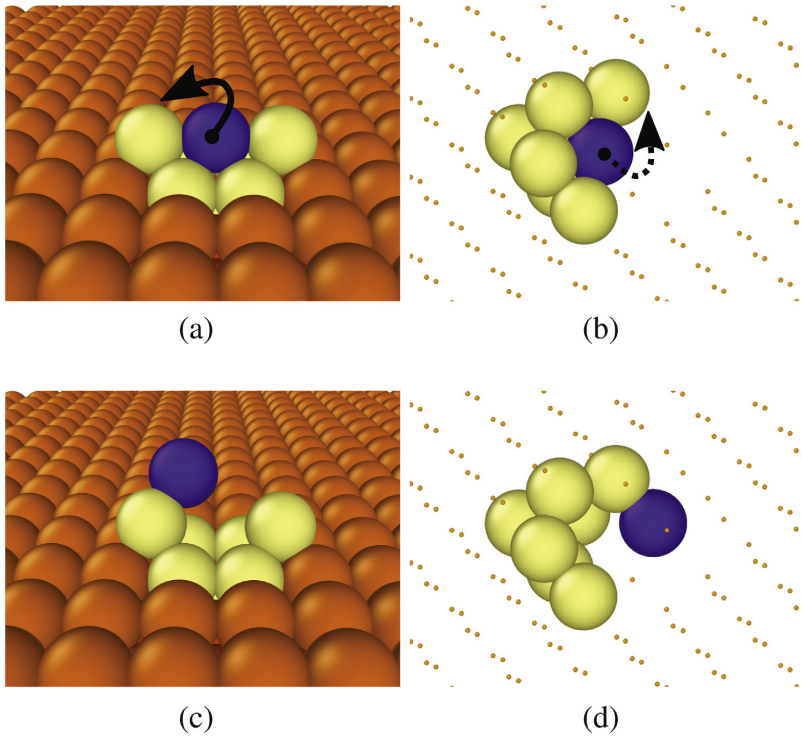

Fig. 5. Example of a configuration on the surface that required the tethering force to enable the calculation of the barrier of an atom shown with blue colour to jump from the position (a) to the position (c). (b) and (d) show the arrangement of atoms corresponding to the same process but inside the bulk. 1nn and 2nn atoms of the jumping atom before and after the jump are shown with yellow colour. Orange atoms correspond to those outside the 2nn shell of the jumping atom (shown with small dots in the bulk pictures). Arrows emphasize that an atom jumps to the 1nn positions one monolayer up (full arrow) or down (dashed). (For interpretation of the references to colour in this figure legend, the reader is referred to the web version of this article.)

present and analyse four sets of barriers: *Cu Set 1*, *Fe Set 1*, *Cu Set 2* and *Cu Set 3*. The full sets of copper and iron barriers are submitted along with this article as Data in Brief entries and can be found in [29,30], respectively. The sets can be used for simulations with Kimocs or other similar codes, which parameterize atomic jumps in the rigid lattice with the number of neighbours of a jumping atom before and after the transition (e.g. [31,32]). For the reader's convenience, we summarize below the ways of how the different sets were calculated and give more technical details.

2.6.1. Cu Set 1

The first set, *Cu Set 1* [29], was calculated as described in Section 2.4.1. More specifically, we did not apply a tethering force or other restrictions during the NEB calculations and some barriers were identified as spontaneous, while some were forbidden. *Cu Set 1* was successfully used to simulate the Cu surface self-diffusion in [3]. In this table, permutations were defined at random on {100}, {110}, {111} surfaces or a bulk system with a random distribution of vacancies. This set includes the barriers for 4289 (a, b, c, d) events, most of which were calculated in the bulk. Among these, 2486 events with $a \leqslant 3$ and only 190 events with $a > 3$ were classified as spontaneous and assigned the barrier values according to Eq. (2). The NEB calculations were done using the MD code PARCAS [33–35]. We used the approach described in [36] for the calculation of the additional NEB spring force between the images. A sequence of 40 images was used for every jump. The initial and final images were relaxed with the conjugate gradient method and then fixed during the NEB calculations. The attempt frequency was fitted to MD simulations of the flattening time obtained for Cu surface nanotips (see [3] for further details). The obtained value of the attempt frequency, $\nu = 7 \cdot 10^{13}\ \mathrm{s}^{-1}$, compares well with the Debye frequency for Cu, $\nu_D = 4.5 \cdot 10^{13}\ \mathrm{s}^{-1}$ [37–40].

2.6.2. Fe Set 1

The second set, *Fe Set 1* [30], includes 1760 barriers, most of which were calculated in the bulk, for 1nn jumps with 214 barriers assessed by using Eq. (2). Barriers for jumps on the {100} and {110} surfaces were calculated separately and are prioritised in the set. The same scheme that was used for *Cu Set 1* was utilised for *Fe Set 1* as well, although here we did not assume the events with too few neighbours in the initial configuration to be spontaneous. Instead, all the barriers for the range of events with $a \leqslant 8$ were calculated directly. The table of 1nn jumps was complemented with the 16 (a, b, c, d) barriers for the direct jumps of adatoms to a vacant 2nn site on the {100} surface (these barriers for 2nn jumps are combined to *Fe Set 2NN* [30]). *Fe Set 1* and *Fe Set 2NN* have been used in [4], where the attempt frequency for all events was assumed to be $\nu_D = 6 \cdot 10^{12}\ \mathrm{s}^{-1}$ [41]. In [30], we also provide the set of exchange processes, *Fe Set Exchange*, on the Fe {100} surface.

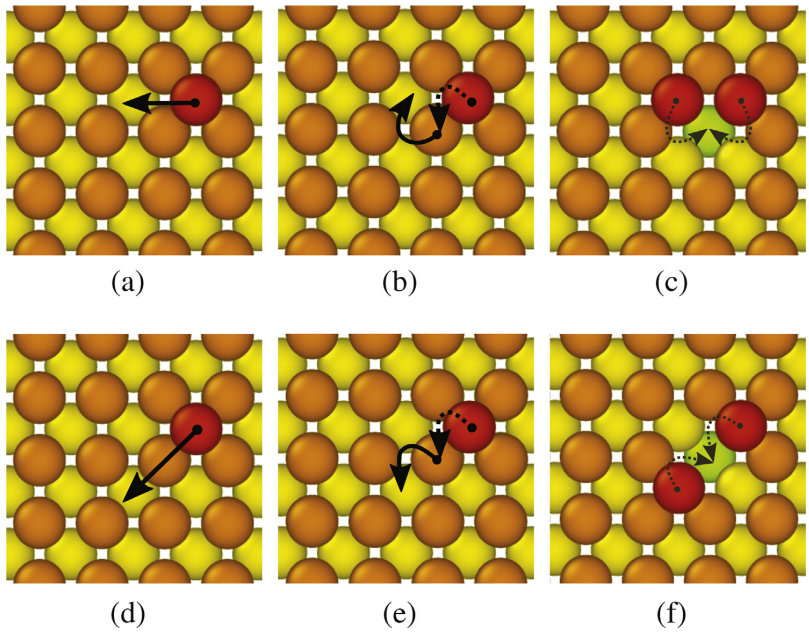

Fig. 6. Illustration of the 2nn (non-diagonal, (a)) and 3nn (diagonal, (d)) jump on the BCC {100} surface, which may take place effectively via an exchange process on a rigid lattice. (b) Illustrates the completion of the non-diagonal jump and (e) the completion of the diagonal jump; (c) and (f) show two possible 1nn jumps that might follow the first 1nn step of the non-diagonal and the diagonal exchange process in Kimocs (see the main text for details). Adatoms are shown with a red colour; straight arrows show jumps within the same monolayer; full curved arrows show jumps to one monolayer up; dashed curved arrows show jumps to one monolayer down. (For interpretation of the references to colour in this figure legend, the reader is referred to the web version of this article.)

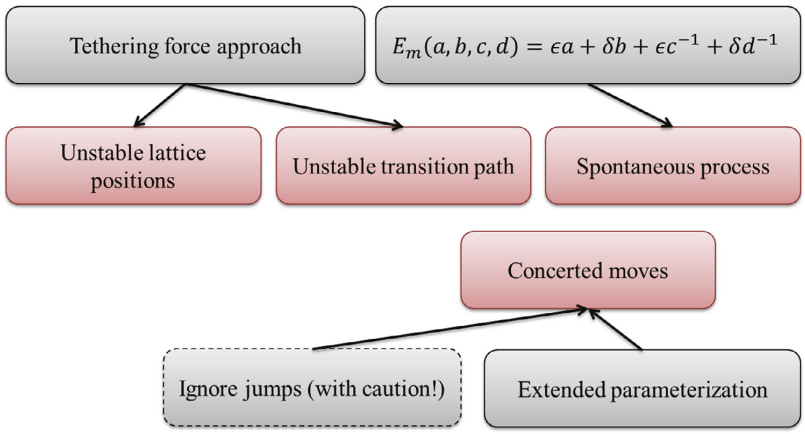

Fig. 7. Diagram of challenges (in pink) and solutions (in grey) discussed in this work. The tethering force approach helps to overcome problems of stabilization both in initial and final positions and in transition paths of the jumping atom. For spontaneous processes, Eq. (2) is used. To take account of concerted moves, a different parametrization scheme would have to be developed. (For interpretation of the references to colour in this figure legend, the reader is referred to the web version of this article.)

2.6.3. Cu Set 2 calculated with the tethering force approach

Cu Set 2 [29] was generated utilizing the tethering force approach, as was discussed it Section 2.4.2, and was thus generated in a more rigorous and systematic way than *Cu Set 1*.

Here, the $E_m(a,b,c,d)$ barriers were first calculated for the hop-on jumps of an adatom on {100}, {110} and {111} Cu surfaces as we were interested in these surface orientations for simulations of nanotips. By hop-on jumps of an adatom we henceforth mean the events where the adatom jumps within the first layer above the surface having its 1nn and 2nn atoms constrained to the same layer of adatoms and below. For configurations (a,b,c,d) that were available on more than one surface, the barrier for the {111} surface was prioritised, followed by the {100} surface, with the {110} surface as the lowest priority. This ordering is based on the surface energies for Cu [42], with the lowest surface energy taken as the most important. Barriers that were not available on

any surface, i.e jumps with a large number of neighbouring atoms in the initial and final configurations that included many atoms in unstable positions on the surface (see an example in Fig. 5c and Fig. 3) were calculated in the bulk. Clusters of vacancies were built around a jumping atom in the bulk (see an example in Fig. 5), which was periodic in the x and y directions, but not in the z direction. The vacancies were created so that the number of neighbours of the jumping atom corresponded to the given (a, b, c, d) combination in order to mimic the surface (a, b, c, d) event, since the permutations of vacancy positions are not taken into account in the 4D parameterization scheme approach. This set of barriers, calculated using the tethering force approach, we will henceforth refer to as *Cu Set 2*.

In *Cu Set 2*, the barriers were calculated both on a surface and in a bulk. The Lammps MD package [43] was used for the NEB calculations with a climbing image [22] and an additional tethering force, with the tethering force constant set to 2.0 eV/Å^2, was applied (see Section 2.4.2) and a total of 24 images were used. The energy barriers for 5103 (a, b, c, d) events were calculated in *Cu Set 2*. Only 211 barriers of jump event with $a \leqslant 3$ were assessed with the use of Eq. (2); the rest of the barriers were calculated with the tethering force approach. An additional 72 processes were marked as spontaneous for processes with $a > 3$. None of the jumps are forbidden in the tethering force approach, thus *Cu Set 2* is complete. The attempt frequency value $v = 3.1 \cdot 10^{14}$ s^{-1} was again found by fitting of tip flattening time to MD results as described in [3]. *Cu Set 2* was used to reproduce the results of [3], which will be discussed in Section 3.2.

2.6.4. Cu Set 3

Cu Set 3 [29] was calculated within the 26D parameterization scheme, which takes into account permutations of the neighbours of the jumping atoms.

For *Cu Set 3*, we first calculated the barriers with many neighbours in the bulk for 334,725 random permutations of random (a, b, c, d) configurations. We noticed that some of the bulk events resulted in unphysically high barriers. Inspection of such situations showed that these barriers resulted from the negative surface stress on the void surface contracting the entire simulation box during the NEB relaxation. This problem motivated the return to the original method to calculate the barriers with too high values (>1.5 eV) on the surface. The same 1nn and 2nn local atomic environment of the jumping atom was constructed close to the surface as it was in the bulk (see an example in Fig. 5). A tethering force constant of 2.0 eV/Å^2 was sufficient to hold the atoms in their positions and only one barrier calculation failed out of more than 330,000.

Cu Set 3 is incomplete, thus we do not recommend this set for any physical simulations. For a complete 26D set, 8 million barriers would need to be calculated, which is infeasible for storage and handling during the present AKMC simulations by Kimocs. A special way to link such a large 26D set to the AKMC simulations has to be designed. Nevertheless, *Cu Set 3* is very useful for the analysis advantages and disadvantages of the 4D versus the full 26D parameterization schemes, used in other above-described sets.

3. Results and discussions

In this section we will focus on the discussion of reliability of different approaches chosen to calculate the surface migration energy barriers described above. For illustrative purpose, we plot the migration barriers for each set as a function of the difference of the number of 1nn atoms in initial and final positions, $a - c$, in Fig. 8. It is clear that many energy barriers may correspond to the same $a - c$ value. However, we can follow the variation of the barriers as a function of a gradual change of the situations: the negative values, $a - c < 0$, show barriers for the jumps from less to more stable positions (more neighbours in the final state) and the positive ones, $a - c > 0$, show barriers for the jumps from more to less stable positions (less neighbours in the final state). The colour scale corresponds to the amount of events which can be described by the same $a - c$ and E_m values.

3.1. Kinetics described by the non-tethered sets

At first, we show that even the barriers of *Cu Set 1* and *Fe Set 1*, which were calculated with the initial simplified schemes, where surface relaxation effects were approximated via events with either near-zero barriers ("spontaneous" events) or very high barriers ("forbidden" events), are able to capture the physics of surface evolution via diffusional processes on copper and iron surfaces, respectively.

We have previously shown that the results of the KMC simulations of the stability of Cu surface nanotips [3] and formation of Fe nanocubes [4], where the sets were used, agreed very well both with MD simulations and experiments. However, in the current paper we still take a closer look into the kinetics of surface events, which may not be crucial for the previous results, but still can be overlooked while using *Cu Set 1* and *Fe Set 1*.

3.1.1. Analysis of the Fe Set 1 barriers

The abundance of the calculated barriers for *Fe Set 1* can be seen in Fig. 8a. Some of the barriers (for no more than 300 events) in this set were calculated on the surface of a nanowire in order to emulate the conditions (a combination of a certain deposition rate and a temperature), where the formation of nanocubes was observed. It was found that the growth of Fe nanoparticles into cubic shapes is due to the difference in the rates of atomic jumps on {1 0 0} and {1 1 0} surfaces, which becomes more significant at low temperatures.

As the analysis of the processes happened during the nanocubes formations showed, most of the (a, b, c, d) jumps were hop-on processes on {1 1 0} and {1 0 0} surfaces. Other processes correspond to the deposition events. Thus, neither barriers calculated in the bulk nor spontaneous processes calculated with Eq. (2) played a crucial role — in contrast to the barriers calculated on {1 1 0} and {1 0 0} surfaces for stable hop-on events.

The hop-on jumps of an adatom surrounded by various numbers of 1nn and 2nn, located only in the layer of adatoms, on the {1 1 0} surface have a wide range of barriers from 0.1 eV to 1.1 eV (Fig. 9). The low barriers correspond to the simple hop-on jumps with few neighbours and the jumps towards the adatom islands. High barriers correspond to the detachment of adatoms from adatom islands. On the {1 0 0} surface, the diffusion is driven by the 2nn jumps and exchange events, as was discussed in the Section 2.5. These processes have barriers higher than 0.6 eV (for simplicity's sake, non-diagonal exchange processes on {1 0 0} surface are not included in Fig. 9, because of much higher barriers than 2nn and diagonal exchange jumps on Fe BCC {1 0 0} surface [28]). Thus, at low temperature conditions (below 1000 K), where nanocube formation was observed in experiments, diffusion of single adatoms and small nano-islands on the {1 1 0} surface is much faster than on the {1 0 0} surface. On the other hand, at high temperatures, events on the {1 0 0} surface become as probable as jumps on the {1 1 0} surface. Nanoparticles may thus grow into a close-to-spherical shape driven by the surface minimisation at high temperatures.

As it was pointed out in Section 2.5, the exchange processes were not explicitly added to the KMC algorithm. Instead, the

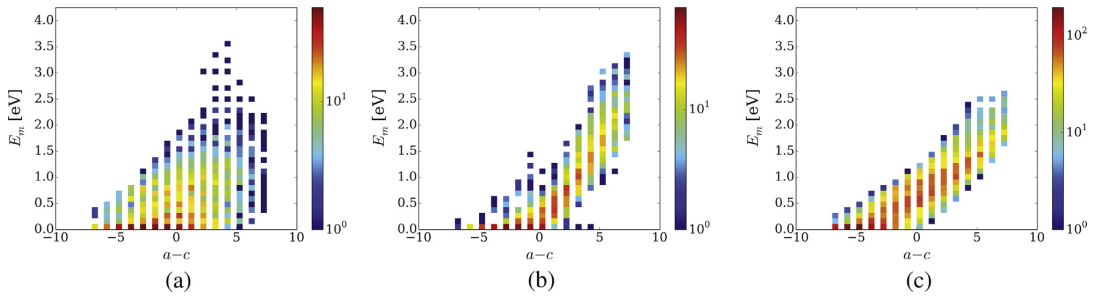

Fig. 8. Distribution of the migration energies vs. the change in the number of 1nn of the initial and final positions of the jumping atom for (a, b, c, d) jumps in (a) *Fe Set 1*; (b) *Cu Set 1* ($a \leqslant 3$ processes are not included); and (c) *Cu Set 2*. colour corresponds to the occurrence of the migration energies for certain values $(a - c)$. For simplicity, c does not include a jumping atom. (For interpretation of the references to colour in this figure legend, the reader is referred to the web version of this article.)

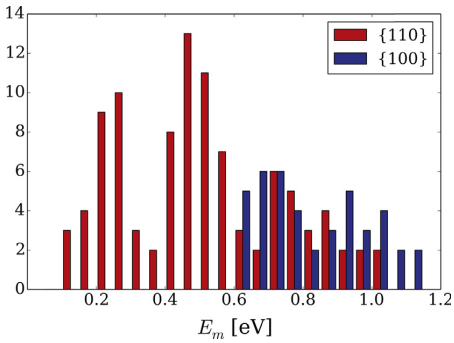

Fig. 9. Comparison between the diffusion events on {100} and {110} iron surfaces. A histogram for {110} surface includes only hop-on jumps, {100} includes the second nearest neighbour hop-on jumps and diagonal exchange processes of *Fe Set 2NN* and *Fe Set Exchange* in [30].

exchange events were treated in two steps as shown in Fig. 6. The first step of the 3nn effective jump corresponds to the 1nn $(5, 5, 4, 1)$ jump event, which is the same as for a vacancy jump inside the bulk close to the {110} surface. On the {100} surface, the $(5, 5, 4, 1)$ event has a barrier 0.72 eV, whereas a vacancy jump close to the {110} surface has a barrier of 1.65 eV. In order to avoid artificial void formation inside the bulk, we had to use a higher barrier for the $(5, 5, 4, 1)$ event in *Fe Set 1*. If so, the 3nn effective jump, which takes place most frequently during adatom diffusion on the {100} surface, was almost inaccessible in our simulations. If such a high barrier is used, the difference between the KMC and MD simulations will still appear even at high temperatures, at which the rates of diffusion on {110} and {100} surfaces become comparable. On the other hand, the rate of the 3nn effective jump at low temperatures (<1000 K) is still much lower than that of hopping events on the {110} surface (the corresponding barriers are 0.72 eV and ~0.27 eV). Within this range of temperatures, our KMC simulations agree well with MD simulations.

To verify that diagonal exchange jumps are not accessible at low temperatures also in MD, we calculated the barrier for this multi-step jump with different neighbourhood arrangements of the adatom's initial and final positions. The lowest barrier, which we found with the Mendelev potential, was 0.63 eV (see *Fe Set Exchange* in [30]), which is still much higher than 0.27 eV barrier of hop-on process on {110}.

Based on this analysis, we conclude that the overall difference in the diffusion rates on {100} and {110} surfaces can be well predicted already within the 4D parameterization scheme of 1nn and 2nn jumps at low temperatures. However, the exchange events must be included into the simulations more accurately to predict reliably the kinetics of events also at high temperatures.

3.1.2. Analysis of the Cu Set 1 barriers

Fig. 8b illustrates the abundance of the barriers in *Cu Set 1*. In this figure, neither forbidden nor spontaneous events assigned close to zero barriers are included. The trend of the plot indicates a clear monotonic growth from smaller barriers for $a - c < 0$ towards the higher barriers for $a - c > 0$. The barriers on the left side are mostly below 0.5 eV. The individual cases of relatively high barriers (blue dots on the top of each column) correspond to the unstable final configurations that were handled using the approach discussed in Section 2.3. The right part of the graph has most of the barriers greater than 1 eV and no barriers less than 0.5 eV, meaning that jumps from stronger bonded states are much less likely to happen. Such a trend is not true for iron barrier distribution (see Fig. 8a), which can be explained by the FCC materials being closer packed compared to BCC: it is harder for atoms to break the bonds in the stronger bonded position in the FCC structure in order to jump to a lesser bonded state ($a - c > 0$).

We also see in Fig. 8b that the red colour is more pronounced for the events with $a - c < 0$ where it is less probable that the final configuration of the atom is unstable. Thus, a smaller number of barriers in the right part could be explained by there being less combinations of (a, b, c, d) processes, for which we were able to obtain the barriers with the approach described in Section 2.4.1. It is also interesting to note that there is a whole range of the barriers (0, 1.5) for the $a - c = 0$ situations, which indicates the effect of the 2nn atoms on the value of the barrier. Those were included in the calculations, but are not shown explicitly in the plot.

Furthermore, we analysed the (a, b, c, d) events that happened during the flattening of a cuboid nanotip of 13 nm height and 2 nm width constructed on a {110} surface, which was simulated using *Cu Set 1* (for details of the KMC simulations, see [3]). As we noticed during the flattening process, {111} facets were quickly built around the foot of the tip, allowing the adatoms to slide down from the top of the tip towards the surface. We analysed all the events, which took place during the flattening of the tip at 1000 K. These corresponded to a wide range of the energy barriers from near-zero (spontaneous) up to 2.0 eV (Fig. 10). Most of the events were below 0.2 eV, which are the transitions from lower to higher number of nearest neighbours. Spontaneous events happened only in 0.1% of the jumps. 1% of all the jumps corresponded to the events calculated in the bulk.

The analysis of individual events revealed the existence of a key event involved in flattening: adatoms on a {100} facet of the tip slide down to the {111} facet near the foot of the tip via the

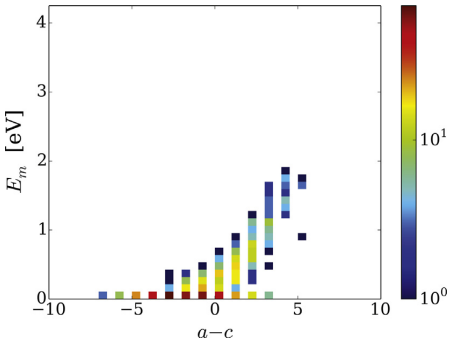

Fig. 10. Distribution of the migration energies vs. the change in the number of 1nn of the initial and final positions of the jumping atom for (a, b, c, d) jumps during the flattening of a Cu cuboid nanotip of 13 nm height and 2 nm width, constructed on a {1 1 0} surface at 1000 K. Colour corresponds to the occurrence of the migration energies for certain values $(a - c)$. For simplicity, c does not include a jumping atom. (For interpretation of the references to colour in this figure legend, the reader is referred to the web version of this article.)

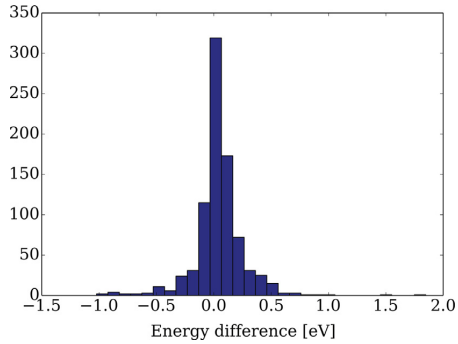

Fig. 11. Histogram of normalised differences between the barriers of the same stable events calculated with and without tethering.

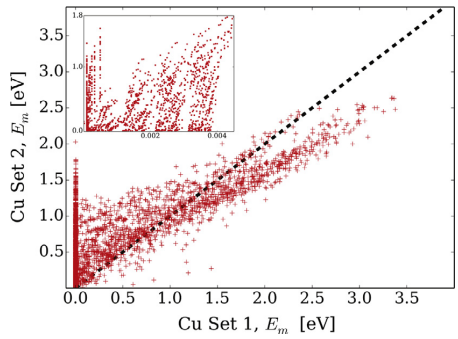

Fig. 12. Correlation of the barriers of *Cu Set 1* with the barriers of *Cu Set 2*. Inserted picture shows the barriers for the events with $E_m \leqslant 0.0047$ eV in *Cu Set 1*.

$(5, 1) \rightarrow (5, 4)$ process with a barrier $E_m(5, 1, 5, 4) = 0.43$ eV. If this process is excluded from the set, hence becoming effectively forbidden, the result shows a detachment of the tip from the substrate instead of its flattening. We simulated the tip geometry without a substrate to identify the events responsible for flattening. Only 0.008% of the events in the tip simulations led directly to flattening, the rest of the time the system spends on faceting, i.e. atoms moving along the crystallographic channels and hopping on facets.

We can also point out that more than 60% of the jumps are not advancing ones. The atoms are trapped between the same two configurations hopping back and forth. These trapping configurations usually have the same number of 1nn atoms. The barriers for those jumps are small, hence the probability for them to happen is high.

Even though the individual barriers might not correspond to reality in *Cu Set 1* and *Fe Set 1*, the overall trends of the barrier distributions predict well the kinetics of the event on Cu and Fe surfaces. Although, both sets include many forbidden barriers, the important events for nanocube formation and tip flattening simulations are included in the sets and have reasonable barriers, thus the overall evolution of the structures in the KMC simulations presented in [3,4] were reliable and compared well with the MD simulations and experiments. The fitted attempt frequencies for *Cu Set 1* and *Fe Set 1* also allowed us to obtain a time evolution comparable with the MD results in [3,4].

3.2. Tethering force approach for strong relaxation effects

We first analysed the effect of tethering on barriers of stable events. The histogram in Fig. 11 shows that the normalised differences between the barriers of most of the stable processes calculated with and without tethering are within 0.1 eV, which indicates that tethering does not affect the stable events significantly. However, there is around 4% of the processes with the normalised difference exceeding 0.5 eV.

We compared the barriers of the whole *Cu Set 1* and *Cu Set 2* in order to investigate the effect of tethering on the calculation of the barriers for the events involving also unstable configurations. The correlation of the barriers of both sets corresponding to the same (a, b, c, d) combination is shown in Fig. 12. The largest disagreement between two sets are for the events with the very small barriers in *Cu Set 1*, i.e. spontaneous, shown in the insert of Fig. 12. Most of them correspond to $a \leqslant 3$. With the tethering force, the spontaneous events of *Cu Set 1* can be assigned finite barriers with the broad range of values up to 2 eV in *Cu Set 2*. Note, nevertheless, that even with the tethering force applied, the use of Eq. (2) was unavoidable for some barriers. However, the number of such barriers decreased to 283, with 211 barriers corresponding to the processes with $a \leqslant 3$, compared to 2676 spontaneous processes (out of which 2486 were for $a \leqslant 3$) in *Cu Set 1*. These 283 barriers are not included in the inserted picture in Fig. 12.

The tethering force approach allows to calculate the barriers for all possible configurations in a rigid lattice. Thus, many (a, b, c, d) jumps that were forbidden in *Cu Set 1*, are now allowed in *Cu Set*

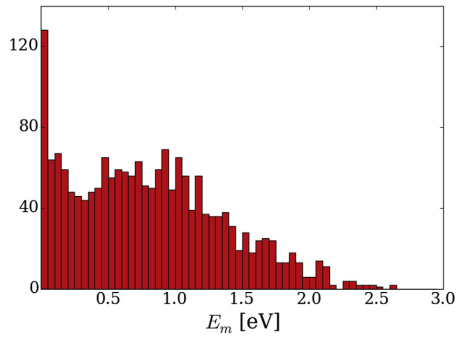

Fig. 13. Histogram of barriers of processes, which are unstable on a rigid lattice (forbidden in *Cu Set 1*), but calculated with the tethering force approach in *Cu Set 2*.

2. As it can be seen in Fig. 13, many of these unstable configurations are now allowed with high probabilities. One of the reasons why previously unstable configurations are now found to be stable and have low barriers is that the permutations in *Cu Set 2* were chosen based on the lowest potential energy of initial and final states and, thus, could differ from the permutations in *Cu Set 1*, which were selected at random. Another reason is that the tethering force approach is not capable to catch the processes with deep minima such as in Fig. 2d; instead a process like this is assigned with a small barrier. Whether these processes have impact on the KMC results or not depends on the considered system. We identified processes with such deep minima along the MEP between two rigid lattice positions in the post processing of the *Cu Set 2* and forbade them from happening in the tip flattening KMC simulations, which will be discussed below. Overall around 10% of the processes were forbidden in post processing, but it made little difference to the results of the KMC simulations of nanotips.

The spread of the barriers in *Cu Set 2* in Fig. 8c looks similar to the spread observed for *Cu Set 1* in Fig. 8b, but it has a much smoother transition from the region of events with $(a-c<0)$ to $(a-c>0)$. This reflects the consistency we had in choosing the permutations and treating the events involving unstable atoms in the calculations of the barriers of *Cu Set 2*.

We reproduced results of {1 1 0} tip flattening KMC simulations in [3] with *Cu Set 2* at 900 K. The profile of the tip flattening is similar: faceting of the tip near the foot occurred first and then adatoms from the top of the tip slid down towards the surface (see Fig. 14). The barrier for the same key events describing the sliding of adatoms downwards is $E_m(5,1,5,4)=0.47$ eV, which is only 0.04 eV higher than that in *Cu Set 1*. However, at temperatures above 900 K, the necking is emphasized and the nanotip detaches from the substrate instead of flattening down as was seen in simulations with *Cu Set 1*. The analysis of the occurred transitions showed that previously forbidden unstable processes in *Cu Set 1* (but now assigned with barriers using the tethering force approach in *Cu Set 2*) start to play a significant role in the system evolution at high temperatures. It should be noted that for such a Cu nanotip, with a thickness of 2 nm, the system will start to melt already at ~900 K due to finite size effects [44]. A rigid lattice model like Kimocs would not be able to accurately simulate molten system.

In order to estimate how the tethering force approach affects the time evolution, we have also compared the time scales of nanotip flattening obtained in KMC simulations with *Cu Set 1* and *Cu Set 2*. The simulations have shown a good agreement for the temperature 900 K: the flattening time of the 11 nm ⟨1 1 0⟩ nanotip with *Cu Set 1* was found to be (2.0 ± 0.20) μs and with *Cu Set 2* — (5.8 ± 0.44) μs.

For the tethering approach, we can conclude that it offers a solution for the parameterization of the events in a rigid lattice in KMC models, especially in those cases when it is not known *a priori* which jumps are crucial for surface evolution and it is important to generate as complete large tables of parameters as possible. The comparison between *Cu Set 1* and *Cu Set 2* indicates that the tethering force not only enables the calculation of the barriers in the unstable configurations (strong relaxation is expected in NEB), but also predicts well the relative distribution of the barriers, although some individual rigid lattice events can be overestimated due to their instability caused by relaxation effects. However, the barriers are not overestimated too much as the distribution of barriers is quite smooth.

3.3. Influence of the interatomic potential on the barrier calculations

Although we have performed most of our calculations of the barriers with the potentials described in Section 2.2, we analyse here the sensitivity of the barriers to the choice of the interatomic potential for the barrier calculations since this is essential for the validity of the KMC simulations.

The barrier calculation of 1024 possible permutations of hop-on jumps on Cu {1 0 0} surface, calculated with the CEM potential (see the next section), were repeated by constructing two new sets using the Mishin [45] and Sabochick-Lam [46] potentials. The average difference between the barriers calculated with CEM and the other two potentials is close to zero. Mishin potential barriers had a difference of 0.0002 ± 0.09 eV compared to CEM. The Sabochick-Lam potential resulted in a 0.008 ± 0.11 eV difference. Although the average difference is clearly not significant, we noticed that some of the rigid lattice adatom positions were identified as unstable during the NEB relaxation step with the Sabochick-Lam and Mishin potentials, whereas the same configurations were treated as stable with the CEM potential.

Here we note that KMC simulations rely mostly on the relative distribution of barriers of different events rather than on the absolute values of the barriers. Fig. 15 shows that the trend in the barriers depending on the change in the number of 1nn atoms of the jumping atom before and after the jump is quite similar for the Mishin and Sabochick-Lam potentials. At the same time, the CEM potential results in a smoother relative distribution of the barriers.

Based on our analysis, we conclude that although the relative distribution of the migration barriers calculated by using different interatomic potentials can be similar, still some differences may exist. This is why it is important to verify the values of crucial barriers for the simulated processes in order to ensure that they are predicted sufficiently accurately by the potential in use. For

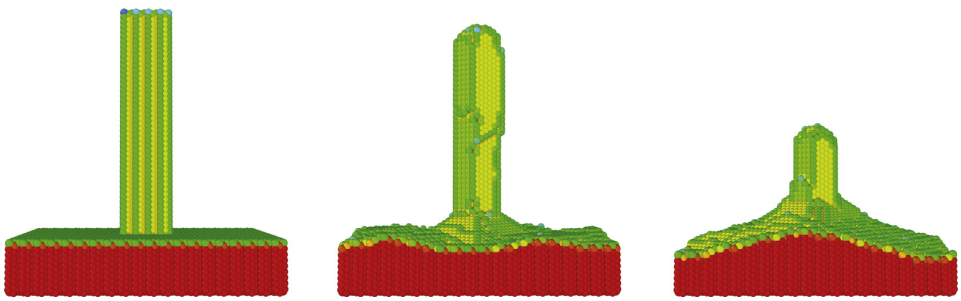

Fig. 14. The profile and corresponding time of the 11 nm height and 2 nm wide ⟨1 1 0⟩ nanotip, which has flattened in the Kimocs simulations at 900 K with *Cu Set 2*. Colours correspond to coordination numbers. (For interpretation of the references to colour in this figure legend, the reader is referred to the web version of this article.)

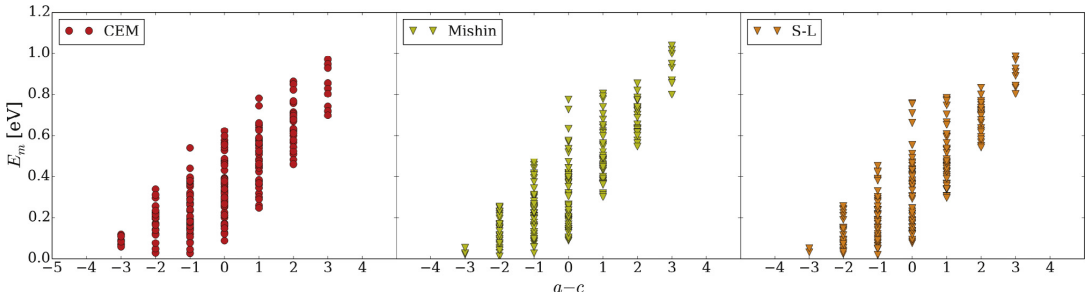

Fig. 15. Migration energy barriers vs. the change in the number of 1nn of the initial and final positions of the adatom hopping-on on Cu {1 0 0} surface calculated with different interatomic potentials. Left - Corrected Effective Medium Theory (CEM) potential [23], middle - Mishin [45], right - Sabochick-Lam [46].

instance, if adatom diffusion is studied, the potential which was used to calculate the energy barriers should be able to predict the barriers for all 1024 hop-on jumps for different arrangements of neighbouring atoms. In case the event cannot be calculated, the use of a tethering force is recommended as it will keep the unstable atoms in their positions, allowing for some relaxation effects during the transition. This way, the relative distribution of the barriers can still be obtained in a reliable manner, which will enable the accurate prediction of the overall evolution of the system.

3.4. 4D approach versus a 26D description

In the 4D approach, as it has been discussed before, events of diffusion jumps are described only by counting the numbers of 1nn and 2nn atoms around the initial and final sites of the jumping atom and the actual position of the neighbours are thus ignored in the characterization. Subsequently, an uncertainty of the value of the calculated barrier is expected. In some configurations, the number of permutations corresponding to the same combination of 1nn and 2nn neighbours can be significant. As it was mentioned above, we dealt with this problem by following two simple principles. A permutation representing a family of events described by the same (a, b, c, d) numbers, was chosen either (i) randomly, as in *Cu Set 1* and *Fe Set 1*, or (ii) according to the lowest energy state of the initial and final configurations, as in *Cu Set 2*. As an example, Fig. 16 shows minimum energy paths for three different permutations of the same $(5, 3, 7, 3)$ hop-on jump on Cu {1 0 0} surface. As it can be seen, one of the permutations shows significantly different MEP with the lowest energy barrier being 0.07 eV, while the other two, — the black and red curves — result in more similar barriers of 0.28 eV and 0.26 eV, respectively. The $(5, 3, 7, 3)$ configuration has overall 25 atomic permutations if only considering 1nn and 2nn atoms in the same layer of the initial and final positions of the hopping atom, while all the neighbouring atoms in the layer below are present and thus do not affect the permutations). The average barrier for the $(5, 3, 7, 3)$ configuration obtained over all 25 permutations is 0.23 ± 0.1 eV. The permutation corresponding to the lowest energy initial and final states is assigned with 0.27 eV by the tethering force approach in *Cu Set 2*. However, the randomly chosen permutation happened to be described by the barrier 0.07 eV, which was used in *Cu Set 1*. We chose the most dramatic case for illustration of this uncertainty, which actually indicates that in the approach chosen initially, i.e. adopting a single value of the barrier for all (a, b, c, d) events, which was calculated for a randomly selected permutation, may affect the simulation results. If a key process is assigned a barrier with too imprecise value, artefacts may appear in the simulations. The validation of the parameterization — and thereby making sure it does not produce artefacts — can usually be done by comparing the KMC results for small systems with MD, as it was done in [3].

In our implementation, surfaces with different crystallographic orientations can be simulated, since all of them can be described within the same 4D formalism. Even if the positions of neighbouring

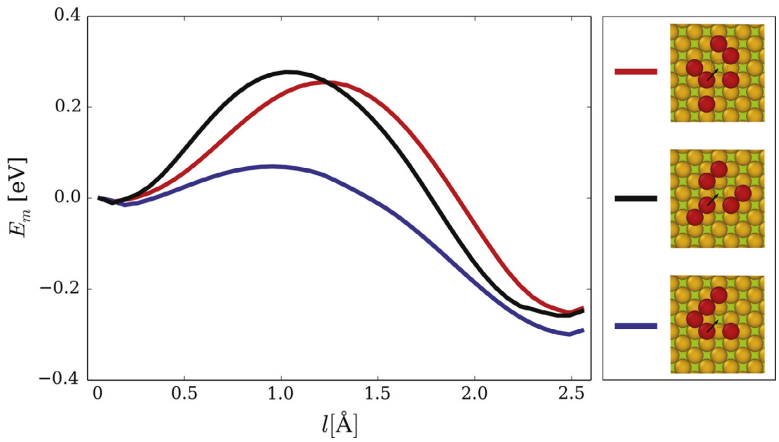

Fig. 16. Minimum energy paths of the different permutations of the $(5, 3, 7, 3)$ jump. l is the distance from the initial position of the jumping atom.

atoms on a rigid lattice are not the same in different facets, the barriers fit together remarkably well.

In the following, we will give a quantitative estimate of the uncertainty, which arises when different permutations for the same number of neighbours are ignored. Consider the case of hop-on jumps on a {1 0 0} FCC surface, where the layer below the jumping atom is filled completely in all considered permutations. In this case, the only neighbour sites that can change are the ten 1nn and 2nn atom positions around the initial and final positions of the jumping atom. The total number of different permutations in this case is $2^{10} = 1024$, based on whether these 10 sites are occupied or vacant. In the Kimocs description, there are overall 196 (a, b, c, d) events with 1024 permutations on the {1 0 0} FCC surface. The energy barriers, which were calculated for all permutations in these 196 configurations for Cu are shown in Fig. 17. Most of the barriers are within the range of $[0.1, 0.6]$ eV. The histogram also includes the barriers for an atom diffusion on the close-packed {1 1 1} Cu surface. There are only 23 combinations of (a, b, c, d) events on the {1 1 1} surface with most of the barriers being less than 0.1 eV. Note that our model does not include the migration to HCP sites on the {1 1 1} surface. The average standard deviation of the energy barriers for the 196 configurations of the {1 0 0} surface was found to be 0.13 eV or 14.8%, which can be used as the estimate of the accuracy of the energy barrier parameterization and, consequently, of our KMC model in general.

To further analyse the effect of permutations on the value of the barrier, we compared the barriers in *Cu Set 2*, obtained in the 4D parameterization scheme, and *Cu Set 3*, obtained in the full 26D parameterization scheme. These are comparable as the barriers in both sets were obtained with the application of the tethering force. The results of this comparison are presented in Fig. 18. Here we plot the values of the barriers corresponding to the same (a, b, c, d) events. If the values agree well, all of them will lie along the dashed line. In *Cu Set 3*, many barriers correspond to the same (a, b, c, d) description due to different permutations. To enable the comparison, we averaged all the barriers, which belong to the same family of (a, b, c, d) and plotted the averaged value against the value found in *Cu Set 2* for the same (a, b, c, d) event. The standard deviation of the mean value shown around the point to indicate how broadly the values of the barriers fluctuate with different permutations. As one can see, the strong fluctuations of the barriers around the mean values are mostly observed for some individual events, while for the vast majority of events, these fluctuations are not strong and overall all the dots cluster quite closely to the dashed line. This confirms that the 4D parameterization scheme is able to capture the relative distribution of barriers quite well.

Our KMC simulations of flattening of Cu nanotips using *Cu Set 1* and *Cu Set 2* showed that 4D parameterization of atomic jumps was

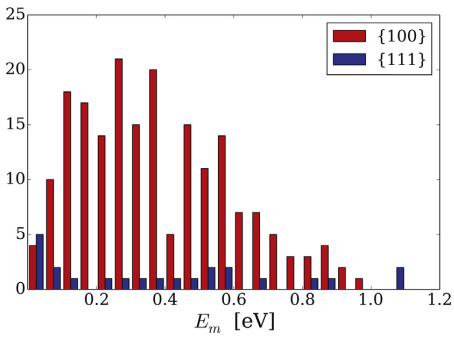

Fig. 17. The occurrence of the migration energies of adatom diffusion on {1 0 0} and {1 1 1} Cu surfaces.

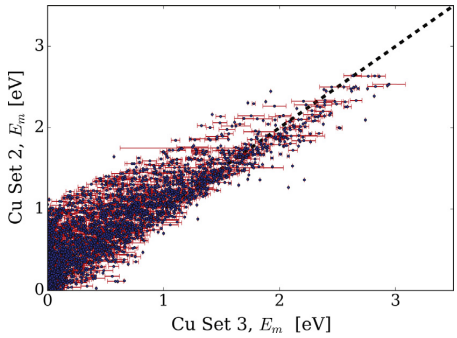

Fig. 18. Cu barriers of *Cu Set 3* in comparison with *Cu Set 2*.

sufficient to obtain good agreement with MD simulations. In Section 3.1.2, we showed that an important role is played by the surface events in simulations of nanotips, i.e. the events that have less than ten 1nn and 2nn atoms. As we showed here, ignoring possible permutations did not introduce a significant uncertainty in barriers of surface events due to the small number of permutations available for such events. We note here that ignoring permutations in *Fe Set 1* for the Fe self-diffusion on flat surfaces did not affect the results obtained for growing iron nanocubes at low temperatures either, since the surface events played a crucial role also in these simulations. On the other hand, as we have shown in Fig. 18, in some cases the 4D description of the events may fail to capture the physics properly as the permutations hidden within such an approach may play a crucial role in some specific cases. For example, it was not possible to include the exchange events on Fe {1 0 0} surface without introducing artefacts on {1 1 0}, thus, at high temperatures, we obtained quite different results in KMC simulations compared to MD simulations.

4. Conclusions

The rigid lattice approximation allows to create fast and efficient Kinetic Monte Carlo models that are capable to simulate big systems of millions of atoms and reach much longer time scales than with e.g. molecular dynamics. The crucial part for any atomistic Kinetic Monte Carlo model is the set of thousands or even millions of transition barriers that defines the probabilities for any atom to make a jump in the system. These barriers need to be calculated separately — in our approach using molecular dynamics in combination with the Nudged Elastic Band method — and then parameterized and tabulated for use in the Kinetic Monte Carlo simulations.

In this paper, we have discussed different approaches for calculating and compiling such barrier sets for FCC and BCC metals. We have shown that many of the problems with a rigid lattice parameterization can be overcome by applying a tethering force in the Nudged Elastic Band calculations of the barriers; these additional spring forces prevent the atoms to relax to a position too far from the lattice positions during the relaxation and the Nudged Elastic Band calculation of the barriers.

We have calculated three sets of barriers for copper using three different approaches, including the tethering force approach, and also sets for iron. Sets of barriers can be found in [29,30]. We have analysed the distributions of the barriers in each set as well as the importance of individual barriers in Kinetic Monte Carlo simulations of surface processes. Our barrier sets of thousands of barriers for Cu and Fe could in principle be used by any Kinetic Monte Carlo model for atom migration processes in a rigid lattice.

We have shown that tethering force approach in the calculation of the migration barriers does not significantly change the physical outcome of Kinetic Monte Carlo simulations where sets of thousands of such barriers are used. On the contrary, this new approach provides a systematic way to calculate all barriers needed for Kinetic Monte Carlo simulations of a single-metal system; especially in systems where surface processes are important.

Acknowledgement

The authors would like to thank Dr. Antti Kuronen for providing his implementation of the NEB method for PARCAS. This work was supported by CERN under the K-contract KE2488/BE/CLIC. E. Baibuz was supported by a CERN K-contract and the doctoral program MATRENA of the University of Helsinki. J. Lahtinen was supported by a CERN K-contract. V. Jansson was supported by Academy of Finland (Grant No. 285382). F. Djurabekova acknowledges gratefully the financial support of Academy of Finland (Grant No. 269696) and MEPhI Academic Excellence Project – Russia (Contract No. 02.a03.21.0005). V. Zadin and S. Vigonski were supported by Estonian Research Council grants PUT 57 and PUT 1372. Computing resources were provided by the Finnish IT Center for Science (CSC) and the Finnish Grid and Cloud Infrastructure (persistent identifier urn:nbn:fi:research-infras-2016072533).

References

[1] CLIC, M. Boland, U. Felzmann, P. Giansiracusa, T. Lucas, R. Rassool, C. Balazs, T. Charles, K. Afanaciev, I. Emeliantchik et al., Updated baseline for a staged Compact Linear Collider, CERN Yellow Reports 4(0). Available from: arXiv:1608.07537.

[2] C. Antoine, F. Peauger, F. Le Pimpec, Erratum to: electromigration occurences and its effects on metallic surfaces submitted to high electromagnetic field: A novel approach to breakdown in accelerators, Nucl. Instrum. Meth. Phys. Res. Sect. A: Accel. Spectrom. Detect. Assoc. Equip. 670 (2012) 79–94, https://doi.org/10.1016/j.nima.2012.01.027.

[3] V. Jansson, E. Baibuz, F. Djurabekova, Long-term stability of Cu surface nanotips, Nanotechnology 27(26), 265708. Available from: arXiv:1508.06870. doi:https://doi.org/10.1088/0957-4484/27/26/265708.

[4] J. Zhao, E. Baibuz, J. Vernieres, P. Grammatikopoulos, V. Jansson, M. Nagel, S. Steinhauer, M. Sowwan, A. Kuronen, K. Nordlund, F. Djurabekova, Formation mechanism of fe nanocubes by magnetron sputtering inert gas condensation, ACS Nano 10 (4) (2016) 4684–4694, https://doi.org/10.1021/acsnano.6b01024, pMID: 26962973.

[5] F. Djurabekova, L. Malerba, R.C. Pasianot, P. Olsson, K. Nordlund, Kinetics versus thermodynamics in materials modeling: the case of the di-vacancy in iron, Philos. Mag. 90 (19) (2010) 2585–2595, https://doi.org/10.1080/14786431003662515.

[6] A.B. Bortz, M.H. Kalos, J.L. Lebowitz, A new algorithm for Monte Carlo simulation of Ising spin systems, J. Comput. Phys. 17 (1) (1975) 10–18, https://doi.org/10.1016/0021-9991(75)90060-1.

[7] G. Henkelman, H. Jónsson, A dimer method for finding saddle points on high dimensional potential surfaces using only first derivatives, J. Chem. Phys. 111 (15) (1999) 7010–7022, https://doi.org/10.1063/1.480097.

[8] O. Trushin, A. Karim, A. Kara, T.S. Rahman, Self-learning kinetic monte carlo method: application to Cu(111), Phys. Rev. B 72 (2005) 115401, https://doi.org/10.1103/PhysRevB.72.115401.

[9] D. Konwar, V.J. Bhute, A. Chatterjee, An off-lattice self-learning kinetic monte carlo method using local environments, J. Chem. Phys. 135 (17) (2011) 174103, https://doi.org/10.1063/1.3657834.

[10] F. El-Mellouhi, N. Mousseau, L.J. Lewis, Kinetic activation-relaxation technique: an off-lattice self-learning kinetic monte carlo algorithm, Phys. Rev. B 78 (2008) 153202, https://doi.org/10.1103/PhysRevB.78.153202.

[11] Y.L. Bouar, F. Soisson, Kinetic pathways from embedded-atom-method potentials: influence of the activation barriers, Phys. Rev. B 65 (2002) 094103, https://doi.org/10.1103/PhysRevB.65.094103.

[12] C. Mottet, R. Ferrando, F. Hontinfinde, A. Levi, A monte carlo simulation of submonolayer homoepitaxial growth on Ag(110) and Cu(110), Surface Sci. 417 (2) (1998) 220–237, https://doi.org/10.1016/S0039-6028(98)00611-6.

[13] M.I. Larsson, Kinetic monte carlo simulations of adatom island decay on Cu (111), Phys. Rev. B 64 (2001) 115428, https://doi.org/10.1103/PhysRevB.64.115428.

[14] S. Verma, T. Rehman, A. Chatterjee, A cluster expansion model for rate constants of surface diffusion processes on Ag, Al, Cu, Ni, Pd and Pt(100) surfaces, Surface Sci. 613 (2013) 114–125, https://doi.org/10.1016/j.susc.2013.03.022.

[15] A. Van der Ven, G. Ceder, Vacancies in ordered and disordered binary alloys treated with the cluster expansion, Phys. Rev. B 71 (2005) 054102, https://doi.org/10.1103/PhysRevB.71.054102.

[16] K. Sastry, D.D. Johnson, D.E. Goldberg, P. Bellon, Genetic programming for multitimescale modeling, Phys. Rev. B 72 (2005) 085438, https://doi.org/10.1103/PhysRevB.72.085438.

[17] N. Castin, R. Pinheiro Domingos, L. Malerba, Use of computational intelligence for the prediction of vacancy migration energies in atomistic kinetic monte carlo simulations, Int. J. Comput. Intell. Syst. 1 (4) (2008) 340–352, https://doi.org/10.1080/18756891.2008.9727630.

[18] N. Castin, L. Malerba, Prediction of point-defect migration energy barriers in alloys using artificial intelligence for atomistic kinetic monte carlo applications, Nucl. Instrum. Meth. Phys. Res. Sect. B: Beam Interact. Mater. Atoms 267 (18) (2009) 3148–3151, https://doi.org/10.1016/j.nimb.2009.06.041.

[19] N. Castin, L. Malerba, Calculation of proper energy barriers for atomistic kinetic monte carlo simulations on rigid lattice with chemical and strain field long-range effects using artificial neural networks, J. Chem. Phys. 132 (7) (2010) 074507, https://doi.org/10.1063/1.3298990.

[20] H. Jónsson, G. Mills, K.W. Jacobsen, Nudged elastic band method for finding minimum energy paths of transitions.

[21] G. Henkelman, G. Jóhannesson, H. Jónsson, Methods for finding saddle points and minimum energy paths, in: Theoretical Methods in Condensed Phase Chemistry, Springer, 2002, pp. 269–302, https://doi.org/10.1007/0-306-46949-9_10.

[22] G. Henkelman, B.P. Uberuaga, H. Jónsson, A climbing image nudged elastic band method for finding saddle points and minimum energy paths, J. Chem. Phys. 113 (22) (2000) 9901–9904, https://doi.org/10.1063/1.1329672.

[23] M.S. Stave, D.E. Sanders, T.J. Raeker, A.E. DePristo, Corrected effective medium method. v. simplifications for molecular dynamics and monte carlo simulations, J. Chem. Phys. 93 (6) (1990) 4413–4426, https://doi.org/10.1063/1.458724.

[24] S.B. Sinnott, M.S. Stave, T.J. Raeker, A.E. DePristo, Corrected effective-medium study of metal-surface relaxation, Phys. Rev. B 44 (16) (1991) 8927.

[25] M. Mendelev, S. Han, D. Srolovitz, G. Ackland, D. Sun, M. Asta, Development of new interatomic potentials appropriate for crystalline and liquid iron, Philos. Mag. 83 (35) (2003) 3977–3994, https://doi.org/10.1080/14786430310001613264.

[26] M. Müller, P. Erhart, K. Albe, Analytic bond-order potential for bcc and fcc iron-comparison with established embedded-atom method potentials, J. Phys.: Condens. Matter 19 (32) (2007) 326220.

[27] G. Antczak, G. Ehrlich, Jump processes in surface diffusion, Surface Sci. Rep. 62 (2) (2007) 39–61, https://doi.org/10.1016/j.surfrep.2006.12.001.

[28] H. Chamati, N. Papanicolaou, Y. Mishin, D. Papaconstantopoulos, Embedded-atom potential for fe and its application to self-diffusion on Fe(100), Surface Sci. 600 (9) (2006) 1793–1803, https://doi.org/10.1016/j.susc.2006.02.010.

[29] E. Baibuz, S. Vigonski, J. Lahtinen, J. Zhao, V. Jansson, V. Zadin, F. Djurabekova, Data sets of migration barriers for atomistic kinetic monte carlo simulations of cu self-diffusion via first nearest neighbours atomic jumps, Data In Brief, submitted for publication.

[30] E. Baibuz, S. Vigonski, J. Lahtinen, J. Zhao, V. Jansson, V. Zadin, F. Djurabekova, Data sets of migration barriers for atomistic kinetic monte carlo simulations of fe self-diffusion, Data In Brief, submitted for publication.

[31] S. Plimpton, C. Battaile, M. Chandross, L. Holm, A. Thompson, V. Tikare, G. Wagner, E. Webb, X. Zhou, C.G. Cardona, et al., Crossing the mesoscale no-man's land via parallel kinetic monte carlo, Sandia Report SAND2009-6226.

[32] Spparks.Sandia.Gov., Spparks Kinetic Monte Carlo Simulator, 2017. <http://spparks.sandia.gov/index.html>.

[33] K. Nordlund, M. Ghaly, R.S. Averback, M. Caturla, T. Diaz de la Rubia, J. Tarus, Defect production in collision cascades in elemental semiconductors and fcc metals, Phys. Rev. B 57 (1998) 7556–7570, https://doi.org/10.1103/PhysRevB.57.7556.

[34] M. Ghaly, K. Nordlund, R.S. Averback, Molecular dynamics investigations of surface damage produced by kiloelectronvolt self-bombardment of solids, Philos. Mag. A 79 (4) (1999) 795–820, https://doi.org/10.1080/01418619908210332.

[35] K. Nordlund, Molecular dynamics simulation of ion ranges in the 1–100 kev energy range, Comput. Mater. Sci. 3 (4) (1995) 448–456, https://doi.org/10.1016/0927-0256(94)00085-Q.

[36] G. Henkelman, Methods for Calculating Rates of Transitions with Application to Catalysis and Crystal Growth, Ph.D. thesis, University of Washington, 2001.

[37] J. Hook, H. Hall, Solid State Physics, Manchester Physics Series.

[38] F. Soisson, C.-C. Fu, Cu-precipitation kinetics in αFe from atomistic simulations: vacancy-trapping effects and cu-cluster mobility, Phys. Rev. B 76 (2007) 214102, https://doi.org/10.1103/PhysRevB.76.214102.

[39] E. Vincent, C. Becquart, C. Pareige, P. Pareige, C. Domain, Precipitation of the fecu system: a critical review of atomic kinetic monte carlo simulations, J. Nucl. Mater. 373 (1) (2008) 387–401, https://doi.org/10.1016/j.jnucmat.2007.06.016.

[40] N. Castin, M.I. Pascuet, L. Malerba, Modeling the first stages of cu precipitation in α-fe using a hybrid atomistic kinetic monte carlo approach, J. Chem. Phys. 135 (6) (2011) 064502, https://doi.org/10.1063/1.3622045.

[41] Simulation of the nanostructure evolution under irradiation in Fe-C alloys, J. Nucl. Mater. 443(1–3) (2013) 274–285. doi:https://doi.org/10.1016/j.jnucmat.2013.07.046.

[42] The surface energy of metals, Surface Sci. 411(1) (1998) 186–202. doi: https://doi.org/10.1016/S0039-6028(98)00363-X.
[43] S. Plimpton, Fast parallel algorithms for short-range molecular dynamics, J. Comput. Phys. 117 (1) (1995) 1–19, https://doi.org/10.1006/jcph.1995.1039.
[44] F. Granberg, S. Parviainen, F. Djurabekova, K. Nordlund, Investigation of the thermal stability of Cu nanowires using atomistic simulations, J. Appl. Phys. 115 (21) (2014) 213518, https://doi.org/10.1063/1.4876743.
[45] Y. Mishin, M.J. Mehl, D.A. Papaconstantopoulos, A.F. Voter, J.D. Kress, Structural stability and lattice defects in copper: ab initio, tight-binding, and embedded-atom calculations, Phys. Rev. B (22), 224106. doi:https://doi.org/10.1103/PhysRevB.63.224106.
[46] M.J. Sabochick, N.Q. Lam, Radiation-induced amorphization of ordered intermetallic compounds cuti, $cuti_2$, and $cu_4$$ti_3$: a molecular-dynamics study, Phys. Rev. B (7), 5243–5252. doi:https://doi.org/10.1103/physrevb.43.5243.

IOP Publishing Nanotechnology
Nanotechnology 29 (2018) 015704 (10pp) https://doi.org/10.1088/1361-6528/aa9a1b

Au nanowire junction breakup through surface atom diffusion

Simon Vigonski[1,2], Ville Jansson[2], Sergei Vlassov[3], Boris Polyakov[4], Ekaterina Baibuz[2], Sven Oras[3], Alvo Aabloo[1], Flyura Djurabekova[2] and Vahur Zadin[1,2]

[1] Institute of Technology, University of Tartu, Nooruse 1, 50411, Tartu, Estonia
[2] Helsinki Institute of Physics and Department of Physics, PO Box 43 (Pehr Kalms gata 2), FI-00014, University of Helsinki, Finland
[3] Institute of Physics, University of Tartu, W. Ostwaldi 1, 50411, Tartu, Estonia
[4] Institute of Solid State Physics, University of Latvia, Kengaraga 8, LV-1063, Riga, Latvia

E-mail: vahur.zadin@ut.ee

Received 27 September 2017, revised 30 October 2017
Accepted for publication 13 November 2017
Published 5 December 2017

Abstract

Metallic nanowires are known to break into shorter fragments due to the Rayleigh instability mechanism. This process is strongly accelerated at elevated temperatures and can completely hinder the functioning of nanowire-based devices like e.g. transparent conductive and flexible coatings. At the same time, arranged gold nanodots have important applications in electrochemical sensors. In this paper we perform a series of annealing experiments of gold and silver nanowires and nanowire junctions at fixed temperatures 473, 673, 873 and 973 K (200 °C, 400 °C, 600 °C and 700 °C) during a time period of 10 min. We show that nanowires are especially prone to fragmentation around junctions and crossing points even at comparatively low temperatures. The fragmentation process is highly temperature dependent and the junction region breaks up at a lower temperature than a single nanowire. We develop a gold parametrization for kinetic Monte Carlo simulations and demonstrate the surface diffusion origin of the nanowire junction fragmentation. We show that nanowire fragmentation starts at the junctions with high reliability and propose that aligning nanowires in a regular grid could be used as a technique for fabricating arrays of nanodots.

Supplementary material for this article is available online

Keywords: nanowire junctions, rayleigh instability, kinetic monte carlo, gold, fabrication of nanodots

(Some figures may appear in colour only in the online journal)

1. Introduction

Gold nanostructures are of considerable interest for their optical, mechanical and electrical properties. For example, gold nanopillar arrays have been used as highly efficient electrodes for detecting bioelectrical signals [1, 2], where their aspect ratio has proven to be of great importance. Plasmonic trapping of colloidal particles has been demonstrated using a gold nanopillar [3]. Other structures with a high surface to volume ratio are porous gold films [4] and nanoparticles [5], which are used in catalysis and electrochemical sensors. In particular, ordered arrays of gold nanoparticles can be used for biochemical sensing [6], as well as wavelength-specific photodetectors [7]. Precise fabrication techniques allow for a significant level of control of the resulting geometries and properties [8, 9]. Production of nanodot arrays is currently performed using vacuum evaporation [10] or using a polystyrene template [11].

Metal, including gold, nanowires are a rapidly expanding area of research as well. For example, gold nanoparticles are used as a catalyst in the production of nanowires for solar cell applications [12]. Gold nanowires themselves can be used in

transparent electrodes for flexible displays [13]. A particularly important point relating to electrodes is the stability of nanowires under thermal loading—surface energy minimization driven by thermally activated diffusion leads to breakup of nanowires. This has been observed for Ag [14], Cu [15], as well as Au [16].

The behavior of nanostructures at elevated temperatures can differ drastically from the macroscopic situation. It is well known that small nanoparticles melt at a significantly lower temperature compared to bulk, and the melting temperature depends on size [17]. Moreover, if we consider the time factor, then the situation becomes even more complicated. Given enough time for surface diffusion processes to happen, it is possible to observe drastic changes in nanostructure morphology at very moderate temperatures. For instance, an Au nanoparticle of 5 nm in diameter starts to melt at approximately 1100 K (830 °C) [18], and for particles over 10 nm melting temperatures are comparable to bulk values (1337 K/1064 °C). When we consider processes like surface diffusion and Rayleigh instability [16], we can see fusion and fragmentation of Au nanostructures at temperatures as low as 473 K (200 °C) [19]. This phenomenon is of great importance in all applications where nanowires are exposed to elevated temperatures or require thermal treatment before use to remove surfactant and other organic residuals. In particular, for proper functioning of nanowires-based transparent conductive coatings [20], continuous pathways are absolutely essential for electrons to ensure sufficient electrical conductivity. Heat-induced fragmentation of nanowires will prevent functioning of nanowire-based electronics.

Using atomistic computer simulations provides insights into the microscopic processes driving nanoparticle evolution which are difficult to observe experimentally. Molecular dynamics (MD) simulations have been used extensively to study the elasticity and plasticity of gold nanowires (e.g. [21]) and nanopillars (e.g. [22]), where the significant role of surface stress has been determined. Pareira and Silva [23] simulated a cold welding process of gold and silver nanowires with MD, where they identified diffusion, surface relaxation and reconstruction as the main mechanisms of interest. Monte Carlo (MC) methods are used to simulate longer time periods than those approachable by MD simulations. For example, Kolosov *et al* [24] studied the coalescence of gold and copper nanoparticles. The kinetic Monte Carlo (KMC) method was used by He *et al* [25] to simulate structural transitions in gold nanoparticles. Müller *et al* [26] showed the formation and breakup of a Ge nanowire using lattice KMC simulations.

In this paper we examine the breakup of Au nanowire junctions under thermal treatment and develop a gold parametrization for the kinetic Monte Carlo code Kimocs [27] in order to simulate the breakup process. Kimocs is specially designed to simulate atomistic diffusion processes on metal surfaces. It was initially developed for copper, but has also been successfully applied for Fe nanoparticle simulations [28], where it was demonstrated that certain combinations of temperature and deposition rate result in cubic nanoparticle shapes. Kimocs requires that the transition energy barriers for all possible surface processes are known in advance.

We show that the thermally activated diffusion of surface atoms results in preferential breakup at the nanowire junction. Based on the experimental and simulation analysis we suggest a method for manufacturing periodic, well controlled arrays of nanodots.

2. Materials and methods

2.1. Experimental setup

The experimental part of this work was done using gold and silver nanowires. Silver nanowires were purchased from Blue Nano (USA), while gold nanowires were prepared by us as described below.

2.1.1. Synthesis of nanowires. The Au nanowires used in the current study were synthesized using a 3-stage process according to a technique described in detail in [29]. First, a seed solution (SS) of Au nanoparticles was prepared with 18 ml of 0.025 M sodium citrate and 0.1–0.2 ml of 0.0005 M $HAuCl_4$ solution added into a 25 ml glass bottle. Ice cold solution of 0.01 M $NaBH_4$ was separately prepared. A volume of 0.6 ml of the $NaBH_4$ solution was added into the solution of sodium citrate with gold precursor while stirring vigorously. The resulting SS, slightly orange in color, was used for synthesis of Au nanowires within 10 min after preparation.

Next, a growth solution (GS) was prepared in a 300 ml vessel by mixing 238.5 ml of 0.2 M hexadecyltrimethylammonium bromide (CTAB) and 10 ml of 0.0001 M of $HAuCl_4$. The solution had intensive yellow color. Next, 1.5 ml of 0.1 M ascorbic acid was added, making the solution colorless. The freshly prepared GS was divided into two 25 ml glass bottles labeled A and B, and 200 ml in vessel C. A volume of 0.25 ml of concentrated HNO_3 was added into vessel C. An amount of 200 μl of the gold SS was added into bottle A and stirred for few seconds (the solution color was pink). Then 200 μl of solution in bottle A was transferred to bottle B and stirred for several seconds (the solution color was crimson–violet). Finally, 100 μl of solution in bottle B was transferred to vessel C and mixed for several seconds (the solution was colorless in the beginning, but became slightly orange–brick color after 1 h). The solution was kept in at 25 °C for 12 h. Precipitates of gold nanowires can be observed on the bottom of the tube after the reaction. The supernatant was poured out, and the precipitation was re-dispersed in 5 ml deionized water. Remaining CTAB allows storing the Au NWs suspension at least for 1 year.

2.1.2. Preparation and experimental analysis of samples. The solution with nanowires contained a high amount of surfactant (hexadecyltrimethylammonium bromide). In order to reduce the amount of the surfactant, a special procedure was performed. The solution containing the nanowires was left intact for several hours until all nanowires settled out and the solution became transparent. Immediately prior to the preparation of samples the liquid above the precipitate was

removed and replaced by distilled water. The new solution was stirred until formation of a uniform mixture and then transferred to separate Si wafers by drop-casting. In total, five samples were prepared.

A series of annealing experiments were performed at fixed temperatures 473, 673, 873 and 973 K (200 °C, 400 °C, 600 °C and 700 °C) during a time period of 10 min. However, only one temperature was used for each sample. In addition, one sample was treated at 973 K (700 °C) for 1 min. The procedure of thermal treatment consisted of heating the furnace up to the required temperature and then inserting the sample for the chosen period of time. Thermal treatment was performed in air atmosphere.

Micrographs of nanowires before and after thermal treatment were obtained with high-resolution scanning electron microscope (Helios Nanolab 600, FEI) and transmission electron microscope (TEM, Tecnai GF20, FEI).

2.2. KMC model development

For simulating the Au nanowires we use the kinetic Monte Carlo for Surfaces code (Kimocs) [27]. Kimocs is an atomistic kinetic Monte Carlo code for simulating single crystal structures. Kimocs is based on a rigid lattice where atoms can occupy well-defined lattice sites. A transition occurs when an atom jumps from an occupied lattice site to a neighboring vacant lattice site with a rate given by an Arrhenius type equation:

$$\Gamma = \nu \exp\left(-\frac{E_{\mathrm{m}}}{k_{\mathrm{B}}T}\right), \tag{1}$$

where ν is the attempt frequency, E_{m} is the migration energy barrier for the transition, T is the temperature and k_{B} is the Boltzmann constant.

To conduct a simulation, the attempt frequency and migration barriers for all possible transitions must be known in advance. Different transitions are characterized by the number of first and second nearest neighbors of the jumping atom in the initial and final positions (see [27] for details). For simplicity we do not take into account the positioning of the neighbors, only their number, thus drastically reducing the number of possible transitions. For each such transition, the migration barrier is calculated using an automated tethered NEB process (see section 2.2.2 below). As a further simplification, the attempt frequency is taken to be equal for all transitions and calculated by fitting nanopillar relaxation times to MD results (section 2.2.3 below).

As a result, atom jumps are characterized by migration barriers, which are calculated in MD from the interactions of the jumping atom with the local atomic environment. Any atom can move to any neighboring vacant lattice site by overcoming the energy barrier. Although only first nearest neighbor jumps are included in the current work, other transitions are in principle possible as a sequence of jumps that may include intermediate metastable positions. In this way, an adatom can, for example, cross the edge between two different surfaces.

2.2.1. Potential selection. In order to adjust the model for use with Au, a full parametrization of an Au potential had to be made. We selected the Embedded Atom Method (EAM) potential by Grochola *et al* [30]. The energy barriers calculated for our model are based on an interatomic potential, which describes the interactions between all the atoms in the system. The choice of the potential is of utmost importance as it determines the values for all the energy barriers, which in turn dictate the evolution of the system. Interatomic potentials are typically fitted to specific experimental or *ab initio* parameters of interest. For our purposes, the most important properties are the surface energies, specifically the ordering between the energies of {111}, {110} and {100} surfaces. According to *ab initio* calculations by Vitos *et al* [31], the surface energies for gold are (in increasing order; J m^{-2}): {111}—1.283, {100}—1.627, {110}—1.700. Thus, the {111} surface is the most stable and the {110} surface least stable of the ones mentioned. Although the surface energies reported by Grochola *et al* using their potential (J m^{-2}; {111}—1.197, {100}—1.296, {110}—1.533) are somewhat lower than the *ab initio* values, as well as the experimental average surface energy (1.851 J m^{-2} at 25 °C and decreasing with increasing temperature [32]), it has the closest surface energy values to the *ab initio* or experimental results, while maintaining correct surface stability order.

2.2.2. Migration barrier calculations. Transition processes in Kimocs are defined by the number of first and second nearest neighbors of the jumping atom in the initial and final positions. Although the specific positions of the neighbors are not taken into account during KMC simulations, a single specific neighborhood, defined as a permutation, must still be selected when calculating migration energies. Several different permutations correspond to the same Kimocs process. For each process, we look at all possible permutations and choose the one with the lowest sum of initial and final position energies to use for calculating the migration barrier.

After a permutation has been selected, we proceed with migration barrier calculations using the Nudged Elastic Band (NEB) method [33]. The spring constant for NEB was 1 eV Å^{-2}. In addition, a tethering approach was used, where background atoms are tethered to their initial positions in each NEB image using an additional tethering spring constant 2 eV Å^{-2}. This greatly improves the stability of the system in case of processes with few neighbors. As a result, almost all of the possible processes can be calculated in this way. For processes that remain unstable despite the tethering, the formula for spontaneous processes from [27] is used.

The details of permutation selection and tethered NEB migration barrier calculations are more fully presented in [34].

2.2.3. Attempt frequency calculations. The physical time for each KMC step is calculated based on the sum of transition

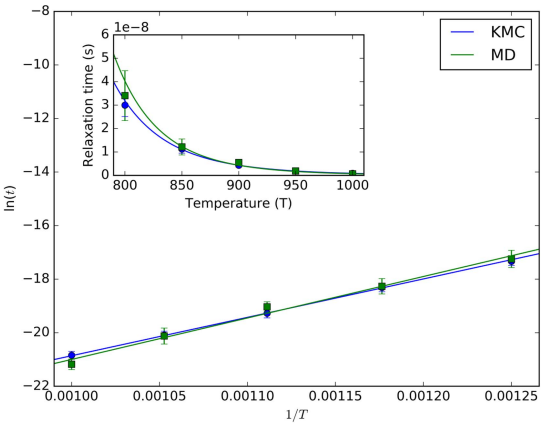

Figure 1. Relaxation time for a nanopillar in MD and KMC simulations depending on temperature for the temperatures 800, 850, 900, 950, 1000 K. KMC relaxation time has been normalized to the MD time to minimize discrepancies. Insert: nonlinearized version of the same data.

rates of all possible processes at that time [27]:

$$\Delta t = \frac{-\log u}{\sum_i \Gamma_i}, \tag{2}$$

where Γ_i is the rate for a single process calculated using equation (1) and $u \in (0, 1]$ is a uniform random number.

Since ν is taken to be equal for all processes, it can be taken out of the summation. Thus, the total time for a process to occur is $t = N \cdot \langle \Delta t \rangle$, where N is the number of steps and $\langle \Delta t \rangle$ is the average time interval for a single step. Taking into account equation (1), and assuming that the number of possible processes at each step and their migration barriers do not vary considerably over the whole simulation, the expression for the total time is

$$t = \frac{1}{\nu} c \cdot \exp\left(\frac{E}{k_B T}\right), \tag{3}$$

where E is the average effective transition energy barrier and c is a factor which incorporates the average number of possible transitions in the system and is proportional to the number of simulation steps.

As a result, simulations can be conducted using the value 1 for the attempt frequency, leading to results in normalized time units. The total normalized time can later be divided by the fitted attempt frequency to transform it into physical time.

To estimate the attempt frequency, we use the same approach as detailed in [27]. We fit the relaxation time of a nanopillar on the {110} surface to MD results. A nanopillar with a rectangular cross-section (dimensions 2.0 × 2.8 × 1.7 nm; 12 monolayers, see [27] for details) is relaxed in both MD (using LAMMPS [35]) and KMC. The time taken for the pillar to reach half its original height is recorded from the MD simulations and compared with the normalized time for the same process to occur in KMC. The attempt frequency is then calculated from the ratio of these two times.

Figure 1 shows the relaxation time of the pillar for MD and KMC simulations at different temperatures. For each temperature, the system relaxation was performed for 10 cases with different random seeds to obtain a statistical estimate. Taking into account equation (3), the graph has been linearized by plotting the logarithm of the relaxation time against the inverse of the temperature. The different slopes indicate that the average effective transition energy barrier (parameter E in equation (3)) differs between MD and KMC. This is not surprising, since the method of calculating migration barriers makes several assumptions and simplifications (e.g. the rigid lattice and only nearest neighbor jumps).

The intercepts of the linear fits depend on the attempt frequency. Because of the difference in slopes between MD and KMC, the relaxation times cannot be made equal for all temperatures simultaneously. We selected an attempt frequency value that minimizes the sum of the differences between the measurement points. The resulting value is $\nu = 1.22 \times 10^{17}\ \mathrm{s}^{-1}$ and it has been used to normalize the KMC data points. The fitted lines intersect at 895 K.

The difference from typical MD atom oscillation frequency of $\sim 10^{13}\ \mathrm{s}^{-1}$ could possibly be explained by the fact that second nearest neighbor or longer jumps are not included in the model. These long jumps are known to have attempt frequencies that can be even four to seven orders of magnitude higher than the nearest neighbor jumps in the case of tungsten [36]. However, in our model, the same surface evolution is achieved by only allowing nearest neighbor jumps while second nearest neighbor jumps etc are covered by almost immediate follow-up jumps from unstable locations to stable ones. Since a series of such short jumps may happen with a different probability compared to a single long jump, the high attempt frequency we obtain by comparing with MD might be an indication that the long jumps may play a role. The sum of transition rates in equation (2) does not include these long jumps, increasing the time taken at each KMC step. However, since our model gives good agreement with experiments for the surface evolution (see section 4), the inclusion of long jumps would likely only affect the time estimate and thus lower the attempt frequency. The attempt frequency used in the current model can be seen as a normalization factor to fit the timescale to the more accurate MD method.

Similarly to previous results of attempt frequency calculations for Cu [27], the general temperature dependence using the two methods is similar. KMC tends to underestimate the relaxation time at lower temperatures and slightly overestimate it at higher temperatures. The variance in both MD and KMC increases significantly with decreasing temperature. The fact that the variance between repeated runs is the same for both MD and KMC, shows that it is caused by the underlying energetics of the system, rather than the method used to calculate the relaxation process.

The set of calculated migration barriers is included as supplementary material and is available online at stacks.iop.org/NANO/29/015704/mmedia.

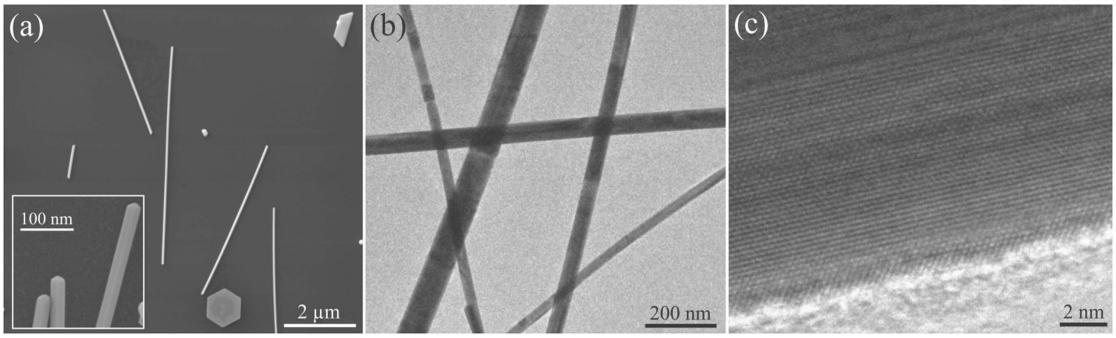

Figure 2. SEM (a) and TEM (b, c) images of untreated Au nanowires.

3. Results

3.1. Experimental results

According to SEM observation of an untreated sample (figure 2), synthesis yielded uniform high-aspect ratio nanowires with regular shape, well-pronounced facets (inset in figure 2(a)) and smooth surface, indicating a crystalline structure, confirmed by TEM imaging (figures 2(b) and (c)). Based on the SEM and TEM images, as well as according to the literature data [37, 38], obtained nanowires were grown along ⟨110⟩ direction and had pentagonal structure with outer planes being {100}. In addition to nanowires, the mixture contained nanorods, nanoparticles and plates.

After treatment at 473 K (200 °C) for 10 min, most of the separate nanowires did not show any noticeable signs of changes in morphology and unity. However, decomposition (fragmentation) of nanowires was observed at places where they cross or contact (figure 3(a)). Initial positions of nanowires can be deduced from traces left on the substrate by the surfactant. It can be seen that Au atoms migrated towards the contact point causing decomposition of nanowire ends.

At 673 K (400 °C) the phenomenon known as Rayleigh instability [39] appeared. Namely, in addition to decomposition at crossing and contact points (inset in figure 3(b)), some nanowires appeared to be fragmented to shorter pieces (figure 3(b)). Fragments had the same regular faceted structure as original nanowires.

At 873 K (600 °C) a large fraction of the nanowires was fragmented and fragments were shorter, although still had regular faceted structure (figure 3(c)).

At 973 K (700 °C) both for 1 min and 10 min most of the nanowires were fragmented to faceted nanoparticles (figure 3(d)).

It should be noted, that even at 973 K (700 °C) some intact nanowires or long nanowire fragments were found indicating that thermal stability and onset of fragmentation process may be very sensitive to the presence of certain critical defects in nanowires.

Similar annealing experiments were performed also on Ag nanowires and it was found that silver is even less stable at mild heating. Already after 10 min at 398 K (125 °C), a considerable fraction of the nanowires were broken at crossing points (figure 4). Note, that in figure 4(b) the intermediate state of fragmentation at the crossing point is pictured. It can be seen that material starts to diffuse from one nanowire to another.

We would like to note, that we made a series of high-magnification SEM images of crossing nanowires before heating to compare the same nanowires before and after thermal treatment. However, it was found that all crossing nanowires that were previously exposed to focused electron beam (e-beam) irradiation, survived thermal treatment without any noticeable signs of morphological changes. At the same time surrounding nanowires were fragmented and broken. We believe that this effect is caused by electron beam induced carbon deposition caused by the presence of surfactant (carbon containing organics) on the surface of nanowires and substrate before heating. This phenomenon is well known in the field of electron microscopy and is called 'electron beam induced deposition' [40–42]. Organic molecules decompose under focused e-beam and re-deposit on the surface of the nanowires forming a dense carbon coating. This coating, for instance, may hinder the mobility of atoms and prevent fusion and fragmentation of nanowires.

3.2. KMC simulation results

3.2.1. Rayleigh instability of a nanowire. The Rayleigh instability driven breakup of nanowires was simulated using the developed KMC model in order to validate it. This process is driven by surface energy minimization, where the resulting nanoclusters tend to be bounded by {111} surfaces.

Figure 5 shows four snapshots of a ⟨111⟩ nanowire (the ⟨111⟩ crystal direction was along the wire) as the breakup progresses. The nanowire's initial radius is 1 nm and the simulations are run at 1000 K. Atoms are colored according to type of surface they belong to. The surface type is determined by inspecting the number of nearest neighbors. The wire surfaces are initially {110}, which transition into the more energetically favorable surfaces {111} and {100}. As a result, the nanowire breaks up into three nanoclusters.

To obtain sufficient statistics of the resulting nanoparticle size and separation, we used smaller nanowires with a radius of 0.5 nm. For surface diffusion driven nanowire breakup, the average nanoparticle diameter and separation are related to

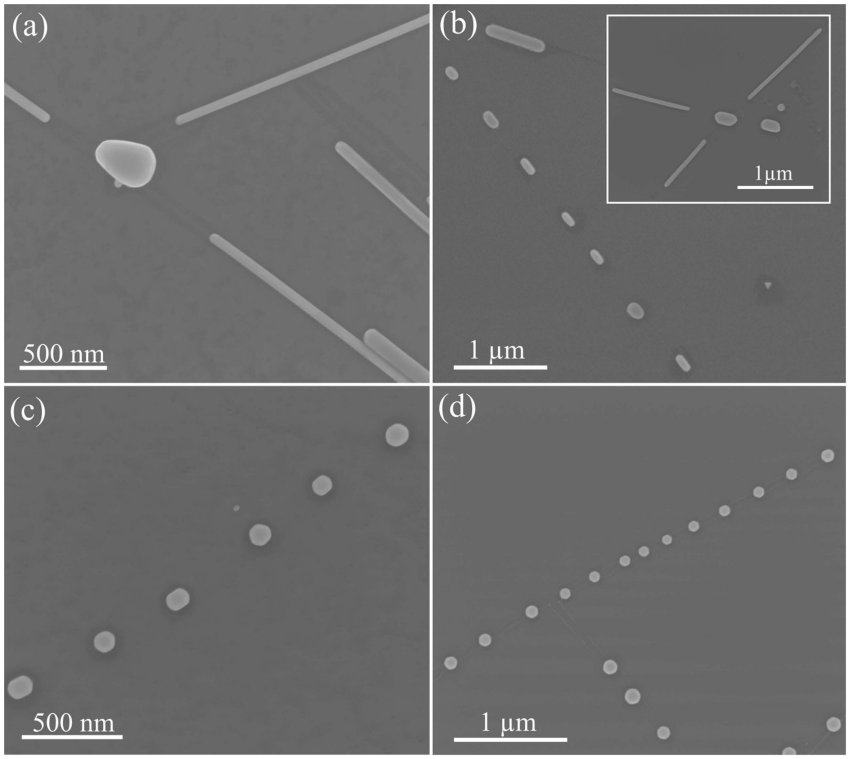

Figure 3. SEM images of Au nanowires after thermal treatment for 10 min at 200 °C (a), 400 °C (b), 600 °C (c) and 700 °C (d).

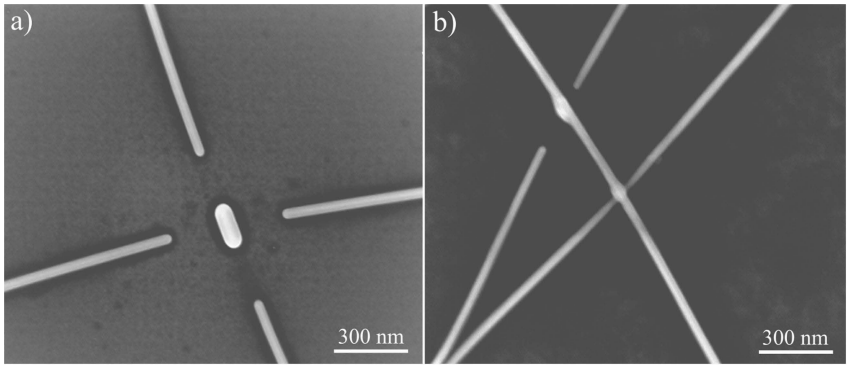

Figure 4. Fragmentation of Ag nanowires at crossing points as a result of thermal treatment for 10 min at 398 K (125 °C).

the initial nanowire radius. For a 0.5 nm nanowire, the theoretical average particle diameter is $d = 1.89$ nm and the average separation is $\lambda = 4.45$ nm [16, 39, 43]. From a series of simulations with $\langle 100 \rangle$ and $\langle 111 \rangle$ nanowires, we observed the formation of a total of 210 clusters. $\langle 110 \rangle$ wires are much more stable when it comes to surface diffusion processes and they do not break up in a reasonable simulation timeframe. The average measures for the 210 observed particles in our simulations are: $d = 2.01 \pm 0.17$ nm and $\lambda = 4.92 \pm 1.07$ nm. These results correspond very well with theoretical predictions, as well as other simulations [26], and confirm the validity of our parametrization.

3.2.2. Nanowire junctions. The same surface diffusion mechanism that is responsible for the breakup of a single nanowire acts when two wires are touching. Figure 6 depicts a sequence of simulation snapshots as a nanowire junction undergoes breakup. The simulation box is periodic along the wires, so both wires can be thought of as being infinitely long.

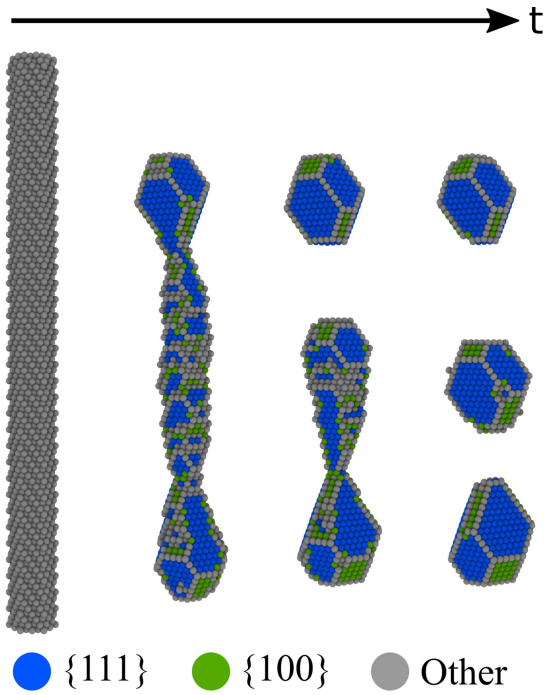

Figure 5. Breakup of ⟨111⟩ gold nanowire with radius 1 nm into clusters due to Rayleigh instability at 1000 K. The system is periodic along the wire. Atoms are colored according to surface type.

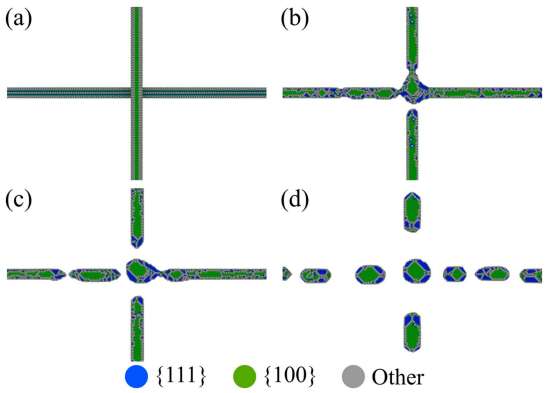

Figure 6. Breakup of a 1 nm radius nanowire junction where the crossing wires lie on top of each other at 1000 K (a). Atoms start collecting in the junction region (b), leading to a separation of the central droplet (c). Eventually, wires decompose into droplets (d).

Both wires are ⟨100⟩ in this case. The nanowire radius was 1 nm and the simulations were performed at 1000 K.

The simulation was repeated 20 times and the time of the first detachment was recorded (the moment in figure 6(b)). The average time for a first detachment to occur was 4.0 ± 0.8 ns. In all cases the first detachment happened near the junction and almost always the central cluster was the first to form completely, although in some cases a nearby cluster would form before the central cluster could detach from all four sides. A single longer simulation was run at 800 K where the time until the first detachment was 140 ns (see movie 1 in supplementary materials).

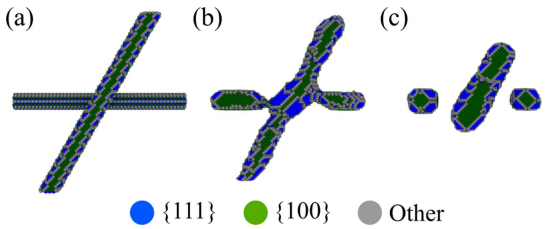

Figure 7. Breakup of a junction of non-periodic 1 nm radius wires at an oblique angle (1000 K). Initial configuration (a), intermediate state (b), and fragmented state (c). Available as movie 2 in supplementary materials.

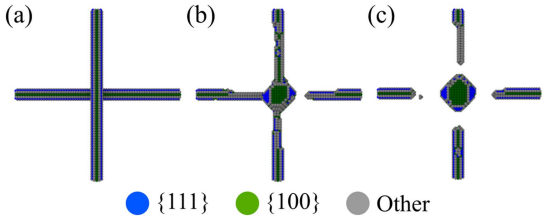

Figure 8. Crossing 0.6 nm ⟨110⟩ wires that break around the junction (1000 K). Initial configuration (a), first detachment (b) and completely separated central cluster (c). Available as movie 3 in supplementary materials.

Simulation of a less perfect system where the wires cross at an oblique angle (figure 7) also results in the wires breaking at the junction, even though in this case the wires are much shorter (the system is non-periodic). The horizontal wire was ⟨100⟩, as before.

In order to more closely approach the experimental five-fold twinned nanowires, we simulated crossing ⟨110⟩ nanowires. Figure 8 shows two periodic ⟨110⟩ wires breaking up around their point of contact. Because ⟨110⟩ nanowire breakup is much slower, the system had to be reduced in size to nanowire radius of 0.6 nm.

We simulated an explicit array of nanowires. In a larger system, significantly more computational resources need to be spent to reach the same physical time. Even so, already at 5.4 ns we can see fragments forming at both junctions where two of the wires have separated (figure 9).

4. Discussion

From the simulations we can see that nanowire breakup around junctions is driven by surface diffusion of atoms, similarly to the Rayleigh instability breakup. In case of a single nanowire, the size and positioning of the resulting clusters is random, though, the average size and separation can be predicted based on the initial nanowire radius. In case of a nanowire junction, however, a cluster always forms at the

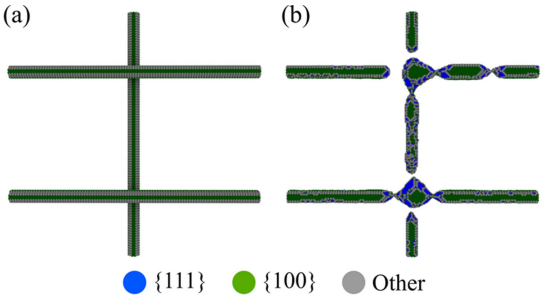

Figure 9. Formation of fragments at two nearby junctions in an array of crossing nanowires. Initial configuration (a) and partially detached central fragments at 5.7 ns (b). Available as movie 4 in supplementary materials.

point where the wires intersect, and its size tends to be larger than the surrounding clusters due to the contribution of atoms from two wires instead of just one. Additionally, the breakup always starts at the junction because the intersecting nanowire surfaces act as defects, breaking the symmetry and encouraging atom diffusion.

In general, atoms have a higher probability to jump to sites with more neighbors. This explains the preference of atoms to accumulate at the wire crossing because the presence of two intersecting surfaces creates vacant sites with more neighbors than available on a single surface.

⟨100⟩ FCC nanowires are unstable due to the shape memory effect [44] as they tend to rearrange their lattice to have the ⟨110⟩ direction along the wire. Such a rearrangement is outside the scope of fixed lattice KMC simulations. However, both ⟨100⟩ and ⟨111⟩ led to the same end result with fragmentation driven by surface energy minimization. Even though simulating the Rayleigh instability breakup of a single ⟨110⟩ wire proved impractical, placing two of them into contact in a reduced system resulted in a breakup process around the junction point, as seen in figure 8. Therefore, it is reasonable to assume that the characterization of the junction breakups seen in ⟨100⟩ wire simulations is applicable also to the ⟨110⟩ case.

The wires used in experiment have a five-fold twinned structure, where the crystal direction along the wire is ⟨110⟩. Because of the on-lattice nature of the KMC model, simulating such a structure is impossible. The closest structure, which we could use in the simulations to imitate the experiment, is to use a single crystal NW with the ⟨110⟩ direction along the wire. However, we can see similar structures forming both in experiments and in simulations irrespective of wire orientation, which indicates that the breakup process is driven by atom diffusion that is independent of the specific configuration.

Because of the thermally activated nature of the atomic diffusion, the timeframe of nanowire breakup is highly temperature dependent. Reducing the simulation temperature by just 20% resulted in a 30-fold increase in the time until the first detachment from the junction. In the experiment, treating nanowires at a temperature of 473 K (200 °C) for 10 min showed fragmentation almost exclusively at junctions only, which clearly shows the accelerating effect these sites have on nanowire fragmentation. Separate nanowires were significantly more stable at elevated temperatures.

The size of wires in simulations is necessarily much smaller than in experiments because of the large amount of computational resources required. However, as the KMC model does not include size effects, the result of atom diffusion is similar to the larger experimental systems. To further speed up the calculations, the temperature is also elevated compared to experiments. This is justified as we are still below melting temperature in its classical meaning, so that heating only accelerates processes that happen also at lower temperatures.

The breakup of nanowires due to Rayleigh instability has been observed for other FCC metals as well, and we have previously simulated this effect for Cu. Thus, the junction effect should behave in a similar manner for nanowires made of these metals. This is confirmed experimentally for the case of Ag, as seen in figure 4. Here we note that the non-spherical shapes can be explained by rather low temperatures used in the experiments with Ag NWs ($T = 398$ K; 125 °C), which resulted in only partial decomposition of the junction and an elongated central fragment. This is also observed for Au NWs in figures 3(a) and (b) for the temperatures $\leqslant$400 °C. At higher temperatures or longer thermal treatment times, all the NWs will break into fragments due to Rayleigh instability and the fragments will relax to spherical shapes as seen in figures 3(c) and (d). Because the temperature in KMC simulations is much higher (1000 K), fragments quickly become spherical, although elongated intermediate shapes can be seen in figure 6(d).

Because a cluster is always expected to form at a nanowire junction during annealing, we hypothesize that it is possible to fabricate regular arrays of nanodots by arranging nanowires in a grid and annealing them to induce the clusters to form at junctions. Furthermore, between the junctions, the nanowires will form nanodots with an average spacing $\lambda = 8.89 \cdot r$ given by the Rayleigh instability, where r is the radius of the original wire [39, 43]. Nanowires can be relatively easily arranged and aligned e.g. by dielectrophoresis [45]. The simulation with an array of wires (figure 9) indicates that the clusters can be expected to form at the junction points with high reliability. When fragmentation is undesirable, a dense coating can be applied on nanowires to prevent diffusion of atoms as was found in present work.

5. Conclusions

We performed annealing experiments and corresponding kinetic Monte Carlo simulations which show that two touching Au nanowires will break up in a specific manner where a cluster will form at the former junction of the nanowires. Annealing was conducted with Au and Ag nanowires at fixed temperatures 473, 673, 873 and 973 K (200 °C, 400 °C, 600 °C and 700 °C) during a time period of 10 min. In all cases, the junction breakup happened in a

similar fashion for both metals. The experiments showed that junctions tended to break up even at lower temperatures when the wires themselves remained whole. We have developed a gold parametrization for the KMC code Kimocs which we have used to show that the breakup can be entirely explained by atom diffusion processes and the breakup of nanowires will always start at the junction. The point of nanowire contact acts as a preferential site for atomic diffusion due to the greater number of neighboring atoms present near surface intersections. The accumulation of atoms results in the formation of a cluster that is cut off from the nanowires. Thermal treatment significantly accelerates this process. We propose that nanowire junctions can be used to control the positioning of nanodots after thermal annealing of nanowires and that regular arrays of nanodots can be fabricated by aligning the nanowires in a grid.

Acknowledgments

This work has been supported by Estonian Research Council grants PUT 1372 and PUT 1689. V Jansson was supported by Academy of Finland (Grant No. 285382) and Waldemar von Frenckells Stiftelse. E Baibuz was supported by a CERN K-contract and the doctoral program MATRENA of the University of Helsinki. F Djurabekova was supported by Academy of Finland (Grant No. 269696). B Polyakov was supported by the Latvian National Research Program IMIS2. The authors wish to acknowledge High Performance Computing Centre of University of Tartu and CSC—IT Center for Science, Finland, for computational resources. Authors are also grateful to Mikk Vahtrus for SEM images of thermally treated Ag nanowires.

ORCID iDs

Simon Vigonski https://orcid.org/0000-0002-2849-2882
Ville Jansson https://orcid.org/0000-0001-6560-9982
Sergei Vlassov https://orcid.org/0000-0001-9396-4252
Boris Polyakov https://orcid.org/0000-0002-6626-1065
Ekaterina Baibuz https://orcid.org/0000-0002-9099-1455
Sven Oras https://orcid.org/0000-0002-8313-8608
Alvo Aabloo https://orcid.org/0000-0002-0183-1282
Flyura Djurabekova https://orcid.org/0000-0002-5828-200X
Vahur Zadin https://orcid.org/0000-0003-0590-2583

References

[1] Brüggemann D, Wolfrum B, Maybeck V, Mourzina Y, Jansen M and Offenhäusser A 2011 Nanostructured gold microelectrodes for extracellular recording from electrogenic cells *Nanotechnology* **22** 265104
[2] Cherevko S and Chung C-H 2009 Gold nanowire array electrode for non-enzymatic voltammetric and amperometric glucose detection *Sensors Actuators* B **142** 216–23
[3] Wang K and Crozier K B 2012 Plasmonic trapping with a gold nanopillar *ChemPhysChem* **13** 2639–48
[4] Zhang R and Olin H 2014 Porous gold films—a short review on recent progress *Materials* **7** 3834–54
[5] Jin W and Maduraiveeran G 2017 Electrochemical detection of chemical pollutants based on gold nanomaterials *Trends Environ. Anal. Chem.* **14** 28–36
[6] Lin Y, Zou Y, Mo Y, Guo J and Lindquist R G 2010 E-beam patterned gold nanodot arrays on optical fiber tips for localized surface plasmon resonance biochemical sensing *Sensors* **10** 9397–406
[7] Lim S H, Derkacs D and Yu E T 2009 Light scattering into silicon-on-insulator waveguide modes by random and periodic gold nanodot arrays *J. Appl. Phys.* **105** 073101
[8] Chen Y, Wang Y, Peng J, Xu Q, Weng J and Xu J 2017 Assembly of ultrathin gold nanowires: from polymer analogue to colloidal block *ACS Nano* **11** 2756–63
[9] Elechiguerra J L, Reyes-Gasga J and Yacaman M J 2006 The role of twinning in shape evolution of anisotropic noble metal nanostructures *J. Mater. Chem.* **16** 3906–19
[10] Anon 1996 Fabrication of gold nanodot array using anodic porous alumina as an evaporation mask *Japan. J. Appl. Phys.* **35** L126
[11] Li H, Low J, Brown K S and Wu N 2008 Large-area well-ordered nanodot array pattern fabricated with self-assembled nanosphere template *IEEE Sens. J.* **8** 880–4
[12] Otnes G and Borgström M T 2017 Towards high efficiency nanowire solar cells *Nano Today* **12** 31–45
[13] Sannicolo T, Lagrange M, Cabos A, Celle C, Simonato J-P and Bellet D 2016 Metallic nanowire-based transparent electrodes for next generation flexible devices: a review *Small* **12** 6052–75
[14] P Langley D, Lagrange M, Giusti G, Jiménez C, Bréchet Y, D Nguyen N and Bellet D 2014 Metallic nanowire networks: effects of thermal annealing on electrical resistance *Nanoscale* **6** 13535–43
[15] Li H, Biser J M, Perkins J T, Dutta S, Vinci R P and Chan H M 2008 Thermal stability of Cu nanowires on a sapphire substrate *J. Appl. Phys.* **103** 024315
[16] Karim S, Toimil-Molares M E, Balogh A G, Ensinger W, Cornelius T W, Khan E U and Neumann R 2006 Morphological evolution of Au nanowires controlled by Rayleigh instability *Nanotechnology* **17** 5954
[17] Granberg F, Parviainen S, Djurabekova F and Nordlund K 2014 Investigation of the thermal stability of Cu nanowires using atomistic simulations *J. Appl. Phys.* **115** 213518
[18] Buffat P and Borel J P 1976 Size effect on the melting temperature of gold particles *Phys. Rev.* A **13** 2287
[19] Gonzalez-Garcia L, Maurer J H M, Reiser B, Kanelidis I and Kraus T 2016 Ultrathin gold nanowires for transparent electronics: breaking barriers *Proc. Eng.* **141** 152–6
[20] De S, Higgins T M, Lyons P E, Doherty E M, Nirmalraj P N, Blau W J, Boland J J and Coleman J N 2009 Silver nanowire networks as flexible, transparent, conducting films: extremely high DC to optical conductivity ratios *ACS Nano* **3** 1767–74
[21] Diao J, Gall K, Dunn M L and Zimmerman J A 2006 Atomistic simulations of the yielding of gold nanowires *Acta Mater.* **54** 643–53
[22] Zepeda-Ruiz L A, Sadigh B, Biener J, Hodge A M and Hamza A V 2007 Mechanical response of freestanding Au nanopillars under compression *Appl. Phys. Lett.* **91** 101907
[23] Pereira Z S and da Silva E Z 2011 Cold welding of gold and silver nanowires: a molecular dynamics study *J. Phys. Chem.* C **115** 22870–6
[24] Kolosov A Y, Sdobnyakov N Y, Myasnichenko V S and Sokolov D N 2016 Investigation into the structure and

features of the coalescence of differently shaped metal nanoclusters *J. Synchrotron Invest.* **10** 1292–9
[25] He X, Cheng F and Chen Z-X 2016 The lattice Kinetic Monte Carlo simulation of atomic diffusion and structural transition for gold *Sci. Rep.* **6** 33128
[26] Müller T, Heinig K-H and Schmidt B 2002 Template-directed self-assembly of buried nanowires and the pearling instability *Mater. Sci. Eng.* C **19** 209–13
[27] Jansson V, Baibuz E and Djurabekova F 2016 Long-term stability of Cu surface nanotips *Nanotechnology* **27** 265708
[28] Zhao J *et al* 2016 Formation mechanism of Fe nanocubes by magnetron sputtering inert gas condensation *ACS Nano* **10** 4684–94
[29] Kim F, Sohn K, Wu J and Huang J 2008 Chemical synthesis of gold nanowires in acidic solutions *J. Am. Chem. Soc.* **130** 14442–3
[30] Grochola G, Russo S P and Snook I K 2005 On fitting a gold embedded atom method potential using the force matching method *J. Chem. Phys.* **123** 204719
[31] Vitos L, Ruban A V, Skriver H L and Kollár J 1998 The surface energy of metals *Surf. Sci.* **411** 186–202
[32] Vermaak J S and Kuhlmann-Wilsdorf D 1968 Measurement of the average surface stress of gold as a function of temperature in the temperature range 50–985.deg. *J. Phys. Chem.* **72** 4150–4
[33] Henkelman G, Jóhannesson G and Jónsson H 2002 Methods for finding saddle points and minimum energy paths *Theoretical Methods in Condensed Phase Chemistry Progress in Theoretical Chemistry and Physics* ed S D Schwartz (Netherlands: Springer) pp 269–302
[34] Baibuz E, Vigonski S, Lahtinen J, Zhao J, Jansson V, Zadin V and Djurabekova F 2017 Migration barriers for surface diffusion on a rigid lattice: challenges and solutions *Submitted to Comput. Mater. Sci.* arXiv:1707.05765
[35] Plimpton S 1995 Fast parallel algorithms for short-range molecular dynamics *J. Comput. Phys.* **117** 1–19
[36] Antczak G and Ehrlich G 2004 Long jump rates in surface diffusion: W on W(110) *Phys. Rev. Lett.* **92** 166105
[37] Chen H, Gao Y, Zhang H, Liu L, Yu H, Tian H, Xie S and Li J 2004 Transmission-electron-microscopy study on fivefold twinned silver nanorods *J. Phys. Chem.* B **108** 12038–43
[38] Gryaznov V G, Heydenreich J, Kaprelov A M, Nepijko S A, Romanov A E and Urban J 1999 Pentagonal symmetry and disclinations in small particles *Cryst. Res. Technol.* **34** 1091–119
[39] Nichols F A and Mullins W W 1965 Morphological changes of a surface of revolution due to capillarity-induced surface diffusion *J. Appl. Phys.* **36** 1826–35
[40] Randolph S J, Fowlkes J D and Rack P D 2006 Focused, nanoscale electron-beam-induced deposition and etching *Crit. Rev. Solid State Mater. Sci.* **31** 55–89
[41] Furuya K 2008 Nanofabrication by advanced electron microscopy using intense and focused beam *Sci. Technol. Adv. Mater.* **9** 014110
[42] Song M and Furuya K 2008 Fabrication and characterization of nanostructures on insulator substrates by electron-beam-induced deposition *Sci. Technol. Adv. Mater.* **9** 023002
[43] Molares M E T, Balogh A G, Cornelius T W, Neumann R and Trautmann C 2004 Fragmentation of nanowires driven by Rayleigh instability *Appl. Phys. Lett.* **85** 5337–9
[44] Veske M, Parviainen S, Zadin V, Aabloo A and Djurabekova F 2016 Electrodynamics—molecular dynamics simulations of the stability of Cu nanotips under high electric field *J. Phys. D: Appl. Phys.* **49** 215301
[45] Raychaudhuri S, Dayeh S A, Wang D and Yu E T 2009 Precise semiconductor nanowire placement through dielectrophoresis *Nano Lett.* **9** 2260–6